

Nikolas Thomas Weissmueller

University of Oxford, St. Cross College

Supervisor

Professor Andrew J. Pollard
Dr. Heiko A. Schiffter

NEEDLE-FREE VACCINATION: Formulation and Dermal Delivery of Diphtheria Toxin CRM_{197} Mutant

A thesis submitted for the degree of Doctor of Philosophy

Trinity Term 2013

"I shall endeavour still further to prosecute this inquiry, an inquiry I trust not merely speculative, but of sufficient moment to inspire the pleasing hope of its becoming essentially beneficial to mankind."
– *Edward Jenner*

A thesis submitted for the degree of Doctor of Philosophy.

Needle-free Vaccination: Formulation and Dermal Delivery of Diphtheria Toxin CRM_{197} Mutant

By Nikolas Thomas Weissmueller, University of Oxford, St. Cross College.

Submitted Trinity Term 2013.

Abstract

The unsafe use of needles propagates cross infections with bloodborne pathogens and reduces the positive impact of vaccinations on global health. While a plethora of needle-free injection devices exist, the reformulation of protein-based vaccines is largely empirical and costly, which presents a barrier to their widespread clinical application.

This thesis contributes to the identification of approaches that facilitate rapid vaccine reformulation and enhance the immunogenicity of needle-free dry-powder vaccines with the help of novel antigen delivery platforms.

We hypothesised that the thermodynamic stabilisation of diphtheria toxin mutant 197 (CRM_{197}), a glycoconjugate vaccine carrier protein, may enhance its structural preservation during spray-freeze-drying (SFD), and that its formulation in either soluble, surface-adsorbed, or nanoparticle form impacts the elicited immune response.

Differential scanning fluorimetry was used to study the effect of excipients on the thermal stability of CRM_{197}. Dry-powder formulation of CRM_{197} used i) encapsulation into a thermodynamically stabilising excipient matrix by SFD, ii) surface-immobilisation via physisorption onto a novel potassium-doped hydroxyapatite (kHA) carrier microparticle formed by molten salt synthesis, and iii) chemical conjugation and surface presentation on amphiphilic block copolymer nanoparticles that were incorporated into SFD-powders (SFD-NP). The structural integrity of CRM_{197} was assessed by size separation in addition to various spectral and thermal analysis methods. The immunogenicity of dry-powder CRM_{197} formulations was subsequently tested *in vivo*.

The results suggest that the thermodynamic stability of CRM_{197} in solution does not ensure its structural stability during SFD. While needle-free dermal vaccination with kHA-adsorbed CRM_{197} induced comparable antibody titres to conventional IM injection of alum-adjuvanted CRM_{197}, needle-free SFD and SFD-NP powders were less immunogenic. The highest mean IgG titre and most balanced Th1/Th2 response was achieved with nanoparticle-conjugated CRM_{197} by IM, which outperformed the current clinical standard. Therefore, future vaccine design should combine thermodynamic and kinetic stability screening, and place special emphasis on the delivery and structural presentation of the antigen to the immune system.

(300 words)

Statement of Originality

I hereby declare that this submission is my own work and to the best of my knowledge it contains no materials previously published or written by another person, or substantial proportions of material which have been accepted for the award of any other degree or diploma at the University of Oxford or any other educational institution, except where due acknowledgement is made in the thesis.

Any contribution made to the research by others, with whom I have worked at the University of Oxford or elsewhere, is explicitly acknowledged in the thesis.

I also declare that the intellectual content of this thesis is the product of my own work, except to the extent that assistance from others in the project's design and conception or in style, presentation and linguistic expression is acknowledged.

Nikolas Thomas Weissmueller
10 October 2013.

Acknowledgements

The highly collaborative project that I have been fortunate to dedicate myself towards over the past 3 years has allowed me to learn from and work with a large number of inspiring academics across various disciplines, to all of whom I am genuinely grateful.

First and foremost, I would like to thank my supervisors Professor Andrew J. Pollard and Dr. Heiko A. Schiffter for their support. Their expert advice and guidance has allowed me to explore broadly yet think deeply while keeping my aim true to the straight and narrow of my project.

I owe a great deal to Dr. Robert Carlisle and Dr. Christine Rollier who have been my first point of contact for any enquiry, not to mention their patience and enthusiasm that has helped me identify and achieve one goal at a time. Similarly, I would like to express my sincere gratitude to Professor Robert K. Prud'homme and Dr. Adam York from Princeton University. The time and research with the RKP-Lab in Princeton, New Jersey, has been tremendously enriching.

Without the funds generously provided by the Department of Paediatrics and the Oxford Martin School at the University of Oxford, and the Oxford-Princeton Seed Fund along with funds provided by Professor Prud'homme at Princeton University, the realisation of this project would not have been possible. I would also like to thank Novartis Vaccines and Diagnostics for providing the CRM_{197} protein free of charge, and ParticlesTherapeutics Ltd for providing the Venturi needle-free injector.

A special 'thank you' is due to Professor Constantin C. Coussios and the Biomedical Ultrasonics, Biotherapy and Biopharmaceuticals Laboratory (BUBBL) and the Oxford Vaccine Group (OVG) for providing a stimulating and enabling framework that fostered my academic growth.

I would like to thank all who have contributed to my work in any way: Dr. Andrew Norton for his support with the nanoindentation experi-

ments, Dr. Philip Holdway for his assistance with XRD, Dr. Cuneyt Tas for his advice on material characterisation, Mr. Felix Wolf for his help with SEM imaging, and Mr. James Fisk and Mr. David Salisbury of the IBME workshop for expertly engineering any designs my experiments required.

To those whose love and encouragement have supported, inspired, and guided me over the years: I would not have reached this far without you. Mom, Dad, Michael, and Valentine, this thesis is dedicated to you.

This thesis template was created by Brett Tully (2010) and further developed by Nikolas Weissmueller (2013)

Dissemination

Peer Reviewed Journal Papers

Weissmueller, N.T., Schiffter, H.A., and Pollard, A.J. Intradermal powder immunization with protein-containing vaccines. *Expert Rev Vaccines*, 12(6):687–702, Jun 2013.

Weissmueller, N.T., Schiffter, H.A., Pollard, A.J, and Tas A.C. Molten salt synthesis of potassium-containing hydroxyapatite microparticles used as protein substrate. *Mater Lett*, Under review.

Weissmueller, N.T., Schiffter, H.A., Carlisle, R.S., Rollier, C.S., and Pollard, A.J. Potassium-doped hydroxyapatite microparticles for needle-free intradermal protein delivery. *Clin Vaccine Immunol*, Under review.

Weissmueller, N.T., York, A., Schiffter, H.A., Carlisle, R.S., Rollier, C.S., Prud-homme, R.K., and Pollard, A.J. Needle-free co-delivery of antigen-conjugated block copolymer nanoparticles enhances the humoral immune response to Diphtheria Toxin Mutant 197, Manuscript in preparation.

Peer Reviewed Abstracts and Posters

Weissmueller, N.T., Schiffter, H.A., Carlisle, R.S., Rollier, C.S., and Pollard, A.J. Diphtheria Toxin Mutant CRM_{197} Aluminum Adjuvantation Alters Secondary Structure and Thermal Unfolding Behavior. American Association of Pharmaceutical Scientists (AAPS), National Biotech Conference, San Diego, USA, May 2013.

Weissmueller, N.T., Schiffter, H.A., Rollier, C.S., and Pollard, A.J. Manufacture of Spray-freeze-dried (SFD) Micropaticles for Needle-Free Ballistic Powder Immunization (BPI) with Protein-based Vaccines. American Association of Pharmaceutical Scientists (AAPS), Annual Meeting and Exposition, Washington DC, USA, October 2011.

Weissmueller, N.T., Rollier, C.S., Pollard, A.J., and Schiffter, H.A. Protein-coated beta-Tricalcium Phosphate Microcrystals For Needle-Free Ballistic Delivery. American Association of Pharmaceutical Scientists (AAPS), Annual Meeting and Exposition, Washington DC, USA, October 2011.

Grants

Weissmueller, N.T., Schiffter, H.A., and Prud-homme, R.K. Nanoparticle Therapeutics for Needle Free Vaccine Delivery. Oxford – Princeton Collaborative Research Grants. Planned research, wrote proposal, received £12,000. http://www.princeton.edu/international/doc/OP-2012-13-Prudhomme-Nanoparticle-Therapeutics-for-Needle-Free-Vaccine-Delivery.pdf. Cited October, 2013.

Abstracts

Weissmueller, N.T., Rollier, C.S., and Pollard, A.J. Thermal stability of the adjuvanted diphtheria toxin mutant CRM_{197}. Nuffield Department of Obstetrics and Gynaecology and Department of Paediatrics Graduate Symposium, Oxford, UK, November 2012.

Talks

Weissmueller, N.T. Microparticle approaches to needle-free delivery of Hib vaccines. Nuffield Department of Obstetrics and Gynaecology and Department of Paediatrics Graduate Symposium, Oxford, UK, January 2012.

CONTENTS

Contents xiii

List of Figures xvii

List of Tables xx

Acronyms xxii

1 Needle-free Vaccination: Introduction and Literature Review 1

1.1 Background and Context 2
1.2 The Picture in 2012 4
1.3 Needle-free Powder Immunisation: Challenges and Possible Solutions 6
1.4 Polysaccharide Encapsulated Bacteria: Disease Burden and Prevention 8
1.5 Immunological Underpinnings: Glycoconjugates and the Skin 10
1.5.1 The Immunogenicity of Glycoconjugates 10
1.5.2 The Immunocompetence of Skin 13
1.5.3 Intramuscular and Mucosal Inoculation 15
1.6 Needle-free Cutaneous Vaccination: Target and Technologies 17
1.6.1 The Target - Composition of the Dermis 17
1.6.2 Intradermal Powder Injection: Basic Particle Injection Considerations 22
1.7 Protein Fundamentals: Stability, Denaturation, and Dry-Powder Formulation 22
1.7.1 The Need for Thermostable Protein Formulations 22
1.7.2 Modes and Implications of Protein Degradation 23
1.7.3 The Rationale for Formulation Excipients 26
1.7.4 Basic Energetics of Protein Aggregation 28
1.8 Needle-free Intradermal Powder Injection: Literature Review 31
1.9 Diphtheria Toxin Mutant 197: Structure and Chemical Conjugation . . 34

1.9.1 CRM_{197} Structure and Function 34
1.9.2 Use of CRM_{197} in Conjugate Vaccines 37
1.10 Alternate Drug Delivery Particles: Bioceramic Microparticles and Polymer Nanoparticles 39
1.10.1 Hydroxyapatite as Drug Delivery Substrate 39
1.10.2 Molten Salt Synthesis (MSS) of Hydroxyapatite Particles 40
1.10.3 Polymer Nanoparticles: Flash NanoPrecipitation and Therapeutic Applications 41
1.11 Needle-free Ballistic Injection: Mathematical Models of Particle Penetration Depth 43
1.12 Needle-free Ballistic Injection: Injectors 47
1.13 Dissertation Aims and Objectives 49

2 Materials and Methods **53**
2.1 Excipient Screen and SFD Powder Manufacture and Characterisation 53
2.1.1 Manufacture of Spray-Freeze-Dried Powders 53
2.1.2 Asymmetric Flow Field Flow Fractionation (AF_4) 54
2.1.3 Differential Scanning Fluorimetry 58
2.1.4 Karl-Fisher Titration- Residual Moisture Determination 60
2.1.5 Differential Scanning Calorimetry - (m)DSC 60
2.1.6 Helium-Pycnometry and Tapped Density Measurements . . . 61
2.1.7 Particle Size Analysis with Laser Light Diffraction 62
2.1.8 Fluorimetry 63
2.1.9 Scanning Electron Microscopy 63
2.1.10 Turbidity Measurement 63
2.1.11 CRM_{197} Loss During Ultrasound Atomisation with Surfactants 64
2.2 Bioceramic Crystal Manufacture and Characterisation 64
2.2.1 K-HA Particle Manufacture and FTIR 64
2.2.2 HA and kHA Protein Loading 65
2.2.3 kHA CRM_{197} Dry-Powder Formulation and *In Vitro* Release . . 66
2.2.4 Structural Characterisation of Surface Adsorbed CRM_{197} . . . 67
2.2.5 X-ray Diffraction and Energy Dispersive X-ray analysis 68
2.2.6 Nanoindentation of Single kHA Crystals 69
2.2.7 Atomic Adsorption Spectroscopy 69
2.3 Nanoparticle Manufacture, CRM_{197}-conjugation and Structural Analysis 70
2.3.1 Block Co-polymer Nanoparticle Formation by Flash Nano-Precipitation 70

2.3.2 Design of Experiments (DOE) - Nanoparticle Size 73
2.3.3 SDS-PAGE 74
2.3.4 Structural Analysis of CRM_{197} on NPs 75
2.4 Particle Injection and Vaccine Immunogenicity Study 76
2.4.1 Agarose Targets 76
2.4.2 Injection Depth and Dermal Measurements 77
2.4.3 Histology Staining 78
2.4.4 Needle-free Immunisation Study Setup: SFD, SFD-NP, and kHA Dry CRM_{197} Powders 79
2.4.5 Manufacture of NP-CRM_{197}-containing TMDD by SFD 80
2.4.6 Enzyme-linked Immunosorbent Assay 81
2.5 Statistical Analysis 82

3 Spray-lyophilisation of CRM_{197} 83
3.1 Introduction 83
3.2 Results and Discussion 85
3.2.1 Spray-lyophilisation Process 85
3.2.2 Formulation Design 89
3.2.3 Physical Characterisation of SFD Formulations 105
3.2.4 Evaluation of SFD Formulations by AF_4 113
3.3 Chapter Summary 121

4 Bioceramic Powder as Protein Delivery Vehicle 125
4.1 Introduction 125
4.2 Results and Discussion 127
4.2.1 Bioceramic Microparticles Prepared by Molten Salt Synthesis . 128
4.2.2 Microparticle Manufacture from Pure HA and the Effect of K_2SO_4 Salt Flux on Particle Characteristics 135
4.2.3 Surface Functional Group Characterisation Using FTIR 138
4.2.4 BSA and CRM_{197} Surface Adsorption onto kHA Microparticles and CRM_{197} Release *In Vitro* 141
4.2.5 Secondary Structure and Thermal Unfolding Behaviour of CRM_{197} in the Surface Adsorbed State 143
4.3 Chapter Summary 149

5 Functionalised Block Copolymer Nanoparticles as Novel Adjuvant 151
5.1 Introduction 151
5.2 Results and Discussion 153
5.2.1 Investigation of Nanoparticle Size by Design of Experiments . 153

5.2.2 CRM_{197} Conjugation to NP . . . 157
5.2.3 NP in SFD Powder . . . 162
5.2.4 Structural Analysis of CRM_{197} on NPs . . . 163
5.3 Chapter Summary . . . 165

6 Particle Injection and Immunogenicity of CRM_{197} Formulations 169
6.1 Introduction . . . 169
6.2 Results and Discussion . . . 171
6.2.1 Particle Penetration- Comparison of Three Particle Types in Agar and Murine Pinna . . . 171
6.2.2 Intradermal Particle Placement by Injection-site Location . . . 174
6.2.3 Novel Approach to Injection Depth Modelling for Ballistic Particle Injection . . . 176
6.2.4 Needle-free vaccination: Immunogenicity of CRM_{197}-adsorbed Bioceramic Powders . . . 184
6.2.5 Needle-free vaccination: Immunogenicity of CRM_{197}-conjugated NPs loaded in TMDD Microparticles Manufactured by SFD . . . 188
6.3 Chapter Summary . . . 196

7 Conclusions and Future Directions 199
7.1 Background and Aims . . . 199
7.2 Results in Context and Future Directions . . . 200
7.2.1 Spray-lyophilisation of CRM_{197} . . . 200
7.2.2 Bioceramic Powder as Protein Delivery Vehicle . . . 202
7.2.3 Functionalised Block Copolymer Nanoparticles As Novel Adjuvant . . . 204
7.2.4 Particle Injection and Immunogenicity of CRM_{197} Formulations . . . 207
7.3 Societal Impact and Commercial Benefit . . . 209

References 211

A Appendix - Tables 227

List of Figures

1.1 Hib Disease Prevalence World Map . . . 9
1.2 Glycoconjugate Immune Cell Activation . . . 11
1.3 Cutaneous Immune Surveillance . . . 14
1.4 Needle-free Cutaneous Drug Delivery Approaches . . . 19
1.5 Preferential Protein Interaction or Exclusion of Osmolytes . . . 27
1.6 Effect of Stabilising Co-Solutes on Protein Energetics . . . 30
1.7 Molecular Structure of CRM_{197} Superimposed on Diphtheria Toxin . . . 36
1.8 Lysine Groups on CRM_{197}: Conjugation Sites for Capsular Polysaccharides 38
1.9 Charge Density Distribution on Hydroxyapatite Crystal Surface . . . 40
1.10 Kendall Model Fit to Data . . . 46
1.11 Needle-free Particle Injector Devices . . . 48

2.1 SFD - Setup . . . 55
2.2 AF4 Separation Channel Schematic . . . 56
2.3 AF4 CRM_{197} Separation Method . . . 57
2.4 Differential Scanning Fluorimetry - Protein Unfolding Profile . . . 59
2.5 Nanoparticle Formation and Ligand Conjugation . . . 72
2.6 SDS-PAGE MW Estimation Correction . . . 75
2.7 Particle Injection Depth Measurement . . . 78
2.8 Immunogenicity Study Design . . . 80

3.1 SFD Stress Evaluation After Procedural Steps . . . 86
3.2 SFD Process Stress Evaluation - Turbidity . . . 87
3.3 SFD Process Stress Evaluation - Surfactants . . . 88
3.4 DSF - Buffer Salts and pH . . . 91
3.5 DSF - Coupled and Decoupled Thermal Unfolding . . . 93
3.6 DSF - Saccharides and Polysaccharides . . . 96
3.7 DSF - Amino Acids and Polymers . . . 99
3.8 DSF - Formulations . . . 100

3.9 T_m by TRP Fluorescence Scatter Plot . . . 103
3.10 Linear Regression of T_m and Tryptophan Emission . . . 104
3.11 Lyophilisation Process Data for TMDD(3:3:3:1) . . . 107
3.12 SEM of Sucrose and Trehalose Powders . . . 109
3.13 SEM of TMDD and TGDD Powders . . . 111
3.14 AF_4 Method Validation . . . 115
3.15 AF_4 Analysis of TMDD-BSA Formulation . . . 118
3.16 AF_4 Separation of TMDD and TGDD Formulations . . . 120
3.17 Turbidity of TMDD and TGDD Solutions after Atomisation and SFD Re-suspension . . . 121

4.1 X-ray Diffractograms of Reaction Products . . . 129
4.2 HA Batch Morphology by SEM . . . 131
4.3 Hardness and Young's Modulus of Single Rod-like and Spheroidal HA Crystals by Nanoindentation . . . 132
4.4 Protein Adsorption Propensity of HA Crystals Manufactured by Method I 133
4.5 SEM of MSS kHA Powders . . . 136
4.6 XRD Spectra of HA and kHA Manufactured by MSS . . . 137
4.7 EDS and BSA-TRITC Adsorption as Function of K_2SO_4Flux . . . 139
4.8 FTIR Spectrum of HA and kHA Particles . . . 140
4.9 CRM_{197} Adsorption and Release from kHA *in vitro* . . . 142
4.10 CRM_{197} Thermal Unfolding in PBS Measured by FTIR . . . 144
4.11 FTIR Unfolding Curves of CRM_{197} Secondary Structures . . . 146
4.12 CRM_{197} Thermal Unfolding in Surface-adsorbed State . . . 148

5.1 Linear Regression and Sweet Spot of Nanoparticle Sizes as Function of PS and PEG by DOE: . . . 155
5.2 Design Space of Nanoparticle Sizes as Function of PS and PEG by DOE . . 155
5.3 CRM_{197}-conjugation to NPs . . . 158
5.4 SDS-PAGE of CRM_{197}-conjugated NPs . . . 159
5.5 SDS-PAGE Quantitive Analysis of CRM_{197}-NP . . . 161
5.6 NP-loaded TMDD particles manufactured by SFD . . . 164

6.1 Particle penetration into Agarose Gel . . . 173
6.2 kHA Particle Injection into Murine Pinna . . . 175
6.3 Kendall Model Fit to kHA Particles Injection Depth . . . 177
6.4 Chi-square Goodness-of-fit Test on kHA Particle Size and Penetration Depth Data . . . 178
6.5 kHA Particle Distribution and Cumulative Density Function . . . 180

6.6 Correlation of Particle Size and Penetration Depth by Cumulative Density 183
6.7 kHA-CRM_{197}-Study: IgG Titres 185
6.8 kHA-CRM_{197}-Study: IgG Subclass titres 187
6.9 Day 28: IgG titres of SFD With and Without NP 190
6.10 Day 42: IgG titres of SFD With and Without NP 191
6.11 Day 42: IgG1 Subclass titres of SFD With and Without NP. 193
6.12 Day 42: IgG2a Subclass titres of SFD With and Without NP 194

List of Tables

2.1 SFD- and NP Immunogenicity Study Formulations. 81

3.1 Physical Properties of Formulations after SFD: Size distribution, density, and impact parameter. 108
3.2 Thermal Analysis of Formulations: Glass transition, heat capacity change, and residual moisture. 113
3.3 AF_4 Results on SFD CRM_{197} Formulations. Note: These data only capture the soluble protein fraction but not any precipitated protein. 117

4.1 Effect of Flux-to-HA Ratio on the Properties of HA Particles Manufactured by MSS. 136
4.2 Secondary Structure of Surface-adsorbed CRM_{197}. Note: The BioATR was used to measure the relative structural changes of CRM_{197}. The comparator here is CRM_{197} in PBS. 145

5.1 Intensity-weighted DLS measurements of NP mean diameter throughout FNP manufacture and CRM_{197}-conjugation. 156
5.2 Molecular Weights by SDS-PAGE of NPs, CRM_{197}-conjugated NPs, and CRM_{197} Stock Solution. 159
5.3 Physical Characteristics of TMDD-NP Powder Prepared by SFD. 163
5.4 Thermal Analysis of NP-Formulations: Glass transition, heat capacity change, and residual moisture. 163
5.5 Secondary and Tertiary Structure of CRM_{197} in the NP-conjugated State Assessed by FTIR, Deconvoluted and Peak-fitted. 165

6.1 Particle Penetration Study in Agar and Murine Skin. 172
6.2 Microscopy measurements on histology describing kHA powder placement in the skin and dermal dimensions. 174

A.1 DSF - Salts and pH. Standard Deviation for T_m values range from ± 0.0°C to ± 0.5°C. . . . 228
A.2 DSF - Saccharides. Standard Deviation for T_m values ranges from ± 0.0°C to ± 0.5°C. . . . 229
A.3 DSF - Polyols, polymers, polypeptitdes, and polysaccharides. Standard Deviation for T_m values range from ± 0.0°C to ± 0.5°C. . . . 230
A.4 DSF - Amino acids. Standard Deviation for T_m values range from ± 0.0°C to ± 0.5°C. . . . 231
A.5 T_m and TRP Peak Emission. Standard deviations for T_m values ranged from ± 0.0°C to ± 0.5°C, and tryptophan excitation/emission peas from ± 0nm to ± 1nm. . . . 232
A.6 Catalogue Numbers for Chemicals and Reagents Used in the Experiments - Part I. . . . 233
A.7 Catalogue Numbers for Chemicals and Reagents Used in the Experiments - Part II. . . . 234
A.8 Catalogue Numbers for Non-standard Consumables Used in the Experiments. . . . 235
A.9 Part 1 of 5 – Findings of past IPI *in vivo* studies by vaccine type, study plan, antigen formulation and adjuvantation. . . . 236
A.10 Part 2 of 5 – Findings of past IPI *in vivo* studies by vaccine type, study plan, antigen formulation and adjuvantation. . . . 237
A.11 Part 3 of 5 – Findings of past IPI *in vivo* studies by vaccine type, study plan, antigen formulation and adjuvantation. . . . 238
A.12 Part 4 of 5 – Findings of past IPI *in vivo* studies by vaccine type, study plan, antigen formulation and adjuvantation. . . . 239
A.13 Part 5 of 5 – Findings of past IPI *in vivo* studies by vaccine type, study plan, antigen formulation and adjuvantation. . . . 240
A.14 Summary of IPI challenge studies. . . . 241

ACRONYMS

AB	Antibody
AF_4	Asymmetric flow field flow fractionation
ANOVA	Analysis of variance
APC	Antigen-presenting cell
API	Active pharmaceutical ingredient
BCA	Bicinchoninic acid
BCR	B cell receptor
BOT	Base of tale
BPI	Ballistic powder injection
BSA	Bovine serum albumin
CAM	Cell adhesion molecule
CDF	Cumulative distribution function
CIJ	Confined impinging jet
CLA	Cutaneous lymphocyte antigen
CPS	Capsular polysaccharides
CPS	Counts per second
CRM_{197}	Cross-reacting material 197 - diphtheria toxin mutant 197
DLS	Dynamic light scattering
DOE	Design of experiments
DSC	Differential scanning calorimetry
DSF	Differential scanning fluorimetry
DT	Diphtheria toxoid
DTP	Diphtheria-tetanus-whole cell pertussis
EDS	Energy-disperse X-ray spectroscopy
EF-2	Elongation factor-2
ELISA	Enzyme-linked immunosorbent assay
FITC	Fluorescein isothiocyanate
FNP	Flash nano precipitation
FTIR	Fourier transform infrared spectroscopy

GAVI	Global Alliance for Vaccines and Immunisation
GRAS	Generally regarded as safe
HA	Hydroxyapatite
HB-EGF	Heparin binding EGF-like growth factor
HIB	*Haemophilus influenzae* type b
HNS	Hypodermic needle and syringe
ICAM-1	Intracellular adhesion molecule-1
ICDD	International Centre for Diffraction Data
IGG	Immunoglobulin isotype G
IM	Intra muscular
IPI	Intradermal powder immunisation
KHA	Potassium-doped hydroxyapatite
LD_{50}	Median lethal dose
LC	Langerhans cell
LFA-1	Lymphocyte function-associated antigen
LN_2	Liquid nitrogen
LTR72	Mutant heat-labile enterotoxin of *Escherichia coli*
MALS	Multi angle light scattering
MHC	Major histocompatibility complex
MPD	Mean particle penetration depth
MSS	Molten salt synthesis
MW	Molecular weight
NAD	Nicotinamide dinucleotide
NF-κB	Nuclear factor kappa-light-chain-enhancer of activated B cells
NP	Nanoparticle
NSI	Needle stick injuries
OMP	Outer membrane protein
PAMP	Pathogen associated molecular pattern
PDF	Probability density function
PDI	Polydispersity index
PEG	Polyethylene glycol
PNP	Para-nitrophenol
PPD	Particle penetration depth
PRP	Polyribosylribitol phosphate
PS	Polystyrene
PSD	Particle size distribution
QBD	Quality by design
RI	Refractive index

sc	*Stratum corneum*
SC	Subcutaneous
SD	Spray-drying
SDS-PAGE	Sodium dodecyl sulfate-polyacrylamide gel electrophoresis
SEM	Scanning electron microscopy
SED	Safety-engineered devices
SFD	Spray-freeze-drying
T_c	Collapse temperature
TCR	T cell receptor
T_g	Glass transition temperature (solid)
T_g'	Glass transition temperature (frozen)
TLR	Toll-like receptor
T_m	Melting temperature
TMDD	Trehalose, mannitol, dextran (150k), dextran (10k)
TGDD	Trehalose, glycine, dextran (150k), dextran (10k)
T_{prod}	Product temperature
TRITC	Tetramethylrhodamine isothiocyanate
TRP	Tryptophan
VCAM-1	Vascular-cell adhesion molecule-1
ve	Viable epidermis
VLA-4	Very late antigen-4
XRD	X-ray diffraction

CHAPTER 1

NEEDLE-FREE VACCINATION: INTRODUCTION AND LITERATURE REVIEW

The struggle to prevent disease globally is perpetual. While much progress has been made, vaccines and delivery strategies can be further improved. Needle-free dermal immunisation may expand the medical arsenal that is used to combat infectious diseases, but current trends in the pharmaceutical industry combined with the persisting challenge of vaccine reformulation and targeted delivery impede its uptake. First, this chapter describes the rationale for the development of needle-free vaccination against polysaccharide encapsulated bacteria and juxtaposes the need with the current trends in the pharmaceutical industry. Second, this chapter introduces formulation design considerations that critically impact the structural stability and retention of the antigen in solution and in the dry state. Furthermore, it provides an overview of dermal immune surveillance, glycoconjugate immune activation, and ballistic particle delivery to the skin. The structure and function of CRM_{197} is delineated individually and as substituent of glycoconjugate vaccines. Past results of intradermal powder immunisation with protein-containing vaccines are briefly reviewed. Some alternate particle and formulation approaches are introduced. Finally, the aims of this thesis are outlined.

1.1 Background and Context

Since their advent in 1798, following the description of the first smallpox vaccine by Edward Jenner, vaccinations have markedly reduced morbidity and mortality associated with a plethora of infectious diseases. As concentrated efforts broaden the spectrum of vaccines and their global coverage, the increased number of needle and syringe injections in this form of prophylactic medical intervention, may increasingly become a vector of disease. The unsafe use of needles may lead to cross infections with bloodborne viruses, which is a problem especially in countries where needles are routinely reused. In 2003, the Grand Challenges in Global Health Initiative described the development of needle-free systems for vaccines "that do not require refrigeration" as two of the "scientific or technological innovations that remove a critical barrier to solving an important health problem in the developing world with a high likelihood of global impact and feasibility" [Varmus et al. (2003)]. Specifically, a technology that successfully removes these barriers to widespread dissemination of vaccines should have a low cost per dose ratio, sufficient stability of the bioactive compound during transport and storage without refrigeration, an inoculation procedure that obviates the need for trained medical personnel, and an inoculation device that protects the care provider and vaccinee from blood borne pathogens [Varmus et al. (2003)]. Despite substantial advances in needle-free delivery devices and in the manufacture of stable vaccines over the past decade, the initial grand challenge persists [Mitragotri (2005); Prausnitz and Langer (2008); Senior (2011)].

In 2004, approximately 12 billion injections were given annually worldwide, of which 5% were immunisations. At the reported rate of 5 accidental needle-stick injuries (NSIs) per 100 injections, this suggests that approximately 30 million vaccina-

tions resulted in NSIs. NSIs may cause cross infections with bloodborne pathogens, including HIV, hepatitis B, and hepatitis C, and present a significant threat to patients and health care professionals [Kermode (2004); World Health Organization (2002); Cardo et al. (1997)]. An estimated 2 million NSIs are incurred by healthcare workers annually, with 90% of the burden sustained in developing countries [Wilburn and Eijkemans (2004)]. Up to 84% of American healthcare workers experience NSIs annually. Immediate treatment costs in 2002 were reported to range between US$ 51 and US$ 3,766 per incident, and potential individual long-term treatment costs were in excess of several hundred thousand dollars if diseases such as HIV, or hepatitis B or C had been contracted [Wilburn and Eijkemans (2004)].

Young children are at greatest risk of infection. By the age of 18 months, toddlers in the US and the UK will have received approximately 10 prophylactic inoculations containing 20 – 25 vaccine doses [CDC (1999)]. Therefore, in many industrialised nations, needle-free vaccinations would have an important impact on acceptability of immunisation. In addition to accidents, the misuse of needles is a serious concern. In the developing world, annually up to 50% of injections are unsafe and give rise to 21 million, 2 million and 260,000 new cases of hepatitis B, hepatitis C and HIV respectively [World Health Organization (2004)].

By example of *Haemophilus influenzae* type b (Hib), only 10 years ago, despite the staggering global need and the availability of a 95%-100% protective vaccine [World-Health-Organization:2006uq], Hib vaccinations essentially remained the privilege of affluent countries [Booy (1998)]. This stood in stark disproportion to the burden of disease, which mainly lay with the developing countries [Scott (2007); Booy (1998)]. Given a "widespread use of conjugate vaccines in the developing world", experts remarked, the impact may "prevent millions of deaths in the next decade" [Pollard et al. (2009)]. Although the price had declined to US$ 2 per dose,

the total cost of US$ 6 per individual for a complete vaccination routine proved to be insurmountable for many resource-deprived countries [CDC (1994)].

1.2 The Picture in 2012

Over the last 7 years, the remarkable efforts by the GAVI and the WHO have provided Hib vaccines to numerous developing countries. In 2005, GAVI invested US$ 37 million to create the Hib Initiative with the aims of spreading awareness of Hib disease and establishing global vaccination coverage. Further catalysed by the WHO health report on Hib disease in 2006, by 2008, 50% of all low-income countries had obtained access to the Hib vaccine [GAVI (2011)]. A first field study in 2008, conducted in Uganda, reported an 85% decrease in Hib disease incidences [Lee et al. (2008a)]. One year later, in 2009, Hib vaccines had reached almost all low-income countries [GAVI (2011)]. The near completion of this important aim raises the question of whether resources should still be directed towards the attainment of cheaper Hib vaccines. A closer look at GAVI's future directions demonstrates that this is still an important and urgent goal. Thus far, GAVI has shouldered all costs of providing the expensive Hib vaccine to minimally affluent countries. However, in December 2010, the GAVI board passed a new co-financing policy that "phased-out" full Hib vaccine subsidy in 2012 and requires countries to finance the vaccine autonomously, first partially, then completely [GAVI (2010)]. Initially, the poorest countries will be required to contribute 20 cents per dose with an annual 15% increase in cost until the vaccine is fully self-financed [GAVI (2010)]. It seems questionable whether the poorest countries will see an economic growth in line with these steep requirements. Factually, without GAVI subsidy, the state of 2005 prevails. The Hib vaccine may once again prove to be too expensive for the countries with the greatest need. A

sustainable solution to cater to the continued need during fading GAVI support will likely require a technological innovation that effectively reduces vaccine production and supply costs. A pharmaceutical company that meets this challenge could enjoy a lucrative competitive advantage, particularly once the scramble for the most cost-effective Hib vaccine recommences.

In contrast to the apparent clinical need for needle-free vaccines, the current trends in the pharmaceutical industry complicate the required research and development (R&D) investments. Over the last 10 years, the industry as a whole has seen a value destruction of US$ 550bn along with an increase in R&D spending from 10% to 16% [Dhankhar et al. (2012)]. Conversely, the average economic return on investment dropped from 13%-15% in 1990, to 4%-9% in the past decade. Some key challenges that contributed to the loss in profitability are growing clinical trials costs, falling discovery rates in therapeutics, more crowded markets, and higher bars for commercial success [Dhankhar et al. (2012)]. The industry response has been a migration away from a "shots on goal" approach to investigational new drugs and consolidated R&D divisions with the directive for design of experiment (DOE) and quality by design (QbD) to reduce spending. Furthermore, vaccines are complex therapeutics that are difficult to produce consistently, and in addition to their generally costly licensure may be subject to merely cyclic demand. Therefore, vaccines simultaneously present a challenge and an opportunity to pharmaceutical companies: high barriers to entry need to be overcome, but the successful licensure of a vaccine may enable a lucrative competitive advantage for the company with the most efficacious, economical, and ‘consumer-friendly’ product.

1.3 Needle-free Powder Immunisation: Challenges and Possible Solutions

Intradermal powder immunisation (IPI) uses pressurised gas to deliver dry-powder vaccines to the superficial dermal layers and thereby may avoid the pain and bleeding associated with hypodermic needles. However, IPI faces several challenges in addition to the prevalent forces of the pharmaceutical market. The successful stabilisation and prolonged retention of bioactivity of a therapeutic protein molecule in dry-powder form requires the repeated empirical investigation of various vaccine reformulations. This aspect presents a reoccurring challenge due to the complex, highly variable, and poorly understood physicochemical interactions at molecular level. Regulatory bodies require evidence of efficacy and safety determined by clinical data, even for existing vaccines, which is expensive to provide. Precise dosing presents a challenge as the governing ballistic equations amplify minor variations in particle size, density, or speed to a potentially unacceptable variation in dermal penetration depth [Kendall et al. (2004a)]. Additionally, animal models are only marginally predictive of vaccine efficacy in humans, due to inherent differences in skin properties and the underlying immune response. Furthermore, the requirement of pressurised helium capsules for ballistic powder injectors, and sterility of device and particles, adds to the cost per vaccine dose and may render IPI unfeasible for resource-deprived countries [Weissmueller et al. (2013)].

However, the aforementioned challenges may not impede a more specialised success of IPI technology. For example, the recent use of safety-engineered devises (SED) was correlated with a substantial reduction in the incidence of NSIs (22%-100%). However, SEDs were also reported to account for 21% of NSIs [Tosini et al. (2010)], and so while SEDs reduce NSIs, they are not needle-free and therefore have

iatrogenic potential. It therefore seems that truly needle-free technologies are required to fully eliminate NSIs. New technologies may help to overcome the long-standing obstacles to IPI. Novel high-throughput screening tools may facilitate protein vaccine formulation. A wide array of nanoparticle carriers may be used to protect and deliver antigens when loaded inside a micron-sized powder particle [Leleux and Roy (2013); Gutierro et al. (2002)]. The immobilisation of diphtheria toxoid onto carrier crystals reported promising results for long-term vaccine preservation and subsequent delivery [Murdan et al. (2005)]. Combinations of traditional formulation processes, such as spray-drying and spray-lyophilisation, with these novel technologies may facilitate antigen reformulation. Furthermore, a recent design alteration to the powder injector device uses a converging-diverging supersonic nozzle that achieves a more uniform particle velocity profile and may significantly improve dose targeting [Liu and Kendall (2007)]. Vaccine reformulation may be less expensive than the development of new vaccines, as the existing knowledge of the effects of the already licensed vaccine may enable a streamlined process from bench to bedside with a high probability of success. Although IPI will likely remain too expensive for cheap vaccines such as diphtheria-tetanus-whole cell pertussis (DTP) at US$0.05-0.30 per dose, a potential dose sparing in bacterial conjugate vaccines with US$35-60 per dose may prove profitable [Kersten and Hirschberg (2007)]. Even at an additional price premium, IPI would suitably meet the needle-free requirements posed by industrialised countries and emergency vaccination programs [Kersten and Hirschberg (2007)]. There are benefits and barriers to each of the possible parenteral delivery routes and an obviously superior approach is not apparent at this time. Therefore, a renewed investigation of powder delivery to the skin may be equally as promising as other needle-free devices, particularly since several new technologies appear to be readily incorporated with conventional powder formulation for needle-free powder injection [Weissmueller et al. (2013)].

1.4 Polysaccharide Encapsulated Bacteria: Disease Burden and Prevention

The propensity of polysaccharide encapsulated bacteria to evade the immune system contributes to the severe morbidity and mortality associated with infection. Capsular polysaccharides (CPS) can physically mask immunogenic subcapsular components of the pathogen, bind serum proteins to their charged moieties, and reduce the binding affinity of factor B, all of which inhibit the activation of the alternative complement pathway that promotes phagocytosis [Edwards et al. (1980); Avci and Kasper (2010)]. Therefore, *Haemophilus influenzae*, *Neisseria meningitidis*, and *Streptococcus pneumoniae* are effectively shielded by their polysaccharide capsule from the destruction and clearance by the host immune system.

Infection can be devastating. The Gram-negative coccobacillus *Haemophilus influenzae* type b (Hib), for example, was estimated to be the cause of 3 million cases of disease associated with severe morbidity and 386 000 deaths annually (Figure 1.1) [World Health Organization (2006)]. Amongst the 6 polysaccharide-encapsulated strains (a – f), the polyribosylribitol phosphate (PRP) encapsulated type b accounts for more than 90% of observed systemic infections. While in most cases *Haemophilus influenzae* are generally benign nasopharygeal commensal bacteria, in some few cases, Hib does invade body fluids such as blood, cerebrospinal fluid or peritoneal fluid [Peltola et al. (1977); Peltola (2000)]. Invasive Hib primarily causes pneumonia and meningitis, but may also give rise to epiglottitis, septicemia, osteomyelitis, cellulitis, septic arthritis and pericarditis [Kelly et al. (2004)]. In particular, Hib is the major cause of non-epidemic bacterial meningitis during the first year of life and despite immediate antibiotic treatment, mortality rates range from 3 – 20%, and up to 30 – 40% of survivors suffer severe neurological sequelae [Pel-



Figure 1.1: Hib Disease Prevalence World Map: The majority of the Hib disease burden falls on resource-deprived countries [World Health Organization (2006)]. *Note: This figure is not available in the electronic version due to copyright.*

tola (2000)]. *Neisseria meningitidis* and *Streptococcus pneumoniae* further add to the disease burden of CPS encapsulated bacteria [Kelly et al. (2011)].

CPS significantly contribute to bacterial virulence, but they also present an excellent target for disease prevention. Over the past 20 years, the inoculation with purified CPS motifs that are covalently linked to immunogenic protein carriers have drastically reduced the disease burden caused by *Haemophilus influenzae*, *S. pneumoniae*, and *N. meningitidis* [Kelly et al. (2004); Lesinski and Westerink (2001)]. Despite their enormous impact, glycoconjugates require further optimisation. For instance, a single dose rarely confers protection, especially in very young, elderly, or immunocomprised patients [Kamboj et al. (2003)]. Evidence from a 1999-2002 UK study in infants suggests, that despite a significantly improved glycoconjugate vaccine efficacy, antibody titres induced by a single inoculation wane swiftly and render the infant susceptible to disease [Barbour et al. (1993); Kelly et al. (2004)]. Therefore,

immunisation schedules with elaborate prime and booster regimens were further revised to ensure lasting protection. Frequently, the first vaccine dose is given at around 6–8 weeks of age and is followed by two additional prime doses in 4–8 week intervals, and eventually followed by a booster dose administration at 12–18 months of age[Pollard (2007)].

1.5 Immunological Underpinnings: Glycoconjugates and the Skin

1.5.1 The Immunogenicity of Glycoconjugates

Although glycoconjugates have been extensively researched, their mechanism of immunogenicity is still a matter of active investigation [Mazmanian and Kasper (2006); Avci et al. (2011)]. In children less than two years of age, the administration of the purified type-b PRP polysaccharide antigen alone has been shown to induce low serum antibody titres, which frequently prove insufficient to grant protection from invasive disease [Peltola et al. (1977); Peter (1998)]. While the antigen is recognised by B-cell receptors via surface receptor cross-linking, antigen presentation to T helper cells does not occur and therefore, without germinal centre formation, neither isotype-switched and avidity matured B-cells, nor memory B-cells arise [Lai and Schreiber (2009); Blanchard-Rohner and Pollard (2011)]. Thus, the immunogenicity of the antigen is considerably reduced without immune memory and long term protection [Kelly et al. (2004); Schmitt et al. (2001)]. However, once covalently conjugated to a protein carrier such as CRM_{197}, diphtheria toxoid, tetanus toxoid, or *Neisseria meningitidis* outer membrane proteins (OMPs), the glycoconjugate antigen is highly immunogenic across all ages [Schneerson et al. (1980)].



(a)



(b)

Figure 1.2: Glycoconjugate Immune Cell Activation: a) Pure polysaccharides are largely T-cell independent antigens, but their conjugation to an immunogenic peptide make them T-cell dependent. The current understanding of a glycoconjugate vaccine's bidirectional activation of B and T cells proceeds via the MHC II presentation of a T-cell epitope peptide to T-cells [Pollard et al. (2009)], and differs from a b) new model in which a truncated polysaccharide-peptide complex is presented to T cells on the MHC II of the B cell [Avci et al. (2011)]. *Note: This figure is not available in the electronic version due to copyright.*

The established model of glycoconjugate function states that the polysaccharide chain on the glycoconjugate can bind and cross link polysaccharide-specific surface B cell receptors (Figure 1.2, a). Upon internalisation, the endosome-resident acidic proteases split the carrier protein into peptides, and the generated T cell epitopes are presented on MHC II molecule on the B cell surface. In the event of recognition of the T-cell epitope-MHC II complex by the $\alpha\beta$ T cell receptor on CD4+ T cells, and in the presence of a co-stimulatory interaction between the CD80/86 molecule on the B cell with CD28 on the T cell, T cell activation occurs [Caux et al. (1994); Avci and Kasper (2010)]. The T cell upregulates its IL-2 secretion and IL-2 receptor expression. The activated T cell then activates the B cell. The T cell secretes IL-4 to signal to the IL-4 receptor on the B cell. Additionally, the CD40L costimulatory molecule on the T cell ligates with CD40 on the B cell. This bidirectional activation of B and T cell in turn stimulates the formation of germinal centres, in which hypersomatic mutation and class switching from IgM-to-IgG of antibody can occur. The result is the secretion of high affinity antibody (IgG) by plasma cells and improved preparedness for future infections by the same pathogen mediated by long-lived memory B cells [Martini et al. (2011); Guttormsen et al. (1999); Pollard et al. (2009)].

Previously it was believed that the CPS on glycoconjugates merely target the peptide to the PS-specific B-cell. However, the most recent working model suggests that both protein and polysaccharide are chemically cleaved and that a truncated polysaccharide-peptide complex is presented to T cells via the MHC II molecule [Avci et al. (2011)]. This is novel because most PSs in isolation cannot be presented in MHC II molecules and are therefore T cell independent antigens (Figure 1.2, ba). However, zwitter-ionic polysaccharides were found to be T cell dependent antigens, which suggests that $\alpha\beta$ TCR on the CD4+ T cells can recognise some PS [Kalka-Moll et al. (2002)]. If this theory holds true, then the potency of glycoconjugate vac-

cines may be significantly improved by vaccine constructs that form a large number peptide-glycan moieties during endolysosomal digestion. Impressive data in favour of this theory has been presented [Avci et al. (2011)]. In addition to the underlying glycoconjugate immunobiology, it is important to appreciate the cutaneous immunocompetence to further inform vaccine formulation and delivery.

1.5.2 The Immunocompetence of Skin

Phenotypically immature Langerhans cells (LCs) line the epidermis in a tightly woven network of cytoplasmic processes which cover 25% of the epidermal area. Upon contact with an antigen, LCs endocytose the antigen, detach from their network due to inflammatory cytokine cues provided by the innate response of surrounding keratinocytes, and migrate and mature in the lymphatic system to antigen-presenting cells (APCs) before interacting with naïve T cells in the lymph nodes [Dean et al. (2003)]. Endocytosed antigen may be transported from vesicles into the APCs cytosol. Cytosolic protein is processed by proteasomes into smaller peptides and presented in a peptide-MHC I complex on the APCs surface, while processed vesicular proteins are expressed as a peptide-MHC II complex, which present to CD8+ (cytolytic) and CD4+ (helper) T cells respectively [Abbas et al. (2000); Bosch et al. (2013); Trowsdale and Campbell (1992)]. The antigen presentation by APCs to naïve T-cells induces glycosylation enzymes that modify P-selectin glycoprotein ligand-1 to express cutaneous lymphocyte antigen (CLA) on the cell surface of the resultant memory T-cells [Fuhlbrigge et al. (1997)]. CLA integrally participates in the attachment of memory T-cells on the endothelium in cutaneous postcapillary venules followed by abluminal extravasation, which enables specific homing to the skin [Robert and Kupper (1999); Picker et al. (1993)]. CLA positive memory T-cells are recruited to the site of inflammation via upregulated NF-κB gene transcription



Figure 1.3: Cutaneous Immune Surveillance: Cytokine release and the activation of local Toll-like receptors (TLRs) by microbial motifs and other danger signals upregulate NF-κB gene transcription in the tissue to recruit CLA positive T-cells to the site of injury via an increased presentation of various adhesion molecules on the interior venule surface close to the site of injury [Robert and Kupper (1999)]. *Note: This figure is not available in the electronic version due to copyright.*

of adhesion molecules E-selectin, intercellular adhesion molecule-1 (ICAM-1), and vascular-cell adhesion molecule-1 (VCAM-1) on the luminal side of endothelial cells [Kupper and Fuhlbrigge (2004)].

CLA-positive memory T-cells tether to epithelial E-selectin with their surface CLA-PSGL-1. The uptake of various chemokines, which are diffused into the venule from the inflamed surrounding tissue, allows the CLA positive T cell to bind to ICAM-1 and VCAM-1 as they structurally alter lymphocyte function-associated antigen 1 (LFA-1) and very late antigen-4 (VLA-4) respectively. Once securely bound, the T-cell flattens and extravasates out of the venule to actively participate in the immune reaction at the site of original pathogen entry [Von Andrian and Mackay (2000); Stein et al. (1999)]. For instance, T-cell originated chemokines have been shown to induce chemoattractant CXCL9, 10 and 11 secretion in keratinocytes to

further recruit APCs [Klunker et al. (2003)]. CLA-positive memory T-cell homing is summarised in Figure 1.3. In addition to the innate immune response and the subsequent feedback loop involving the adaptive immune response of skin-homing effector memory T-cells, the cutaneous immune system also increases pathogen recognition systemically. Next to CLA-positive memory T-cells, the initial APCs antigen presentation to naïve T-cells in skin draining lymph nodes also gives rise to antigen-specific central memory T-cells, that express ligands CD62 and CCR7 and have been found to patrol the systemic lymphatic system [Sallusto et al. (1999)]. These three interconnected components of the cutaneous immune response extend from the site of pathogen entry, to tissue homing antigen specific cell mediated immunity, to systemic immunity of the entire organism and confer an unique immunological potency to the skin, which renders it an especially appealing target for alternate immunisation procedures such as IPI [Bal et al. (2010)].

1.5.3 Intramuscular and Mucosal Inoculation

The utility of needle-free inoculation methods in the skin should be weighed against other approaches. The ability to mediate protection at distant effector sites and to engage the humoral and cellular branch of the systemic immune system is common to mucosal, intra muscular, and cutaneous vaccination [Neutra and Kozlowski (2006); Girardi (2007)]. However, there are also apparent differences. Vaccine delivery to oral, nasal, pulmonary, or urogential mucosa has high local relevance since most pathogens invade via the mucosal surfaces. Patient compliance and ease of access are high for oral and nasal delivery, while delivery device cost and complexity are comparatively low. Mucosal success stories are the oral polio vaccine and the pulmonary measles vaccination [Zhaori et al. (1988); Fernández-de Castro et al. (1997); Lin et al. (2011)]. Barriers to mucosal vaccine delivery include the difficulty

of protection of the bioactive compound from inactivation by secretory antibodies, enzymatic digestion, dilution and excretion by the mucous, which complicate targeted vaccine delivery and is evidenced by mixed clinical outcomes [Woodrow et al. (2012)]. Additionally, the need for a high dose of antigen and aggressive adjuvantation, such as cholera toxin or LTR72 heat-labile enterotoxin mutant of *Escherichia coli*, and the potential interference with concomitant infections are current limitations of mucosal delivery. In the case of pulmonary and urogenital delivery, device costs and poor patient compliance can be additional limiting factors respectively [Mitragotri (2005)]. Since imprecise dosing to the mucosa could induce tolerance instead of protection, the room for error is small [Chase (1946); Holmgren and Czerkinsky (2005)].

Although skeletal muscle actively participates in immune reactions, very few professional APCs actually reside within muscle tissue [Page et al. (2002)]. Skeletal muscle *in vivo* expresses no detectable MHC under physiological conditions, but inflammation or a combination of local injury and adjuvant presentation may induce facultative antigen-presenting capabilities [Wiendl et al. (2005)]. Upon inflammatory stimuli *in vitro*, myoblasts have been reported to process antigens in MHC type I and type II pathways, secrete soluble factors, express cell adhesion molecules (CAMs), cytokine receptors, Toll-like receptors (TLRs) and costimulatory molecules [Michaelis et al. (1993); Goebels et al. (1992); Mantegazza et al. (1991); Boyd et al. (2006); Marino et al. (2011)]. Only upon inflammatory stimuli, which are sustained by myoblasts to perpetuate the immune response, more professional APCs are recruited [Marino et al. (2011)]. Initially low numbers of APCs in the vaccination target tissue could cause a delay, which may prove detrimental to injected protein antigens, as physiological conditions could denature the antigen before APC uptake. While skeletal muscle tissue presents a readily accessible and

reliably targetable injection site with conventional needle and syringe, immunobiological considerations suggest dermal rather than intramuscular vaccine delivery to be more efficacious.

1.6 Needle-free Cutaneous Vaccination: Target and Technologies

1.6.1 The Target - Composition of the Dermis

The viable epidermis (*ve*), a layer of 50 – 100 μm thickness, lies directly beneath the 10 – 20 μm thick most outer layer of the skin, which comprises of keratinised epidermal cells and is known as stratum corneum (*sc*) [Sandby-Møller et al. (2003); Madison (2003)]. The 10 – 60 layers of flattened corneocytes are cast in an intercellular matrix comprising free fatty acids, long-chain ceramides, cholesterol, cholesterol sulfate, wax esters, and triglycerides, which bestow a "mortar-and-brick" like structure to the *sc* [Torin Huzil et al. (2011)]. This "wall" of hydrophilic cells and hydrophobic lipids presents an effective barrier to molecules and organisms greater than 500 Da [Bos and Meinardi (2000)]. The *sc* presents the physical "road-block" to needle-free percutaneous and transcutaneous vaccination [Kendall et al. (2004c)]. Variable physiological properties of the skin further complicate proper epidermal dry-powder vaccine placement. The skin's mechanical resistance to penetration varies significantly with species, age, ethnicity, injection site, gender, relative humidity, and ambient temperature [Holbrook and Odland (1974); Yosipovitch et al. (1998); Darlenski and Fluhr (2012)]. For example, a temperature rise of 20°C was associated with a doubling of penetration depth, and an 80% increase in humidity caused a 1.8 fold increase [Kendall et al. (2004c)]. In light of needle-free powder

injection, the lack of vasculature and low density of sensory nerve endings in the epidermis mean that epidermal vaccine delivery can avoid the bleeding and pain associated with hypodermic needle injections and may thereby circumvent needle-phobia [Dean et al. (2003); Hamilton (1995)].

A plethora of approaches to achieve permeation or penetration of the *sc* barrier are shown in Figure 1.4. A physical disruption of the *sc* can be achieved by electroporation, which disrupts the lipid bilayer structures in the skin using a high voltage pulse [Denet et al. (2004)], and cavitational ultrasound, which causes the formation, oscillation, and collapse of bubbles in an ultrasonic field [Ogura et al. (2008)], and ultimately increases *sc* permeability to topically applied substances [Misra et al. (1999)]. Unfortunately, while these technologies are promising, the devices are largely too expensive to find application in resource deprived countries. A cost-effective physical method is tape stripping of the *sc*, which reported enhanced vaccine absorption in animals and humans [Kahlon et al. (2003)]. Encapsulated bioactive molecules and some vaccines have successfully been delivered with microneedles that pierce the *sc* and dissolve *in situ* [Miyano et al. (2005); Lee et al. (2008b)]. A microneedle influenza vaccine patch is currently under investigation in clinical trials [Sullivan et al. (2010)].

Alteration of *sc* permeability can be achieved with chemical enhancers, lipophilic colloidal carriers, iontophoresis, and noncavitational ultrasound for example. IgG titres similar to intramuscular injection were achieved with lipid encapsulated tetanus toxoid [Gupta et al. (2005)]. Recently, a combination of chemical enhancers achieved a clinically acceptable balance between permeation enhancement and tissue irritation [Karande et al. (2004)]. In 2006, Alza brought to market a fentanyl and morphine patch that delivers the analgesic according to the patients needs, in direct correlation with manual adjustment of the continuous low voltage



Figure 1.4: Needle-free Cutaneous Drug Delivery Approaches: a) Liquid jet injectors access the deeper dermal regions and even muscle tissue, b) ballistic powder injection deposits dry-powder particles to the epidermis, while c) various methods are used to increase the permeability of the *stratum corneum* to large therapeutic molecules [Mitragotri (2005)]. *Note: This figure is not available in the electronic version due to copyright.*

current for iontophoresis [Mayes and Ferrone (2006); Bonnet et al. (2009)]. Non-cavitational ultrasound disrupts the *sc* lipid structure and thereby increases permeability to topically applied vaccines. Results in an animal study reported a 10-fold higher immune response per tetanus toxoid vaccine dose in the ultrasound treated group compared to control [Tezel et al. (2005)]. While topical application technologies show great promise, some require aggressive adjuvantation or chemical enhancement, expensive and technologically complex devices, a power supply, and frequently, only little clinical data are available [Kogan and Garti (2006); Zempsky et al. (2004)].

Liquid-jet injection delivers liquid vaccines intradermally and intramuscularly in a high-velocity jet of sub hypodermic needle dimensions [Hingson and Figge

(1952)]. In form of multi-use-nozzle jet injectors, this technology has been used successfully in measles, smallpox, cholera, hepatitis B, influenza and polio immunisations [Weniger (2003)]. Although liquid-jet injection does not rely on hazardous sharps, it was likely responsible for the spread of hepatitis-B virus in the 1980s due to a back-splash of blood and interstitial fluid into the injector nozzle which was determined to have caused cross contamination [Canter et al. (1990)]. Disposable-cartridge jet injectors were introduced to successfully address this problem [Cann et al. (2005)]. Liquid-jet injection is a well documented and efficacious needle-free alternative to hypodermic needle injection, but it does not address vaccine stability at ambient temperature, as liquid vaccines generally require refrigeration. Furthermore, liquid-jet injectors cannot deliver antigen superficially enough to effectively target LCs in the epidermis. Epidermal powder immunisation is a dry-powder particle-based vaccination technology that was first developed in 1986. Initially, DNA-adsorbed gold particles were used to transfect plants. Ballistic powder injection (BPI) for vaccination was intensively investigated in the early 2000s [Haensler et al. (1999); Mitragotri (2005)]. The performance of this technology in animal and human models is reviewed in more detail in the following section (1.8).

When examined independently of costs such as the vaccine cold chain, need for healthcare personnel, and societal costs, the cost per injection can be disaggregated into the vaccine cost per dose and the operating cost of the delivery device per injection. Hypodermic needles and syringes are relatively inexpensive at US$ 0.06–0.15 per injection, while needle-free injections using disposable elements (e.g. liquid jet, or ballistic powder) were estimated at US$ 0.30–1.00 per injection [Lev-Ram (2010); Giudice and Campbell (2006)]. The vaccine cost per dose depends largely on the type of vaccine, with vaccines such as DTP on one end of the spectrum ($0.05–0.30) and glycoconjugates on the other (US$ 35–60) [Kermode (2004)]. Vaccine costs

for needle-free formulations should not exceed the cost of existing vaccines, which are produced at US$ 0.01–0.60 per dose. Therefore, even when needle-based and needle-free vaccines are formulated at similar costs, based purely on device operation costs per dose, needle-free devices are more expensive than HNS. Although current needle-free injection technologies that use disposable cartridges or nozzles have a lower profit margin than HNS injections, needle-free injections reportedly have a greater societal benefit. It was estimated that the societal cost of HNS can range up to US$ 26.77 per injection while needle-free injections were less costly [Giudice and Campbell (2006)]. Unfortunately, a specific number was not provided. In the larger context, the cold chain maintenance costs between $200–300 million per year and accounts for 80% of the cost of vaccination [Chen et al. (2011); Das (2004)]. Therefore, substantial savings may be realised by thermostable needle-free vaccine formulations, which may make needle-free injections similarly profitable as HNS injections. However, to the best of our knowledge at the time of writing, there are no published data that quantify these respective costs and savings.

The plethora of innovative approaches to needle-free drug delivery, and their promising initial results, suggest that no single needle-free technology will emerge as the most suitable choice for all vaccinations. Much rather, advantages and limitations, and costs and savings of each technology will likely determine a "niche application" for the respective cutaneous or mucosal vaccine delivery method, and will likely be dependent on the type of vaccine and the clinical setting [Mitragotri (2005)].

1.6.2 Intradermal Powder Injection: Basic Particle Injection Considerations

The narrow epidermal target region dictates the need for an optimisation process of injector device parameters and vaccine powder particle characteristics. Powder injector devices accelerate vaccine particles in the stream of expanding helium gas (at 30 – 60 bar pressure), and achieve velocities of up to 1050 m/s [Kendall et al. (2000); Liu (2007)]. According to Kendall, the impact parameter (ρrv) required for particles to breech the *sc* ranges from 7 – 12 (kg/m·s) and is a function of particle density (ρ), radius (r) and velocity (v) [Kendall et al. (2004a)]. Desirable skin penetration depths are only achieved with sufficiently robust sugar and polymer-based particles of diameter 20 – 100 μm, and density of 0.7mg/mL or more [Quinlan et al. (2001); Kendall et al. (2004a)]. Particles less than 100 μm in diameter have been reported as pain-free, while particles smaller than 20 μm were unable to penetrate into the epidermis. If the overall amount of powder per injection is kept below 1 – 2 mg, bleeding can be almost entirely avoided [Burkoth et al. (1999)]. Balancing particle characteristics with adequate protein stabilisation and achieving a precisely targeted delivery depth to a very narrow dermal region presents a technical challenge.

1.7 Protein Fundamentals: Stability, Denaturation, and Dry-Powder Formulation

1.7.1 The Need for Thermostable Protein Formulations

Alternatives to current vaccines are needed to better conserve the potency of thermo-sensitive vaccines during storage and handling subsequent to production

[Alcock et al. (2010); Pipkin and Minor (1998); Milstien et al. (2006)]. Despite readily available expertise on proper vaccine handling, breaches to the cold chain protection are recurrent events in developing and developed nations alike, and present a significant problem [Weir and Hatch (2004); Rogers et al. (2010)]. Common causes that compromise vaccine quality include exposure of vaccines and adsorbed vaccines to excessive heat or cold during storage and transport, imprecise temperature monitoring and record keeping, and the failure to discard unused vaccines after prolonged handling at ambient temperatures [Rogers et al. (2010); Bell et al. (2001)]. In addition to further cold chain optimisation, improved retention of protein vaccine potency in particular, can be achieved by alterations to vaccine formulation [Chen and Kristensen (2009)].

1.7.2 Modes and Implications of Protein Degradation

Aggregation of biotherapeutic proteins has been linked to substantial cytotoxicity [Poon et al. (2009); Kayed et al. (2003)], decreased biological activity and increased immunogenicity [Ring et al. (1979); Gamble (1966)], which is why regulators require careful analysis of aggregates and proteinaceous particles in Investigational New Drug and Biological Licensing Applications [Wang et al. (2012)]. Protein aggregates and proteinaceous particles are believed to achieve increased immunogenicity relative to pure monomer through several mechanisms that include: i) "T cell-independent activation of B-cells through cross-linking mechanisms by repetitive and ordered structures", ii) "aggregation-induced structural changes toward more foreignness", iii) higher epitope density, and iv) improved uptake and presentation of proteinaceous particles by APCs [Wang et al. (2012); Sauerborn et al. (2010)]. In the case of vaccines, increased immunogenicity may be a desirable quality. For example, enhanced immunogenicity of protein oligomers was reported for

an influenzae hemagglutinin [Weldon et al. (2010)], but on the other hand, ovalbumin aggregation showed reduced vaccine immunogenicity in one instance [Koch et al. (1996)], and increased immunogenicity in another [White et al. (2008)]. While there is a growing body of literature that investigates methods to harness the increased immunogenicity of insoluble protein aggregates [Rosenberg (2006); Wang et al. (2012)], the dangers of cytotoxicity and the incomplete understanding of how aggregates may impact the immunogenicity of a vaccine leads regulators to insist on small amounts of aggregates in formulations or the comprehensive analysis of these aggregates [Carpenter et al. (2009); Singh et al. (2010)].

Vaccine formulations that stabilise thermolabile vaccines need to balance the benefits of reduced chemical instabilities during storage, with the potentially detrimental effects of dry-powder manufacture. During storage, the presence of water in a vaccine formulation promotes chemical and physical degradation of the bioactive macromolecule [Patel et al. (2011)]. The formation or breaking of covalent bonds within a protein by deamination, hydrolysis, oxidation, or reduction is considered a chemical instability, while aggregation, denaturation, dissociation, precipitation and unfolding are physical instabilities [Manning et al. (1989)]. Often, chemical and physical instabilities can mutually amplify one another. Many principal degradation pathways are encouraged in the presence of water and can be significantly slowed or even halted in a dry solid state [Wang (2000); Chang et al. (2005)]. Nonenzymatic deamination frequently proceeds via the removal of an amide from either asparagine or glutamine and can lead to isomerisation, racemisation or truncation of the peptide [Geiger and Clarke (1987)]. Deamination can be counteracted by solution pH adjustments, lyophilisation, increased steric hindrance about asparagine, and a decrease in solvent dielectric strength via the addition of sucrose, glycerol or ethanol to the solution [Wakankar and Borchardt (2006)]. Oxidation preferentially

targets methionine, cysteine, histidine, tryptophan, and tyrosine and can lead to the formation of intermolecular disulfide bonds and unfavourable inter- and intramolecular van der Waals interactions, and eventually induce protein aggregation or fragmentation [Li et al. (1995); Mirzaei and Regnier (2008)]. Protection from oxidative degradation can be achieved by amino acid replacement, solution degassing, solution pH adjustment, or the addition of antioxidants, sugars and other polyols [Li et al. (1995)].

By contrast, in the dry-powder state, the shelf life of vaccines can be prolonged and their temperature-sensitivity improved, as the prevalence of both chemical and physical vaccine instabilities are significantly reduced [Carpenter et al. (1997); Pikal et al. (1991)]. While water promotes protein degradation, it also governs the stability, structure and function of biological macromolecules by defining intramolecular hydrophobic attractions and hydrophilic interactions and hydrogen bonds with the solvent [Levy and Onuchic (2004)]. Therefore, the removal of a protein's hydration shell can result in aggregation via protein unfolding and subsequent inter- and intramolecular charge association among the hydrophobic patches, particularly at solution interfaces [Wang (2005)]. Aggregation is largely affected by solution conditions such as pH, protein concentration, temperature and ionic strength of the solution and is sensitive to mechanical- and temperature-induced stresses such as pipetting, stirring or shaking, or freezing and thawing [Philo and Arakawa (2009)]. Aggregates can be soluble, insolube, reversible or irreversible, and the latter may decrease the concentration of the active therapeutic molecule [Akers et al. (2002)]. To overcome protein denaturation during dry-powder formulation, the addition of lyo- and cryoprotectant excipients can reasonably preserve the native protein structure in a chemically inert matrix with low residual moisture content [Fang et al. (2012)]. However, even in a dried solid, the long-term stability of a protein is not guaranteed.

For example, residual moisture and plasticisers in the dried formulation can lead to molecular mobility of the formulation constituents and promote protein degradation [Yoshioka and Aso (2007)]. Therefore, the choice of suitably stabilising excipients, buffers, and drying processes for a given therapeutic compound are crucial [Wang (2005, 2000)].

1.7.3 The Rationale for Formulation Excipients

Proteins are subjected to denaturing stresses in the liquid state, in the solid state, and during the interconversion of these states. Knowledge of the type of degradation that a protein experiences can suggest means of its stabilisation. In the liquid state, next to chemical degradation, shear stresses can perturb the molecular structure and lead to aggregation [Wang (2005)]. The addition of antioxidants such as epigallocatechin gallate for example, can reduce oxidative stress on the protein by providing a more reactive target for oxidation. The addition of non-ionic surfactants such as polysorbate and pluronics can oppose protein aggregation through their tendency to competitively accumulate at hydrophobic interfaces. Poloxamer surfactants increase the solution viscosity which may reduce protein mobility [Lechmann and Reinhart (1998); Wang and Roberts (2010)]. However, while surfactants protect proteins during solution shear, they were implicated in the decrease of protein stability during storage. The addition of co-solutes such as saccharides, polyols, or amino acids can thermodynamically stabilise proteins by means of preferential exclusion (Figure 1.5) [Pikal-Cleland et al. (2002)]. While these solutes are excluded from the protein backbone, the protein is preferentially hydrated, which increases the Gibbs free energy barrier between the native and denatured state by raising the energy cost associated with the exposure of the protein's interior hydrophobic patches to the protic solvent [Timasheff (2002); Carpenter et al. (1997); Bhat and



Figure 1.5: Preferential Protein Interaction or Exclusion of Osmolytes: a) Osmolytes such as urea preferentially surround the protein and thus would be situated within a hypothetical dialysis membrane around the protein, while b) osmolytes such as saccharides or polyols are preferentially excluded from the protein backbone to form a hydration shell [Arakawa et al. (2006)]. *Note: This figure is not available in the electronic version due to copyright.*

Timasheff (1992)]. Transferring proteins from the liquid state into the solid state customarily involves freezing and drying. During freezing, in addition to thermal destabilisation, proteins may denature due to formation of ice-water interfaces, solute concentrations and pH changes and phase separation [Costantino and Pikal (2004)]. Fortunately, similar molecular mechanisms to protein stability in the liquid state underly freezing, and therefore the same co-solutes can act as cryoprotectants.

Different stresses are imposed on proteins during dehydration and in the anhydrous state, and as consequence, different stabilisation strategies must be applied [Wang (2000)]. Two prevalent theories describe the stability of proteins in solids as a function of their molecular mobility: the glass dynamic hypothesis; and as a function of hydrogen-bonding: the water substitute hypothesis. Some excipients

can hydrogen bond with the protein and can thereby prevent aggregation by providing a substitute for the hydration shell. However, these excipients need to be of the right molecular geometry and need to form an amorphous glass for stabilising hydrogen bonding to occur [Taylor and Zografi (1998)]. Surrogate hydrogen bonds raise the free energy of unfolding during drying and thereby increase the thermodynamic stability of the protein. Saccharides and disaccharides such as sucrose or trehalose are frequently-used lyoprotectants. Arrested mobility and uniform dispersion of the protein in a chemically inert glass prevents intra and inter molecular interactions and slows degradation pathways. Protein stability has been correlated with the mobility of the matrix it is suspended in, a parameter which can be related to the glass transition temperature of the matrix (T_g) [Zhou et al. (2007)]. Additionally, while saccharides can serve as cryo- and lyoprotectants, they may crystallise in the solid, which releases water into the glass and reduces the T_g, and provides interfaces at which proteins may denature [Miller and Lechuga-Ballesteros (2006)]. A higher matrix T_g provides a higher mechanical robustness, and the prevention of saccharide crystallisation such as mannitol, can be achieved with the addition of polymers such as dextran [Rochelle and Lee (2007)]. A more complete review of the idiosyncrasies of additives was compiled by Wang (2005, 2000).

1.7.4 Basic Energetics of Protein Aggregation

The amino acid sequence of a protein gives rise to its secondary structure elements such as alpha-helix coils and beta-sheets through charge and hydrophobic intramolecular interactions, and the secondary structure defines the protein's tertiary and quaternary structure [Anfinsen (1973); Dobson (2003)]. However, protein folding and structure are not rigid, but are subject to rapidly interchanging structural oscillation about the most stable energetic conformation [Dill and Chan

(1997)]. Folding states are usually described as the native state, unfolded state, the intermediate state between native and unfolded state, the chemically degraded state, the aggregated state, and the precipitated state [Eliezer et al. (1998); Wang and Roberts (2010)]. Each of these states have their own Gibbs free energy level and the interconversion between these states may be reversible or irreversible but are largely controlled by folding kinetics and thermodynamics [Dobson (2003)]. It has been demonstrated that partially unfolded proteins are more prone to aggregation, mainly due to association of exposed hydrophobic patches that have become accessible [Zhang et al. (2008)]. However, the relative free energy difference between the folding states are dynamic and change in magnitude with influences from the environment, such as solution pH, temperature, salt concentration, co-solutes, and ligands [Kumar et al. (2000)]. Additionally, chemical alterations such as oxidation or deamination change the energetic landscape. However, it generally holds true that the higher the Gibbs free energy difference (ΔG_{unf}) between the native and unfolded or partially unfolded state, the more stable the protein towards external stresses such as temperature. Unfortunately, this does not necessarily impact a protein's aggregation propensity [Jaenicke (2000)]. The intricate relationship between temperature (T) and ΔG_{unf} at constant solution conditions and pressure has been described by Rees and Robertson (2001):

$$\Delta G_{unf} = \Delta H_m\left(1 - \frac{T}{T_m}\right) - \Delta C_p\left(T_m - T + T\,ln\left(\frac{T}{T_m}\right)\right) \tag{1.1}$$

According to equation 1.1, regardless of what the enthalpy of thermal unfolding (ΔH_m), or the heat capacity of thermal unfolding (ΔC_p), when the temperature is equal to the melting temperature (T_m), then ΔG_{unf}=0. Therefore, at T_m proteins are likely to unfold. At higher temperatures, in addition to decreased thermodynamic stability, more frequent molecular collision due to increased protein diffu-

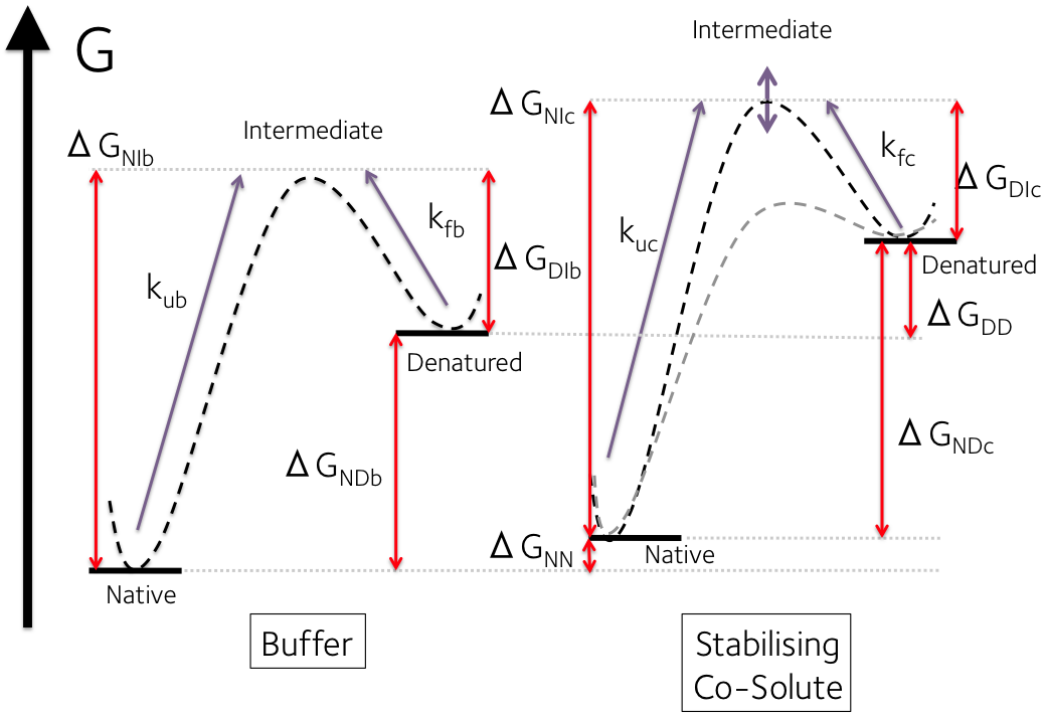


Figure 1.6: Effect of Stabilising Co-Solutes on Protein Energetics: The Gibbs free energy difference between native and denatured state (ΔG_{ND}) gives no information on the protein's kinetic stability and its rates of unfolding (k_u) or folding (k_f). The energy difference between native and intermediate state (ΔG_{NI}), and denatured and intermediate state (ΔG_{DI}) directly impact kinetic stability. Preferential solute exclusion from the protein backbone makes the native state less energetically favourable relative to buffer (ΔG_{NN}>0), but makes the unfolded state even more unfavourable (ΔG_{DD}»0), which increases ΔG_{ND}. While the addition of a stabilising co-solute increases ΔG_{NDc}, it may simultaneously lower the energetic level of the intermediate state, and therefore kinetic stability and rate constants ($k_u c$ and $k_f b$) may be increased or decreased.

sion occurs and makes aggregation more likely if hydrophobic patches are exposed [Damodaran and Song (1988)]. However, it has also been shown that some proteins do not aggregate at temperatures above their T_m. Conversely, some other proteins have been shown to aggregate well below their T_m [Fitzsimons et al. (2007)]. At large, this may be due to solution conditions, but also the kinetic activation energy required to convert native protein to a partially unfolded state is not necessarily dependent on Gibbs free energy [Ricchiuto et al. (2012)]. The energy barrier that

opposes native protein denaturation is the difference between the energetic levels of the native state and the unfolding intermediate (ΔG_{NIb}, ΔG_{NIc}). Therefore, the kinetic stability of a protein that is described by its rate of unfolding (k_u, native to denatured) and folding (k_f, denatured to native), are not necessarily linked to its thermodynamic stability (Figure 1.6). This invites the possibility, that while the addition of a thermodynamically stabilising co-solute may widen the ΔG_{unf} between native and denatured states, the activation energy required (ΔG_{NIb}, ΔG_{NIc}) may increase, but it may also stay the same or even decrease, depending on how the energy state of the intermediate denaturation step is altered in the presence of the co-solute (Figure 1.6). Therefore, thermodynamic stabilisation of proteins is a possible mean to prevent protein aggregation, but it is not a universal cure-all.

1.8 Needle-free Intradermal Powder Injection: Literature Review

In 2000, the potential of a reduced antigen dose to elicit comparable or superior protection to conventional SC injections was reported by Chen et al. (2000) using a formalin inactivated influenza virus vaccine. In their study, not only did unadjuvanted IPI induce significantly higher IgG titres with viral protein doses of 25 μg, 5 μg, and 1 μg, but it also conferred 100% protection in mice against a virus challenge with a median lethal dose (LD_{50}) across all three IPI vaccination conditions. On the other hand, conventional unadjuvanted SC injections conferred only 80% (25 μg), 60% (5 μg), or 0% (1 μg) protection respectively (Appendix A.9) [Chen et al. (2000)]. These initial results lead to an intensive investigation of intradermal powder immunisation in the years 2000 through 2004. In this time frame, various antigens, such as influenza strains [Dean and Chen (2004); Chen et al. (2000); Maa et al. (2004b); Chen

et al. (2003, 2001b, 2002a, 2004a)], hepatitis B-surface antigen [Maa et al. (2003b); Osorio et al. (2003); Maa et al. (2003a, 2004a, 2007)], diphtheria and tetanus toxoid [Maa et al. (2003b, 2004a); Chen et al. (2001a)], HIV 120 envelope protein [Chen et al. (2002b)], and inactivated equine herpes virus [Kondo et al. (2004)] were formulated in dry-powder form, with and without adjuvants, and tested in several animal models and in one human clinical trial. The results of these studies are summarised in tables A.9, A.10, A.11, A.12, and A.13. Most immunisation studies used 1 – 25 μg of the respective antigen per injection in a prime-boost regimen that was administered on days 0 and 28, with time points for analysis of the immune response at 0, 28 and 42 days of the experiment. A 2001 study confirmed the promising results of the 2000 Chen et al paper using diphtheria toxoid in Balb/c mice [Chen et al. (2001a)]. This study similarly reported significantly higher IgG titres induced by IPI compared to conventional hypodermic needle injection, and showed that adjuvants increased IgG titres both in IPI and in conventional injection conditions [Chen et al. (2001a)]. These findings were mostly consistent across various antigens and adjuvants used in Balb/c mice. Interestingly, these trends towards a higher IPI efficacy could not be confirmed in hairless guinea pigs, macaques and humans, where IgG titres of intradermal powder immunisation and conventional IM injection were similar independent of adjuvantation [Dean and Chen (2004); Chen et al. (2003); Maa et al. (2003b,a, 2004a, 2007)]. A 2004 clinical study reported an identical 21 – 28-fold geometric mean titre (GMT) level increase in both IM and IPI groups, but showed 100% seroprotection with IM and only a 83% – 92% seroprotection with IPI inoculations [Dean and Chen (2004)]. The reasons postulated for the failure to reproduce the impressive murine data in this range of other species include underlying differences in the immune system and in the cutaneous physiology, and suboptimal particle delivery and adjuvantation. It is also notable that in humans “mild to moderate erythema, oedema and petechiae” at the IPI site were reported, all of which were self-

limiting over a period of 0 to 21 days, but a slight skin discolouration persisted up to day 28 after the injection in 50% of all cases. In a few instances, mild bleeding and pain was reported [Dean and Chen (2004)]. The bleeding and pain reported in the clinical trial suggests that vaccine-loaded particles may have penetrated too deep into the skin as to encounter blood vessels and nerves. These interspecies and inter-individual differences in efficacy and tissue damage perhaps reflect the difficulty in obtaining reproducible delivery depth across such a variable barrier [Weissmueller et al. (2013)].

From 2000 to 2004, the field saw a shift in antigen formulation with exclusively compacted and ground trehalose to the more complex spray-freeze-drying (SFD) manufacture of trehalose, mannitol, and dextran particles. Only the most recent study in 2007 directly compared a pure trehalose formulation with SFD [Maa et al. (2007)]. Trehalose formulations showed a 20 – 30% potency recovery of HBsAg, while SFD formulations comprising trehalose, mannitol and dextran, achieved a 90% recovery of HBsAg potency. However, in this particular study, the trehalose formulation was freeze-dried before compaction and grinding, while all earlier studies merely dried the formulation in a nitrogen gas-purged desiccator [Maa et al. (2007)]. Therefore, more data are required to substantiate any claims of superiority of one particle manufacture method over another. Nevertheless, a comparison across individual studies suggests that both SFD and desiccation of the antigen with trehalose, prior to IPI induce a greater IgG response than their respective IM and SC controls in mice (Appendix A). Interestingly, aggregates were reported after SFD and SD particle manufacture when the antigen was adjuvanted with alum, but not with the desiccation and grinding method [Maa et al. (2003b); Osorio et al. (2003); Maa et al. (2003a)]. Particle manufacture by spray-drying was directly shown in two studies to be significantly less immunogenic than when the same formulation was prepared

by SFD [Maa et al. (2003b, 2004a)], and also showed only 50% potency when compared with the untreated stock solution in a HBsAg system [Maa et al. (2007)]. Since formulations were injected shortly after their manufacture, the various long-term merits and drawbacks of an individual formulation may not have come to bear in the immunological assessment [Weissmueller et al. (2013)]. The study design and findings of all protein-containing formulations that have been tested *in vivo* to date using ballistic intradermal injection are summarised in the appendix tables (A.9, A.10, A.11, A.12, and A.13).

Although glycoconjugate vaccines are promising candidates for profitable needle-free vaccines, they have not yet been reformulated and investigated for use in needle-free powder injection. As previously mentioned in section 1.5.1, the immunogenicity of glycoconjugates depends critically on the carrier protein. Diphtheria toxin mutant 197 is a frequently used carrier protein in bacterial conjugate vaccines [Shinefield (2010)], and was kindly provided by Novartis Vaccines and Diagnostics as model protein for this thesis. Since CRM_{197} is not a cross-linked toxoid but a purified non-toxic mutant protein, it is inherently less stable than toxoids and therefore presents a challenging model for reformulation efforts.

1.9 Diphtheria Toxin Mutant 197: Structure and Chemical Conjugation

1.9.1 CRM_{197} Structure and Function

In 1885, Loeffler identified *Cornybacterium diphtheriae* as the cause of diphtheria, and its secreted diphtheria toxin (DT) was later on shown as the cause of toxicity

[Pappenheimer and Gill (1973)]. While diphtheria toxoid, which is formaldehyde-crosslinked diphtheria toxin, can also serve as immunogenic carrier protein in polysaccharide-conjugate vaccines, it has a greater structural variability compared to diphtheria toxin mutant CRM_{197}. CRM_{197} comprises of 535 amino acids and differs from wild-type diphtheria toxin by one point mutation at location 52 of the amino acid sequence [Chang et al. (1998)]. This mutation replaces glycine-52 with glutamate-52 in the catalytic domain of the protein. Albeit small, this alteration of local conformation renders CRM_{197} non-toxic under reducing conditions, without the ability to enzymatically inhibit intracellular protein synthesis via chemical modification of elongation factor 2 (EF-2) [Giannini et al. (1984)]. The molecular structure of DT has been well described and its function extensively researched [Pappenheimer et al. (1972); Louie et al. (1997); Bennett et al. (1994a); Kent et al. (2008); Bennett and Eisenberg (1994); Giannini et al. (1984); Choe et al. (1992)]. DT is synthesised as single polypeptide AB toxin, and comprises of 3 domains arranged into a Y-shape, each of which serves a specific function (Figure 1.7). The receptor-binding doming (R domain), composed of residues 387 – 535, enables CRM_{197} and DT to bind to the heparin binding EGF-like growth factor (HB-EGF) receptor on cell membranes [Kent et al. (2008)]. Once bound, the cell endocytoses the protein-receptor complex. The acidified intra-enodsomal pH of 5.0 – 5.3, prevalent in the vesicle due to H^+-pumping ATPases, induces a conformational change of DT, which allows its hydrophobic 201 – 384 residue transmembrane-domain (T domain) to embed itself into the endosomal membrane. The thus created membrane pore allows the protein to insert its 1 – 187 residue catalytic-domain (C domain) into the intracellular space, where furin cleaves the peptide backbone connection within a disulfide bond stabilised loop between the T and C domain [Ratts et al. (2003)]. The disulfide bond between the Cys186 and Cys201 residues of this protease-sensitive loop is cleaved in the reducing environment, and allows for the dissociation of the catalytic domain



Figure 1.7: Molecular Structure of CRM_{197} Superimposed on Diphtheria Toxin: The molecular structure of CRM_{197}'s catalytic domain (C) in light grey (residues 1-187), transmembrane domain (T) in dark grey (residues 201-384), and receptor (R) domain in red (residues 387-535) is superimposed on nucleotide-free DT, which is shown as yellow cartoon. The active-site loop (CL2) of DT is shown in blue. The symmetry-related, domain-swapped dimer of CRM_{197} is depicted as ghost [Malito et al. (2012)]. *Note: This figure is not available in the electronic version due to copyright.*

(fragment A, 21 kDa) from fragment B (37 kDA) [Choe et al. (1992)]. The partially unfolded catalytic domain, refolds into its native structure after membrane translocation and complexes with NAD to catalytically inactivate EF-2 via the transfer of ADP-ribose [Bennett and Eisenberg (1994); Falnes et al. (1994)]. Specifically, once fragment A complexes with NAD, it catalyses the cleavage of the N-glycosidic bond between the nicotinamide ring and N-ribose. This transfers ADP-ribose to the modified diphthamide (Histidine 715) on the elongation factor EF-2, and impairs protein synthesis that eventually leads to cell death [Malito et al. (2012)]. One DT molecule is enough to kill a cell [Collier (2001)]. The exact mechanism of translocation is yet to be completely understood [Kent et al. (2008)].

Since the point mutation in CRM_{197} is in the catalytic domain of the protein, the

transmembrane domain and the receptor binding domain of the protein are intact, and therefore CRM_{197} acts functionally indistinguishable from diphtheria toxin minus the toxicity [Pappenheimer et al. (1972)]. Recently, Malito et al. (2012) demonstrated on a molecular level that the lack of toxicity of CRM_{197} is based on the absence of stabilising hydrogen-bond interactions between the residue W153 and the backbone atoms of residue Q43 of the active-site loop. This allows the active-site loop to be structurally dislodged and mobile relative to DT. Although the catalytic cleft on CRM_{197} is structurally identical to DT, and has under nonreducing conditions NAD-glycohydrolase activity, the introduced mobility of the loop destabilises the NAD binding pocket and significantly impairs NAD binding in reducing conditions [Lory et al. (1980); Malito et al. (2012)]. This instability of the NAD binding pocket also reduced the thermal stability of the entire CRM_{197} molecule by 10°C compared to DT [Malito et al. (2012)].

1.9.2 Use of CRM_{197} in Conjugate Vaccines

Vaccines that use CRM_{197} as carrier protein in glycoconjugates currently include "Menveo®, a recently approved tetravalent conjugate vaccine against serogroups A-C-W135-Y of *Neisseria meningitidis*, Menjugate® and Meningitec®(against serotype C of *N. meningitidis*), Vaxem-Hib® and Hibtitre® (against *Haemophilus influenzae* type b, Hib), and the multivalent pneumococcal conjugate Prevenar™", and have been administered to millions of children world wide [Shinefield (2010); Malito et al. (2012)]. Polysaccharide antigens are linked to CRM_{197} by initial chemical activation and subsequent covalent conjugation to one of the 39 lysine residues [Bröker et al. (2009)]. Frequently, activation uses ammonium acetate and sodium cyanoborohydride to induce reductive amination of the oligosaccharide terminal, prior to the addition of an adipic acid linker with the terminal active succinimidyl



Figure 1.8: Lysine Groups on CRM_{197}, Conjugation Sites for Capsular Polysaccharides: CRM_{197} protein structure with point mutation glutamate-52 highlighted (white and red). Any of the 39 lysine groups on CRM_{197} (purple highlights) may be conjugated to the repeating PRP monomer unit via the adipic acid linker [Bröker et al. (2009); Verez-Bencomo et al. (2004)]. *Note: This figure is not available in the electronic version due to copyright.*

diester CRM_{197}(Figure 1.8).

The highly selective adipic acid linker conjugates to the lysine groups on CRM_{197} and induces consistent glycosylation of the protein with unentangled polysaccharide antigen chains oriented radially away from the protein [Bröker et al. (2009); Anderson et al. (1989)]. Although CRM_{197} alone, or conjugated to capsular polysaccharide chains, has not been described in literature on epidermal powder immunisation, past IPI studies have used the closely related diphtheria toxoid molecule amongst several other bioactive proteins [Maa et al. (2003b, 2004a); Chen et al. (2001a)].

1.10 Alternate Drug Delivery Particles: Bioceramic Microparticles and Polymer Nanoparticles

1.10.1 Hydroxyapatite as Drug Delivery Substrate

The excellent biocompatibility, biodegradability, and bioactivity of bioceramics have vastly extended the reach of biomedical applications in the field of orthopaedic and dental implants, drug delivery and tissue engineering [Ginebra et al. (2006); Legeros et al. (2003); Viswanath et al. (2008)]. Hydroxyapatite ($[Ca_{10}(PO_4)_6(OH)_2]$), a biocompatible mineral that is naturally found in bone and largely comprises of calcium and phosphate, has been heavily investigated for application in bone defect repair due to its superior time-dependent biodegradability and mechanical strength [Kon et al. (2000)]. Its crystal toughness is strongly influenced by chemical composition (impurities or substituents), temperature treatment, mode of formation, and crystal structure [Tsui et al. (1998)].

A computational visualisation illustrated the charge density distribution on hydroxyapatite (HA) (Figure 1.9), and concluded that the surface charge is patterned with positively charged patches and negatively charged patches due to calcium ions and negatively charged oxygen ions respectively [Canepa et al. (2011)]. At physiological pH, it was determined that HA has an overall neutral surface charge [Harding et al. (2005)]. Based on the charge patterning and neutral surface charge, electrostatic interactions of protein with HA are most favourable when peptide motifs can conform to the crystal lattice to form β-strand or α-helix like interaction between acidic side groups and surface calcium ions [Laila-Huq et al. (2000)]. In fact, HA



Figure 1.9: Charge Density Distribution on Hydroxyapatite Crystal Surface: Estimated charge density of hydroxyapatite surfaces based on chemical surface composition. The model does not account for impurities such as $(CO_3)_2^-$, Na^+, and F^-, etc.), but only displays calcium (green), phosphorous (yellow), oxygen (red), and hydrogen (grey) [Canepa et al. (2011)]. *Note: This figure is not available in the electronic version due to copyright.*

has been shown to strongly adsorb proteins and to provide sustained release of the bioactive molecule [Shen et al. (2008)]. However, for application in ballistic powder injection, the common physical forms of HA as either nanocrystalline powder or as elongated microneedles are unfavourable in either mass or shape for suitable ballistic delivery. Instead, ideal particles should have a high density and fracture toughness, along with a spheroidal morphology and a closely controlled diameter. These particle characteristics may be influenced using molten salt synthesis (MSS).

1.10.2 Molten Salt Synthesis (MSS) of Hydroxyapatite Particles

Powder morphology and characteristics may essentially be designed through a careful choice of parameters in MSS [Taş (2001)]. MSS uses a lower temperature melting flux, such as sulfate, carbonate or hydroxide salts to provide a controlled reaction environment for ceramics formation. In the liquid salt, i) reaction rates are

increased due to higher mass transport in the salt compared to solid state sintering, ii) the salt reduces the required temperature at which reactions can proceed, and iii) the liquid salt provides more homogenous reaction conditions that aid in controlling particle sizes, and iv) the liquid environment allows for surface tension and Oswald ripening to influence particle morphology [Kimura (2011)]. Previously, hydroxyapatite whiskers and spheroidal β-tricalcium phosphate single crystals have been prepared by MSS [Taş (2001); Viswanath et al. (2008)]. The eventual morphology and characteristics of the powder strongly hinge on the choice of flux salt, stoichiometric ratio of reactants to flux, as well as heating and cooling rates [Taş (2001)]. In 2001, Tas reported that salt flux (K_2SO_4) to HA ratios could range from 1.2 to 3.0 without a significant effect on the HA whisker morphology. However, there have been no reports on the effect on HA crystal shape at higher salt-to-HA ratio flux conditions. If crystal size can be controlled, this method may be used to form high impact parameter carrier particles for IPI with favourable surface chemistry, and may allow for protein immobilisation onto the particles' surface.

1.10.3 Polymer Nanoparticles: Flash NanoPrecipitation and Therapeutic Applications

Although amphiphilic block copolymer nanoparticles (NPs) have attracted considerable attention for the improved delivery of poorly water-soluble therapeutic agents, their application as vaccine adjuvant system has not yet been established. Some of the claimed benefits of particle-based vaccine carriers include i) an enhanced uptake of antigens by APCs [Reddy et al. (2006)], ii) controlled and extended antigen release [Thomasin et al. (1996)], iii) protection of the antigen's integrity from degradation [Slutter et al. (2010)], iv) and a modulation of the immune response

[Mallapragada and Narasimhan (2008)]. Although much progress has been made, nanoparticle platforms that meet most desired qualities for particle-based vaccines are not yet available. Ideally, these particle-based platforms are safe, efficacious with a single dose, easy and cheap to prepare, maintain chemical and physical stability of the antigen, and maintain their size during manufacture and secondary processes such as co-formulation with excipients, drying, and storage [Oyewumi et al. (2010); Wang et al. (2013)].

The effect of the NP carrier size on the elicited response *in vivo* is still a matter of active research and much conflicting data has been published [Oyewumi et al. (2010)]. It is believed that 20-200nm particles are endocytosed, while particles larger than 500nm but smaller than 10μm are preferentially phagocytosed or taken up by DCs via micropinocytosis [Rice-Ficht et al. (2010); Mottram et al. (2007)]. Small particles are thought to induce a Th1-type response with CD4+ and CD8+ T cell activation, while larger particles are thought to induce a Th2-type response due to sustained antigen release and presentation [Brewer et al. (2004)]. However, much conflicting data have been presented and the effect of particle size on the immune response is not yet clear [[Oyewumi et al. (2010)]. The underlying problem that likely contributed to these strongly opposing reports on the effect of NPs in the immune response, is an inherent heterogeneity in nanoparticle size and antigen-particle constructs. NP manufacture frequently consists of multi-step processes and uses approaches such as solvent-evaporation, sonication, emulsion, and dialysis methods which can introduce substantial variability into final products [Quintanar-Guerrero et al. (1998)].

Flash NanoPrecipitation (FNP) achieves turbulent mixing within milliseconds at high levels of supersaturation with confined impinging jets of a miscible organic (e.g. tetrahydrofuran) and an aqueous solution [Johnson and Prud'homme

(2003a)]. The hydrophobic block of the amphiphilic block copolymers (e.g. polyethylene glycol$_{(1-10kDa)}$-b-polystyrene$_{(1-2kDa)}$) precipitates into NPs “with a minimum of processing steps, control over particle size, drug loading," and the relative composition of the polymer core and the functionalised outer shell [Gindy et al. (2008)]. Since the amphiphilic polymers can be functionalised and purified in a homogenous solution prior to NP formation, this eliminates sources of heterogeneity. After NP formation, peptides, proteins, and other ligands can be attached in second step. Gindy et al. (2008) reported that the reactive ligand density on the surface of the NP can be engineered by FNP, and when the NP-to-protein conjugation uses quantitative coupling chemistry, the surface ligand density can be precisely determined. With this platform, it is possible to co-deliver multiple peptides, such as TLR agonists, targeting antibodies, and immunogenic proteins. This may provide ample means to target immune cells and to influence the immune response. Additionally, the hydrophobic core of the NPs allows for the incorporation of hydrophobic drugs, dyes, or MRI-active substances such as ferrites, which may be used to trace the antigen *in situ* [Ansell et al. (2008); Gindy and Prud'homme (2009)]. However, a first proof of concept for the utility of FNP NPs as vaccine adjuvant has not yet been presented.

1.11 Needle-free Ballistic Injection: Mathematical Models of Particle Penetration Depth

Much of the therapeutic potential of ballistic powder injection (BPI) hinges on the precise deposition of the vaccine payload in the narrow dermal layer just below the *sc* [Burkoth et al. (1999); Kendall et al. (2007)]. While experimentally obtained penetration depth values provide the best description for a given set of parameters such

as particle density, radius, impact velocity, or skin toughness, the use of ballistic models on skin penetration by pharmaceutically active particles could obviate the need for costly experiments should any of these system parameters change [Kendall et al. (2004a,b)]. Kendall et al have proposed an analytical model that relates particle parameters and the physical properties of the skin to particle penetration depth using the concept of momentum [Kendall et al. (2004a); Guha et al. (2010)]. Albeit greatly simplified, the Kendall model provides helpful guidelines on the physical properties of successful therapeutic BPI particles [Guha et al. (2010); Mitchell et al. (2003)]. The starting assumption was that penetration depth (D_p) is proportional to the particle momentum (M_p) relative to its cross section (A_p):

$$D_p \propto \frac{M_p}{A_p} = \frac{v_p m_p}{A_p} \tag{1.2}$$

Since particle mass can be expressed as m_p=$\rho_p V_p$, and the particle volume (V_p) comprises of the particle's diameter (d_p) and its cross-sectional area (A_p), expression 1.2 simplifies to the impact parameter:

$$D_p \propto v_p d_r \rho_p \tag{1.3}$$

Their model borrows heavily from Dehn's "unified theory of penetration" [Dehn (1987)]. Kendall et al used the same approximations to arrive at their penetration model [Kendall et al. (2004a)]. They assumed that the friction between the particle and the skin is negligible due to a separating fluid layer, and that the 1μm sphere metal particles they used, would have a constant mass throughout penetration. Furthermore, the deformation of skin was assumed to be purely plastic without any elastic components [Kendall et al. (2004a)]. Based upon these assumptions, they argued that the change in momentum of the particle is the sum of the opposing forces,

namely: the impact force of the particle on the skin, and the deceleration force of the skin on the particle. Assuming that skin penetration is due to ductile failure of the tissue only, the following relationships can be established [Ziegler (2008)]:

$$\frac{d}{dt}\left(m_p v_p\right) = -\left(F_{target-inertial} + F_{target-yield}\right) \tag{1.4}$$

$$F_{target-inertial} = \frac{1}{2}\rho_t A_p {v_p}^2 \tag{1.5}$$

$$F_{target-yield} = 3A_p\sigma_y \tag{1.6}$$

$$F_{target} = \frac{1}{2}\rho_t A_p {v_p}^2 + 3A_p\sigma_y \tag{1.7}$$

Equations 1.5 and 1.6 were derived by Dehn (1987). Equation 1.5 describes the resistive force of the target as a function of the target density (ρ_t), and the particle velocity (v_p) and cross-sectional area (A_p). Equation 1.6 describes the yield force of the target as function of its yield stress (σ_t) and the cross-sectional area that is indented upon it (A_p). Together, these equations approximate the forces acting during particle impact (Equation 1.7). Based on the momentum model (1.2), theoretical penetration depth of particles into a uniform target can be integrated to:

$$D_{ve} = \frac{4\rho_p r_p}{3\rho_{ve}}\left\{ln(\frac{1}{2}\rho_{ve}v_i^2 + 3\sigma_{ve}) - (3\sigma_t)\right\} \tag{1.8}$$

Equation 1.8 holds true for only one layer, but during injection, particles breech the *sc* first, and then continue in the epidermis. Both dermal layers have different mechanical properties [Kendall et al. (2007)]. A solution for this, is to calculate the velocity of the particles after they have breeched the *sc*, and then use that velocity in equation 1.8 along with the values for the physiologic properties (density, yield stress) of the epidermis. The velocity of particles after *sc* penetration can be expressed as:



Figure 1.10: Kendall Model Fit to Data: Although the model parameters have been optimised, there is substantial error associated between the theoretical prediction of the penetration depth of particles with varying diameter (colours) and the actual experimental data [Kendall et al. (2004a)]. *Note: This figure is not available in the electronic version due to copyright.*

$$v_{i,ve} = \left\{ \left({v_i}^2 + \frac{6\sigma_{sc}}{\rho_{sc}} \right) e^{\frac{-3\rho_{sc} t_{sc}}{4\rho_p r_p}} - \frac{6\sigma_{sc}}{\rho_{sc}} \right\}^{\frac{1}{2}} \tag{1.9}$$

Finally, the total penetration depth of particles into the target can be approximated as the thickness of the *sc* (t_{sc}) plus the penetration into the epidermis:

$$D_t = t_{sc} + D_{ved} \tag{1.10}$$

Kendall et al adjusted some parameter constants, such as the skin yield stress, to match the predictions of the presented analytical model to the observed experimental data [Kendall et al. (2004a)]. However, a considerable amount of variability is still evident and calls into question the validity of the model (Figure 1.10).

1.12 NEEDLE-FREE BALLISTIC INJECTION: INJECTORS

Injector devices use high-speed gas jets to accelerate microparticles sufficiently to breech the *sc.* Upon depression of the actuation button on the PowderJect injector, compressed helium gas is released from the microcartridge (Figure 1.11, a). This leads to a rapid increase of pressure on the polycarbonate diaphragms of the vaccine powder cassette that is placed in the path of the expanding gas and separates the propellant chamber from the converging-diverging barrel with silencer nozzle [Liu and Kendall (2007)]. Both diaphragms instantly rupture at a given pressure, which leads to the gas entrainment and acceleration of powder particles [Quinlan et al. (2001)]. Due to the conical widening of the barrel, after a converging acceleration channel, the gas is decelerated substantially before exiting the nozzle and impacting on the skin. Particles maintain their speed, however, and reportedly reach up to 1050m/s at the nozzle exit [Quinlan et al. (2001)]. The early design has been improved to better control particle penetration, but the shockwave created upon diaphragm rupture makes injections noisy [Kendall (2002); Kendall et al. (2004b)].

The Venturi injector similarly uses compressed helium gas as propellant, but it utilises a pressure gradient to draw vaccine powder from the cassette into the expanding gas stream (Figure 1.11, b). An area of low pressure is created at the opening of the vaccine powder cassette as a direct result of the supersonic jet of gas that streams past. The supersonic jet enters the Venturi gallery after being focussed by a centrally located sonic throat [Costigan et al. (2004)]. A past comparison of both devices has shown that the Venturi device is quieter and delivers a larger fraction of the powder payload [Mitchell (2003)]. Additionally, the Venturi injector uses a swirl-disc to achieve a turbulent gas flow in the nozzle which results in its characteristic annulus injection pattern on the target. Both devices can successfully deliver dry-powder



(a)



(b)

Figure 1.11: Needle-free Particle Injector Devices: a) The bursting membrane device by PowderJect, and the b) Venturi injector by ParticlesTherapeutics Ltd have both been used for needle-free dermal inoculation [Chen et al. (2000); Weissmueller et al. (2013); Kendall et al. (2006)]. *Note: This figure is not available in the electronic version due to copyright.*

vaccines [Chen et al. (2000); Kendall et al. (2006)]. Throughout this dissertation, the Venturi injector was used. In 2012, two investigational formulations for the Venturi device were in clinical trial phases I and III.

1.13 Dissertation Aims and Objectives

The aim of this doctoral thesis is to identify novel approaches to dry-powder formulation and needle-free delivery of diphtheria toxin mutant 197 (CRM_{197}), a relevant model antigen, by means of ballistic dermal injection. Successful reformulations might elicit similar or higher antibody titres than the current clinical standard of the alum-adjuvanted antigen administered by IM. The protein antigen CRM_{197} provides a challenging but valuable model protein for this aim. CRM_{197} is frequently used as immunogenic carrier protein in glycoconjugate vaccines, which is a group of vaccines that may prove profitable in form of a needle-free dry-powder formulation. The major objectives are the identification of an economical and scalable process for dry-powder formulation additive screening, the precise targeting of the vaccine particles to the epidermis, the structural retention of CRM_{197} during formulation, and the amplification of the immune response through sustained antigen presentation and the activation of the innate immune response.

Three different approaches to antigen formulation and presentation were investigated. First, SFD was used to reformulate CRM_{197} into a soluble dry-powder. Second, a novel bioceramic was used to present CRM_{197} in a surface adsorbed state to the immune system. Third, antigen-coated polymer nanoparticles were loaded into SFD-powder particles, and were used to deliver CRM_{197} in soluble and particulate form. The research was divided into 4 parts:

Chapter 3 investigates the potential of a novel high-throughput screening tool

(Differential Scanning Fluorimetry) with the goal to make excipient screening and dry-powder vaccine formulation more economical, less time-consuming, and more predictable. The thermodynamic stability of CRM_{197} in the presence of various co-solutes was correlated to its tertiary structure and the most promising excipient formulations were subsequently manufactured by SFD. Dry powder vaccine formulations were physically characterised and the structural integrity of CRM_{197} analysed by asymmetric flow field flow fractionation (AF_4).

Chapter 4 discusses the manufacture and physical properties of novel bioceramic microparticles. While sugar-based powder formulations release their payload immediately after injection, it was investigated whether the bioceramic may retain the antigen at the injection site and provide its sustained release. Furthermore, simple surface-adsorption of the protein followed by almost instantaneous chemical dehydration of the protein may obviate the need for costly and time-consuming lyophilisation. The material composition of the novel bioceramic and its protein adsorption propensity are characterised. Finally, the structural integrity of CRM_{197} is assessed on the bioceramic surface using Fourier transform infrared spectroscopy (FTIR).

Chapter 5 presents a novel nanoparticle-construct for improved protein antigen presentation. Conventional alum adjuvants are largely unsuitable for dermal injection. Therefore, a novel adjuvant system that presents the antigen on the surface of monodisperse block copolymer nanoparticles by chemical conjugation was investigated. The chapter describes the manufacture and characterisation of CRM_{197}-conjugated NPs and their incorporation into dry-powder by means of SFD.

Chapter 6 analyses the penetration depth of particles when injected into murine skin and agar gels, and introduces a concept that describes the particle location in the target in fundamentally different terms than previous models. Subsequently,

the immunogenicity of dry-powder CRM_{197} formulations that were presented in the preceding chapters (3, 4, 5) is discussed based on the analysis of IgG and IgG subclass titres produced following administration to murine models.

CHAPTER 2

EXPERIMENTAL MATERIALS AND METHODS

Chapter 2 provides a detailed description of the experimental methods and materials used to obtain the data presented in the subsequent “Results and Discussion" chapters. Further particulars on the chemicals and consumables used are summarised in tables A.6, A.7, and A.8 respectively.

2.1 EXCIPIENT SCREEN AND SFD POWDER MANUFACTURE AND CHARACTERISATION

2.1.1 Manufacture of Spray-Freeze-Dried Powders

Dry-powder formulations of CRM_{197} for application in needle-free injection were prepared by a process previously described by Johnson et al. (1997); Costantino et al. (2000). Formulations (1) trehalose, mannitol, dextran (150kDa), dextran (10kDa) (3:3:3:1) 30% (w/v) in 10mM K_2HPO_4 buffer pH 7.2; (2) trehalose 10% (w/v) in 10mM

K_2HPO_4 buffer pH 7.2; (3) sucrose 10% (w/v) in 10mM K_2HPO_4 buffer pH 7.2; (4) trehalose, glycine, dextran (150kDa), dextran (10kDa) (3:3:3:1) 30% (w/v) in 10mM K_2HPO_4 buffer pH 7.2; contained 2mg/mL of dialysed CRM_{197} (provided by Novartis Vaccines and Diagnostics, Siena, Italy). Stainless steel collection vessels were fitted with precision fine wire thermocouples (Omega Engineering, LTD). Formulations were sprayed into collection vessels filled with liquid nitrogen, using a 48kHz ultrasound nozzle (Sono-Tek, Milton, NY, USA) at 3.6W (Broadband Ultrasounic generator, Sono-Tek, NY, USA) and a flow rate of 0.5mL/min set by a Minipuls3 peristaltic pump (Gilson, Villers Le Bel, France). Once LN_2 had boiled off, the collection vessels were sealed with a Gore Lyoguard lid (W.L. Gore & Associates, Newark, USA). The closed collection vessels were transferred onto pre-cooled shelves (–40°C) and lyophilised in a FTS Systems LyoStar I (SP Industries, Warmister, PA, USA) at 100mTorr and a primary drying temperatures of –10°C for 48h. Secondary drying was conducted at 25°C for 16h. All SFD formulations were lyophilised above their respective glass transition temperatures T_g' to obtain less porous and more robust particles via viscous flow compaction of the amorphous glass [Costantino et al. (2000)]. The powders were transferred from the stainless steel collection vessels into freeze drying vials in a low humidity glove box at RT, stoppered, crimped, sealed with parafilm, and frozen to –80°C for storage.

2.1.2 Asymmetric Flow Field Flow Fractionation (AF_4)

Field flow fractionation achieves size separation through orthogonal fluid flows. The axial flow profile in the direction of sample elution assumes a parabolic profile (assumed Newtonian fluid) with no flow at the walls and a maximum in the centre due to the small height of the channel that is similar to a capillary tube (Figure 2.2). A flow that is applied orthogonally to the parabolic flow transports the sample to-

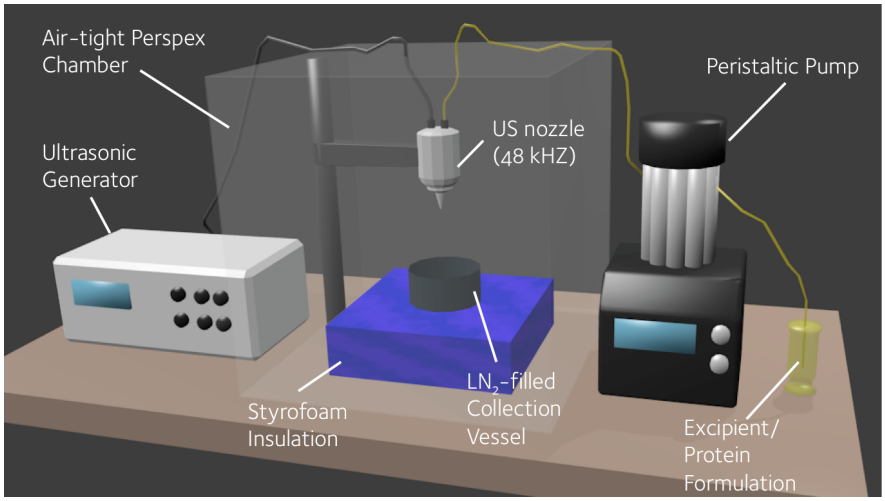


Figure 2.1: Blender3D Animation of the Spray-freeze-drying Set-up: The set up consisted of an air-tight perspex box containing a styrofoam insulation pad (blue) upon which a metal collection vessel filled with liquid nitrogen was placed. A 48kHz nozzle (SonoTek) was mounted 5-7cm above the collection vessel. The nozzle was powered by an external ultrasound generator (SonoTek) at 3.6W. A constant flow of liquid feed was achieved with an external peristaltic pump and set to a flow rate of 0.5mL/min and atomised in air into the liquid nitrogen.

wards the membrane-side of the channel, while the diffusion of the sample particles behave according to Fick's Law and therefore oppose this diffusion. A steady state of these two opposing forces is achieved in which each sample component is situated at a unique height position in the channel based on their hydrodynamic radius, with larger particles being in the slow-flow region (close to the membrane) of the parabolic flow, and the small particles in the fast-flowing region. Therefore, small particles elute first, followed by increasingly larger particles.

CRM_{197} samples were suspended in 0.1μm-filtered PBS pH7.4 running buffer before injection into the AF_4 (AF2000MT, PostNova Analytics, Landsberg, GER). Measurements were conducted at room temperature. Two isocratic pumps (Postnova, PN1130) were used to create the tip flow and focus flow, while a Kloehn syringe pump (Postnova, PN1610) provided the cross flow. The running buffer was degassed (Postnova, PN7520) prior to entering the isocratic pumps. After the pumps,

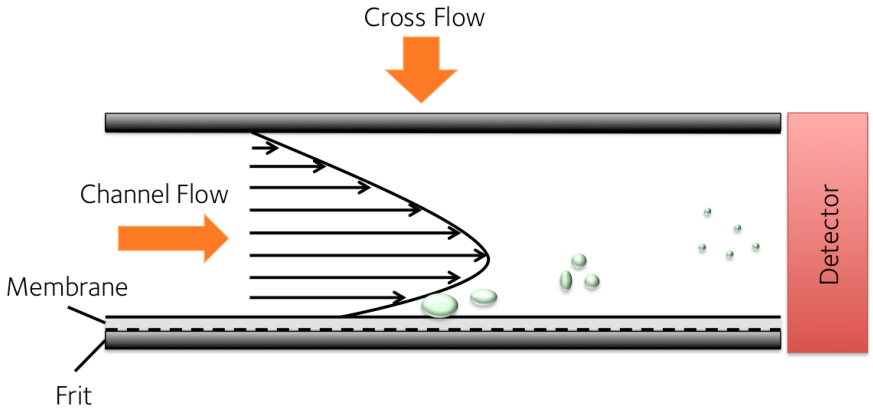


Figure 2.2: AF4 Separation Channel Schematic: Side view of the AF_4 separation channel shows the superposition of the parabolic flow profile induced by the channel flow, and the orthogonal cross flow that transports particles based on their hydrodynamic diameter towards the membrane.

in-line 0.1μm VVPP filters (Durapore, VVLP04700, Millipore) filtered the running buffer a second time. Protein concentrations were determined with a UV-Vis unit from Shimadzu (SPD-20A, Postnova, PN3211) that measured absorbance at wavelength λ=280nm. The MALS molecular weight analyser (BI-MwA, Brookhaven Instruments Corporation) was set to 20mW and the RI detector (Postnova, PN3150) to Int.1. The fractionation chamber was equipped with a 10kDa MWCO regenerated cellulose (RC) membrane (Postnova, Z-AF4-MEM-612) and a 500μm spacer.

Prior to sample analysis, the system was flushed with running buffer with the flow rates of 2mL/min, 2mL/min, 3mL/min for tip, focus and cross flow respectively for about 15min. The method settings as displayed in Figure 2.3 were applied and the system allowed to equilibrate to the new prescribed flow rates until the chamber pressure was stable. The 20 μL sample was then injected into the column with a flow rate of 0.2mL/min. To achieve a better separation of the protein monomer, dimers and higher order aggregates, the crossflow during the sample focussing step was set to 4mL/min for 5min.

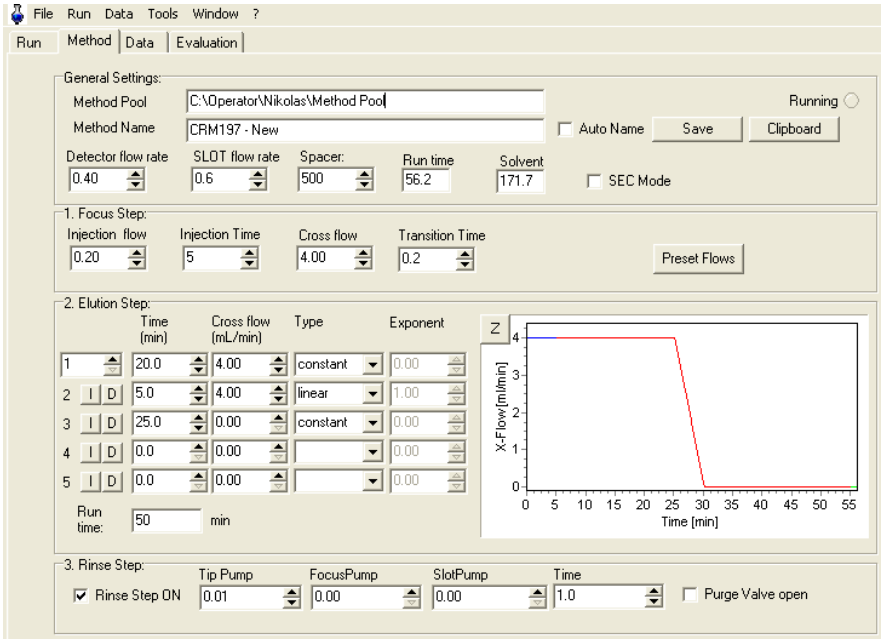


Figure 2.3: AF4 CRM_{197} Separation Method: AF2000 software interface display of the developed CRM_{197} separation method, using a 500μm separation column spacer and 0.1μm filtered PBS pH7.4 as running buffer.

Although the 500μm spacer increases the internal lumen of the separation column, and may thereby dilute the injected sample, the greater luminal volume also allows for an improved size separation and thus increased spacing between the individual elution peaks, which facilitates the subsequent evaluative analysis. To counteract luminal dilution of the sample, the sample was concentrated and the elution peaks amplified during separation in the column with the use of a reduced detector flow rate of 0.4mL/min and the slot flow rate set to 0.6mL/min, which together maintained a constant 1mL/min flow out of the column. After 20min at 4mL/min cross flow, a linear gradient of the cross flow from 4mL/min to 0mL/min over 5min reduced the spacing between smaller and higher molecular weight aggregates. To ensure that even the largest aggregates eluted from the fractionation chamber, a constant flow was maintained in the chamber with 1mL/min tip flow and 0.4mL/min detector flow, and 0.6mL/min slot flow for 25min. This was fol-

lowed by a rinse step of 0.01mL/min which was added to reduce buffer throughput, but keep a constant flow in the channel. All UV, RI, and MALS signals of a given elution profile were baselined in the AF2000 software version 1.1(PostNova Analytics, Landsberg, GER). Regions of interest were defined for each peak of interest. Depending on whether the concentration detector or light scattering detector was used, either the amount of protein per peak or per entire sample could be calculated, or the size of the molecules eluting at a given peak. The viscosity of the elution buffer was 0.0088g/cms and had a refractive index of 1.330. The CRM_{197} sample concentration was used at 1mg/mL as displayed in Figure 2.3. The extinction coefficient of CRM_{197} was previously determined to be ϵ_{CRM}=0.759 [mL/(mg*cm)], and the dn/dc was 0.165mL/g, as previously reported by Jumel et al. (2002). SFD powders with 2% wt CRM_{197} were resuspended in 10mM K_2HPO_4 pH7.2 at 10mg in 0.5mL. The resuspended solution was concentrated in centrifuge tubes (Corning Spin-X UF, 10k MWCO) at 2,000x*g* for 5min, and resuspended to 0.25mL with K_2HPO_4 buffer for a final CRM_{197} concentration of 1mg/mL.

2.1.3 Differential Scanning Fluorimetry

The model antigen CRM_{197} (Novartis Vaccines and Diagnostics, Sienna, Italy) was provided in 10% (w/v) sucrose, 10mM K_2HPO_4 at pH 7.2 and was dialysed against 10mM K_2HPO_4 pH7.2 buffer, made from milliQ water and subsequently sterile filtered (0.2μm), for 12 hours using Mini Slide-A-Lyzer (FisherScientific, Loughborough, UK) with a 10 kDa molecular weight cut off prior to use. The protein concentration of the dialysed CRM_{197} was measured using micro BCA Assay (Simga Aldrich, UK) as advised by the manufacturer. Excipient formulations were prepared at their respective saturation solubility limit at 20°C in K_2HPO_4 and adjusted to pH 7.2 using 1M NaOH or 1M HCl. A complete list of screened excipients is presented



Figure 2.4: Differential Scanning Fluorimetry - Protein Unfolding Profile: The thermal unfolding of proteins exposes their hydrophobic patches and leads to a fluorescence increase based on reduced quenching of the SYPRO Orange dye [Niesen et al. (2007)]. The curve is well described by the Boltzmann function equation 2.1. *Note: This figure is not available in the electronic version due to copyright.*

in the Appendix (A.1, A.2, A.3, A.4).

The DSF protocol previously published by Niesen et al. (2007) was adapted to screen for CRM_{197}-stabilising excipients in solution. Briefly, 38μL of each excipient formulation at 1:1, 1:2, and 1:4 dilution in K_2HPO_4 was pipetted into white QPCR low-profile plates. Sypro Orange (Invitrogen, 5,000x) was diluted 1:1,000 into K_2HPO_4 containing 80μM of dialysed CRM_{197} solution shortly before DSF measurement. 2μL of the SYPRO/CRM_{197} mixture was added to the bottom the excipient solutions on the 96-well plate, for a total volume of 40μL per well, at a final protein concentration of 2μM per well. The plate was then securely sealed with optical PCR seals and centrifuged at 200x*g* for 1min. The plate was transferred to the pre-heated real-time PCR instrument Mx3005p (Agilent, UK). The temperature scan was performed from 25°C to 95°C at a rate of 3°C/min or an approximate run time of 25min. Data were analysed in MxPro Software. The inflection point of the fluorescence in-

tensity values of the sigmoidal protein dissociation curve was calculated from the Boltzmann function,

$$y = LL + \frac{(UL - LL)}{1 + exp\big((T_m - x)/a\big)} \tag{2.1}$$

where "LL" is lower limit and "UL" is the upper limit of the fluorescence intensity values, and "a" is the slope of the curve at T_m. The minimum of the derivative of the Boltzmann function was reported as T_m.

2.1.4 Karl-Fisher Titration- Residual Moisture Determination

A Karl-Fischer DL39 titrator with Stromboli oven and autosampler (Mettler Toledo, Leicester, UK) was used to determine the residual moisture content of 100mg powder samples. Titration was performed at 125°C for 30min. Results are reported as % wt of water relative to the powder mass.

2.1.5 Differential Scanning Calorimetry - (m)DSC

Differential Scanning Calorimetry was used to determine the glass transition of the freeze concentrate (T_g') and the dry-powder after SFD (T_g). For T_g' determination, 20μL of excipient solution with either 2mg/mL CRM_{197}, or without, was pipetted into hermetic Tzero aluminium pans (TA Instruments, T111208) and hermetically sealed with the corresponding aluminium lid (TA Instruments, T1111019). Samples were analysed on a Q2000 DSC, and computer operated with Thermal Advantage Software interface Version 2.8. Samples were equilibrated at -60°C and held isothermal for 20min. The temperature was then modulated with ±0.5°C every 100 seconds. After 5min isothermal, the temperature modulation had stabilised. The temperature was ramped to 0°C at 1°C/min. For T_g determination, approximately 5mg of SFD-powder was weighed, and sealed into the same hermetic pans and lids.

The protocol equilibrated the sample at -10°C and held it isothermal for 20min. The temperature was ramped to 90°C at 10°C/min. Analysis of the thermal signals was performed with TA Universal Analysis 2000 Software (Version 4.7A). The heat capacity thermogram (J/g°C) was plotted and used for analysis. The temperature at the inflection point of the endothermic shift in heat capacity was reported as the glass transition temperature.

2.1.6 Helium-Pycnometry and Tapped Density Measurements

The density of powders (ρ_{He-pyc}) was measured with a helium pycnometer (Pycnomatic ATC, ThermoFisher, Loughborough, UK). The measurement chamber was fitted with a small volume vessel unit (6.95255 cm^3). The sample chamber volume was further reduced by 3.28743cm^3 using a unit filler to allow for the accurate density determination of very small powder samples. Density measurements were performed on 0.1-0.5 g of powder. Prior to measurement, the sample chamber was purged with helium for 20 cleaning cycles at 20°C. A total of 5 sample measurements within a maximum error of 1% was used to calculate the reported density. Tap density (ρ_{tap}) was determined according to Method A in document QAS/11.450, published by the WHO in 2012 for addition to the International Pharmacopeia [WHO (2012)]. However, instead of a 250mL volumetric glass cylinder, a converted volumetric 5mL pipette tube was used to measure the small powder samples. The machine used for tapped density determination was built in house by the IBME workshop. Briefly, a small electronic motor moves a circular brass disc according to a preset speed and raises a metal plateau upon which the graded volumetric plastic pipette cylinder is attached. The plateau with the sample containing cylinder is raised about 1cm in height and drops by force of gravity alone, before being raised and dropped again. While the tap height remains constant, the tap frequency can

be adjusted based on the supplied voltage to the motor, which alters the rotational speed of the disc. The total number of taps required according to the International Pharmacopeia recommendation before each measurement was divided by the frequency (taps per minute). The thus calculated required time (min) was kept using a stop watch. From helium pycnometry and tapped density values, the porosity of particles was calculated according to the equation:

$$\epsilon = 1 - \frac{\rho_{tap}}{\rho_{He-pyc}} \tag{2.2}$$

2.1.7 Particle Size Analysis with Laser Light Diffraction

Size volume and number distribution of particles, were obtained on a Malvern Mastersizer S (Malvern Instruments Ltd, Malvern, UK), in a small volume dispersion cell. A 300RF lens with backscatter detector with an active beam length of 14.3mm was used to obtain an average of 6 times 6000 measurements according to Mie theory. Particles were added until 10 – 13% detector obscuration was achieved at 2000rpm stirring rate. Particles were characterised by median diameter, D(v, 0.5) and span of the volume distribution:

$$Span = \frac{d(v,0.9) - d(v,0.1)}{d(v,0.5)} \tag{2.3}$$

D(v,0.5) corresponds to the median diameter of the volume distribution, and d(v,0.1) and d(v,0.9) to the particle diameter at 10% and 90% of the cumulative distribution. Refractive indices for HA particles (RI 1.6510) or polystyrene spheres (RI 1.5900) dispersed in dI water (RI 1.3300), and SFD particles (RI 1.5376) in isopropanol (RI 1.3776) were used in the method.

2.1.8 Fluorimetry

The tertiary structure of CRM_{197} when suspended in various excipient solutions at 100μg/mL and pH7.2 was assessed in high-throughput on a 96-well plate (Corning, UK) with a Varioskan Flash® Fluorimeter (Thermo Scientific, Hemel Hempstead, UK). Samples were excited at λ=295nm and emissions were measured from λ310-450nm, with a 12nm slit width for both excitation and emission monochromators. Emission peaks of spectra were identified using SkanIt Software (Thermo Scientific, Hemel Hempstead, UK).

2.1.9 Scanning Electron Microscopy

The morphology of powder particles was examined on an Amray 1810 T Scanning Electron Microscope at 20 kV. The samples were fixed on an aluminium disc (model G 301, Plano) using a carbon adhesive sheet. Samples were gold-sputtered at 20 mA and 5 kV (Hummer JR Technics, Germany) for 1-5 min prior to imaging.

2.1.10 Turbidity Measurement

Solution turbidity of ultrasound-atomised excipient solutions containing 2mg/mL CRM_{197} was measured on a Varian Cary 50Bio UV- Visible Spectrophotometer (Varian, Yarton, UK) with a quartz precision cell (Hellma, GER) of 10mm light path at λ=500nm at RT. Untreated excipient-CRM_{197} solutions served as control. Turbidity is expressed as the absorbance value at λ=500nm.

2.1.11 CRM_{197} Loss During Ultrasound Atomisation with Surfactants

CRM_{197} concentration in excipient solutions containing 2mg/mL CRM_{197} were measured by BCA before and after ultrasound-atomisation. Solutions were sprayed at 48kHz (Sono-Tek) and 3.6W (Broadband Ultrasounic generator, Sono-Tek) into 1.5mL Eppendorf tubes. Both initial and atomised solutions were 0.02μm filtered (Whatman Ltd, GER). BCA was conducted according to supplier's instructions. Briefly, BCA working reagent was prepared from of a 1:1 dilution of solution QA with QB, and activated with copper(II)sulfate reagent QC in a ratio of 1:50 to QA-QB. CRM_{197} containing samples were added to the working reagent in a 1:1 ratio per well on an optically clear 96-well plate (Corning, UK). CRM_{197} concentration was determined relative to a BSA standard curve with concentrations 0, 0.5, 5, 10, 20, 30 μg/mL made in identical buffer to the samples. The plate was incubated at 37°C for 2h and absorbance was measured on a FLUOstar Omega (BMG Labtech LTD, Aylesbury, UK) plate reader at λ=562nm. Concentrations were adjusted to blank and related to the BSA concentration curve.

2.2 Bioceramic Crystal Manufacture and Characterisation

2.2.1 K-HA Particle Manufacture and FTIR

Potassium-substituted hydroxyapatite microparticles were manufactured by molten salt synthesis. The protocol was adapted from Viswanath et al. (2008). Briefly, method I used calcium carbonate ($CaCO_3^-$), calcium pyrophosphate

($Ca_2P_2O_7$) and potassium sulfate ($K_2SO_4^-$). Calcium pyrophosphate and calcium carbonate were combined in the stoichiometric ratio of 1:1 and ball milled for 5 hours, to assure sufficient homogeneity of the mixture. The mixture was transferred into an aluminium oxide crucible (Sigma, UK) with cover (Sigma, UK), heated at 5°C/min to 1350°C, and reacted for 3.5 hours before passively cooling to room temperature (RT). The resultant cake was broken-up into powder with mortar and pestle, before adding potassium sulfate in the stoichiometric ratio of 1:6 respectively. Method II used pure HA powder (Sigma-Aldrich, Dorset, UK), which was mixed with potassium sulfate salt (Sigma-Aldrich, Dorset, UK) in a 1:3, 1:6, and 1:9 ratio by weight. The blended powders were sintered in a covered high alumina crucible at 1200 °C for 3.5 h before cooling to room temperature by passive furnace cooling. Excess salt was removed with hot deionized water. The surface functional groups on the synthesised powders were examined on a Varian Excalibur FTS3500 FT-IR (Agilent, UK). Briefly, 3-5mg of powder sample was ground with 300mg KBr (Sigma, UK) and pelleted for 1min at 95kN on a hydraulic press (Apex Construction, UK) using a 10mm die-set (Specac, UK). Pure KBr pellets served as background. Spectra were acquired at $4cm^{-1}$ resolution and added over 64 scans from 4500-400cm^{-1}. The thus acquired data were not post processed.

2.2.2 HA and kHA Protein Loading

HA and kHA 10 mg powder samples were incubated at room temperature (RT) for 3 hours with 5 mg of bovine albumin tetramethylrhodamine isothiocyanate (TRITC) (Sigma-Aldrich, Dorset, UK) in 1 mL of PBS pH 7.4 (Sigma-Aldrich, Dorset, UK) on a VWR rotating shaker (VWR, Dublin, Ireland). Protein loading of albumin-TRITC on dry-powder HA and K-HA was assessed using fluorescence imaging at 80 ms exposure and 4x magnification on Nicon Eclipse Ti (Nikon Instruments Europe B.V.,

Kingston, UK) and NIS Elements AR 3.0 software. Albumin-TRITC was excited at 550 nm, and fluorescence monitored at 600 nm. Fluorescence intensity was averaged over the respective particle area using ImageJ analysis software (available at http://rsb.info.nih.gov/ij; developed by Wayne Rasband, National Institutes of Health, Bethesda, MD, USA), and reported from low to high on an 8-bit (0-255) grey scale intensity spectrum.

2.2.3 kHA CRM_{197} Dry-Powder Formulation and *In Vitro* Release

The model antigen CRM_{197} (Novartis Vaccines and Diagnostics, Sienna, Italy) was provided in 10 % (w/v) sucrose, 10mM K_2HPO_4 at pH 7.2 and was dialysed against PBS pH 7.4 for 12 hours using Mini Slide-A-Lyzer (FisherScientific, Loughborough , UK) with a 10 kDa molecular weight cut off prior to use. Dialysed CRM_{197} was adsorbed onto 10mg of kHA particles in 1mL of PBS pH 7.4 for 3 hours at 1.6 mg/mL on a VWR rotating shaker. The slurry was centrifuged for 3 min at 2,000x*g* (MSE, London, UK) and the supernatant subsequently decanted. The kHA-CRM_{197} particles were washed thrice with isopropanol (FisherScientific, Loughborough , UK). The wet powder was then transferred into lyophilisation vials (Schott, Müllheim, GER) and vacuum dried for 24 hours at 100mTorr at 20 °C, with a FTS Lyostar I (SP Industries, Warminster, PA, USA). The vials were sealed, crimped, and stored at room temperature until further use. CRM_{197} initial loading and release from kHA in PBS was quantified by BCA micro assay (Sigma-Aldrich, Dorset, UK) after 0, 0.5, 1.5, 6, and 24 hours of incubation in PBS pH 7.4 at 37 °C on a rotating shaker. Absorbance at 562 nm was measured on a Cary 50 Bio ultraviolet-visible spectrophotometer (Varian, CA, USA). Concentrations (C) were plotted as percent release relative to total protein loading (C/C_0 %). The total protein loading on kHA (C_0) was determined as the percentage of the mass difference between CRM_{197} in solution before and af-

ter adsorption (measured by BCA) and divided by the mass of kHA. The Langmuir isotherm is described by the equation:

$$y = \frac{abx^{1-c}}{1 + bx^{1-c}} \tag{2.4}$$

and was iteratively fitted using GaphPad Prism 5 (GraphPad Software, Inc., San Diego, USA). The dependent variable y (mg/g) is the amount of CRM_{197} per mass of kHA, the independent variable x (mg/L) is the CRM_{197} concentration in solution. Variable a is the adsorption capacity, while b and c are model constants.

2.2.4 Structural Characterisation of Surface Adsorbed CRM_{197}

The secondary structure of CRM_{197} when adsorbed on kHA or aluminium hydroxide (Al-Hydrogel®, Brenntag Biosector, Frederikssund, Denmark), or aluminium phosphate (Adju-Phos®, Brenntag Biosector, Frederikssund, Denmark) was determined using a LN_2-cooled FTIR Tensor 37, equipped with the attenuated total reflection BioATR II sample compartment (Bruker Optics, Ettlingen, GER). Over the range 4000 – 800 cm^{-1}, 128 scans were averaged at a 4 cm^{-1} resolution. The ATR unit was temperature controlled at 20°C. OPUS 6.7 software data post-processing included atmospheric compensation, vector normalisation, base-line correction, and integration of the amide I and II band regions from 1720 cm^{-1} to 1480 cm^{-1}. The spectra were evaluated against the structural database “Quant II” provided by Bruker Optics. The “Quant II” software is based on measurements with the transmission cell, and therefore only relative structural changes but not absolute structure can be measured using the BioATR unit. Thermal unfolding of CRM_{197} in the surface-adsorbed state was measured from 20°C – 80°C at 2.5°C increments and 120sec equilibration time. Data processing included atmospheric compensation, vector normalisation, baseline correction, spectral subtraction, and integration of

the amide I and II bands, and was conducted with OPUS 6.7. Unfolding curves were obtained by creating a QuantPro method using spectra at 20°C – 25°C as reference for 0% unfolding and 85 °C – 90°C as 100% unfolding, against which all spectra were evaluated. Sample preparation used 2mg of CRM_{197} that was incubated with 850μg of kHA, $Al(OH)_3$, or $AlPO_4$ for 1 hour at room temperature and suspended in low strength PBS pH 7.2. The suspension was washed with PBS, centrifuged for 5 min at 2000xg, the supernatant was discarded and the CRM_{197}-adsorbed alum gel or kHA was transferred onto the BioATR crystal and measured against protein-free alum gel or kHA. CRM_{197} release from aluminium salts could not be determined as the BCA assay interacted with the aluminium salts, and UV-Vis was not capable to accurately measure the low protein concentrations.

2.2.5 X-ray Diffraction and Energy Dispersive X-ray analysis

X-ray diffraction (XRD) analysis was carried out using a fully automated Siemens D5000 (Siemens, GER) powder diffractometer employing copper $\kappa\alpha$ radiation (λ=0.15406nm) and a secondary monochromator. The sample which was supported on a single crystal of silicon, was continuously spun during data collection and scanned using a step size of 0.04° 2θ between the range of 5°-75° 2θ and a count time of 12 seconds per step. Phase identification using XRD is achieved by comparing the obtained diffraction pattern to a standard data base that is compiled by the International Centre for Diffraction Data (ICDD).

A JSM-840A scanning electron microscope (JEOL Ltd, Japan) equipped with an Oxford Instruments INCA X-ray analysis system was used for energy dispersive X-ray analysis (EDX). EDX analyses the characteristic X-rays produced by the interaction between the primary electron beam and the sample. The technique identifies

all elements present with atomic numbers of 5 and greater (boron) with a detection limit of approximately 0.1 weight %. The measurements are semi-quantitative.

2.2.6 Nanoindentation of Single kHA Crystals

kHA particles were coated onto the bottom of circular cast and embedded in epoxy resin (Buehler, GER) using 5 parts resin to 1 part hardener by weight. After 24 hours, the hardened resin was removed from the cast. Particles were immobilised on the surface of the resin stub. Nanoindentation experiments used a Berkovich indenter tip and were conducted on a Nanoindenter XP (MTS System Corporation, Oak Ridge, TN). Nanoindentation tests used a standard continuous-stiffness-measurement (CSM) method with an indent depth of 800nm. The indent load varied depending on the response of the material but did not exceed 10 mM during loading. Indent load versus penetration depth was continuously measured and analysed according to the Oliver-Pharr method to obtain the hardness and elastic modulus of the single crystals during unloading [Oliver and Pharr (1992)]. The Poisson ratio for HA particles was estimated at 0.26. Fused silica was used as a calibration material, by indenting to the same depth as the test indents and using Analyst Software (MTS Systems) to calculate the area coefficients for the tip.

2.2.7 Atomic Adsorption Spectroscopy

Particles manufactured at 1:3, 1:6, and 1:9 HA to salt flux ratios were dissolved in 3M nitric acid. An absorbance standard curve for Ca_2^+ was prepared from $Ca(OH)_2$ dissolved in 3M nitric acid and diluted with ultra pure milliQ water (Millipore) to 1, 2, 4 ng/mL concentration in 0.1% nitric acid. K^+ ions were obtained from KCl and related to an absorbance standard curve with 0.6, 0.4, and 0.2 ng/mL in 0.1%

nitric acid. Samples were analysed on a Varian AA240 Atomic Absorption Spectrophotometer (Varian, Mulgrave, Australia), using 10mA lamp current, 0.5R spectral bandwidth in argon gas at λ=422.7nm at an ash temperature of 1200°C for Ca_2^+. K^+ analysis used a 5mA lamp current, 1.0R nm spectral bandwidth, and the wavelength λ=766.5nm at an ash temperature of 800°C. The ion content of MSS powders was measured in triplicate and derived from to the respective absorbance standard curve. Machine operation and data collection was done on SpectrAA240 Version 5.01 software.

2.3 Nanoparticle Manufacture, CRM_{197}-conjugation and Structural Analysis

2.3.1 Block Co-polymer Nanoparticle Formation by Flash Nano-Precipitation

All functionalised polymers used in this thesis were synthesised and kindly provided by the Prud'homme Lab (Princeton University, USA). A detailed description of the chemical synthesis steps used to produce polyethylene glycol-b-polystyrene (PEG_{5k}-b-$PS_{1.6k}$) was previously published by Zhang et al. (2011). Briefly, in a first step, hydroxyl terminated polystyrene (PS-OH) was synthesised by combining 1.3M *sec*-butyllithium in cyclohexane with 140g of styrene in 800mL cyclohexane with 10% benzene under an inert argon (Ar) atmosphere. The reaction was quenched after 2 hours with 10mL cold ethylene oxide. The second step produced the block copolymer by anionic ring opening polymerisation and used 50g of PS-OH in THF, which was reacted with a suitable amount of potassium naphthalide under Ar gas. After 1 hour, a stoichiometric amount of ethylene glycol was added and reacted over

night at room temperature. The reaction was quenched with methanol, the polymer precipitated, and subsequently dried (Zhang et al. (2011)). 75% of PEG chains were functionalised with amine reactive para-nitrophenol (pNP). NPs were prepared by Flash NanoPrecipitation as previously described by Johnson and Prud'homme (2003b). Equal amounts (1mL) of organic and aqueous solution contained separately in a 3mL Leur Lock Syringe (National Scientific Company, Rockwood, TN) were rapidly mixed using a hand-held confined impinging jet (CIJ) mixer as described by Han et al. (2012). The organic feed comprised of pNP-PEG_{5k}-b-$PS_{1.6k}$ at 10, 15, or 30 mg/mL in tetrahydrofuran (THF) (FisherScientific, UK) and 10, 30, or 50mg/mL $PS_{1.5k}$ in THF. The aqueous feed was 5mM sodium acetate at pH 4.8 to avoid hydrolysis of pNP group during NP-formation. The product stream was collected into a scintillation vial containing 8mL of sodium acetate buffer (5mM, pH 4.8) and was magnetically stirred during collection. THF was removed by centrifugation in 100k MWCO 15mL Amicon Ultra centrifugation tubes (Millipore, Watford, UK) at 7,200x*g* for 15min. NPs were washed thrice with sodium acetate buffer.

NPs were reacted with CRM_{197} such that the pNP group concentration on NPs was 1000μM and of a 1:1 molar equivalent to primary amines on CRM_{197}, and was based on calculations of initial concentrations. The solution pH was raised to 8.3 using 1M PBS (pH 8.3) to favour the primary amine-pNP reaction. NPs were reacted with CRM_{197} over night on an orbital shaker under light agitation. A yellow coloration of the NP-CRM_{197} solution indicates successful conjugation. Excess CRM_{197} was removed by centrifugation at 7,200x*g* for 15min in 100k MWCO 15mL Amicon Ultra centrifugation tubes. NP-CRM_{197} was washed thrice with PBS pH7.4, and resuspended to the desired concentration. Protein loading was assed by BCA relative to non-CRM_{197} coated NPs from the same batch. Prior to absorbance measurement, NP-BCA solutions were 0.02μm filtered, to remove NPs and avoid

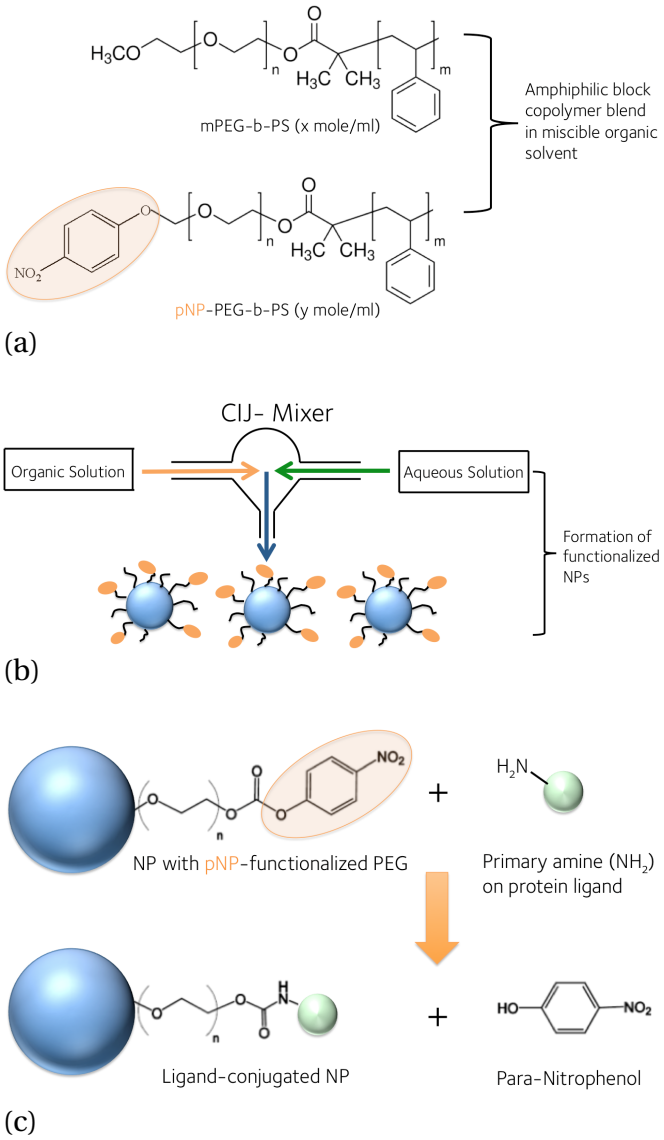


Figure 2.5: Nanoparticle Formation and Ligand Conjugation: a) The surface functionalisation of NPs can be precisely engineered by adjusting the respective molarity of functionalised-to-non-functionalised amphiphilic block copolymer (PEG-b-PS) in the organic phase prior to NP formation by FNP. b) The mixing of confined impinging jets (CIJ), induces NP self-assembly of amphiphilic block copolymer in one step at high supersaturations in turbulent mixing conditions, which allows precise control over NP size. c) Para-Nitrophenol (pNP) terminated PEG chains on the hydrophilic corona of the NPs are reacted with primary amines on the protein ligand, creating a stable peptide bond between the polymer, with pNP as leaving group.

measurement error due to light scattering. Nanoparticle sizes were measured on a ZetaSizer Nano ZS (Malvern Instruments. Worcestershire, U.K.) using an intensity-weighted average at 25°C and the company refractive index settings for polymer (RI=1.590) and dispersant (RI=1.330). NP solutions were 60-fold diluted into milliQ water for for measurement in a disposable optical plastic cuvette (FisherScientific, UK).

2.3.2 Design of Experiments (DOE) - Nanoparticle Size

A two-level fractional factorial analysis was conducted using MODDE 9.1 software (Umetrics, Cheshire, UK) to test the contribution, significance level, and possible interaction of PEG_{5k}-b-$PS_{1.6k}$ and $PS_{1.5k}$ concentrations (mg/mL) in tetrahydrofuran, prior to FlashNanoprecipitation (2.3.1), on the eventual nanoparticle sizes as measured by DLS. Briefly, the Experimental Wizard in MODDE 9.1 was used to define the quantitative outcome variable (nanoparticle size in nm), and the two quantitative predictor variables (polymer concentration in mg/mL in THF) within their respective lower and upper concentration limits (10mg/mL and 50mg/ml for $PS_{1.5k}$, and 10mg/mL and 20mg/mL for PEG_{5k}-b-$PS_{1.6k}$). Based on these parameters, MODDE suggested 7 permutations of concentrations which allowed the program to statistically determine individual contributions and relative contribution of each predictor variable. Experiments were conducted, as previously described (2.3.1), and the nanoparticle size data were fitted with MODDE. The summary of fit plot was used to validate the experiment and model. A model and experiment was valid when all factors (R^2, Q^2, Model Validity, and Reproducibility) were positive and of similar magnitude. Since only two factors were researched and both were significant, and the model and experiment was valid, no factors were excluded from the final DOE model.

2.3.3 SDS-PAGE

SDS-PAGE used the Hoefer SE250 (Hoefer, Holliston, MA) set-up and a PowerPac (BioRad, Hercules, CA) power unit in combination with a precast 4-20% Precise Tris-Glycine gel, 15-Well (Thermo Scientific, Piers Protein Research, USA) and the PrecisionPlus Protein Dual-colour 500ul (BioRad, USA). Running buffer (5x- concentrated) was prepared from 14.5g Tris base, 72g glycine, 5g SDS in 1L MilliQ water, and filtered with 0.22μm Millipore SteriCup. Sample stain comprised of 2mL 1M Tris-Cl pH6.8, 6g glycerol, 1.6g SDS, 4mg Brilliant Blue, 0.62g DTT, for a 20mL final volume. The staining solution comprised of 0.05% (w/v) Coomassie R Brilliant Blue (CBB), 10% (v/v) acetic acid, 45% (v/v) methanol, 45% (v/v) milliQ water, and the destaining solution of 10% (v/v) acetic acid, 30% (v/v) methanol, 60% (v/v) milliQ water. Protein sample concentrations ranged between 20μg/mL to 300μg/mL, and 20μL were used per well, and 5μL of the PrecisionPlus protein ladder (BioRad, UK). Gels were run for 45min at 185V. After the run, the SDS-PAGE gel was rinsed in milliQ water for 5min with 3 complete changes. The gel was stained overnight in a sealed tupperware-box placed on a rocker. Destaining was conducted for 4hours or until the gel was clear, with at least 2 full changes of destaining solution. PEG moieties in the gel were stained by a method adapted from Kurfürst (1992). Briefly, gels were soaked in 40 mL of perchloric acid (0.1M) for 15min. Then 10mL of 5% barium chloride solution was added. After 5min, 4mL of iodine solution (0.1 M) was added. PEG stained brown almost immediately. Staining was terminated by decanting the liquid and submerging the gel in milliQ water. The gel was imaged on Gel Doc™ XR (BioRad, USA) with Quanti One 4.66 software and analysed in GelAnalyser2010 (Freeware, http://www.gelanalyser.com/).

However, the function provided in GelAnlyser2010 did not accurately fit MW bands for the 4%-20% gradient gel. When a second order exponential function was

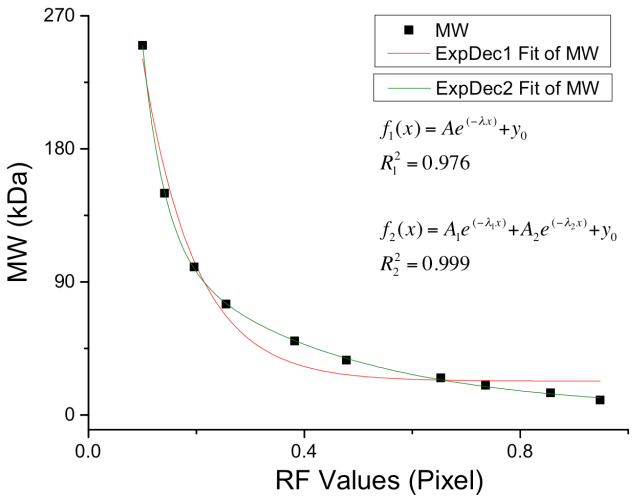


Figure 2.6: SDS-PAGE MW Estimation Correction: The function provided in GelAnalyser2010 (ExpDec1) can determine the MWs of bands for continuous gels, but in the 4%-20% gradient gel it overestimates some MWs and underestimates others. A second order exponential decay function (ExpDec2) can accurately fit MW bands for the 4%-20% gel, with RF values being the distance in pixels.

used to fit the bands, excellent correlation could be achieved R^2=0.999 (Figure 2.6).

2.3.4 Structural Analysis of CRM_{197} on NPs

The tertiary structure of CRM_{197} was assessed on a F-7000 FL Spectrophotometer (Hitachi High-Tech, USA). NP-CRM_{197} and CRM_{197} were suspended in 10mM K_2HPO_4 pH7.2 CRM_{197} at a CRM_{197} concentration of 100μg/mL. The sample was excited at λ=295nm and emissions were measured from λ310-450nm at 1200nm/min, with a 10nm slit width for both excitation and emission.

FTIR analysis of surface-bound CRM_{197} on NPs was conducted on a mid-IR Thermo Nicolet NEXUS 670 (ThermoScientific, West Palm Beach, FL) equipped with 45° ZnSe SmartArk cell in a nitrogen-purged chamber. The bench was set to collect from the main sample compartment with a broad-band liquid nitrogen-cooled mercury cadmium telluride (MCT/A) detector, using a KBr beam splitter and

IR source with the Smart ARK accessory. The SmartArc ATR was used, instead of the CaF_2 optical transmission cell to avoid any light scattering effects of NPs. Spectra were obtained from 2000-650cm^{-1} with co-addition of 64 scans at 4cm^{-1} resolution with auto gain, and 0.6329 mirror speed with an aperture of 12. Prior to spectrum acquisition, the ATR was cleaned with 5% SDS, then rinsed thoroughly with milliQ water. The buffer background spectrum was then acquired, and the ATR dried before 500μL of the sample was added and measured. The background was subtracted automatically. Data post-processing included baseline-correction and data-normalisation to 1.0 for the amide I region of 1710-1590 cm^{-1}. Automatic smoothing used a nine-point Savitsky-Golay function, and H_2O and CO_2 atmospheric correction. Amide I band spectra were deconvoluted using Lorenzian peak-fitting at a full width half hight of 4.0. Peak positions and structural contents were categorised according to Vonhoff et al. (2010).

2.4 Particle Injection and Vaccine Immunogenicity Study

2.4.1 Agarose Targets

To provide a basic tissue mimicking material, standard grade agarose (Sigma-Aldrich, UK) was suspended in deionized water (Millipore, MA) to form a 3% w/v solution. The beaker was covered with an hourglass to prevent the loss of moisture while the solution was microwaved (Proline MicroChef ST44) at 950 Watts for 1 minute. The solution was immediately transferred to a sonicator water bath (Crest Ultrasonics, Trenton, NJ) preheated to 50°C. The ultrasound caused bubbles in the agarose to rise to the top, therefore, bubble-free agarose was pipetted from the bot-

tom of the beaker into a 35mm x 10mm Petri dish (Corning, UK) until a convex meniscus formed at the top rim. To prevent 'skin' formation during the gelling process and subsequent storing, the Petri dish lid was placed onto the convex meniscus, which caused agarose gel to flow out the sides, but created a smooth, bubble-free, and 'skin-free' agarose top surface. After initial gelling, the Petri dish was sealed with parafilm and stored at 4°C. Prior to use, the sealed agarose targets were allowed to equilibrate to room temperature. Prior to particle injection at 55 bar, the Venturi device was securely clamped such that the nozzle opening lightly touched the surface of the agar gel. Targets were sectioned post injection to slices of <1mm to obtain images under a Nikon Eclipse T*i* light microscope. Particle penetration depth was measured with the image analysis program ImageJ.

2.4.2 Injection Depth and Dermal Measurements

Female BALB/c mice were purchased from Harlan (Harlan, Oxfordshire, UK). All animals and procedures were used in accordance with the terms of the UK Home Office Animals Act Project License. Procedures were approved by the University of Oxford Animal Care and Ethical Review Committee. The fur was clipped and shaved on the abdomen and at the base of the tail. Injection sites were prepped with 70% ethanol prior to injection. kHA microparticles were injected at 55 bar gas pressure using the inline Venturi needle-free powder injection device (Particle Therapeutics Ltd, Yarton, UK). Histology samples from the injection sites were excised immediately post-cull fixed in 10% buffered formalin, dehydrated in alcohol, embedded in paraffin wax, 5 μm sectioned and stained with hematoxylin and eosin (Sigma-Aldrich, Dorset, UK). Images were obtained on Nikon Eclipse Ti with NIS Elements AR 3.0 software. Particle penetration depth, and viable epidermis (*ved*) and *stratum corneum* (*sc*) thicknesses were assessed using ImageJ.

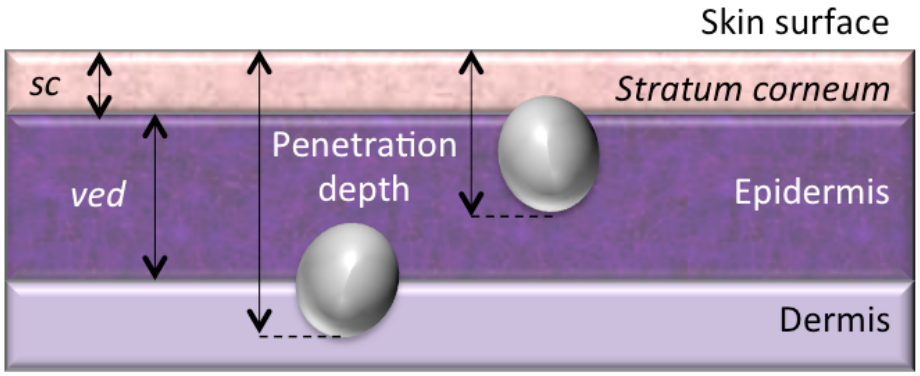


Figure 2.7: Particle Injection Depth Measurement: The thickness of *sc* (pink tissue layer) and *ved* (deep purple tissue layer) were measured as depicted. The particle penetration depth was measured as the length of the line that connects the deepest part of a particle in the tissue to the outer part of the *sc* and is perpendicular to the latter (depicted). The distances in pixels were related to the microscope's calibration scale to obtain distance measurements in μm.

The particle injection depth was measured based on the microscope's calibrated size scale and is reported as the distance between the outer part of the *sc* and the location on the particle furthest in the tissue (Figure 2.7). The co-localisation of particles in the epidermis was determined by comparing the mean particle penetration depth to the deepest acceptable location in the skin, that was defined to comprise of mean *sc* + *ved* thickness at a given injection location. Because the diameter of kHA particles is larger than *sc* thickness, if their penetration depth was similar or less than the *sc* + *ved* threshold, particles were located at least partially in the epidermis.

2.4.3 Histology Staining

The tissue was cut longitudinally through the centre and processed by routine automated procedures. First, dehydration using ascending grades of industrially methylated spirit (IMS), followed by clearing in toluene and embedding in paraffin wax. The tissue was embedded on edge. One 5 μm section was cut using the microtome. The section was flattened on warm de-ionised water in a water bath (60°C), then

mounted onto an appropriately labelled glass slide. The section on the slide was dried overnight at 60°C on a hotplate. The section was stained with Haematoxylin and Eosin by routine procedures. Briefly, the sample was dewaxed in xylene and rehydrated in descending grades of IMS and washed in tap water. Samples were then stained with Gill's III Haematoxylin and washed in tap water. Samples were differentiated in acid-alcohol and blue-stained in tap water. Then, samples were counterstained with eosin and rinsed in tap water. Eventually, samples were dehydrated in ascending grades of IMS, cleared in xylene and mounted with a coverslip using DPX mountant. The as described histology and sectioning was performed by Northwick Park Institute For Medical Research, UK.

2.4.4 Needle-free Immunisation Study Setup: SFD, SFD-NP, and kHA Dry CRM_{197} Powders

Six weeks old female Balb/C mice (Harlan, Oxfordshire, UK) were fully anaesthetised with isoflurane gas. Before needle-free administration of kHA-CRM_{197}, the murine pinna was sterilised with 70% ethanol solution. The inline Venturi Device (Particle Therapeutics Ltd, Yarnton, UK) was placed onto the dorsal pinna for injection. Medical grade helium pressured at 55 bar was used to accelerate the kHA powder containing 10μg CRM_{197} into the skin. In the SFD- formulations and nanoparticle immunogenicity study, each dose injected 5μg CRM_{197} into the murine pinna skin. Intramuscular injection with 0.125mL of aqueous CRM_{197} was administered into the medial thigh of each hind leg using a 29-gauge needle. The total volume of 0.25mL contained 10μg CRM_{197}in the kHA study, with or without 85μg alum (n = 8). In the nanoparticle and SFD-formulations immunogenicity study 5μg CRM_{197} was injected. Naïve mice served as negative control (n = 4). Mice were primed on day

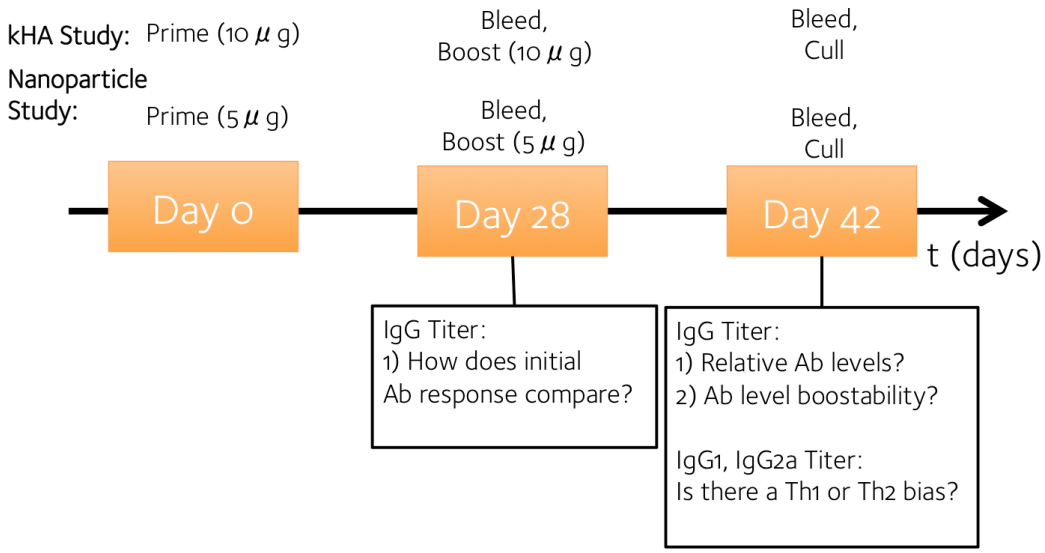


Figure 2.8: Immunogenicity Study Design: Prime and boost used the same formulations for each respective treatment group. (~ 6wk old female Balb/c mice); n = 8 per treatment group, n = 4 control (naïve)

0 and boosted on day 28 with the same formulations and antigen dose. Blood was collected from the tail vain on days 28 and 42.

2.4.5 Manufacture of NP-CRM_{197}-containing TMDD by SFD

Nanoparticles were prepared by FNP as previously described (2.3.1). Briefly, 12mg/mL PEG and 24mg/mL PS in 1mL THF was impinged with 1mL of sodium acetate using the CIJ-mixer. CRM_{197}-loading on NPs was measured by BCA as previously described (2.3.1), and was determined to be 1.2% by weight. Since 5μg of CRM_{197} would have corresponded to 0.4mg of polymer carrier per dose, the final antigen dose was delivered as a combination of CRM_{197} immobilised in the 30% wt TMDD (3:3:3:1) excipient matrix and CRM_{197} conjugated to NPs. From the final FNP NP-suspension, 10mg of CRM_{197}-NP was added to 1.5g of excipients and suspended to a total volume of 5mL in K_2HPO_4 pH7.2. Therefore, lyophilised powders contained a total of 0.67% wt of PEG(5k)-b-PS(1.6k)-PS(1.5K) NPs. For 1.5g of

dry-powder to contain 5μg of CRM_{197} for every 1mg of powder, there has to be a total of 7.5mg of CRM_{197} in the formulation. Since 10mg of NP-CRM_{197} contained 120μg of CRM_{197} 7.38mg of liquid CRM_{197} from the dialysed stock was added to 0.12mg of NP-bound CRM_{197}. Subsequent processing and SFD, were conducted as previously described (2.1.1). Powder cassettes were loaded with 1mg of formulation (Table 2.1) using a microbalance (MT5, Mettler Toledo, UK), sealed, and stored at 4°C until use (less than 3 days).

Table 2.1: SFD- and NP Immunogenicity Study Formulations.

Group	Route	CRM_{197} dose	Formulation
Naïve	NA	0 μg	NA
CRM-PBS	IM	5μg	CRM_{197} in PBS pH 7.4.
CRM-TMDD	IM	5μg	CRM_{197} in 30% wt. trehalose, mannitol, dextran (150kDa), dextran (10kDa) (3:3:3:1) in 10mM K_2HPO_4 pH7.2.
CRM-Alum	IM	5μg	CRM_{197} in TRIS pH 7.5 with 85μg K_2HPO_4.
CRM-NP	IM	5μg	CRM_{197} in 30% wt. trehalose, mannitol, dextran (150kDa), dextran (10kDa) (3:3:3:1) in 10mM K_2HPO_4 pH7.2, with CRM-NP. CRM-NP: 160-200nm mean diameter; 1.2% wt. CRM_{197} conjugated NP (PEG(5k)-b-PS(1.6k) shell and PS(1.5k) core) per dose. Note: The total dose of NP-bound CRM_{197} plus the excipient encapsulated CRM_{197} was designed to equal 5μg.
CRM-TMDD	NF (ear)	5μg	CRM_{197} in 30% wt. trehalose, mannitol, dextran (150kDa), dextran (10kDa) (3:3:3:1) in 10mM K_2HPO_4 pH7.2. Sprayed at 48kHz, 3.6W, LN_2 frozen, lyophilised at -10°C (primary, 48hrs) and +20°C (secondary, 15hrs), size 54μm mean diameter. 1mg powder injected at 50bar into ear
CRM-NP	NF (ear)	5 μg	CRM_{197} in 30% wt. trehalose, mannitol, dextran (150kDa), dextran (10kDa) (3:3:3:1) in 10mM K_2HPO_4 pH7.2, with CRM-NP CRM-NP: 160-200nm mean diameter; 1.2 % wt. CRM_{197} conjugated NP (PEG(5k))-b-PS(1.6k) shell and PS(1.5k) core) per dose. Note: The total dose of NP-bound CRM_{197} plus the excipient encapsulated CRM_{197} was designed to equal 5 μg. Sprayed at 48kHz, 3.6W, LN_2 frozen, lyophilised at -10°C (primary, 48hrs) and +20°C (secondary, 15hrs), size 50μm mean diameter 1mg powder injected at 50bar into ear.

2.4.6 Enzyme-linked Immunosorbent Assay

Antibody responses were assessed by ELISA after coating plates (FisherScientific, Loughborough , UK) with 0.5μg of CRM_{197} antigen per well (5μg/mL CRM_{197} working concentration and 100μL per well) in carbonate–bicarbonate buffer (Sigma-Aldrich, Dorset, UK). Plates were blocked with PBS containing 5% (v/v) newborn

calf serum (Sigma-Aldrich, Dorset, UK). Serum samples were serially diluted in PBS–Tween with 5% (v/v) newborn calf serum, at a starting dilution of 1:200. After incubation at 25 °C for 2 hours, a detecting goat anti-mouse antibody (Southern Biotech, Cambridge, UK) was added at a dilution of 1:2000 in PBS-Tween with 5% (v/v) newborn calf serum. After 1 hour incubation, plates were developed with 3,3',5,5'-tetramethylbenzidine substrate (Sigma-Aldrich, Dorset, UK) for 10min and stopped with 2M sulfuric acid (Sigma-Aldrich, Dorset, UK). The optical density (OD) was read at 405nm with a Multiskan EX (Thermo Scientific, Loughborough, UK). Results were expressed as endpoint titres where the cutoff value is the mean blank value plus 2 standard deviations.

2.5 Statistical Analysis

Statistical analysis was performed and graphically displayed using GraphPad Prism 5 (GraphPad Software, Inc., San Diego, USA). A two-tailed student t-test was used for single paired comparisons, for which unequal variance was assumed. One-way analysis of variance (ANOVA) was used for multiple group comparisons and was based on the Tukey-Kramer method. An alpha level of 0.05 was considered to be statistically significant. Experiments were performed in triplicate and repeated tree times unless indicated otherwise. Data are presented as means with standard deviation. Sample size (n) and P-values are stated in the figure legends.

CHAPTER 3

SPRAY-LYOPHILISATION OF CRM_{197}

The first section of Chapter 3 aims to make excipient screening and dry-powder vaccine formulation more economical, less time-consuming, and more predictable. To achieve this purpose, the suitability of differential scanning fluorimetry (DSF) as high-throughput excipient screening modality was investigated. The thus determined thermodynamic stability of CRM_{197} in the presence of various co-solutes was correlated to its tertiary structure and the most promising excipient formulations were subsequently manufactured by SFD. Subsequently, dry-powder vaccine formulations were physically characterised and the structural integrity of CRM_{197} analysed by AF_4.

3.1 INTRODUCTION

After 2003, most investigational dry-powder formulations of viral and bacterial protein antigens for application in needle-free ballistic injection were manufactured by spray-freeze drying [A.9, A.10, A.11, A.12, A.13, Weissmueller et al. (2013)]. Briefly, SFD atomises a liquid formulation that conventionally contains an active pharmaceutical ingredient and various excipients into a cryogenic liquid prior to the removal of water from the frozen droplets by ice sublimation at reduced tempera-

tures [Nail et al. (2002)]. Relative to alternative particle manufacture methods such as spray-drying or compaction and grinding, SFD readily produces particles with a larger diameter and a more narrow size distribution respectively [Maury et al. (2005); Schiffter et al. (2010)]. However, many small ice crystals form within single particles due to fast freezing rates, which upon sublimation results in a highly porous construct that mechanically is not suitable for ballistic injection [Costantino et al. (2000, 2002); Schiffter (2007)]. The addition of a high solute content in the liquid feed, the addition of polymers such as dextran, or a temperature adjustment to the lyophilisation procedure may be used to reduce particle porosity and increase structural stability of SFD powders [Sonner et al. (2002); Rochelle and Lee (2007); Schiffter et al. (2010)]. While SFD has been successfully used for needle-free ballistic injection, the atomisation step presents an additional and possibly detrimental step to the preservation of the antigen in the dry formulation [Yu et al. (2006); Tang and Pikal (2004)]. These additional stresses, however, may be compensated for by a smart choice of excipient combinations. While the established approach in formulation development of 'one-factor-at-a-time' (OFAAT) has been very successful, the recent trends in the pharmaceutical industry lead away from 'shots on target' to 'more targeted shots'. This may be achieved with high-throughput screening tools and a statistical approach that achieves quality by design (QBD), ideally by design of experiments (DOE). Lyophilisation is a time and energy costly process, and therefore it would be ideal if most formulation screening and optimisation could be conducted prior to the lyophilisation step. Differential scanning fluorimetry, has emerged as a novel technology that measures the thermodynamic stability of proteins and peptides in solution [Niesen et al. (2007)]. So far, DSF has been successfully used for peptide and protein ligand screening, but not much has been published on its utility in the screening for SFD formulation excipients.

This chapter aims to formulate CRM_{197} as dry-powder with suitable mechanical characteristics for ballistic injection using SFD. The utility of DSF in SFD formulation development is evaluated for CRM_{197} based on the rationale that an increased thermodynamic stability of CRM_{197} in solution may reduce CRM_{197} aggregation during SFD. CRM_{197} is subjected to different physical stresses during SFD and rational formulation development should choose excipients to optimise CRM_{197}-stability against the most detrimental manufacturing step. The best formulation minimises CRM_{197} aggregate content while achieving suitable physical characteristics for ballistic injection such as size, density, residual moisture, and a high glass transition temperature.

3.2 Results and Discussion

3.2.1 Spray-lyophilisation Process

3.2.1.1 Critical Steps in the SFD Process

The sequence of steps in the dry-powder manufacture of CRM_{197}, begins with the solution of CRM_{197} in the liquid excipient matrix, followed by ultrasound atomisation, closely followed by quench-freezing of the droplets in LN_2, and finally the lyophilisation of the frozen microdroplets. Each step along this production chain exerts mechanical or thermal stresses on the protein and may affect the final quality of CRM_{197} in the dry-powder. The SFD production chain is graphically summarised in Figure (3.1).

An initial study used light scattering at OD_{500} to monitor visible aggregates throughout this process. Based on previous reports on needle-free powder in-

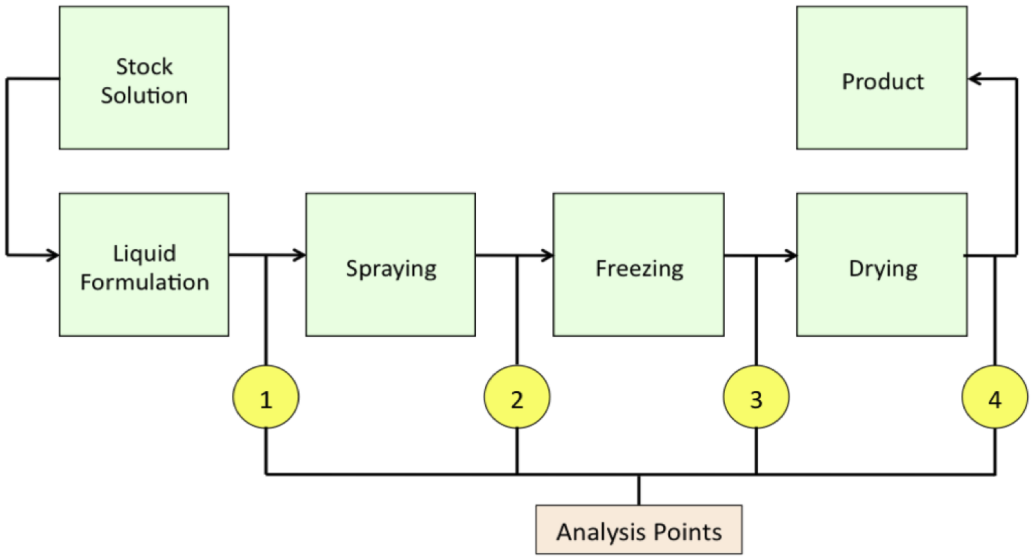


Figure 3.1: SFD Stress Evaluation After Procedural Steps: SFD can degrade CRM_{197} at any stages in the process. To identify the most detrimental step in SFD to CRM_{197} integrity, analysis was conducted after CRM_{197} suspension in the excipient matrix (1), atomisation (2), freezing (3), and lyophilisation (4).

jection, this initial study compared the most commonly used excipients, namely: sucrose, trehalose, mannitol, and dextran, with and without polysorbate surfactant (PS80). ANOVA suggests that there is no difference within groups ($p > 0.05$), but a significant difference between groups ($p < 0.05$). From solution to atomised droplets, there was an approximate 10-fold increase in turbidity (Figure 3.2). From solution to thawed droplets after atomisation and freezing there was an average 100-fold increase in turbidity. Relative to solution, resuspended powders showed an average of 10-fold increased turbidity. While not significant, TMDD solutions (trehalose, mannitol, dextran 150 kDa, dextran 10 kDa, in ratio 3:3:3:1) showed a trend suggesting lower turbidity compared to sucrose and trehalose. The addition of PS80, did not reduce turbidity significantly after atomisation, but showed a trend towards less turbidity after spray-freezing, and spray-freeze-drying (Figure 3.2). Although the figure suggests that TMDD and TMDD+PS80 CRM_{197}-formulations had least turbidity, it was observed that CRM_{197} had formed very large precipitates in

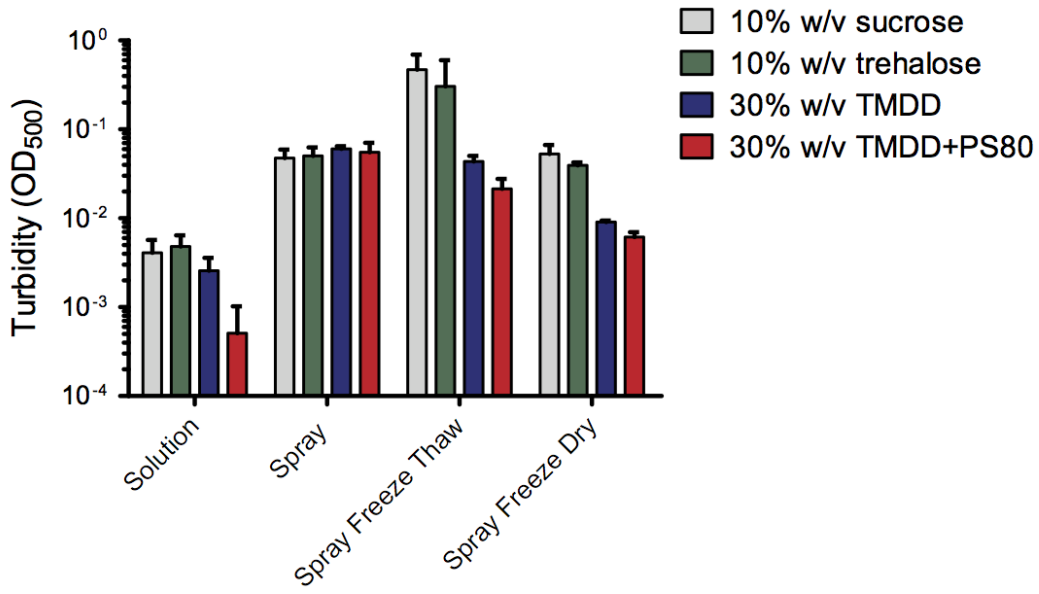


Figure 3.2: SFD Process Stress Evaluation - Turbidity: Atomisation of all four excipient solutions was performed with a 48 kHz nozzle (SonoTek) at 3.6 W power and a 0.5 mL/min flow rate. Turbidity of 2 mg/mL CRM_{197} solutions in 10 mM K_2HPO_4 pH 7.2 was measured by UV-Vis light scattering (OD_{500}) at four critical points along the manufacturing chain from solution to resuspended final product. Materials and methods section 2.1.10.

both solutions after spraying which could not be captured by turbidity measurement. Therefore, although sucrose and trehalose solutions show higher turbidity, they preserved CRM_{197} better during SFD than TMDD or TMDD+PS80.

While turbidity may not be the most robust measurement, it does give a good indication of the presence of some visible aggregates, and the presented data suggests that the atomisation and thawing steps significantly increased turbidity for all formulations. In the actual manufacture process, the thawing step is not present since the frozen droplets are lyophilised while still frozen. Therefore, the formulation of CRM_{197} and process parameters were further optimised against the atomisation step. Atomisation exerts mechanical and thermal stress on the protein at the nozzle tip.

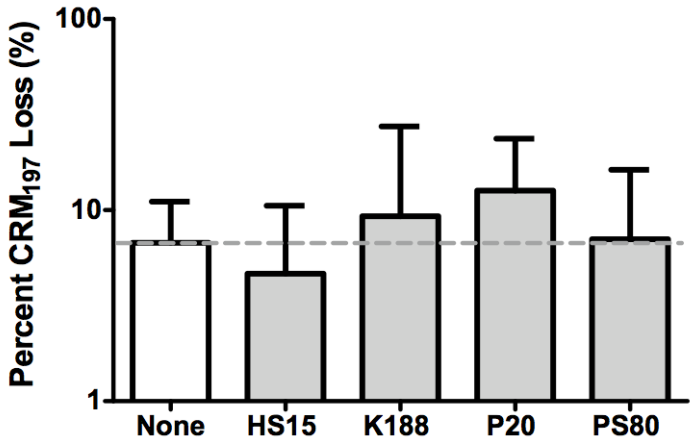


Figure 3.3: SFD Process Stress Evaluation - Surfactants: Surfactants (Polysorbate 80 (PS 80), Polysorbate 20 (PS20), Poloxamer 188 (K188), and Kolliphor HS (HS15)) were added with 0.1% wt to 1 mg/mL CRM_{197} in TMDD 30% wt formulation in 10 mM K_2HPO_4 pH7.2, and atomised with a 48 kHz nozzle (SonoTek) at 3.6 W power and a 0.5 mL/min flow rate. CRM_{197} solutions were 0.02 μm filtered and the protein concentration was determined before and after atomisation by BCA assay (n = 3). Means are expressed relative to the respective filtered but not sprayed CRM_{197} formulations.

3.2.1.2 The Effect of Surfactants on CRM_{197} Aggregation during Atomisation

To investigate the effect of the shear stress and possible hydrophobic patch association of CRM_{197} molecules at interfaces created during atomisation, various pharmaceutical grade surfactants were tested. After solutions were sprayed and 0.02 μm filtered, this filtration step would remove any large aggregates, BCA assay was used to determine the loss of CRM_{197} (Figure 3.3).

ANOVA suggests that there was no difference between the groups ($p > 0.05$). On average there was a 8.1% decrease of CRM_{197} concentration associated with atomisation. Relative to TMDD alone, the addition of surfactant showed no significant reduction in CRM_{197} loss. Therefore, the addition of surfactants to the formulation had no detectable effect on atomisation-induced CRM_{197} loss. This is surprising in that surfactants have been shown to improve the viability of proteins during

spray drying and spray-freeze drying [Wang (2000)]. The most frequently discussed mechanism of protein preservation by surfactants is their preferential accumulation at solution interfaces which can prevent protein molecules from accumulating and interacting at these interfaces [Maa et al. (1998)]. These findings therefore suggest that intermolecular interactions at interfaces are not the only factor in CRM_{197} aggregation during atomisation. In addition to shear at the nozzle tip and the subsequent solution-air interface of the droplets, localised heating and high pressures due to cavitation at the ultrasound nozzle tip may lead to radical formation and oxidative stress, which may play a role in CRM_{197} aggregation. Proteins are generally less likely to aggregate when their free energy of unfolding (ΔG_{unf}) between native and unfolded state increases. Therefore, it was hypothesised that the addition of excipients may enable sufficient thermodynamic stabilisation of CRM_{197} in solution to markedly reduce CRM_{197} monomer loss.

3.2.2 Formulation Design

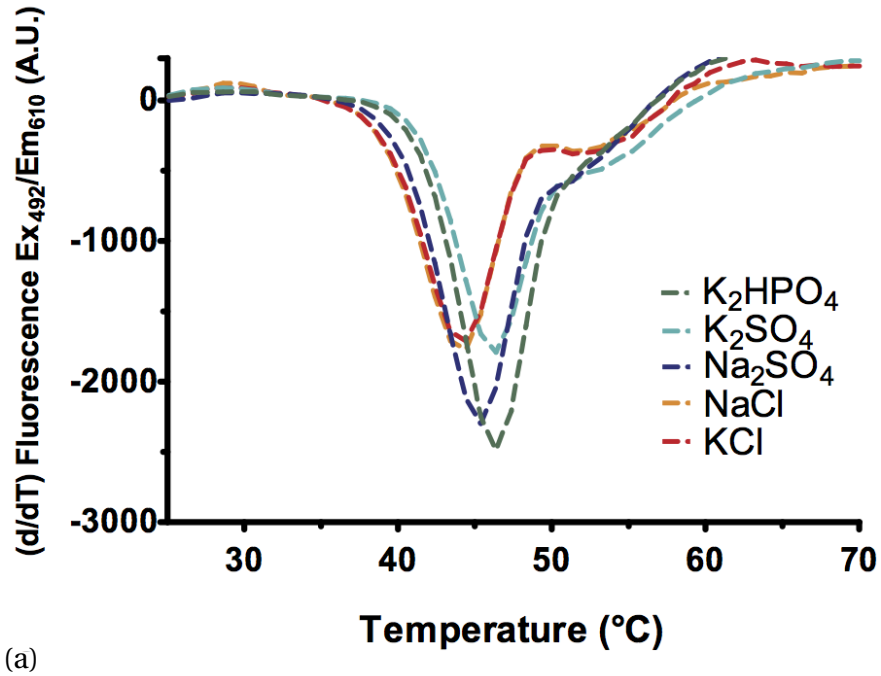
3.2.2.1 Excipient Screen to Increase the Thermodynamic Stability of CRM_{197} using DSF

The thermodynamic stability of proteins is affected by intra- and inter protein interactions, as well as protein-solution conditions and composition. Stabilisation in solution can be achieved through charge interactions such as hydrogen bonding, hydrophobicity and hydrophilicity associations, dilution of the protein by an additive, and preferential exclusion of an additive from the protein. Protective additives raise the free energy of unfolding whereas denaturing additives lower the free energy of the denatured state [Auton and Bolen (2005)]. Important solution factors are the buffer type, pH, and ionic strength, among others. The characteristics of addi-

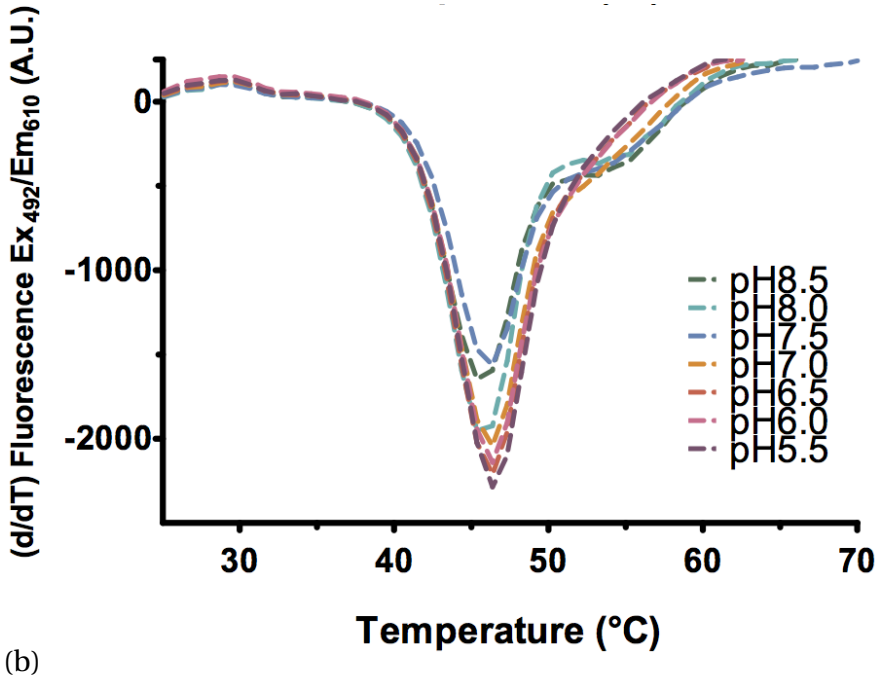
tives, such as sugars, polymers, amino acids also can impact thermal stability. These interactions are not mutually exclusive and hence amount to a complex system of energetic interactions. A simple indicator that describes the overall effect of these factors on the relative thermodynamic stability of a protein is its melting temperature (T_m) [Eisenthal et al. (2006)]. At the melting temperature, a protein's free energy of unfolding is zero. In general, T_m correlates directly with thermal stability [Rees and Robertson (2001)], and proteins with higher T_m are less likely to aggregate [Chi et al. (2003)].

The thermal unfolding of proteins in the presence of a fluorescent dye can be monitored using DSF [Niesen et al. (2007)]. The non-polar SYPRO Orange dye can access hydrophobic pockets of a protein that are exposed during thermal denaturation. In these pockets, the quenching by the polar solvent is substantially reduced and the dye fluoresces. DSF was used to screen the effect of various buffer salts, ionic concentrations, amino acids, polyols, polymers, mono-, di-, tri- and polysaccharides, pH, and various additive combinations on the T_m of CRM_{197} (Figure 3.4, 3.6, 3.7, 3.8).

The data presented in table A.1 show that salt concentrations higher than 10mM tend to reduce the T_m of CRM_{197} in solution. Therefore, buffer salts were investigated at 10mM. Figure 3.4 a) depicts the effect of different salts at 10 mM and pH7.2 on the melting temperature of CRM_{197}. The results suggest that potassium ions in combination with either phosphate or sulphate ions yield the highest T_m for CRM_{197} out of the tested salts with 46.4°C. Sodium sulphate reduced the T_m of CRM_{197} to 45.4°C while sodium and potassium chloride reduced the T_m to 44.4°C (Figure 3.4 a). Protein-salt interactions can impact i) the charged groups on the protein, ii) exposed peptide groups, and iii) and non-polar groups [Curtis et al. (2002)]. In what way potassium and sodium ions interact with CRM_{197} needs to be further



(a)



(b)

Figure 3.4: DSF - Buffer Salts and pH: DSF results are shown for different a) buffer salts, and b) pH levels (10 mM K_2HPO_4). The derivative of the fitted Boltzmann equation for each additive is displayed. The respective minimum corresponds to the T_m of CRM_{197} with the respective additive. Except for a), all additives are suspended in 10 mM K_2HPO_4 buffer. All solutions were adjusted to pH 7.2, except for b). Materials and methods section 2.1.3.

investigated, but the results suggest that potassium cations are preferable to sodium (T_m K_2SO_4 > T_m Na_2SO_4). Although the same salts may have different effects on different proteins, Oobatake et al. (1979) previously reported superior stabilising effect of potassium phosphate on the T_m of ribonuclease compared with sodium chloride.

The presence of chloride ions reduced the T_m of CRM_{197} irrespective of the cation (K^+ and Na^+). Interestingly, chloride-containing salts showed a distinct second minimum at 56.2°C. This suggests that there are major unfolding events at two different temperatures. This is similar to findings by Ramsay et al. (1989). Their paper showed that thermal denaturation of diphtheria toxin is characterised by a minimum of two coupled two-state unfolding processes. With the use of DSC, they determined two characteristic peaks of unfolding with T_m at 44.2°C for the A fragment (catalytic domain) and T_m 58.4°C for the B fragment (transmembrane and receptor-binding domain), and suggested that domain-domain interactions double the free energy of unfolding of the A-domain from -2.2 kcal/mol to -4.7 kcal/mol [Ramsay and Freire (1990)]. The A-B domain stabilisation was modelled and resulted in a single unfolding peak with T_m larger than A, but lower than B, at approximately 53°C [Ramsay and Freire (1990)].

The presented data supports the concept of interdomain stabilisation: the T_m of CRM_{197} was 44.2°C , which is in agreement with the value reported by Malito et al. (2012) (T_m=44.3°C). However, while DT reportedly has a 10°C higher T_m of 55.2°C, the measured subunit unfolding temperatures of CRM_{197} obtained with DSF (T_{mA}=46.3°C, T_{mB}=56.2°C, Figure 3.5) are almost identical to the subunit unfolding temperatures of DT obtained with DSC as reported by Ramsay and Freire (1990). This suggests that the point mutation in CRM_{197} does not markedly alter the thermal stability of the individual subunits, but much rather destabilises the entire protein by reducing the domain-domain interactions. Since the point muta-

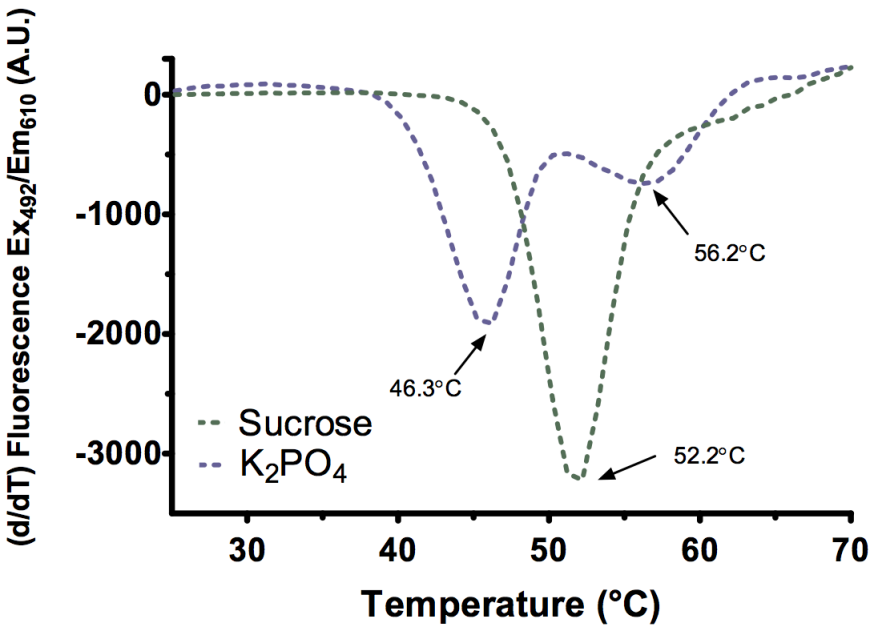


Figure 3.5: DSF - Coupled and Decoupled Thermal Unfolding: DSF of CRM_{197} shows two minima located at 46.4°C and 56.2°C during thermal denaturation in 100mM KCl, pH 7.2. When suspended in 10mM K_2HPO_4 pH 7.2 with 220mM sucrose, only one unfolding peak is observed at the intermediate temperature of 52.2°C.

tion introduces mobility of the catalytic loop as was shown by Malito et al. (2012), then this result suggests that the position of the catalytic loop plays an important role in domain-domain stabilisation of DT against thermal unfolding.

While the unfolding temperatures observed with DSF (Figure 3.5) are remarkably similar to the values reported by Ramsay and Freire (1990), it should be noted that the peak magnitude in DSC corresponds to the heat of unfolding, and the peak magnitude in DSF corresponds to fluorescence intensity of the SYPRO Orange dye and does not provide inference on the magnitude of the energetic event. The larger peak intensity of the lower temperature peak in the DSF scans could suggest that the A-domain has more hydrophobic pockets than the B-domain. This interpretation is supported by the molecular model published by Malito et al. (2012).

In light of the observed DSF data in Figure 3.4 a), it appears that chloride

ions in particular seem to partially disrupt the stabilising domain-domain interactions. The higher the chloride ion concentration the more distinct the two unfolding peaks. Whether this observation is due to alteration in local CRM_{197} surface charge, or possibly due to salting-in or salting-out effects needs further investigation. Past literature suggests that physiological levels of 150mM NaCl have been shown to shift the conformational change of CRM_{197} from pH 4-4.5 to pH 5-5.5 range [Blewitt et al. (1984)]. This change in CRM_{197} conformation from closed to open form is in part achieved by protonation of the acidic residues on salt bridges that stabilise intra and inter CRM_{197} domains [Bennett et al. (1994b)]. Therefore, it is plausible to assume that the addition of salt may impact charge and protonation propensity of residues engaged in salt bridge stabilisation. Based on the presented data, 10mM K_2HPO_4 was chosen as best buffer for CRM_{197} formulation.

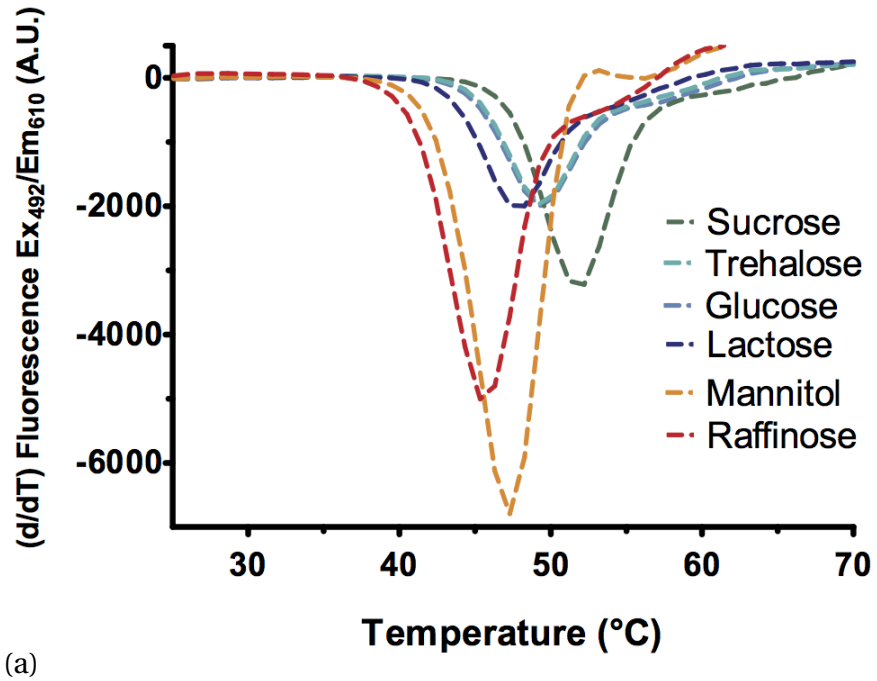
At varying pH, T_m of CRM_{197} was 46.3°C for pH 6.0-7.5 and decreased by 1°C at pH 5.5 and pH 8.0-8.5 (Figure 3.4 b). The conformational change of CRM_{197} occurs at acidic pH, in part due to charge alterations on various amino acid residues. At basic pH, two unfolding minima are observed, while at acidic pH only one unfolding peak is observed. From basic to acidic milieu, there is a progressive decrease in the higher temperature unfolding peak intensity. Based on the theory initially presented by Ramsay and Freire (1990), this observation could suggest that CRM_{197} A and B domain interaction is stronger at lower pH. CRM_{197} was most thermally stable at neutral pH, and therefore further formulation studies were carried out at pH 7.2.

In addition to salts, organic compounds such as saccharides, amino acids, polyols, and polymers can affect protein stability in solution. DSF screening of saccharides suggests that the di-saccharides sucrose and trehalose raise T_m of CRM_{197} to 53.2°C and 51.2°C respectively. This is followed by the reducing sugars lactose (49.2°C) and glucose (47.3°C). The mono-saccharide mannitol only raised the T_m

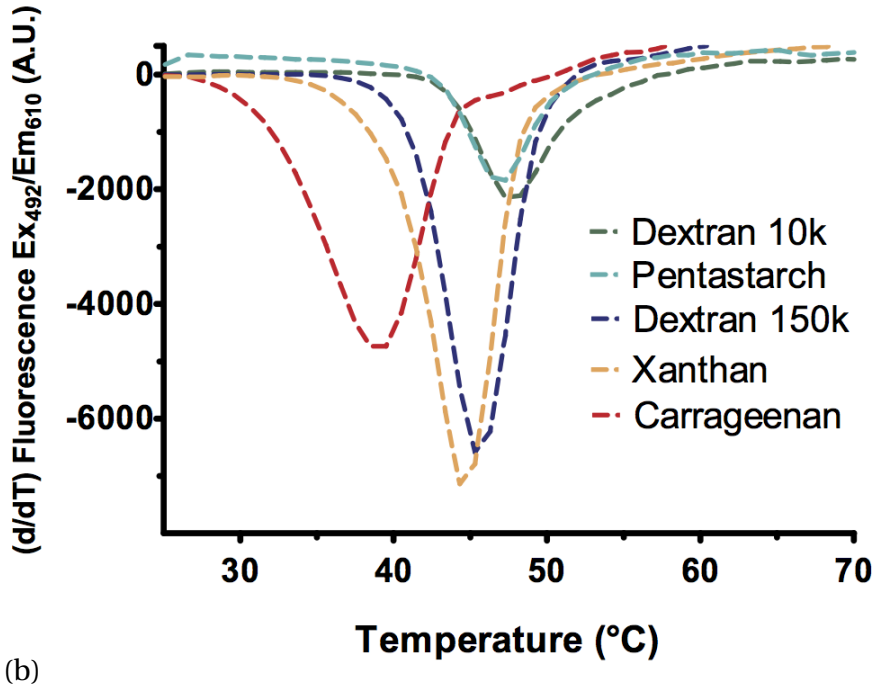
of CRM_{197} by 1°C compared to K_2HPO_4 buffer. Raffinose had a slight destabilising effect that resulted in a T_m of 45.3°C, and given it's low concentration in the suspension this may suggest that CRM_{197}'s thermal stability is sensitive to raffinose. It was unanimously observed, that a higher molarity of saccharides corresponded with an increased T_m of CRM_{197} relative to its melting temperature in buffer.

Osmolytes are organic solutes that are produced by cells to protect the native structure of cellular proteins in response to denaturing stresses [Yancey et al. (1982)]. A possible mechanism by which osmolytes can favor the native protein state is by raising the free energy of the unfolded state through preferential exclusion of osmolytes leading to preferential hydration of the native state [Timasheff (2002); Street et al. (2006)]. Interesting data has been presented by Street et al. (2006) which shows good correlation (R^2=0.88) between the polar surface area of an osmolyte and the change in free energy of the protein relative to water. In their study, sucrose and trehalose increased free energy by being excluded from the protein backbone, while denaturants such as urea and guanidine reduced free energy of unfolding by accumulating around the protein backbone. It is possible that preferential exclusion of saccharides in addition to their respective charges and size may account in part for the increase in T_m of CRM_{197} observed in Figure 3.6 a). Sucrose and trehalose showed the most pronounced effect on T_m and therefore were used in the subsequent CRM_{197} dry-powder formulation as cryo- and lyoprotectants. Mannitol was used as bulking agent based on its good glass forming ability and frequent use in many lyophilised pharmaceutical formulations.

The polysaccharides carrageenan, dextran (150k), and xanthan thermally destabilised CRM_{197} in solution (Figure 3.6 b). The addition of pentastarch had no effect on the T_m, while only dextran (10k) achieved a 1°C increase in T_m in K_2HPO_4 pH7.2. Given the comparatively large size of the polysaccharides, stabilisation mediated by



(a)



(b)

Figure 3.6: DSF - Saccharides and Polysaccharides: DSF results are shown for a) mono-, di-, and trisaccharides, and b) polysaccharides. The derivative of the fitted Boltzmann equation for each additive is displayed. The respective minimum corresponds to the T_m of CRM_{197} with the respective additive. All additives are suspended in 10 mM K_2HPO_4 buffer. All solutions were adjusted to pH 7.2.

preferential exclusion may be reduced, and possibly due to charge interactions, the partially unfolded states of CRM_{197} may be stabilised. Specifically, anionic polysaccharides such as some dextrans, carrageenan [Patil and Speaker (1998)], and xanthan [Gruber (1999)], have been indicated to interact with proteins via the induction of a net positive charge on proteins through electrostatic interactions [Imeson and Ledward (1977)]. Essentially, the induction of a net positive charge on a protein can also be achieved with the protonation of functional groups in an increasingly acidic milieu. Given that acidic pH destabilises the conformation of CRM_{197} in solution [Crane et al. (1997)], it is possible that the induction of a net positive charge by anionic polysaccharides acts in a similarly destabilising manner and translates into a reduced T_m. Further evidence that polysaccharide-CRM_{197} interaction may be driven by electrostatic interactions is the observation that the non-ionic pentastarch had no effect on T_m regardless of its concentration in solution (Table A.3). Based on the DSF thermal stability data, dextran (10k) was used in dry-powder formulations to improve the mechanical robustness of freeze-dried particles.

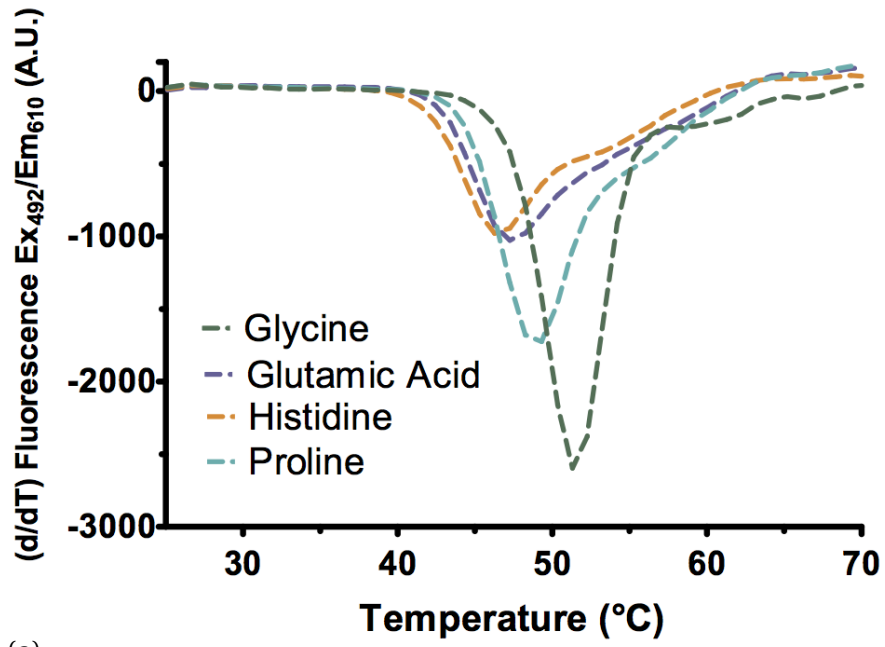
The most pronounced T_m increase of CRM_{197} with the addition of amino acids (Figure 3.7 a) was observed for glycine (49.2°C) and proline (47.3°C). Both amino acids are osmolytes and proline has been reported to impede protein aggregation [Samuel et al. (2000)]. Street et al. (2006) showed an increased energy of unfolding for proline and glycine and thus the increased T_m for CRM_{197} may be based on their preferential exclusion from the protein backbone. Glutamic acid was used at low molarity to maintain a neutral pH. T_m of CRM_{197} was not impacted by glutamic acid despite its charge, likely due to its low concentration in solution. The polar residue L-histidine was found to thermally destabilise CRM_{197} with increasing molarity (Table A.4). A possible explanation is offered by Lee and Timasheff (1974), who postulated that the interaction of the L-histidine with proteins is similar to the

binding of guanidine ions to aromatic side chains and peptide groups. Owing to its significant impact on the thermal stability of CRM_{197} in solution, glycine was further investigated in dry-powder formulations.

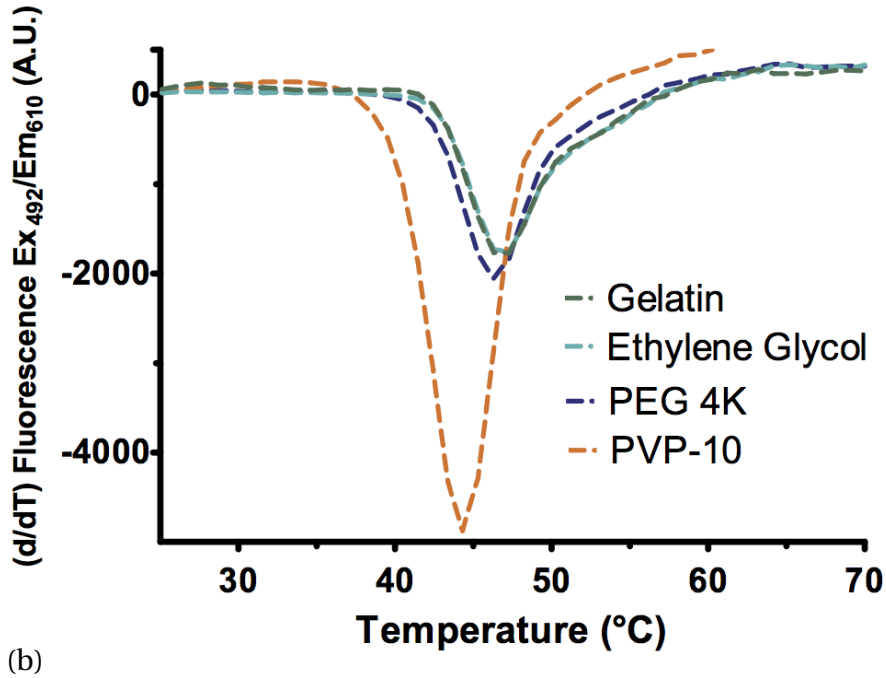
Polyethylene glycol (PEG-4k) showed no effect on the thermal stability of CRM_{197} relative to 10mM K_2HPO_4 buffer (Figure 3.7 b). While the destabilising effect of the hydrophobic polyethylene oxide was indicated to be based on entropically driven hydrophobic polymer-protein interactions [Almeida et al. (2004)], the hydrophilicity and charge neutrality of PEG may be implicated as possible reason of T_m independence from PEG concentration (Table A.3). Although PEG (4K) did not impact the T_m of CRM_{197} it was not further investigated in dry-powder formulation since dextran (10K) was a better performing plasticiser.

Already small amounts of the polyol glycerol increased the thermal stability of CRM_{197} in solution (Table A.3). Glycerol is a naturally occurring osmolyte and hence may stabilise CRM_{197} through preferential exclusion. Street et al. (2006) showed an increased free energy of the unfolded state in proteins in the presence of glycerol. However, ethylene glycol, which is also a polyol, substantially decreased the thermal stability of CRM_{197} to 36.6°C. Commonly used as anti-freeze, ethylene glycol has been implicated to impact the secondary structure of some proteins, which in some cases has lead to degradation [Huang et al. (1995)]. Based on the obtained DSF data and past literature, gycerol was the best-performing polyol.

Assuming that additives stabilise CRM_{197} through various mechanism such as charge and hydrophobic interactions, preferential exclusion, and hydrogen bonding, it was tested whether these effects are additive. When combining sucrose and trehalose, the T_m would be expected to increase based on the fact that the molarity of solutes is higher which theoretically should increase the driving force of their preferential exclusion from the protein backbone. Data suggests, however, that



(a)



(b)

Figure 3.7: DSF - Amino Acids and Polymers: DSF results are shown for a) amino acids, and b) polymers. The derivative of the fitted Boltzmann equation for each additive is displayed. The respective minimum corresponds to the T_m of CRM_{197} with the respective additive. All additives are suspended in 10 mM K_2HPO_4 buffer. All solutions were adjusted to pH 7.2

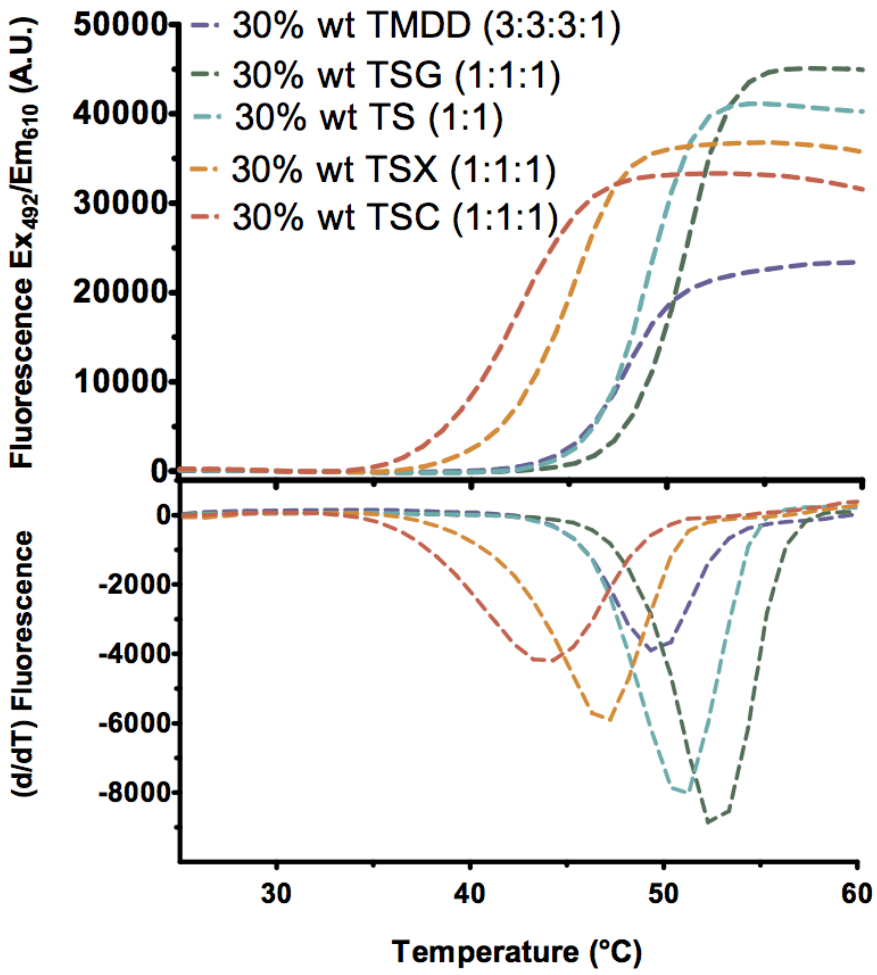


Figure 3.8: DSF - Formulations: DSF results are shown for excipient combinations. The a) DSF unfolding curves and b) their derivative are displayed. The respective minimum corresponds to the T_m of CRM_{197} with the respective additive. All additives are suspended in 10 mM K_2HPO_4 buffer. All solutions were adjusted to pH 7.2. T- trehalose, S- sucrose, M- mannitol, D- dextran (10k), D- dextran (150k), X- xanthan gum, C- carrageenan.

combining sucrose and threhalose reduced T_m by 0.9°C relative to sucrose alone (Figure 3.8). On the other hand, adding glycine to sucrose and trehalose mixture, again increased the T_m to 53.3°C, which is similar to sucrose alone. When combining trehalose, mannitol and dextran, the resultant T_m was higher than each of the excipients' T_m individually. Therefore, it appears that there are more complex interactions between stabilising excipients and the protein than a simple compounding of the individual stabilising effects. Clearly, more work is required to substantiate any claims on the mechanisms that underly the individual or combined effects of additives on the thermal stability of CRM_{197}. Here, the formulation with the highest T_m was trehalose, sucrose, glycine (1:1:1) with 30% wt. However, for use in intradermal powder injection, the TSG (1:1:1) formulation would be too hygroscopic, and without polymer plasticiser, likely not robust enough to withstand the injection forces.

3.2.2.2 Correlating CRM_{197} Tertiary Structure with Thermal Stability

While DSF is a powerful analysis tool, little work has been published on its utility to screen stabilising excipients for large globular proteins. Therefore, it would be helpful to have an orthogonal technology which could be used to link thermal stability to structural stability of globular proteins. Another well-established and high-throughput screening modality is the spectrophotometric determination of a protein's intrinsic fluorescent emission peak based on the selective excitation of tryptophan residues. Identical CRM_{197}-excipient solutions were scanned using DSF and a fluorimeter capable of reading 96-well plates. Data are plotted in Figure 3.9 with T_m as a function of tryptophan emission peak location. CRM_{197} in 10mM K_2HPO_4 pH7.2, served as reference point for T_m and TRP-emissions maximum for native CRM_{197} in pure buffer medium (green dot).

The upper left quadrant includes mainly osmolytes such as sucrose, glycine, proline, and glycerol among others. It seems plausible that preferential exclusion of osmolytes may induce a slight blue-shift of the Trp-emissions peak due to compact molecular folding. Anionic and hydrophobic excipients such as xanthan gum are predominantly found in the lower right quadrant. This suggests that anionic or hydrophobic excipients induce a red-shift in the TRP-emission peak and thermally destabilise CRM_{197} (Figure 3.9). Excipients in the upper right quadrant, such as trehalose, glucose, or dextran, thermally stabilise CRM_{197} relative to K_2HPO_4 buffer, but also induce an emission red-shift. Interestingly, upon general visual inspection, it appears that the excipients which induce a red-shift of CRM_{197}'s TRP-emissions peak appear to have a lower T_m than those who induce a blue-shift. To investigate whether this observation has statistical significance, a linear regression was conducted.

First, peak emissions data and T_m data distributions were checked and conformed well to a normal quantile plot. Various data transformations did not improve the normality of the data (not shown). However, two outliers were identified. T_m values for carrageenan and ethylene glycol deviated more than 3 standard deviations from the mean and hence were excluded from the regression analysis. With T_m as dependent and tryptophan peak emission as independent random variable, the linear regression model (Figure 3.10) suggests that TRP-peak emission is significantly correlated with T_m (p=0.002). The correlation is described by the formula:

$$Tm_{CRM197} = -1.429(\frac{^\circ C}{nm}) * Trp_{ex295/em330}(nm) + 513.785^\circ C$$

The model suggest that for a 1nm red-shift (unfolding) of the CRM_{197} tryptophan emission peak, the T_m decreases by 1.429°C. With R^2 = 0.338, 33.8% of variation in the data is explained by this model.

Although this is not an exceptionally strong model, the result shows that T_m and

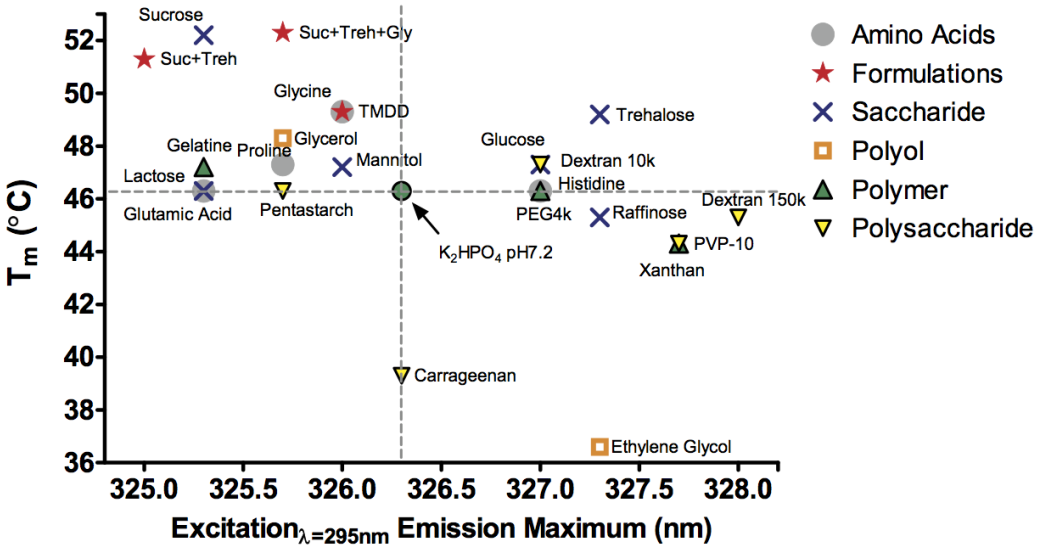


Figure 3.9: T_m by TRP Fluorescence Scatter Plot: For equal molarity and at equal pH, the effect of various excipients on the T_m and the Trp-emissions peak of CRM_{197} was determined by DSF and a high-throughput fluorimeter. The green dot signifies the thermal stability and tertiary structure of native CRM_{197} in K_2HPO_4 buffer. A horizontal and vertical line through the native state help classify the effect of excipients. Shifts up or down, show an increased or decreased thermal stability of CRM_{197}, while a left or right shift shows a folding or unfolding of CRM_{197}respectively.

tryptophan peak emissions are significantly correlated. A possible interpretation for this result could be that upon unfolding (red-shift) of CRM_{197} the reach of its stabilising intramolecular salt bridges may be exceeded, which energetically destabilises the protein and reduces the remaining activation energy that needs to be supplied towards denaturation. Conversely, a blue-shift would suggest a further compaction of the protein, in which case the distance at which salt-bridges act is reduced and may therefore be stronger. Although this is a plausible theory, reality is likely to be much more complex, and therefore additional experiments are necessary to further elucidate the relationship between T_m and the tertiary structure of CRM_{197}.

Although a higher thermodynamic stability raises the Gibbs free energy gap between the native and the denatured state of a protein, it may or may not impact the

Source	SS	df	MS	Number of obs =	25
				F(1, 23) =	11.75
Model	39.0368765	1	39.0368765	Prob > F =	0.0023
Residual	76.4087311	23	3.32211875	R-squared =	0.3381
				Adj R-squared =	0.3094
Total	115.445608	24	4.81023365	Root MSE =	1.8227

tm	Coef.	Std. Err.	t	P>|t|	[95% Conf.	Interval]
FluoPeaks	-1.429229	.4169385	-3.43	0.002	-2.291732	-.5667264
_cons	513.7845	136.0775	3.78	0.001	232.2866	795.2823

Figure 3.10: Linear Regression of T_m and Tryptophan Emission: Linear regression with T_m as dependent and TRP-emission peak as independent random variable. Data was normally distributed. T_m values for carrageenan and ehtylene glycol deviated more than 3 standard deviations from the mean and hence were excluded from the regression analysis.

magnitude of the activation energy required to interconvert native and denatured protein [Baker and Agard (1994)]. For instance, it has been demonstrated that some proteins are trapped in a thermodynamically unfavourable state, but due to a high kinetic energy barrier between their respective native and denatured states are nevertheless remarkably stable and functional [Jaswal et al. (2002)]. Therefore, although a higher thermodynamic stability of CRM_{197} is achieved with the addition of excipients, it does not necessarily follow that it is also more resistant to denaturation. Improving the kinetic stability of proteins against denaturation is often challenging, protracted, and laborious. The most frequent approach to successful kinetic stabilisation of proteins uses selected point mutations to create favourable intramolecular electrostatic and hydrophobic interactions by replacing specific amino acid residues [Foit et al. (2009)]. Although this is a promising approach to improving stability, an attempt to re-engineer CRM_{197} would exceed the scope of this dissertation, and would require clinical safety studies. However, while thermodynamic and kinetic stability are not necessarily related, an increase in the kinetic stability can in some cases be attained through a widened gap in the Gibbs free energy between native and denatured states. It has been demonstrated for some proteins that solution conditions can alter both thermodynamic and kinetic protein stability [Pey et al. (2008)]. Therefore, instead of assessing and modulating kinetic stability of CRM_{197}

on a molecular level, the identified thermodynamically stable CRM_{197} formulations were prepared and the CRM_{197} loss quantified after SFD to determine the formulation composition most suitable for the dry-powder ballistic delivery of CRM_{197}.

3.2.3 Physical Characterisation of SFD Formulations

Excipients can profoundly impact the thermal stability of CRM_{197} in solution, but they also play a critical role in the physical characteristics of the dried-powder and the preservation of CRM_{197} in the solid state [Costantino et al. (2002)]. In addition to a higher T_m and good retention of CRM_{197} tertiary structure in solution, formulation constituents were chosen based on their ability to protect against freezing and dehydration stress during lyophilisation, as well as their glass forming ability to ensure CRM_{197} immobilisation in an inert glass with low molecular mobility and high glass transition temperature. These characteristics may be unrelated to their impact on T_m in solution. Unlike conventional lyophilisates, powders for application in ballistic injection have to withstand substantial acceleration and deceleration forces in addition to preserving the protein [Kendall et al. (2004a, 2000)]. The ideal formulation therefore preserves CRM_{197}, has a low hydroscopicity, a low residual moisture content, a high T_g, high density and mechanical robustness, and a monodisperse particle size distribution [Sonner et al. (2002)]. Unfortunately, the enhancement of some of these attributes frequently comes at the cost of another. Based on past papers, the best performing excipients during SFD that also achieved a high T_m and good structural retention presented in section 3.2.2.1, 3.2.2.2, were sucrose and trehalose as lyo- and cryoprotectant and glass former, mannitol as bulking agent and stabiliser, and dextran 10k and 150k as elasticiser [Maa et al. (2004b); Rochelle and Lee (2007); Weissmueller et al. (2013)]. Mannitol and glycine are commonly used bulking agents. In light of SFD for ballistic injection, they can be used to in-

crease the mass of particles, reduce their hydroscopicity, and provide further utility in the formulation for example as stabiliser or tonicifier [Costantino and Pikal (2004)]. Given that glycine substantially increased the T_m of CRM_{197} in solution, it was investigated as alternative to mannitol.

3.2.3.1 Lyophilisation

Upon transfer of the steel-collection vessels with the spray-frozen formulation micro droplets into the lyophiliser, the product temperatures approach the shelf temperature (Figure 3.11). During primary drying, the pressure was reduced to 100mTorr and ice crystals are sublimed. The mass loss of sublimation cools the product, which is evidenced by the product temperature trailing the shelf temperature (Figure 3.11). The co-occurring pressure oscillation (Pirani) is furthermore indicative of ice sublimation. The shelf temperature is set above the T_g' of the formulations and therefore, plastic flow may occur. At around 900min drying time (still during primary drying), the abrupt step in product temperatures is indicative of complete ice removal around the thermocouples, upon which the immediate surrounding of the thermocouple quickly assumes the shelf temperature. During secondary drying, the protein-bound water is sublimed, and again, the mass loss induced cooling of the product should cause the product temperature to lag behind the shelf temperature. However, the product temperature remained very similar to the shelf temperature and the pressure did not oscillate markedly, which suggests that most protein-bound water had already been removed. This suggests that primary drying time may be reduced.

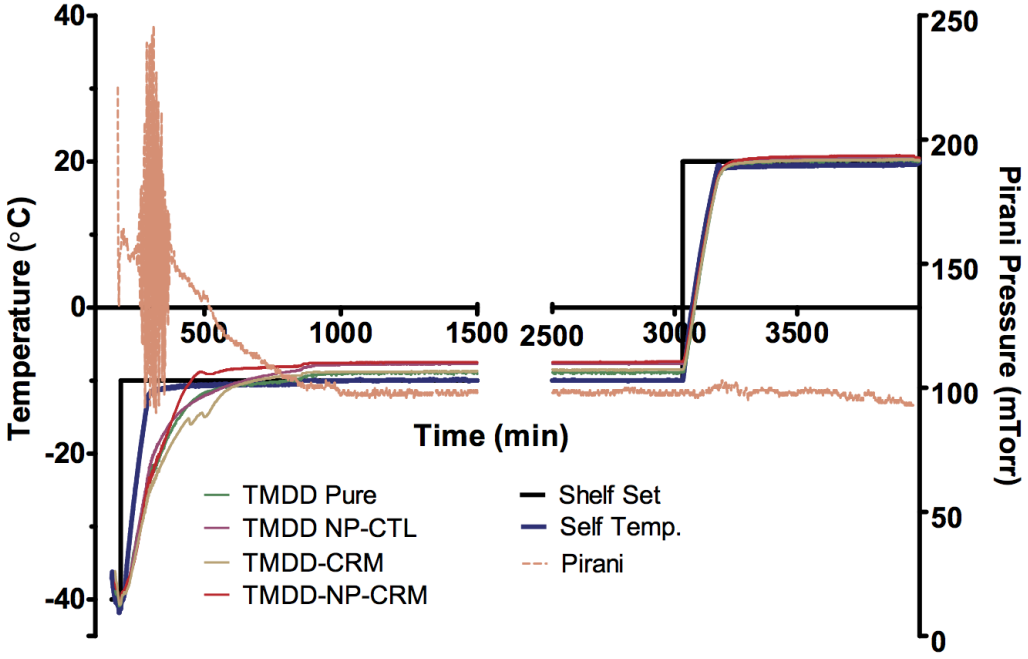


Figure 3.11: Lyophilisation Process Data for TMDD(3:3:3:1): Lyophilisation process data are presented for formulation 30% wt. of TMDD (3:3:3:1) in 10mM K_2HPO_4, with 2% wt CRM_{197} and without CRM_{197}. The spray-frozen droplets (5mL) were lyophilised in cylindrical metal collection vessels with GoreTex membrane lids. Data shows the product temperature T_{prod} relative to the process' set-temperature (black) and the actual shelf temperature (blue). Primary drying was conducted at 100 mTorr pressure at -10°C, and secondary drying at 100mTorr and +20°C. The left y-axis applies to the shelf and product temperatures, and the right y-axis applies to the chamber pressure (Pirani).

3.2.3.2 Influence of Formulation on Particle Size, Morphology, and Density

A pure sucrose solution in 10mM K_2HPO_4 buffer with a solid content of 10% was sprayed at 48kHz and 3.6W dispersion power, with a liquid feed rate of 0.5mL/min. SFD produced spherical particles that had a mean volume distribution diameter of 37.05μm with some variation (Table 3.1). SEM shows a smooth surface with only few pores (Figure 3.12). According to helium pycnometry, the density of the sucrose powder is 1.424 g/cm^3 ±1%, which is similar to the material density of sucrose. This information alone would suggest that sucrose particles have a high density. However, tap density measurements show that particles in fact have a high porosity of

86.7%. However, tap density comprises of the intra- and inter particle porosity of a sample, and therefore individual particles are not actually 86.7% porous. Nevertheless, the relatively high porosity can be explained based on the rapid freezing of atomised droplets, which was approximated by Maa and Prestrelski (2000) to be 3.2ms for a particle of 30μm in diameter. Fast freezing rates allow for numerous small ice crystals to form within the microparticle [Wang (2000)]. Upon ice sublimation at low temperatures, the “crystal-ghosts" stay behind and cumulatively amount to a large void volume of non-interconnected pores [Sonner et al. (2002)]. Helium pycnometry cannot account for individual pores that are not directly accessible via the particle surface, and therefore should be complemented with a tapped density assessment.

Table 3.1: Physical Properties of Formulations after SFD: Size distribution, density, and impact parameter.

Formulations	Solid content (% wt.)	CRM_{197} content	Size distribution D(v, 0.5) (μm), (Span)	He-Pycnometry (g/cm^3)	Tapped Density (g/cm^3)	Porosity (%)	Impact parameter ρvr (kg/ms)
Sucrose	10	None	37.05, (1.24)	1.424±1%	0.189±0.056	86.7	2.63
Sucrose-CRM	10	0.04g in 1g					
Trehalose	10	None	43.16, (0.99)	1.459±1%	0.139±0.043	90.5	2.25
Trehalose-CRM	10	0.04g in 1g					
TMDD (3:3:3:1)	30	None	57.4, (1.25)	1.604±1%	0.467±0.065	70.9	10.05
TMDD-CRM	30	0.02g in 1g	43.1, (1.26)	1.486±1%	0.469±0.071	68.4	7.58
TGDD (3:3:3:1)	30	None	56.9, (1.57)	1.526±1%	0.374±0.037	75.5	7.98
TGDD-CRM	30	0.02g in 1g	54.4, (2.03)	1.633±1%	0.358±0.046	78.1	7.30

SFD of pure trehalose at 10% solid content and with identical atomisation conditions produced similar results. As evidenced by SEM the surface of trehalose microparticles was non-porous, and therefore the helium pycnometry measurement approximated the material density of trehalose (Figure 3.12). Similarly to sucrose, also this trehalose formulation had a high porosity of 90.5%. These low density particles are not suitable for ballistic injection, as they fall short of the required minimum impact parameter of 7.0 kg/ms that has been associated with successful *sc* penetration [Kendall et al. (2004a)]. Although both formulations were lyophilised

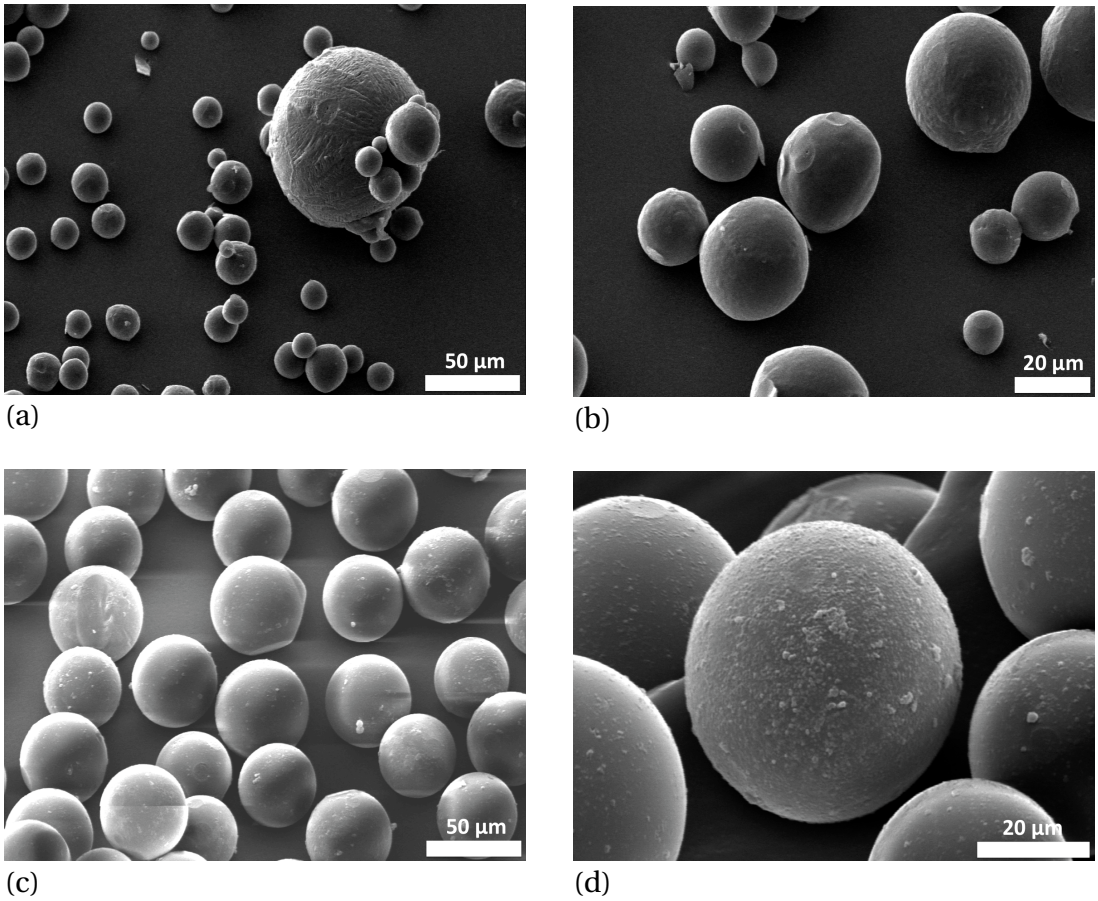


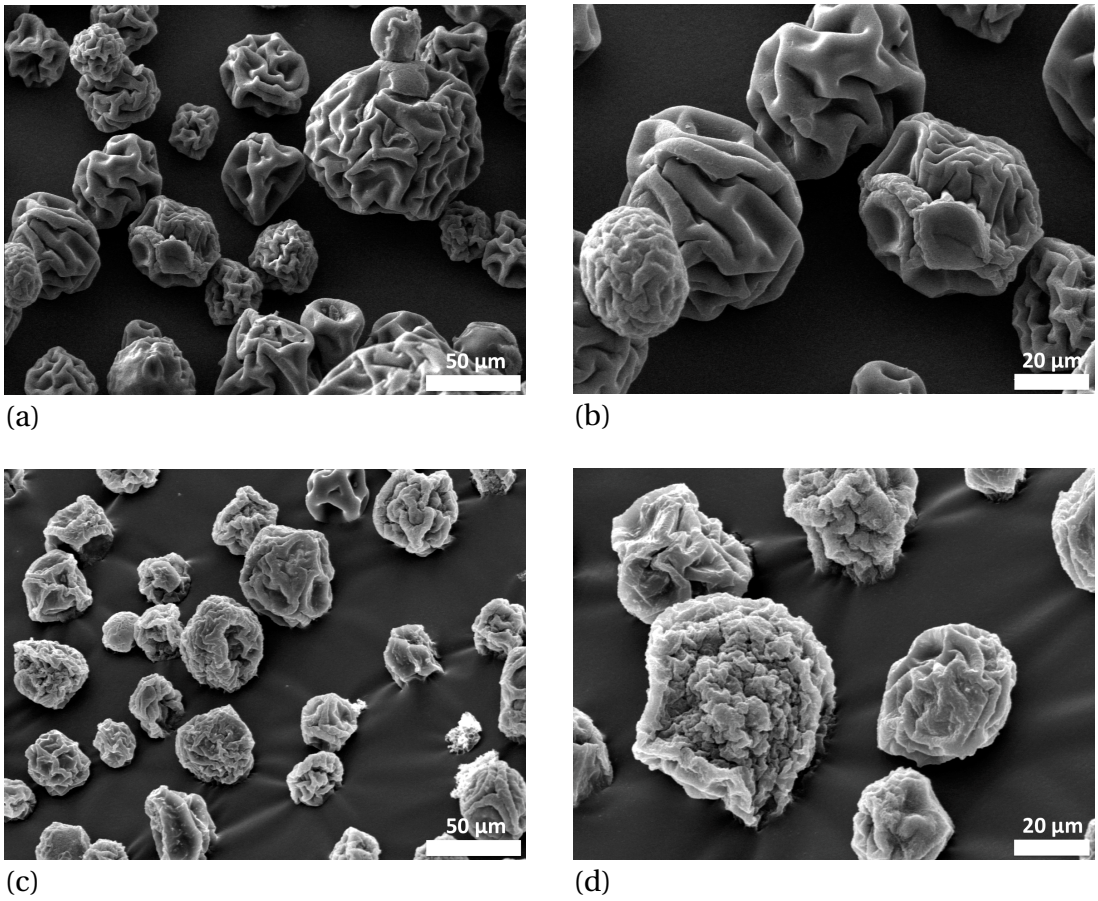
Figure 3.12: SEM of Sucrose and Trehalose Powders: SEM images of formulations 10% wt. of sucrose or trehalose in 10mM K_2HPO_4 without CRM_{197}, sprayed into LN_2 using a 48kHz ultrasound nozzle followed by lyophilisation. a, b) Sucrose particles at 500x and 1000x magnification and c, d) trehalose particles at 500x and 2000x magnification.

above their respective T_g', the achieved compaction was insufficient. While sucrose and trehalose are excellent glass formers and lyo- and cryoprotectants that could preserve CRM_{197} in a dry matrix, the addition of a plasticiser is necessary to achieve the minimum mechanical robustness required for ballistic injection. Mannitol has been shown to induce substantial viscous flow compaction during freeze-drying [Sonner et al. (2002); Maa et al. (2004b); Schiffter et al. (2010)].

With a 3-fold higher solid content of 30% weight, the trehalose-mannitol-dextran (10k)-dextran (150k) (3:3:3:1) formulation had a mean d(v,0.5) diameter of

57.4μm with a span of 1.25 (Table 3.1). At a tapped density of 0.467 g/cm^3 and porosity of 70.9%, these particles were substantially less dense as previously reported by Schiffter et al. (2010) with ρ_{tap} of 0.7-0.8 g/cm^3 and a porosity of 40-50%. However, lyophilisation was conducted at the same temperature for 1° drying, but for an even longer duration, and SEM suggests a similarly shrunken particle with the characteristically wrinkled morphology [Schiffter et al. (2010)]. Given that also ρ_{He} measurements agree, it seems likely that the discrepancy is due to a different set-up used to determine tapped density. Schiffter et al. (2010) used a 5mL volumetric glass flask while the set-up used to measure the presented data was a volumetric plastic tube. Similarly, the method as described by the European Pharmacopeia (5.0/2.915) was followed. It is possible that charge interactions between the plastic tube wall, used in this study, and the particles opposed powder compaction leading to a systematically lower ρ_{tap}. Even at -30°C primary drying Schiffter et al. (2010) reports ρ_{tap} values of 0.662 g/cm^3 while Rochelle and Lee (2007) report ρ_{tap} of 0.420g/cm^3 when dried at -20°C. This difference however may be due to the use of dextran 150k in addition to dextran 10k by Schiffter et al. (2010). Although the presented data may overestimate particle porosity, and underestimate the penetration impact factor ρvr, comparisons between the formulations presented in this report are not affected. Although ρ_{tap} may be underestimated, the presented TMDD and TGDD formulations exceed the minimum required ρvr value for penetration.

When mannitol was replaced with glycine, the mean d(v,0.5) diameter of particles after SFD remained similar to TMDD, with 56.9μm but with a slightly larger span (Table 3.1). Interestingly, although ρ_{He} were comparable, ρ_{tap} of TGDD was about 0.1 g/cm^3 less than TMDD, and therefore, TGDD had a higher porosity of 75.5%. These results suggest that glycine allows for less viscous flow compaction during lyophilisation than mannitol. Nevertheless, the resultant ρvr was sufficient



(a) (b)

(c) (d)

Figure 3.13: SEM of TMDD and TGDD Powders: SEM images of formulations 30% wt. TMDD or TGDD in 10mM K_2HPO_4 without CRM_{197}, sprayed into LN_2 using a 48kHz ultrasound nozzle followed by lyophilisation. a, b) TMDD particles at 500x and 1000x magnification and c, d) TGDD particles at 500x and 1000x magnification.

for successful dermal delivery. The addition of 2% wt. CRM_{197} induced a reduction in the mean d(ν,0.5) diameter for both TMDD and TGDD formulations, but led in both cases to a negligible difference in the eventual particle porosity. SEM images show a more irregular surface wrinkling of TGDD compared to TMDD (Figure 3.13). This may in part be due to lower plastic flow of TGDD during lyophilisation. While the addition of CRM_{197} had little effect on the physical properties of the particles, it had a substantial impact on the formulation T_g and T_g' (Table 3.2). CRM_{197} acted as plasticiser on TMDD, reducing T_g' from -29.16°C to -29.88°C and increasing the

change in heat capacity slightly, when averaged over 3 different batches. In TGDD, CRM_{197} acted as anti-plasticiser and increased T_g' from -39.72°C, to -39.25°C, also at an increased change in heat capacity, but this observation is only based on two individual batches and may not be statistically significant. Interestingly, there is an approximate 10°C difference between TMDD and TGDD formulations, which suggests that glycine lowers the T_g' of the TDD solution more than mannitol. In TMDD, the addition of CRM_{197} reduced the T_g of the dry-powder by more than 7°C, at similar residual moisture content of 1.96±0.33 for TMDD and 1.91±0.35 for TMDD plus CRM_{197}. It is surprising, therefore, to see that the addition of CRM_{197} in TGDD raised the T_g by more than 18°C. However, this dramatic discrepancy may partially be due to the difference in residual moisture content of the TGDD (1.62±0.45) and TGDD-CRM_{197} (0.90±0.27) formulations, as water is a potent plasticiser. Bellavia et al. (2011) suggest that matrix-protein interactions, such as hydrogen-bonding, acts to decrease the T_g of the matrix. A tight association of a solute with a protein in the solid state, therefore, could reduce protein-matrix interactions and thereby act to increase T_g. In this manner, glycine may encapsulate CRM_{197}, thereby preventing it from interacting with the matrix, which according to their theory, could partially explain the high T_g. If this theory applies here, then CRM_{197} is likely not stabilised in the matrix and therefore one would expect a higher denatured protein content with TGDD. Conversely, the drop of T_g in the TMDD formulation suggests that CRM_{197} interacts with the matrix and therefore may be stabilised. However, more experiments are required to make conclusive statements about the observed T_g increase in TGDD, and decrease in TMDD with the addition of CRM_{197}.

The viscosity of an amorphous matrix decreases significantly at temperatures that exceed its T_g'. This behaviour is described by the Williams-Landel-Ferry equation and is a function of the difference between T_{prod} and T_g' [Hancock and Zograf

Table 3.2: Thermal Analysis of Formulations: Glass transition, heat capacity change, and residual moisture.

Formulations	Solid content (% wt.)	CRM_{197} content	Residual Moisture (% w/w)	T_g' (°C)	ΔC_p' (J/g°C)	T_g (°C)	ΔC_p (J/g°C)
Sucrose	10	None	0.30±0.22	-41.84±0.2	0.308	50.59±0.3	0.371
Sucrose-CRM	10	0.04g in 1g	NA	-41.31±0.3	0.313	36.62±0.3	0.624
Trehalose	10	None	0.81±0.41	-40.80±0.2	0.298	65.78±0.2	0.141
Trehalose-CRM	10	0.04g in 1g	NA	-40.73±0.2	0.292	64.99±0.1	0.122
TMDD (3:3:3:1)	30	None	1.96±0.33	-29.16±0.4	0.846	47.89±0.1	0.810
TMDD-CRM	30	0.02g in 1g	1.91±0.35	-29.88±0.3	0.865	40.78±0.2	0.849
TGDD (3:3:3:1)	30	None	1.62±0.45	-39.72±0.4	0.270	40.30±0.3	0.571
TGDD-CRM	30	0.02g in 1g	0.90±0.27	-39.25±0.3	0.295	58.88±0.2	0.696

(1997)]. Plastic flow occurs usually between the T_g' of a matrix and its T_c. The collapse of an amorphous freeze concentrate occurs usually at a temperature (T_c) 2°C above its T_g'. Tang and Pikal (2004) report that plastic flow may occur when T_{prod} exceeds T_g' or even T_c during primary drying. The T_{prod} of TMDD-CRM_{197} and TMDD exceeded T_g' for over 2600min during 1° drying, and the substantially reduced viscosity can cause matrix deformations by plastic flow and collapse [Levi and Karel (1995)]. SEM images show a wrinkled and collapsed morphology. Therefore, TMDD and TGDD, with and without CRM_{197}, are likely compacted via plastic flow as 1°drying was conducted above the T_g'. Structural collapse in conventional lyophilisates would see them eliminated from further use, but in case of ballistic delivery, collapse is desirable since it increases the impact parameter. While all examined dextran-containing formulations resulted in powders physically suitable for IPI after SFD, their ability to preserve CRM_{197} needs to be investigated.

3.2.4 Evaluation of SFD Formulations by AF_4

3.2.4.1 AF_4 Method Validation

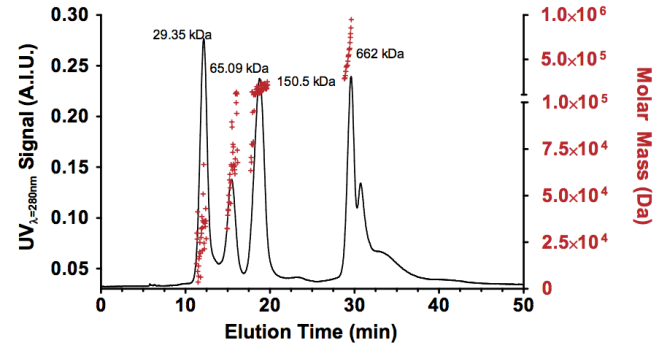
Initially, a series of tests were performed to validate AF_4 as suitable technology to measure CRM_{197} aggregation. Firstly, protein standards with defined MW were

used to determine the separation profile and MW determination accuracy of the employed AF_4 method (Figure 3.14 a). Secondly, a BSA standard solution was separated to determine whether mono-, di-, and trimers could be sufficiently separated in addition to higher order oligomers (Figure 3.14 b). Thirdly, CRM_{197} stock solution was dialysed against K_2HPO_4 and the MW profile determined to check the quality of the initial stock and the accuracy of the AF_4 method (Figure 3.14 c).

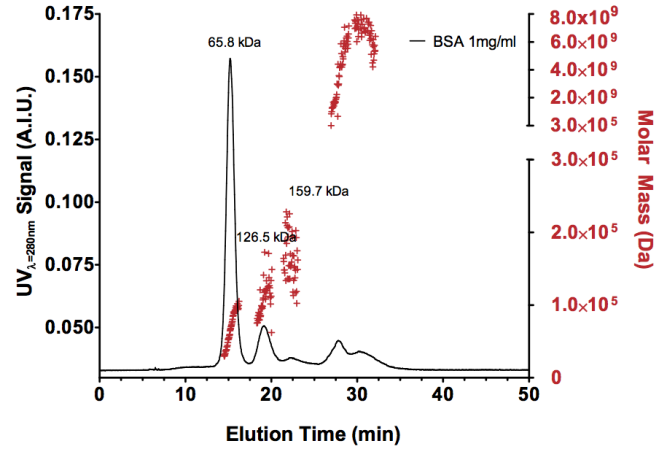
The AF_4 method showed good separation of molecular weight standards (Figure 3.14 a) between 20kDa – 150kDa. After 20min, the cross flow was decreased from 4mL/min to 0mL/min over 5min which resulted in lesser separation at higher MW. MW determination using MALS was accurate to ±1kDa between 20kDa – 150kDa, and at ±7kDa for high MW aggregates. In addition to the main protein peaks, some aggregates were present at lower concentration. Figure 3.14 b shows that the AF_4 method nicely separated BSA di- and trimers from the monomeric peak. While the size estimate 65.8kDa for the monomer was in excellent agreement with the literature value of 66.5 kDa, di- (126.5kDa) and trimer (159.7kDa) were not exact multiples of the monomer. However, these value are closer to the theoretical values than the work recently presented by Yohannes et al. (2010) using AF_4. CRM_{197} stock showed mainly monomeric content and was determined to be at 58.0 kDa which corresponds well with the literature value [Uchida et al. (1971); Pappenheimer and Gill (1973)]. Some higher order aggregates were present which eluted at 30min. Based on these preliminary tests, it was determined that the AF_4 method was sufficiently capable to analyse SFD formulations.

3.2.4.2 Choice of Formulations

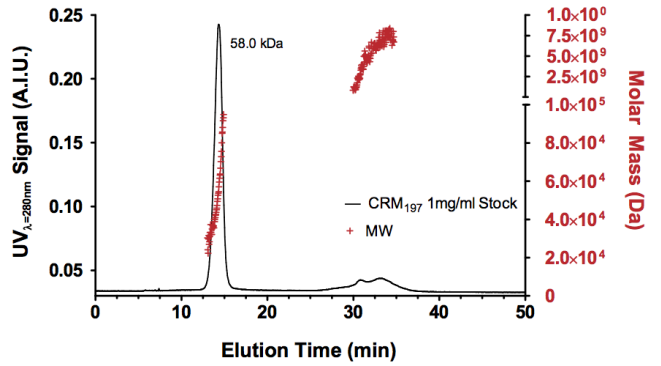
Formulation constituents were chosen based on T_m values and the retention of CRM_{197} tertiary structure in solution, as previously determined, in addition to their



(a)



(b)



(c)

Figure 3.14: AF_4 Method Validation: AF_4 method validation used 1mg/mL of a) carbonic anhydrase (29kDa), bovine albumin (66 kDa), alcohol dehydrogenase (150kDa), and thyroglobulin (669 kDa) to check the accuracy of MW determination, b) BSA 1mg/mL was used to test aggregate separation, and c) CRM_{197} 1mg/mL was used to check CRM_{197} stock quality. Experiments were conducted in PBS pH 7.4 running buffer.

ability to protect against freezing and dehydration stress during lyophilisation, as well as their glass forming ability to ensure CRM_{197} immobilisation in an inert glass with low molecular mobility and high glass transition temperature. Therefore, although some additive combinations may have a higher T_m than others, they may not necessarily also be the best combination in light of SFD and ballistic powder injection.

Sucrose had the highest T_m, induced a blue-shift of TRP-emission, and is a good lyo- and cryoprotectant and was directly compared against trehalose, which had a lower T_m and induced a red-shift of TRP-emission. CRM_{197} at 4mg/mL was formulated with 10% wt sucrose and 10% wt trehalose respectively, in 10mM K_2HPO_4, and atomised with 48kHz at 3.6W, and lyophilised at 100mTorr at -20°C for 48hrs and at 20°C for 12hrs. After resuspension of the two individual dry-powder formulations, there was no significant difference between the two formulations (Table 3.3). Monomeric loss of CRM_{197} in 10% wt sucrose was 8.7% on average, relative to the initial CRM_{197} stock, while 10% wt trehalose showed an average 9.0% loss of monomer. The average total amount of CRM_{197} mass lost during the SFD process, was 14.1% and 17.1% respectively (Table 3.3). Sucrose protected CRM_{197} during SFD slightly better on average, but not significantly so. Since trehalose has a higher glass transition temperature (T_g) than sucrose [Simperler et al. (2006)], trehalose was used in subsequent SFD formulations.

Upon reconstitution from dry-powder, the monomer content of CRM_{197} in 30% wt trehalose/mannitol/dextran10k/dextran150k (3:3:3:1) dropped from 85.7% to 57.8%, while dimer content increased from 0% to 1.4% and higher MW aggregates increased from 14.5% to 40.5% relative to CRM_{197} in the untreated TMDD solution (Table 3.3). This corresponds to an average monomer loss of 32.6% and was associated with a total average mass loss of 22.7%. This suggests that the addition of man-

Table 3.3: AF_4 Results on SFD CRM_{197} Formulations. Note: These data only capture the soluble protein fraction but not any precipitated protein.

Formulation	Concentration	Type	Monomer (%)	Dimer (%)	High MW (%)	Total Mass (μg)	Monomer Loss (%)	Mass Loss (%)
Sucrose 10% wt	4mg/mL CRM	Solution	98.1±1.3	0.0±0.0	1.9±0.5	313.3±9.4		
		SFD Resusp.	89.5±8.4	0.0±0.0	10.5±5.1	269.1±11.3	8.7	14.1
Trehalose 10% wt	4mg/mL CRM	Solution	97.8±2.8	0.0±0.0	2.3±0.8	317.1±8.6		
		SFD Resusp.	89.0±6.2	0.0±0.0	11.0±5.3	262.8±18.1	9.0	17.1
TMDD 30% wt	1mg/mL CRM	Solution	85.7±2.1	0.0±0.0	14.5±3.8	101.3±4.7		
		Sprayed	79.9±7.0	1.1±0.8	19.1±4.5	86.2±14.3	6.8	14.9
		SFD Resusp.	57.8±8.7	1.4±1.5	40.5±7.8	78.3±13.7	32.6	22.7
TGDD 30% wt	1mg/mL CRM	Solution	86.8±1.5	0.0±0.0	13.2±1.3	91.6±7.2		
		Sprayed	46.3±9.1	4.1±3.8	49.6±10.7	15.1±9.3	46.7	83.5
		SFD Resusp.	48.3±11.2	1.5±2.2	49.8±9.8	17.3±12.8	44.4	81.1
TMDD 30% wt	1mg/mL BSA	Solution	57.7±1.2	15.7±0.8	26.6±1.5	57.7±4.1		
		Sprayed	57.6±2.2	16.4±1.8	26.0±2.1	57.1±11.9	0.2	1.1
		SFD Resusp.	57.1±2.0	16.3±1.7	26.6±2.4	57.0±10.2	1.0	1.4

nitol and dextran to trehalose reduced the overall stability of CRM_{197} (Figure 3.16 b). Interestingly, the mass loss associated with atomisation alone, approximately corresponds to the mass lost after atomisation and lyophilisation of CRM_{197} with either sucrose or trehalose. When mannitol was replaced with glycine, trehalose/glycine/dextran(10k)/dextran(150k) in ratio (3:3:3:1) the preservation of CRM_{197} was negatively impacted (Figure 3.16 a). In 30% wt TGDD, CRM_{197} monomer content dropped from 86.8% to 48.3%, while dimer content increased from 0% to 4.1% on average, and higher MW aggregates increased from 13.2% to 49.8% on average, relative to CRM_{197} in the untreated TGDD solution. A total average CRM_{197} mass of 81.1% was lost during SFD. Notably, no further monomer and mass loss was apparent after the atomisation step. This could suggest that glycine may improve CRM_{197} resilience towards freezing and drying stresses (thermal), but increases aggregation during atomisation (kinetic).

It is important to know whether the SFD set-up generally produces high levels of protein aggregation, or whether the high aggregate levels of CRM_{197} are mainly due to formulation and intrinsic CRM_{197} protein properties. When 1mg/mL BSA was formulated in 30% TMDD at the same process parameters (Figure 3.15), AF_4 evaluation showed an average 99.0% retention of monomer content, and only a minimal overall mass loss of 1.4% relative to BSA in TMDD solution (Table 3.3). This

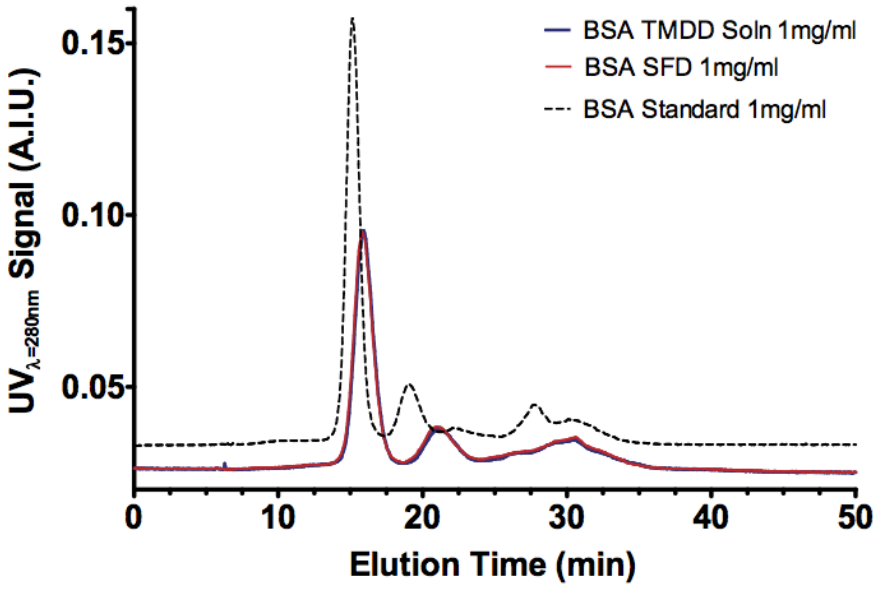
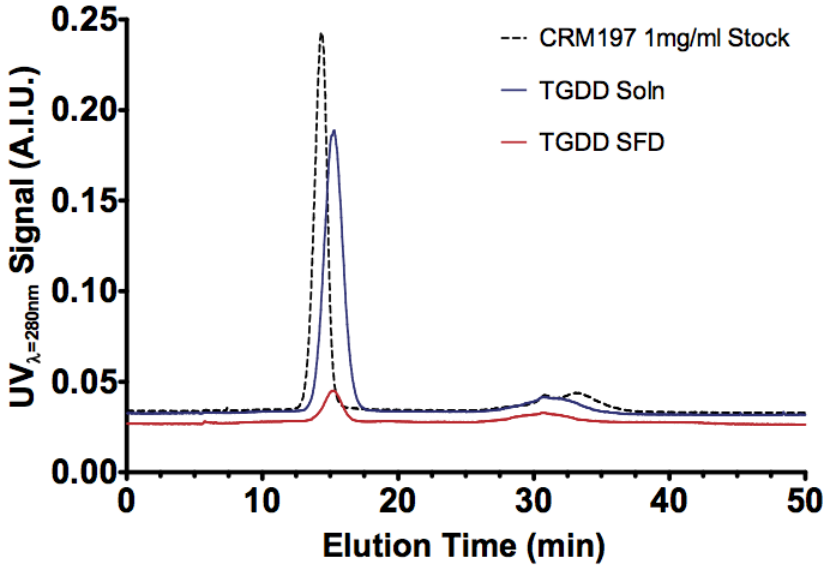


Figure 3.15: AF_4 Analysis of TMDD-BSA Formulation: AF_4 aggregate analysis was performed on a 30% wt $TMD_{10}D_{150}$ (3:3:3:1) BSA SFD-formulation was resuspended to 1mg/mL and analysed. AF_4 analysis was performed according to the previously described method (section 2.1.2). AF_4 was used to determine the changes after SFD and resuspension relative to the untreated liquid BSA formulation, and relative to the protein stock in buffer(10mM K_2HPO_4)

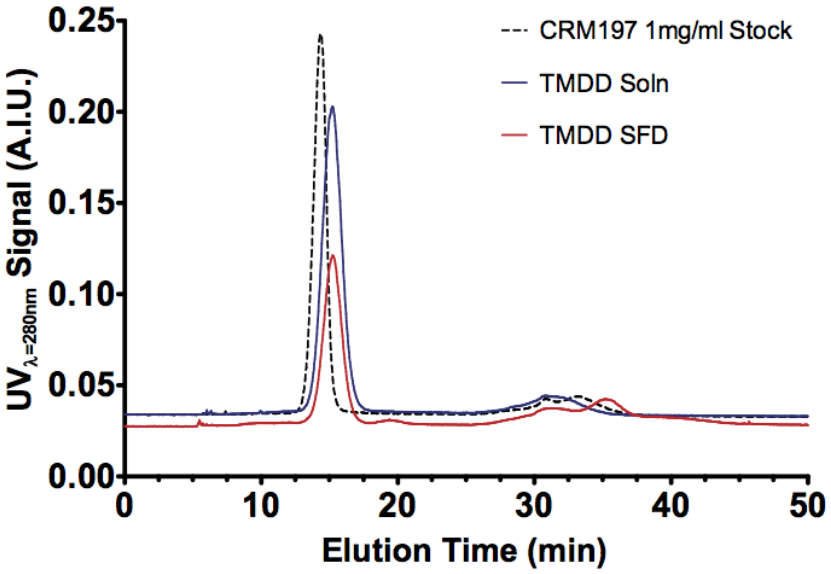
result suggests that dry-powder formulations can be produced with the SFD set-up that preserve the incorporated protein well, and that CRM_{197} is more prone to aggregation during the SFD process than BSA. Previous reports by [Rochelle and Lee (2007)], showed 65% catalase activity after SFD with 35% wt. dextran (10kDa) only, which was similar to catalase in solution without excipient. Thus, the authors concluded that there was little to no protective effect of dextran 10k. They observed that the addition of polymer (dextran 10k) to trehalose and dextran reduced the catalase activity. This corresponds to the presented data in this report. However, Rochelle and Lee (2007) also reported that in TMD (3:3:4), which is similar to the here presented TMDD (3:3:3:1) formulation, reportedly up to 93% of catalase activity was retained. These observations agree in that the addition of polymer to the formulation reduces protein stability during SFD, but unfortunately CRM_{197} was

not similarly well preserved as catalase.

As depicted in Figure 3.16, the monomer peak location of the sprayed and the resuspended SFD formulation elutes at a later time than CRM_{197} in K_2HPO_4 buffer. This peak shift may partially be due to an increased viscosity of the excipient-CRM_{197} solutions relative to buffer with possibly additional electrostatic interactions between the AF_4 channel membrane and CRM_{197}. Based on results from a multitude of experiments, it was observed that peak elution times were directly affected by the excipient concentration of a sample. Therefore, protein peaks coincide when the excipient concentrations are similar. This can be used as a simple check that similar amounts of dry-powder have been resuspended, and thus, the retention of the protein mass can be directly compared if elution peaks coincide. The observed mass loss cannot be accounted for by AF_4 elution data alone. This suggests the possibility that the sample filtration step prior to AF_4 analysis may remove large precipitates. Turbidity evaluation of TMDD and TGDD solutions after atomisation and after SFD show a substantial amount of large visible aggregates that ranged up to millimetre size (Figure 3.17). In good agreement with the AF_4 data, TGDD formulation showed considerably more light scattering, and thus more protein precipitates, as evidenced by the opacity of the solution. It is observed for both TMDD and TGDD formulations, that visible aggregates are present after atomisation and are increased in the resuspended SFD powder. AF_4 and turbidity data indicate that CRM_{197} primarily forms high MW aggregates during SFD and only little dimer or trimer.



(a)



(b)

Figure 3.16: AF_4 Separation of TMDD and TGDD Formulations: AF_4 aggregate content analysis of CRM_{197} formulation used the previously described AF_4 method (section 2.1.2) and was applied to a) 30% wt, $TGD_{10}D_{150}$ (3:3:3:1), and b) 30% wt $TMD_{10}D_{150}$ (3:3:3:1). SFD-formulations were resuspended to 1mg/mL CRM_{197} with 10mM K_2PO pH7.2 buffer. AF_4 was used to determine the changes after SFD and resuspension relative to the untreated liquid CRM_{197} formulation, and relative to the protein stock in buffer (10mM K_2HPO_4).

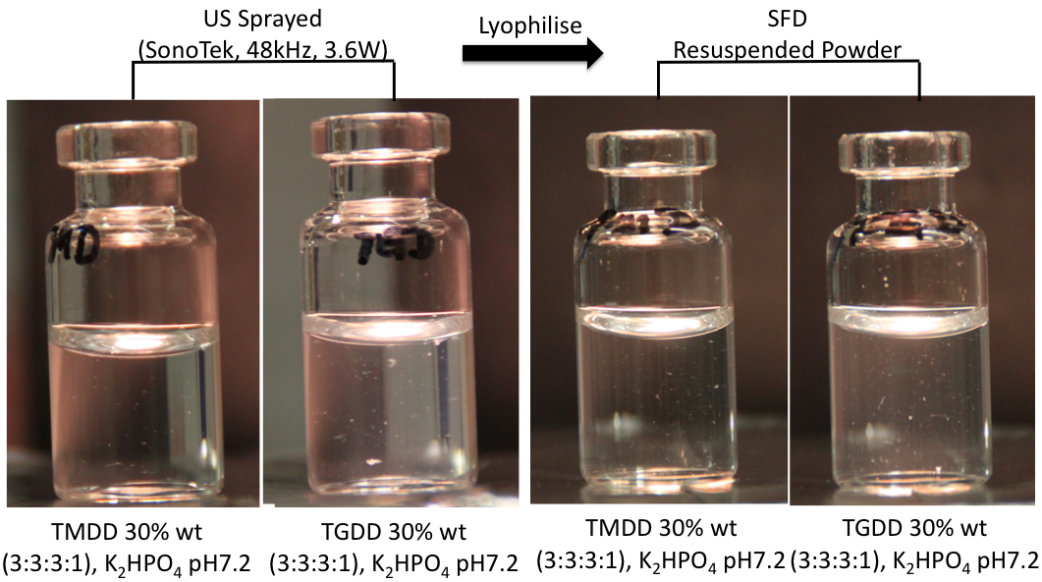


Figure 3.17: Turbidity of TMDD and TGDD Solutions after Atomisation and SFD Resuspension: Formulations TMDD 30% wt (3:3:3:1), and TGDD 30% wt in (3:3:3:1) K_2HPO_4 pH7.2, contained 1mg/mL CRM_{197} and were sprayed at 48kHz (3.6W). Dry-powder formulations, prepared as previously described, were resuspended in 10mM K_2HPO_4, pH7.2 to a total of 1mg/mL CRM_{197} in a 3mL lyophilisation vial. A flashlight was shown through the vial from the bottom up. Visible aggregates scatter light and are visible as white dots or larger precipitates in the otherwise clear solution.

3.3 Chapter Summary

Differential scanning fluorimetry can accurately determine the effect of co-solutes on the thermal stability of CRM_{197}. Additionally, it was shown that the thermal stability of CRM_{197} was significantly correlated with its tertiary structure. Thermodynamically stabilising excipients induced a blue-shift of Trp-emissions and were generally known osmolytes such as sucrose, glycine, and glycerol among others. The data suggest that the effect of preferential exclusion (smaller molecules) was more pronounced than molecular interactions (larger molecules such as polymers or polysaccharides). Also, the induction of charges by pH alterations and salt concentrations were observed to profoundly impact the thermal stability of CRM_{197},

where higher salt concentrations reduced the thermal stability. Interestingly, it was observed that co-solutes can alter CRM_{197} subdomain interaction and thermal stabilisation. Chloride ions seemed to impede domain-domain stabilisation while osmolytes such as sucrose appeared to allow for domain-domain stabilisation. It was further noted that the discrepancy in the thermodynamic stability of CRM_{197} and DT may partially be explained on the basis of reduced domain-domain stabilisation due to the higher mobility of the catalytic loop on CRM_{197}.

CRM_{197} aggregated during SFD with ultrasound nozzle atomisation by forming large and visible aggregates. Possible options to improve the SFD process for CRM_{197}-formulation are a) the use of a different nozzle type (two fluid system nozzles) instead of ultrasound nozzle, b) further optimisation of the excipient choice and composition, c) the reduction of ultrasound-induced cavitation during ultrasound atomisation under reduced pressure. Problems with these options are that two fluid system nozzles have a much broader particle size distribution than ultrasound-driven nozzles, which may lead to imprecise penetration of particles into the skin [Schiffter et al. (2010))]. Excipient optimisation will likely provide marginal improvements, unless the kinetic stability of CRM_{197} is significantly increased. Re-engineering the SFD process to work under reduced pressure is possible, but may prove unfavourable in scale-up and may be problematic with the use of LN_2. Therefore, while SFD is a good method for the manufacture of dry-powder various protein formulations, in combination with CRM_{197} there may be better dry-powder manufacture alternatives for IPI. However, despite the presence of some higher molecular weight aggregates in the formulation, the immunogenicity of the needle-free intradermal injection with TMDD-CRM_{197} was investigated *in vivo*. Findings are presented in chapter 6. While the thermodynamic stability of CRM_{197} was not predictive of CRM_{197} preservation during SFD, thermally stabil-

ising excipients identified by DSF seemed to protect CRM_{197} during lyophilisation. Therefore, DSF may be further investigated in formulation efforts that use conventional lyophilisation.

CHAPTER 4

BIOCERAMIC POWDER AS PROTEIN DELIVERY VEHICLE

Chapter 4 discusses the physical properties of novel bioceramic microparticles manufactured by molten salt synthesis (MSS). While sugar-based powder formulations release their payload immediately after injection, it was investigated whether the bioceramic may retain the antigen at the injection site and provide its sustained release. Furthermore, simple surface-adsorption followed by almost instantaneous chemical dehydration of the protein my obviate the need for costly and time-consuming lyophilisation. The material composition of the bioceramic and its protein adsorption propensity are characterised. Finally, the structural integrity of CRM_{197} is assessed on the bioceramic surface.

4.1 INTRODUCTION

In October 2012, the Novartis vaccines Aggripal® and Fluad® were recalled based on concerns voiced by some health authorities regarding the presence of visible protein aggregates in the vials. The manufacturer explained that "protein aggregates can naturally occur in vaccines in very small quantities, typically dissolve when shaken, and are not uncommon" [Novartis (2012)]. Although minor aggregates in

protein vaccines may not be uncommon, the specificity of the induced antibodies for their intended target, which is the native-state protein antigens, may be diminished [Wang and Roberts (2010); Casadevall et al. (2002)]. This is based on the fact that aggregates can assume greatly varying forms while native-state proteins are structurally unique. Therefore, experts recommend that only well characterised and controlled aggregates are permissible in protein vaccine formulations [Rosenberg (2006); FDA (2013)].

A general observation across many studies links the molecular weight of aggregates to their immunogenicity, with larger aggregates being reported as more immunogenic [Stefani and Dobson (2003)]. The evaluation of aggregate immunogenicity will have to be made on a case-by-case basis and will likely require a large number of studies. The reality is, however, that the immunogenic potential of protein aggregates remains poorly understood [Wang and Roberts (2010); Ponce et al. (2009)]. Therefore, the Food and Drug Administration advises that "it is critical for manufacturers of therapeutic protein products to minimise protein aggregation to the extent possible," and while aggregates need to be well described, the FDA does not provide a hard percentage number that defines an acceptable aggregate content threshold [FDA (2013)].

Across a plethora of antigens, their co-delivery with aluminium salts showed a potentiated and Th1 biased immune response compared to their soluble controls [Weissmueller et al. (2013)]. However, multiple reports have linked the formation of dermal granulomas to aluminium adjuvants, and therefore aluminium salts should not be used in dermal vaccination [Marsee et al. (2008); Fawcett and Smith (1984); Vogelbruch et al. (2000)]. This is a predicament because alum-adsorbed antigens were more immunogenic. Therefore, the investigation of an alternative to alum co-delivery may prove meritorious.

The potential of calcium phosphate-based scaffolds as drug delivery vehicle has been extensively researched and is well documented [Ginebra et al. (2006)]. Especially hydroxyapatite (HA), a biocompatible mineral that is naturally found in bone and largely comprises of calcium and phosphate, has been shown to strongly adsorb proteins and to provide sustained release of the bioactive molecule [Yin et al. (2002)]. Recently, it was described that a commercial calcium phosphate adjuvant consisted of nano-sized HA needles [Jiang et al. (2004)]. Therefore, HA has demonstrated its capability to act as drug and vaccine delivery substrate and has a documented track record of biocompatibility and safety, and may potentiate the immune response to antigens.

While the thermodynamic stability of CRM_{197} was substantially improved with the addition of selected excipients in chapter 3, the stresses inherent to spray-lyophilisation nevertheless lead to the formation of insoluble high molecular weight aggregates. The fact that these aggregates were insoluble when shaken may make their presence in a vaccine problematic. This chapter presents the work done in parallel to SFD and explores the possibility to formulate CRM_{197} as dry-powder using a novel biomaterial carrier on HA basis, e.g. a material that in many aspects is very similar to pure HA but not identical, and that i) facilitates antigen reformulation by simple surface adsorption, ii) has more robust mechanical properties than excipient-based powder particles, and iii) may possibly sustain antigen presentation and release at the site of injection similar to alum.

4.2 Results and Discussion

4.2.1 Bioceramic Microparticles Prepared by Molten Salt Synthesis

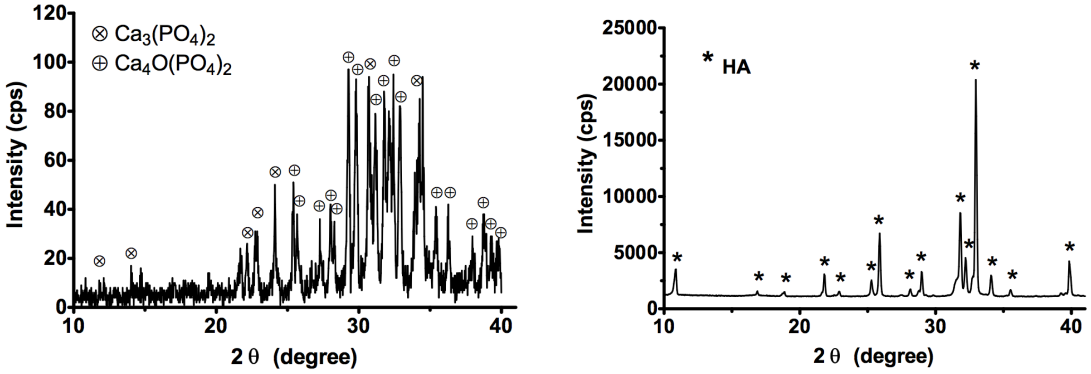
4.2.1.1 Demonstration of Biocompatibility by Material Characterisation

The theoretical reaction equation for the initial step in the bioceramic synthesis predicts the formation of tri-calcium phosphate ($Ca_3(PO_4)_2$) under the emission of carbon dioxide from the reaction of calcium pyrophosphate ($Ca_2P_2O_7$) with calcium carbonate ($CaCO_3$) at 1350°C. The manufacture protocol was adapted from Viswanath et al. (2008). According to their protocol, after the initial reaction of calcium pyrophosphate and calcium carbonate, the resultant polymorphic tri-calcium phosphate is fluxed at the melting point of potassium sulfate salt (K_2SO_4, T_m = 1069°C) to form the beta co-polymorph, which is stable at this temperature [Viswanath et al. (2008)]. These two steps can be theoretically summarised as follows:

$$Step1: Ca_2P_2O_7 + CaCO_3 \longrightarrow poly\text{-}Ca_3(PO_4)_2 + CO_2(g), T = 1350^\circ C$$

$$Step2: poly\text{-}Ca_3(PO_4)_2 + K_2SO_4 \longrightarrow \beta\text{-}Ca_3(PO_4)_2 + K_2SO_4, T = 1200^\circ C$$

X-ray diffraction analysis was conducted to identify the actual composition of the produced powders after the first and second reaction step respectively. After step one, in addition to tri-calcium phosphate also calcium oxide phosphate ($Ca_4O(PO_4)_2$) was detected (Figure 4.1, a). The reactants potassium pyrophosphate and calcium carbonate were not detected in the diffractogram. The presence of calcium oxide phosphate suggests that either the reaction was not stoichiometric, or that small impurities were present either in the starting materials or in the alumina crucible. The low counts per second intensity (CPS) and noisy appearance of the XRD diffractogram suggests a low crystallinity of the powder produced in step one



(a) (b)

Figure 4.1: X-ray Diffractograms of Reaction Products: X-ray diffractograms of the reaction products were compared against the ICDD data base and identified a) tricalcium phosphate and calcium oxide phosphate with low crystallinity after reaction step I, and b) highly crystalline hydroxyapatite after reaction step II. XRD was conducted as described in chapter 2.

(Figure 4.1, a). The second reaction step was predicted to produce $\beta-Ca_3(PO_4)_2$ single crystals. However, according to X-ray diffraction, the main phase after step two consisted of pure hydroxyapatite ($(Ca_{10}(PO_4)_6(OH)_2$), and contained traces of calcium oxide (CaO) in addition to the salt flux (Figure 4.1, b). Based on the theoretical reaction equation alone, it is surprising to observe HA in this instance, but given the identified products from step I, it can be discerned that HA was likely formed according to the following two reaction steps:

$$Step1: 4\,Ca_2P_2O_7 + 6\,CaCO_3 \longrightarrow 2\,Ca_3(PO_4)_2 + 2\,Ca_4O(PO_4)_2 + 6\,CO_2(g), T = 1350^\circ C$$

$$Step2: Ca_3(PO_4)_2 + 2\,Ca_4O(PO_4)_2 + H_2O(g) + K_2SO_4 \longrightarrow$$

$$Ca_{10}(PO_4)_6(OH)_2 + CaO + K_2SO_4, T = 1200^\circ C$$

The XRD peaks for Figure 4.1 b) identically match the ICDD data base reference for HA on the $2°\theta$ scale. Therefore, the major phase of the final product is HA. In this method of molten salt synthesis, crystals of apatitic calcium phosphate are produced and the most intense XRD peak is located on the (300) plane at 32.91 $2°\theta$,

instead of the (211) plane, which was also described by Tas (2001). The high CPS values suggest that HA is highly crystalline, and likely present as single crystals.

4.2.1.2 HA Batch Particle Morphology and Size Distribution

The antigen carrier particles that are most suitable for ballistic powder injection require a nearly spherical morphology and good mechanical strength to reliably penetrate the *sc*. The aforementioned powder batch, synthesised by MSS, comprised of 48.3% spheroidal and 51.7% rod-like particles. Aspect ratios of length (a) relative to width (b) were classified as spheroidal when $\frac{a}{b}$ was less then 2.0, and rod-like when greater then 2.0 (Figure 4.2). Visual inspection suggests that rod-shaped particles are of larger size than spheroidal particles, which allows for the possibility to remove them from the powder by sieving before further processing and use. The as synthesised powder batch had a mean particle diameter of 49.8 μm with a span of 4.25, while aspect ratios varied between 1.0–8.5.

Single HA crystals grown by MSS have previously been reported to have a whisker-like morphology with a high aspect ratio [Taş (2001)]. Therefore, it is surprising that spheroidal HA single crystals are observed. A possible reason for this may be the synthesis conditions, which used a very high salt content in the flux, and also the rounded crucible. Taş (2001) previously reported HA whiskers formed by MSS but advised to use an alumina boat-shaped crucible in combination with a K_2SO_4 salt flux-to-powder ratio of less than 1.6-to-1, while the ratio used in the present synthesis was 6-to-1. The excess of molten salt may allow for increased dissolution of the precursor powder along with increased material mobility in the melt [Kimura (2011)]. Furthermore, potential surface tension at the molten salt and biocermic crystal interface may have contributed to the formation of crystals with lower aspect ratios. Another possible mechanism that may explain the observed

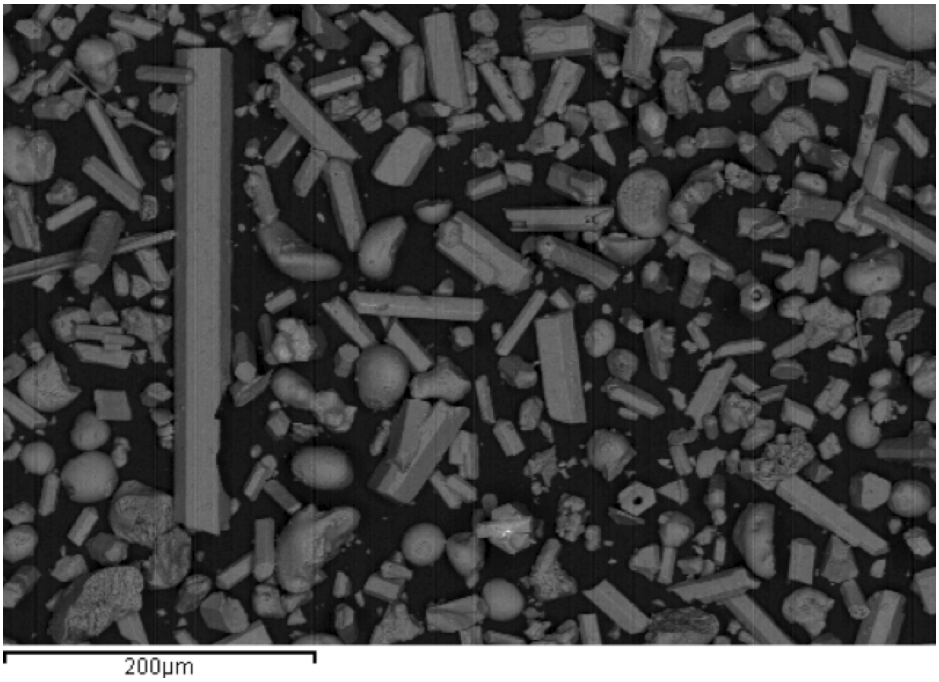
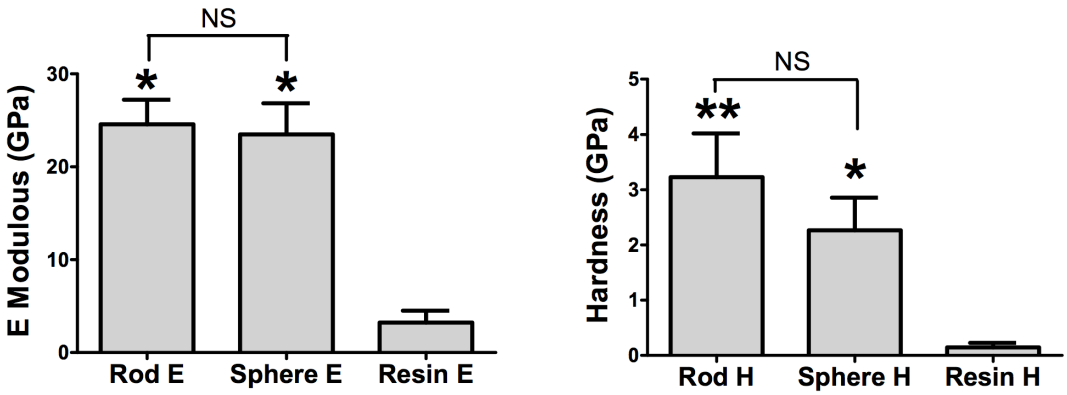


Figure 4.2: HA Batch Morphology by SEM: The scanning electron micrograph shows single HA crystals with individual spheroidal and rod-like particles, as defined by aspect ratios of less than 1.0–2.0, and larger than 2.0 respectively.

difference in size and morphology is based on the incorporation of ionic impurities in the HA crystal lattice during MSS, which could impede HA crystal growth. Given the varied morphologies and sizes of the HA particles, it was further investigated whether there are differences in material properties that correlate with particle morphology.

4.2.1.3 Mechanical Properties of Microparticles as Function of Particle Morphology

Powder particles are subjected to high acceleration and deceleration forces upon delivery in the gas stream and impact on the skin respectively. Therefore, the mechanical characteristics of individual particles are of interest. Nanoindentation data of single rod-like and spheroidal microcrystals suggests that there is no signifi-

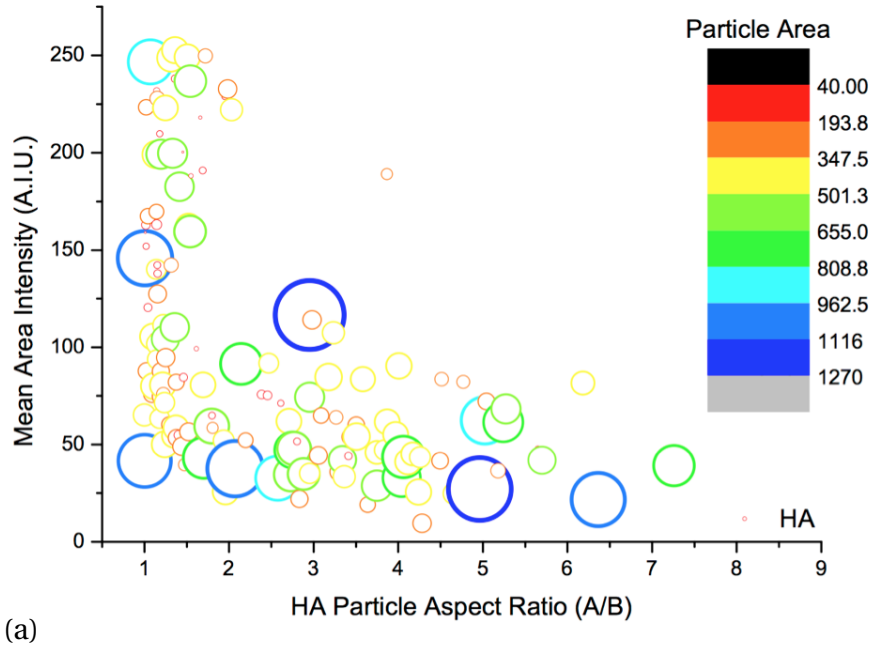


(a) (b)

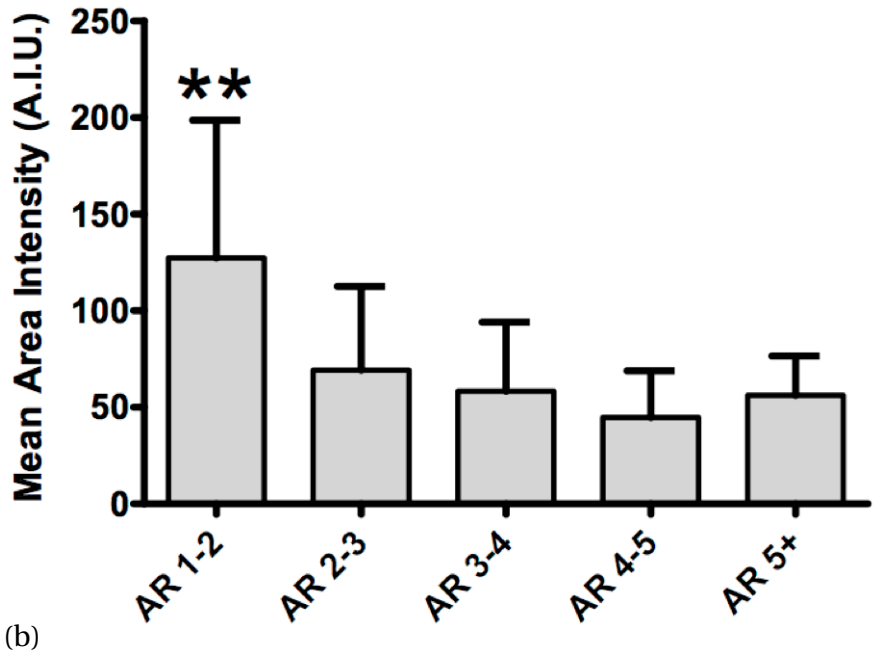
Figure 4.3: Hardness and Young's Modulus of Single Rod-like and Spheroidal HA Crystals by Nanoindentation: Young's modulus (E) and material hardness (H) were obtained from the unloading portion of the nanoindentation curve according to the Oliver-Pharr method. Spheroidal particles were defined to have an aspect ratio of 1.0-2.0, while have rod-shaped particles had an aspect ratio > 2.0. Asterisks indicate comparisons to resin, while brackets compare rods with spheres. Comparison of means was conducted at α=0.05, and p-values adjusted for multiple comparisons using Bonferroni correction, with *($p<0.05$), **($p<0.01$), and NS ($p>0.05$), for n=10 per group.

cant difference for the elastic modulus (E) and the material hardness (H) between the morphologies (Figure 4.3). Specifically, nanoindentation determined an elastic modulus of 24.57±2.65 GPa and a hardness of 3.23±0.79 GPa for rod-shaped HA crystals prepared by MSS. These values were significantly larger than for the epoxy resin substrate (E=1.69±0.44 GPa, H=0.020±0.004, $p<0.05$). For spheroidal particles, the elastic modulus was determined to be 23.49±3.34 GPa and the hardness 3.23±0.79 GPa, which also was significantly larger than the epoxy resin values ($p<0.05$).

Compared to the literature values that were similarly obtained from the unloading portion of nanoindentation curves, the MSS-synthesised particles had a comparable elastic modulus and a higher hardness that human trabecular bone (E=22.5±3.1 GPa, H=1.2±0.15 GPa) and dentin (E=21.1±1.3 GPa , H=0.51±0.02 GPa)



(a)



(b)

Figure 4.4: Protein Adsorption Propensity of HA Crystals Manufactured by Method I (see section 2.2.1 and 2.2.2): Plot a) depicts the mean BSA-TRITC fluorescence intensity normalised to particle area (y-axis) as function of individual particles based on their aspect ratio (x-axis), and particle area (circle circumference and colorscheme). b) BSA-TRITC adsorption was compared by mean area fluorescence intensity across different particle sizes and categorised by aspect ratio (AR). ANOVA was conducted at α=0.05, **(p<0.01).

[Hengsberger et al. (2001); Kinney et al. (1996)]. Therefore, the mechanical strength of bioceramic particles synthesised by MSS likely far surpasses any saccharide and polymer carrier material that may be used for IPI. However, both E and H of the MSS-synthesised particles fall just short of the literature values for single HA crystals (E=35–120GPa, H=3.0–7.0GPa) [Suchanek and Yoshimura (1998)]. These differences and the variation in values may be due to any compositional and structural difference of the as synthesised HA particles, such as the presence of minor phases. A possible factor may be the use of epoxy resin to embed crystals. Previous sample preparations that used wax or a sintered β-TCP matrix to embed HA crystals showed that entire HA particles were indented into the substrate. In fact, it required multiple sample preparation approaches to allow for single crystals not to be visibly pressed into or through the substrate they were immobilised in. Therefore, another possible explanation for the slightly reduced E and H values for HA by MSS, compared to literature is the possibility of single micron-sized crystals to slightly deform the epoxy resin matrix due to the force that was applied with the diamond indenter tip. Regardless, the mechanical robustness of these particles makes them well suited for ballistic injection. Although the morphology of particles as assessed by the aspect ratio did not significantly impact material properties, protein adsorption propensity significantly differed between spheroidal and rod-like crystals. Figure 4.4 suggests that there is a sub population of bioceramic particles, with aspect ratio less than 2, that strongly adsorbs BSA-TRITC, while the main population shows similar protein adsorption across all observed aspect ratios. It was hypothesised that this sub population may contain K^+ ions, which could affect the protein adsorption propensity, and the particle morphology. In light of ballistic delivery of the protein antigen CRM_{197}, an increased delivery capacity per bioceramic particle would be highly desirable.

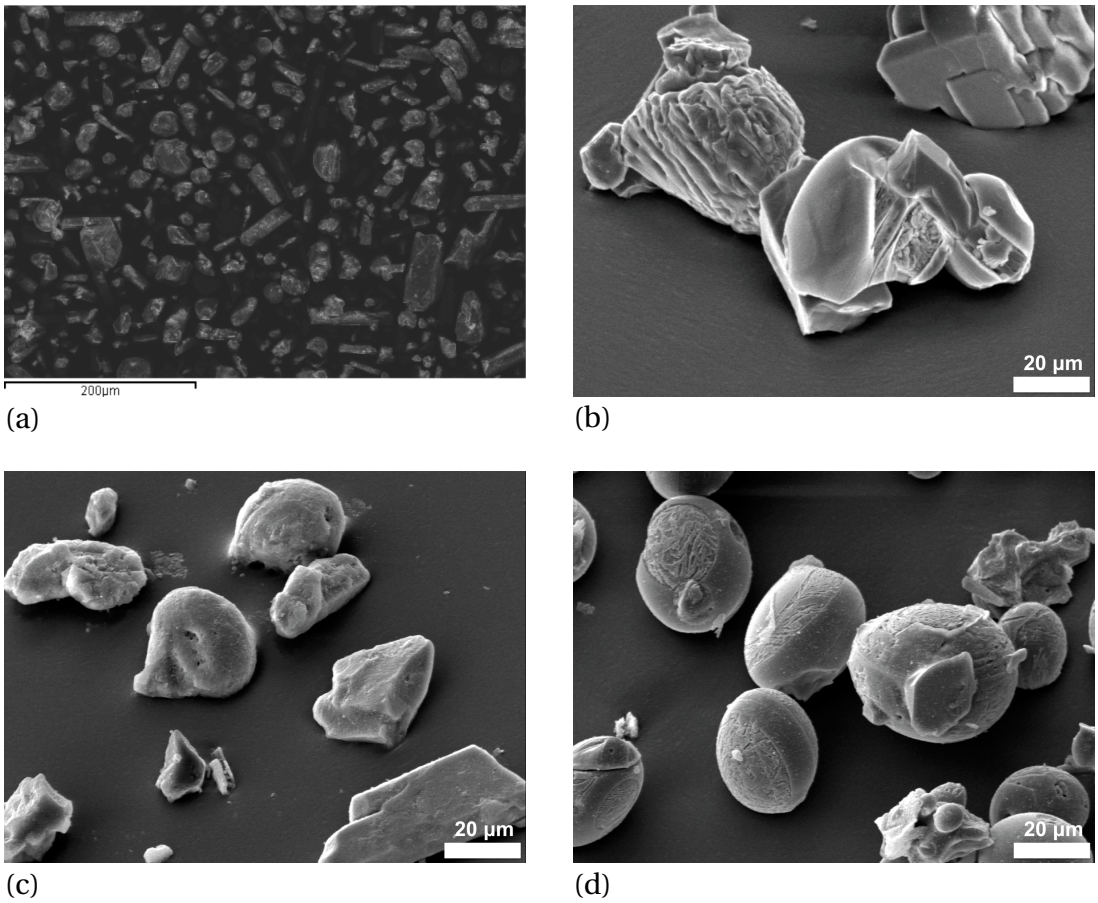
4.2.2 Microparticle Manufacture from Pure HA and the Effect of K_2SO_4 Salt Flux on Particle Characteristics

Instead of synthesising pure HA in a two-step process, it was investigated whether MSS could be used to reshape commercially available HA powder into individual HA microparticles in one step. Additionally, it was investigated if the HA-to-K_2HPO_4 ratios 1:3, 1:6, and 1:9 impact the morphology, composition, and protein adsorption propensity of HA microparticles. The hypothetic reaction equation for MSS from pure HA may be written as follows:

$$Step1 : \mathrm{HA} + \mathrm{K_2SO_4} \longrightarrow \mathrm{HA} + \mathrm{K_2SO_4}, T = 1200^{\circ}C$$

This equation simply states that HA may be reshaped physically but not altered chemically during MSS. Scanning electron micrographs show a progressively spheroidal shape of the synthesised bioceramic microparticles as the K_2SO_4 flux-to-HA powder ratio increases (Figure 4.5). Aspect ratios decreased from 1.0 – 3.1, to 1.0 – 2.0 with increasing salt flux (Table 4.1). Light scattering data suggests that the average particle diameter was less at higher salt flux ratios with size distributions encompassed by a span of 1.0 - 2.0 (Table 4.1). At higher K_2SO_4 mass, the HA concentration in the melt decreases while the distance between seed-particles in the melt increases. These two phenomena could allow for a shift from a solution-diffusion dominated process, to a solution-precipitation dominated process and may partially explain the different morphologies [Kimura (2011)]. However, the detailed mechanism needs to be further investigated.

XRD patterns (Figure 4.6) of the as-synthesised microparticles conformed to the standard d-spacings of HA (ICDD PDF # 09-432). The unusually high peak intensities (>25000 cps) registered for the 1:3 samples of Figure 4.6 indicate the suitability of this process for synthesising single crystals. In this method of synthesis, crystals of



(a) (b)

(c) (d)

Figure 4.5: SEM of MSS kHA Powders: SEM of microparticles show a) mixed crystalline and amorphous morphology for a) pure HA whiskers, b) the HA:Flux (1:3) particles, an c) increasingly spheroidal morphology for HA:Flux (1:6), and d) largely spheroidal particles for HA:Flux (1:9).

Table 4.1: Effect of Flux-to-HA Ratio on the Properties of HA Particles Manufactured by MSS.

Product	Size (d_v μm), (Span)	Aspect Ratio	Ca/K (molar ratio) by AAS	Ca/P (molar ratio) by EDS	Density (g/cc)
HA:K2SO4 (1:3)	54.5, (1.2)	1.0 - 3.1	39.6±5.7	1.3±0.3	2.87±1%
HA:K2SO4 (1:6)	36.1, (2.1)	1.0 - 2.0	6.7±3.2	1.1±0.2	3.16±1%
HA:K2SO4 (1:9)	36.8 (1.4)	1.0 - 2.0	1.1±0.5	0.8±0.3	3.32±1%
HA	49.8 (4.3)	1.0 - 8.5	NA	1.3±0.4	3.19±1%

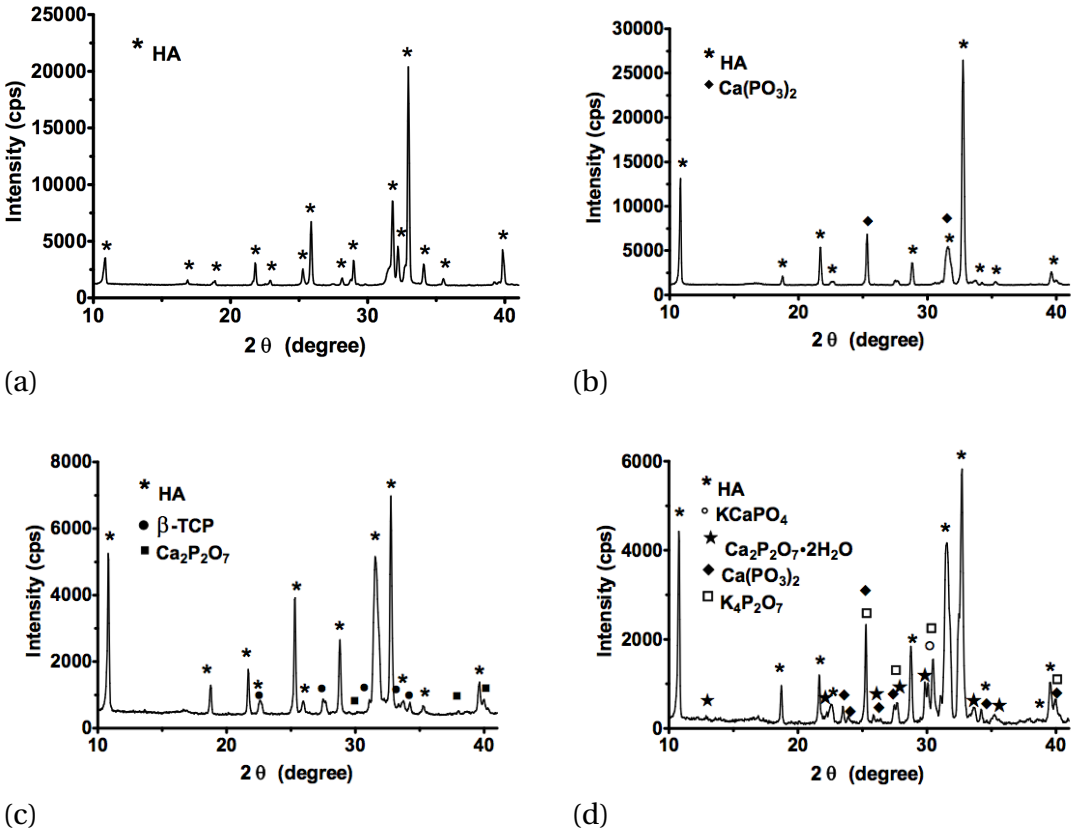


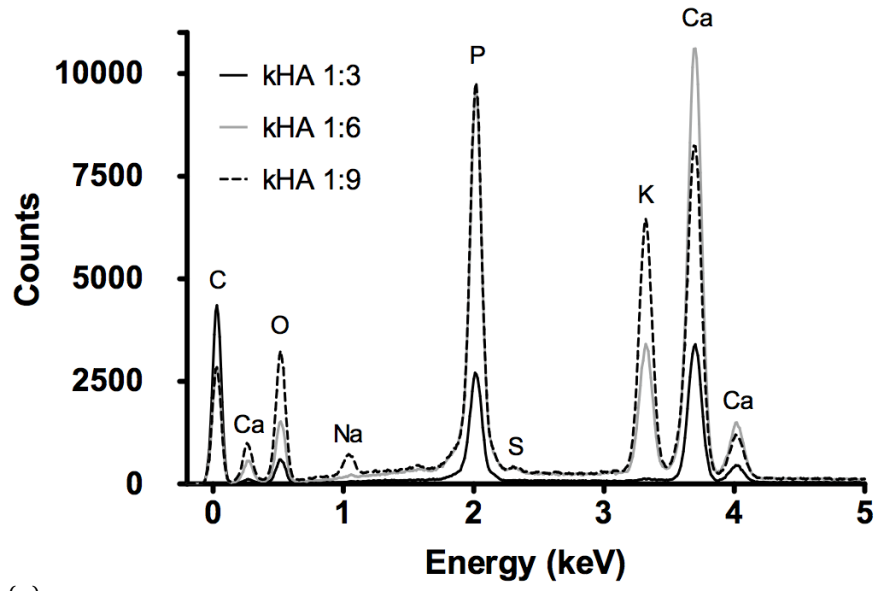
Figure 4.6: XRD Spectra of HA and kHA Manufactured by MSS: XRD of microparticles show HA as the major phase of for all flux conditions along with minor phases for a) pure HA whiskers, b) HA:K_2SO_4 (1:3), c) HA:K_2SO_4 (1:6), and d) HA:K_2SO_4 (1:9). Spectra were referenced against the ICDD data base.

apatitic calcium phosphate are produced and the most intense XRD peak is located on the (300) plane at 32.91 2θ, instead of the (211) plane. This difference is due to HA crystal orientation along the c axis [Tas (2001); Taş (2001)]. As the ratio of K_2SO_4 to HA increases, an overall decrease in crystallinity and the emergence of additional minor mineral phases is observed (Figure 4.6). In the 1:3 condition, the observed minor phase is $Ca(PO_3)_2$ (ICDD PDF # 11-0039). The 1:6 condition produced the minor phases beta-tricalcium phosphate (β-TCP, ICDD PDF # 09-169) and calcium pyrophosphate ($Ca_2P_2O_7$, ICDD PDF # 09-346). Both are known to be biocompatible and to enhance bioresorbability [Augustine et al. (2009); El Kady et al. (2009)]. At a 1:9 ratio, the minor phases are $K_4P_2O_7$ and a potassium-substituted calcium phos-

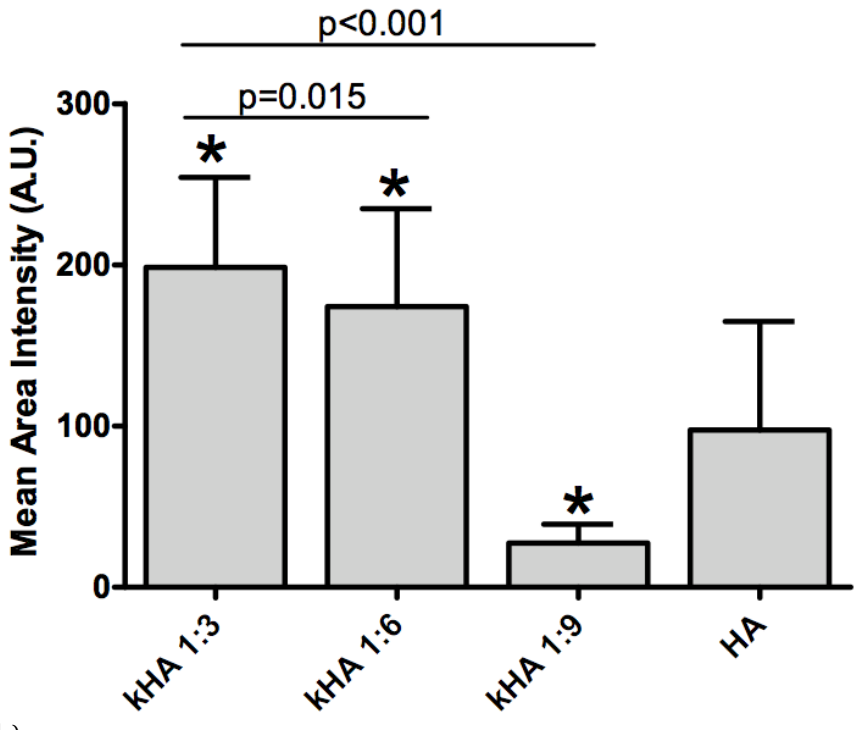
phate with the formula $KCaPO_4$. The incorporation of potassium ions into the bioceramic is confirmed by atomic adsorption spectroscopy (AAS), and was observed to increase at higher salt mass, as is evidenced by the decreasing Ca/K molar ratio (Table 4.1). Figure 4.7 a) furthermore suggests that Ca/P ratio decreases with increasing potassium content (EDS is semi-quantitative). A possible explanation for this decrease would be the substitution of potassium in lieu of calcium ions in the crystal lattice.

4.2.3 Surface Functional Group Characterisation Using FTIR

While X-ray diffraction provides insight into the crystal structure and crystallinity of the produced bioceramic, it is the surface of these particles that interfaces with the organism and therefore its surface composition should be investigated. FTIR spectroscopy can provide information on the functional groups on the surface of a material. For the as synthesised powder, the small band at 3571cm^{-1} indicates the presence of OH^- ions incorporated into the crystal structure of the sample (Figure 4.8). The wider adsorption band at 3400 – 3100 cm^{-1} suggests the presence of water in the sample and the peak absorption band at 2400 cm^{-1} is frequently observed when samples are prepared in potassium bromide (KBr). The band in the region of 1638–1600 cm^{-1}, which is due to H–O–H deformation, suggests that the sample can adsorb water molecules onto its surface. The four vibrational modes of the orthophosphate ions in HA can be observed with FTIR. Asymmetric stretching contributes the v_2 and v_3 (1200-1000cm^{-1}) adsorption bands, symmetric stretching the v_1 absorption band (960–950 cm^{-1}), and symmetric bending vibrations give rise to the v_4 (570–560 cm^{-1}) band. The identified orthophosphate bands are textbook values for apatitic calcium phosphate [Rehman and Bonfield (1997)]. The absence of the P–O–P vibrational mode characteristically located at 740 cm^{-1}, suggests that



(a)



(b)

Figure 4.7: EDS and BSA-TRITC Adsorption as Function of K_2SO_4Flux: a) EDS indicates that Ca/P and Ca/K ratios decrease as HA:Flux ratios increase, but is only semi-quantitative. b) BSA-TRITC adsorption onto microparticle batches measured by mean fluorescence intensity normalised to particle area. ANOVA was conducted and differences relative to pure HA indicated with asterisks (α-level 0.05 was significant, *p(<0.05), n=70 per group).

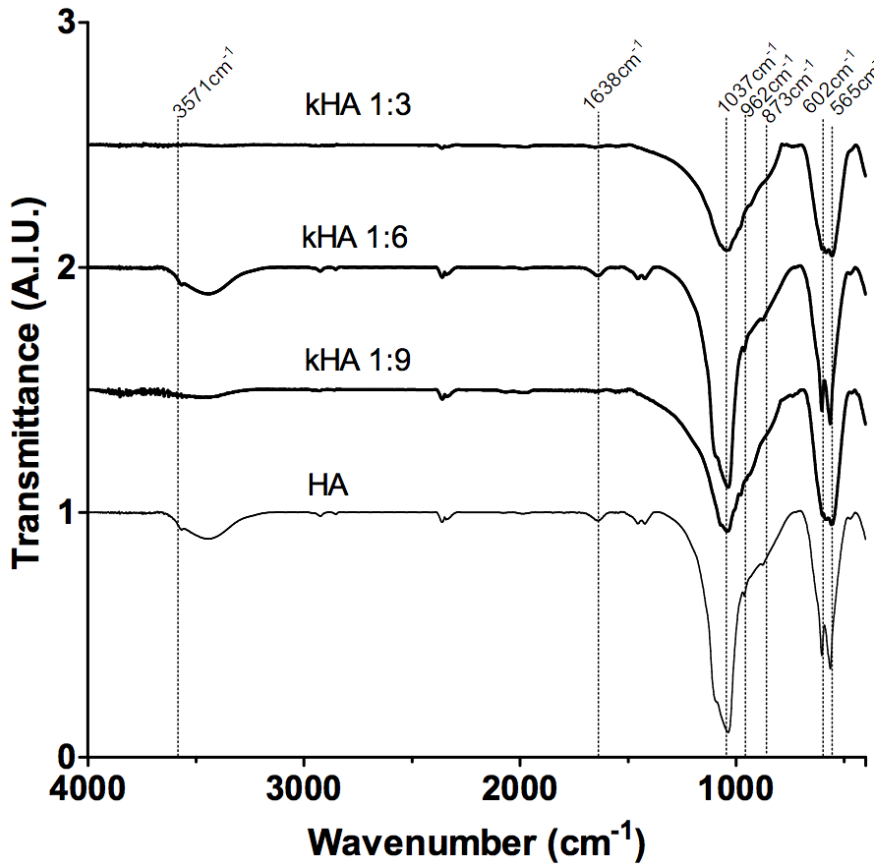


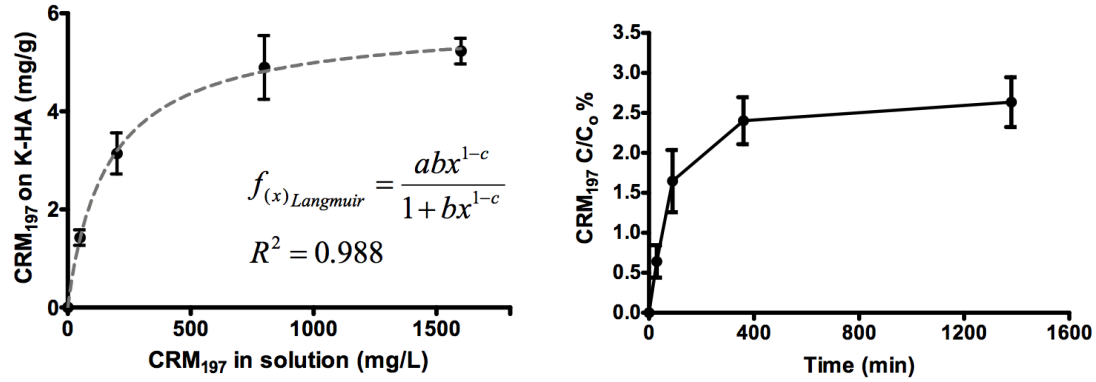
Figure 4.8: FTIR Spectrum of HA and kHA Particles: Surface analysis used 3-5mg of sample per 300mg KBr powder pellet. Spectra were acquired down to 400cm^{-1} on a Varian Excalibur FTS3500 FTIR with 4cm^{-1} resolution. Pure KBr pellets served as background for the averaged 64 sample scans. The FTIR spectra identified functional groups on the surface of the produced bioceramics that are characteristic of carbonated hydroxyapatite.

little to no pyrophosphates are present on the sample surface. However, carbonate groups were identified and are characterised by the absorption bands at 1500–1400 cm^{-1} and 875 cm^{-1}. The presence of carbonate is not a problem but an advantage. The bioresorption of carbonated HA has been shown to be faster than pure HA while maintaining similar properties of biological HA [Pan and Darvell (2010)]. In fact, carbonate is a substituent of biological appetites such as dentine and bone, which further underscores the biocompatibility of the MSS-synthesised bioceramic particles.

4.2.4 BSA and CRM_{197} Surface Adsorption onto kHA Microparticles and CRM_{197} Release *In Vitro*

Adsorption of negatively charged and fluorescently-labeled BSA, measured by fluorescence intensity and normalised to particle area, is depicted in Figure 4.7 b) and showed a more than 7-fold higher protein adsorption onto HA:K_2SO_4 (1:3) particles compared to 1:9 particles (27.4±11.8 AIU) ($p<0.001$). Mean fluorescence of the 1:3 particles was 198.5±55.7 AIU, while 1:6 particles had a mean fluorescence of 174.2±60.6 AIU, with the means being significantly different ($p=0.015$) due to the large sample size of n=70. The data suggest that increased molten K_2SO_4 content decreases the resultant bioceramic microparticles' capability to adsorb BSA-TRITC (Figue 4.7 b). Ratios of 1:3 and 1:6 increase BSA-adsorption, while the 1:9 HA-to-salt condition decreased BSA-adsorption relative to pure HA manufactured by MSS. Whether the change in protein adsorption is a direct effect of the substitution of potassium for calcium in the composite bioceramic, or the presence of minor orthophosphate phases, or the difference in morphology, needs further investigation.

The surface sorption capacity of CRM_{197} on kHA was determined by measuring the mass of CRM_{197} per mass of kHA as a function of protein concentration in the suspension. Figure 4.9 suggests that CRM_{197} adsorption on kHA is closely described by the Langmuir isotherm with the equation 2.4 in the methods section (R^2 = 0.99). Using the fitted curve to extrapolate to the maximum amount of CRM_{197} per gram of substrate, the adsorption capacity is estimated at 5.9mg of CRM_{197} per gram of kHA. When related to the surface area that was obtained from the light scattering particle size distribution, the maximum CRM_{197} adsorption capacity corresponds to a surface protein loading density on kHA of 9.7mg/m^2. The protein-loading density of BSA on pure HA has been reported as 1.5mg/m^2, but naturally, buffer



(a) (b)

Figure 4.9: CRM_{197} Adsorption and Release from kHA *in vitro*: Subfigure a) depicts CRM_{197} sorption onto kHA in 10 mM PBS pH 7.4 at room temperature as function of protein concentration in solution. Change in CRM_{197} concentration in PBS was measured using micro BCA assay. Mean adsorbed CRM_{197} mass with standard deviation plotted relative to kHA follows a Langmuir isotherm (R^2 = 0.988, n = 3, repeated 3 times). For equation details see methods section 2.2.3. b) Mean cumulative release and standard deviation (n = 3, repeated 3 times) of CRM_{197} in PBS pH 7.4 from kHA microparticles was measured using micro BCA assay. The cumulative release (C) is expressed relative to the total adsorbed protein on the kHA microparticles (C_0) over time.

strength, protein type, and substrate affect the loading density and may therefore not be directly compared [Mavropoulos et al. (2011)]. Additionally, light scattering can give an estimate of the surface area, but it cannot account for the surface roughness. Therefore, the average surface loading density of CRM_{197} on kHA can only be regarded as a rough estimate.

Colloidal adjuvants retain the antigen at the injection site, which has been linked to immune response potentiation. kHA microparticles released approximately 1.5% of their maximum CRM_{197} payload within the first 90 min in PBS buffer as initial burst, but provided sustained release of the antigen thereafter (Figure 4.9 b). Therefore, kHA may similarly to alum retain CRM_{197} at the injection site while providing a slow release of the antigen. Whether the remaining 97% of the payload were bioavailable was investigated *in vivo* and results are presented in chapter 6.

4.2.5 Secondary Structure and Thermal Unfolding Behaviour of CRM_{197} in the Surface Adsorbed State

Immunogenic epitopes may be adversely affected by changes in the secondary structure of the antigen, which should be avoided during dry-powder formulation. Partial unfolding of proteins can lead to aggregation via the association of exposed hydrophobic patches to form intermolecular β-sheet. This change is manifested by a decrease in α-helix structure and an increase in β-sheet content [Fink (1998)]. Therefore, it is important to characterise the structure and structural stability of CRM_{197} in the surface-adsorbed state.

FTIR analysis of surface-adsorbed CRM_{197} localised the amide I band peak position of kHA-adsorbed CRM_{197} at 1648 cm^{-1} (Table 4.2). This was also the band position of CRM_{197} when suspended in phosphate buffer. Adsorption onto kHA caused a 1.3% reduction of α-helix and a 5.3% decrease in β-sheet content relative to solution. This suggests that adsorption onto kHA largely conserved the native secondary structure of CRM_{197}. On the other hand, alum ($AlPO_4$)-adsorbed CRM_{197} induced a 5.4% decrease of α-helical content along with a 4.8% increase in β-sheet structures (Table 4.2). These results suggest that a more native state similar form of CRM_{197} may be presented to the immune system on kHA than on alum ($AlPO_4$). The structure of CRM_{197} on $Al(OH)_3$ showed a decrease in α-helix comparable to kHA, but a 5.9% increase in β-sheet. The observation that β-sheet structures increase on aluminium salts but not on kHA suggests that adsorption onto kHA better conserved the native secondary structure of CRM_{197}.

Thermal stress alters the secondary structure of CRM_{197} in PBS pH7.4: A heat ramp from 20 – 80°C of 38mg/mL CRM_{197} in PBS pH7.4, showed that the decades of 20 – 30°C and 30 – 40°C had very little effect on the native secondary structure

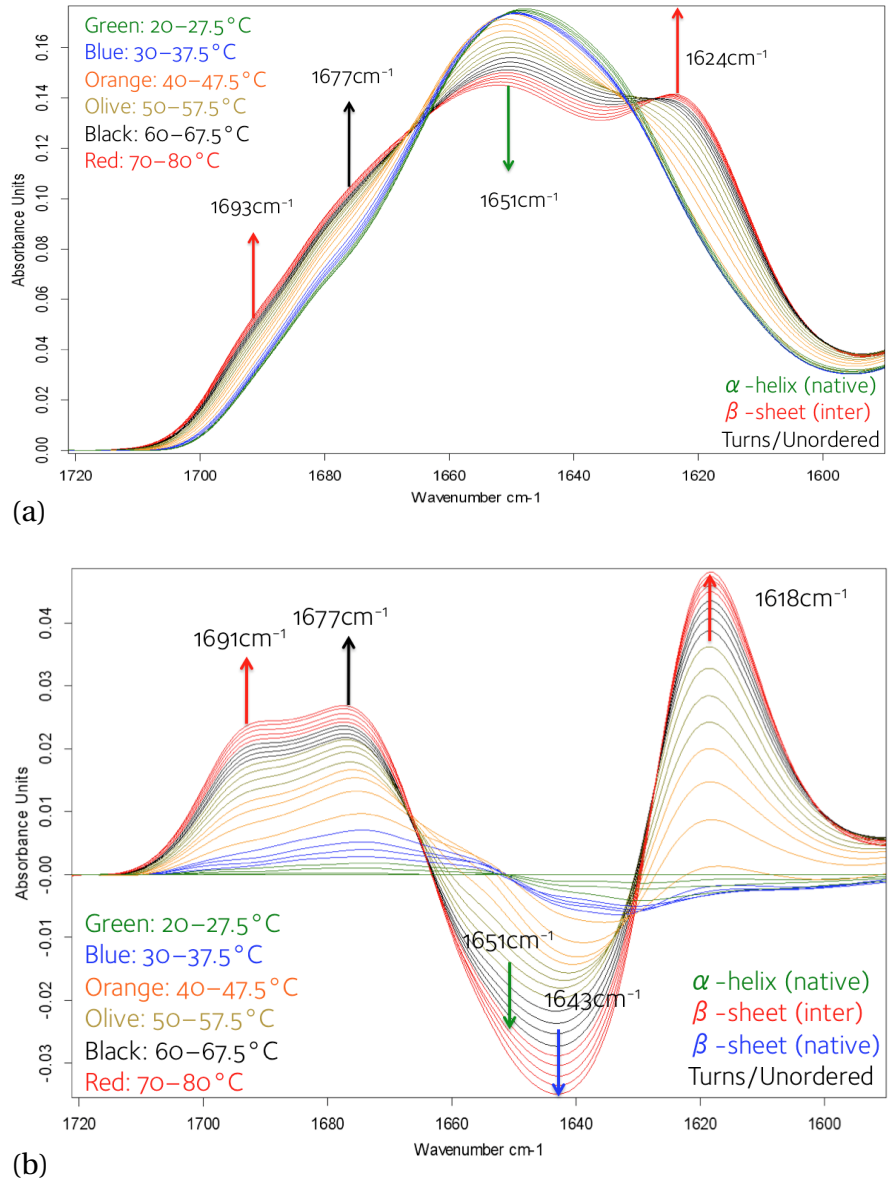


Figure 4.10: CRM_{197} Thermal Unfolding in PBS Measured by FTIR: a) Show the amide I band (1720–1590^{-1}) of 38mg/mL CRM_{197} in PBS pH 7.4, and the spectral changes during a temperature ramp from 20°C – 80°C coloured by decade. Structural changes are indicated with colour-coded arrows that correspond to the various secondary structure components. b) Shows the structural changes of CRM_{197} at temperatures 20°C – 80°C relative to its structure at 20°C.

Table 4.2: Secondary Structure of Surface-adsorbed CRM_{197}. Note: The BioATR was used to measure the relative structural changes of CRM_{197}. The comparator here is CRM_{197} in PBS.

	α-Helix (%)	β-Sheet (%)	Amide I Peak (cm^{-1})	TRP Emission$_{\alpha=295}$ (nm)
PBS	31.1 ± 1.0	33.8 ± 1.1	1648 ± 0.1	342.0 ± 0.5
$Al(OH)_3$	-1.4±2.1	5.9±1.3	-3±0.6	343.0 ± 1.0
$AlPO_4$	-5.4±1.4	4.8±1.0	0.1±0.1	339.5 ± 1.0
kHA	-1.3±0.8	-5.3±1.6	0.2±0.1	342.0 ± 1.0

of CRM_{197} (Figure 4.10). However, at 40°C and beyond, native α-helix at 1651cm^{-1} and native β-sheet at 1642cm^{-1} were lost rapidly while intermolecular β-sheet was formed at 1618cm^{-1} (Figure 4.10). In solution, 50% of CRM_{197} secondary structure was unfolded at 47.6°C (Figure 4.11, a). And 98.4% of CRM_{197} secondary structure was unfolded at 70°C. Interestingly, the thermal unfolding of CRM_{197} slightly deviated from the fitted sigmoidal function. Below the T_m, unfolding was larger, and above the T_m, unfolding was less than the sigmoid indicates. This behaviour seems to suggest the presence of two unfolding events, which may correspond to the B- and A-subunit of CRM_{197}. This observation agrees with the double unfolding peak observed of CRM_{197} in ≈100mM salt buffer by DSF in chapter 3.

The secondary structure of free CRM_{197} is altered upon adsorption to alum and k-HA: Adsorption onto $Al(OH)_3$ at 20°C resulted in an amide I peak shift by 3cm^{-1}, along with a 1.4%±2.1% decrease in α- helix and a 5.9%±1.3% increase in β-sheet content (Table 4.2). Adsorption onto $AlPO_4$ at 20°C resulted in a 5.4%±1.4% reduction in α-helix and a 4.8%±1.0% increase in β-sheet content. No significant amide I band peak shift was observed (Table 4.2). CRM_{197} adsorption onto kHA induced a 1.3%±0.8% decrease of α-helix and a 5.3%±1.6% decrease in β-sheet content, but the amide I peak position remained at 1648 cm^{-1} (Table 4.2). Decrease in both α-helix and β-sheet content can be partially explained by an increase in the unordered structure.

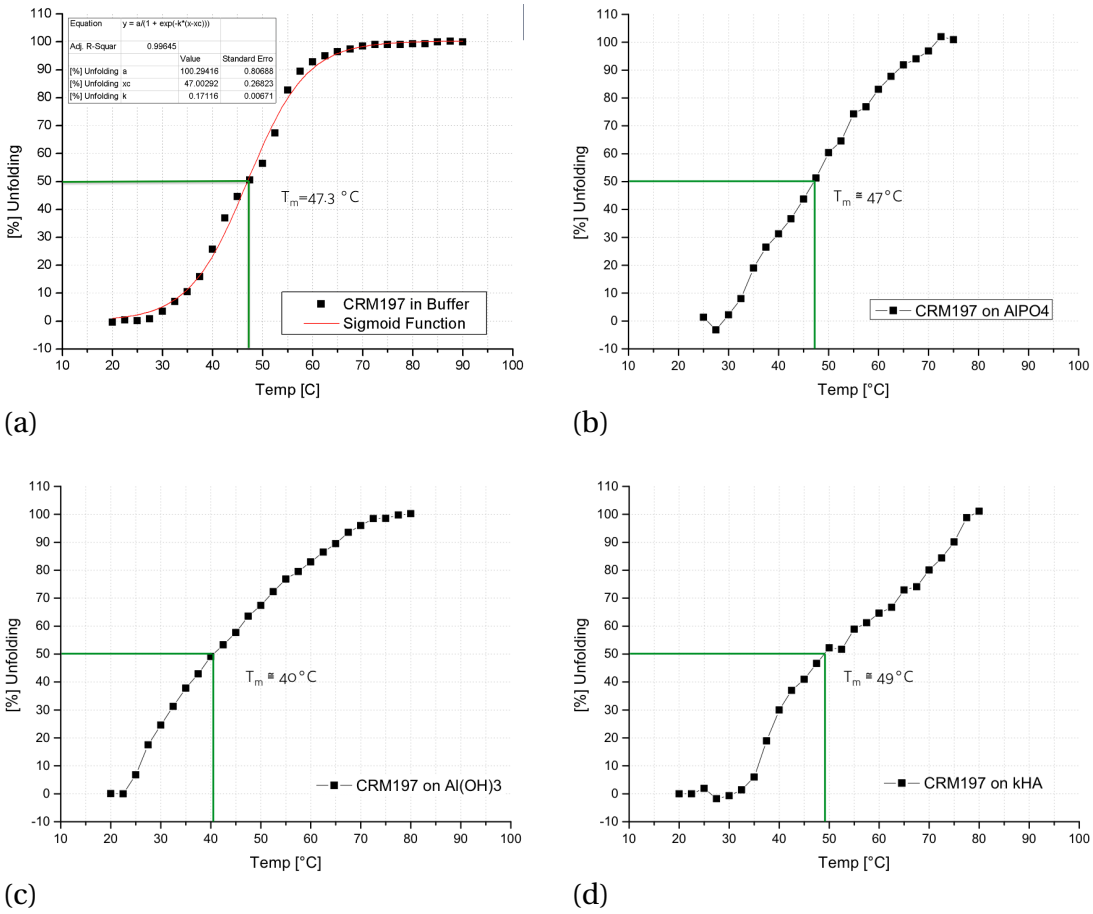


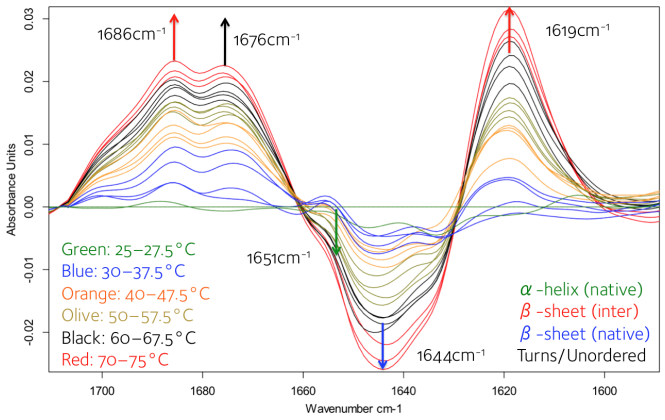
Figure 4.11: FTIR Unfolding Curves of CRM_{197} Secondary Structures: Amide I band scans obtained at 75°C, 77.5°C, and 80°C served as 100% unfolding estimate, while 20°C, 22.5°C, and 25°C served as 0% unfolding estimates. a) Sigmoidal (R^2=0.996) thermal unfolding curve of 38mg/mL CRM_{197} in PBS pH 7.4 with T_m at 47.3°C. Quasi-linear CRM_{197} unfolding curve adsorbed on b) $AlPO_4$ with T_m at 47°C, c) $Al(OH)_3$ with T_m at 40°C, and d) kHA with T_m at 49°C.

Alum adsorption alters the halfway unfolding temperature T_m of CRM_{197}: When adsorbed to $Al(OH)_3$, 50% of CRM_{197} secondary structure was unfolded at approximately 40°C (Figure 4.11, c). When adsorbed to $AlPO_4$, CRM_{197} showed a 50% secondary structure unfolding at about 47°C (Figure 4.11, b). Interestingly, on kHA thermal unfolding of CRM_{197} secondary structure started later than on both aluminium salts. Half-way thermal unfolding of CRM_{197} on kHA was approximately 49°C, which was about 1.6°C higher than CRM_{197} in PBS (T_m=47.4°C), and about

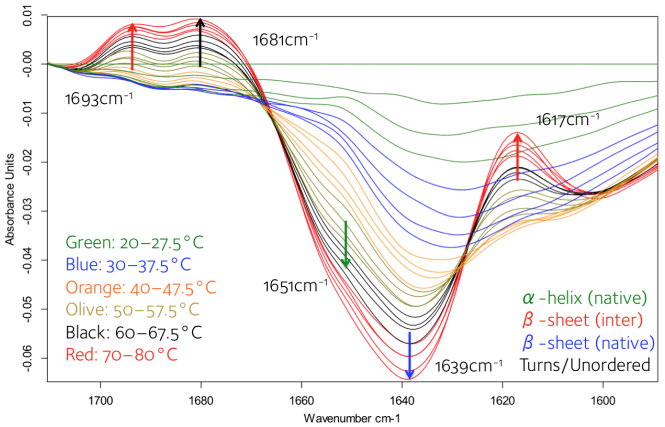
2°C higher than on $AlPO_4$, and approximately 9°C higher than on $Al(OH)_3$.

Thermal unfolding of CRM_{197} is less pronounced when surface-adsorbed: The change in the relative intensity of $Al(OH)_3$ adsorbed CRM_{197} that is associated with the native α-helix (1651 cm^{-1}) suggests that 27.0% of native α-helix was preserved, and that 59.4% less intermolecular β-sheet was formed compared with CRM_{197} in PBS at 80°C (Figure 4.12). When adsorbed to $AlPO_4$, the decrease in relative intensity of native α-helix was approximately 31.1% less compared to PBS at 80°C. The relative intensity increase associated with intermolecular β-sheet content of adsorbed CRM_{197} was approximately 31.3% less compared to PBS at 80°C (Figure 4.12). kHA relative intensities were comparable to $AlPO_4$ for loss of native α-helix and β-sheet, but showed a higher relative intensity increase in intermolecular β-sheet, which was similar to $Al(OH)_3$. This seems to suggest that CRM_{197}-adsorption onto kHA largely retains its secondary structure and stabilises against the thermal unfolding of native structures. However, individual CRM_{197} molecules may be in sufficiently close proximity and mobile enough on the kHA surface to interact and to form intermolecular β-sheet when thermally stressed.

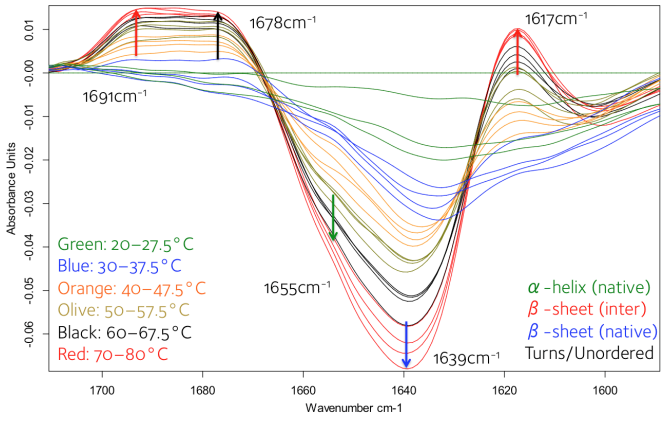
Relative to its structure in PBS, CRM_{197} loses native α-helix and gains intermolecular β-sheet content upon surface adsorption onto $Al(OH)_3$, $AlPO_4$, and kHA. Fewer additional structural changes were observed during heating when adsorbed onto $Al(OH)_3$. This may suggest that CRM_{197} in its kHA or $AlPO_4$ adsorbed state is more similar to its structure in PBS than when adsorbed on $Al(OH)_3$. Therefore, CRM_{197} structure may be better preserved on kHA and $AlPO_4$. Thermal stability of CRM_{197} on $Al(OH)_3$ is less than on $AlPO_4$ and in PBS, and highest on kHA, indicating that $Al(OH)_3$ adsorption may destabilise the protein. The higher approximate T_m of CRM_{197} on kHA suggests a thermal stabilisation in the surface-adsorbed state. The quasi-linear unfolding curve of the surface adsorbed CRM_{197} may par-



(a)



(b)



(c)

Figure 4.12: CRM_{197} Thermal Unfolding in Surface-adsorbed State: a) Temperature ramp spectra of CRM_{197} on a) $Al(OH)_3$, b) $AlPO_4$, and c) kHA at temperatures from 20°C – 80°C relative to 20°C, and colour coded by decade. Structural changes in all figures are indicated with colour-coded arrows according to secondary structure element.

tially be due to i) interactions of the unfolding protein with the surface charges of the respective substrate, and ii) an incomplete sampling of the entire folding and unfolding temperature rage which focuses only on the middle of the sigmoidal unfolding transition but does not completely capture the protein folding at the two extreme temperatures. The immune responses generated by $AlPO_4$-CRM_{197} and kHA-CRM_{197} were subsequently assessed *in vivo*.

4.3 Chapter Summary

A subpopulation of highly BSA-adsorbing particles was identified in HA powders manufactured in a two-step MSS process from precursor calcium phosphates. It was possible to adjust the manufacture method to predominantly produce the highly adsorbing subpopulation with only one step. The bioceramic microparticles mainly comprised of pure HA grown along the c axis. Potassium incorporation was apparent from a decreasing Ca/K molar ratio at higher K_2SO_4 flux content. With the increase of flux-to-HA ratio, the resultant particles were increasingly of spheroidal morphology with a narrow size distribution. The adsorption of negatively charged BSA on the different microparticle batches was investigated. BSA adsorption decreased with higher potassium content, but was higher on kHA than on pure HA for the HA:K_2SO_4 conditions (1:3) and (1:6). Highest BSA adsorption was observed for the HA:K2SO4 (1:3) condition and was 7-fold higher compared to (1:9), and 2-fold higher than pure HA. The functional groups on the kHA surface corresponded well to carbonated HA according to FTIR. Therefore, their use *in vivo* is of little concern since HA is a GRAS substance. The mechanical properties of kHA particles were determined relative to pure HA crystals. The mechanical robustness of the individual particles was similar to tubercular bone and dentine, which makes them well

suited to withstand the acceleration and impact forces of ballistic injection. Simple co-incubation of CRM_{197} with the kHA carrier microparticles, followed by dehydration with isopropanol and vacuum desiccation at room temperature was sufficient to reformulate the antigen. CRM_{197} sorption onto kHA was well described by a Langmuir isotherm which suggests a monolayer adsorption of CRM_{197}. A monolayer adsorption of the antigen may avoid aggregation on the surface due to spacial separation and immoblisation. *In vitro*, after a minor burst in the first hours of incubation in the buffer medium, CRM_{197} release from kHa was sustained over the duration of the experiment. This is a common property of HA [Iafisco et al. (2011)]. In the surface-adsorbed state, CRM_{197} largely retained its secondary structure on kHA, and according to FT-IR measurements, the structural retention was as good or better than when adsorbed on conventional alum adjuvants. Recently, the structural retention of lactoferrin on the surface of HA was also demonstrated with similar methods [Iafisco et al. (2011)]. Therefore, CRM_{197}-kHA may be an interesting alternative to dry-powder protein-containing vaccines manufactured by SFD. The immunogenicity of ballistically delivered CRM_{197}-adsorbed kHA particles with HA-to-flux ratio 1:6 was investigated *in vivo* and findings are presented in chapter 6.

CHAPTER 5

FUNCTIONALISED BLOCK COPOLYMER NANOPARTICLES AS NOVEL ADJUVANT

Chapter 5 introduces a novel nanoparticle-construct for improved protein antigen presentation. Conventional alum adjuvants reportedly induced granulomas and hence they are largely unsuitable for intradermal injection. Therefore, a novel block copolymer nanoparticle adjuvant system was investigated that presents the covalently conjugated antigen on its surface. The chapter describes the manufacture and characterisation of CRM_{197}-conjugated NPs and their incorporation into dry-powder microparticles by SFD.

5.1 INTRODUCTION

Vaccines can protect vaccinees from devastating disease via the induction of a strong immune response that results in persisting immune memory and the capacity to quickly mount a competent humoral and cellular response against a specific pathogen. However, the immunogenicity of isolated and purified antigens is limited and frequently requires adjuvantation [O'Hagan and Valiante (2003)]. Clinically approved adjuvants are few. Aluminium salts have a long track record of safety but

their immune stimulus induces a one-sided Th2 response, leading to good efficacy in treating extracellular pathogens but not intracellular pathogens [Gupta (1998)]. Other adjuvants such as enterotoxins have been successfully used but can vary in their reactogenicity by injection site [Pizza et al. (2001)]. A recent success story is the novel MF59®, a surfactant-coated squalene oil-in-water emulsion, that serves as delivery system of antigens. It induces "the creation of a transient 'immunocompetent' local environment at the injection site, resulting in the recruitment of key immune cells, which are able to take up antigen and adjuvant and transport them to the local lymph nodes, where the immune response is induced" [O'Hagan et al. (2012)]. In that way, it acts similarly to alum. In essence, the emulsion is a particulate system. The presentation and delivery of antigens as part of a particulate system has been an area of active research [Leleux and Roy (2013)]. For example, the surface presentation of the malaria antigen VMP001 on a nano-sized particle induced a more Th1/Th2 balanced immune response than the release of its soluble form from the same particle [Moon et al. (2012)]. Surface-presented VMP001 was found to boost immunity via the induction of germinal centres and the expansion of antigen-specific follicular T helper cells which induced a prolonged B-cell response. Whether emulsion, liposomes, or other nanoscale particulates, their co-delivery with an antigen has shown promising immunogenicity potentiation.

Although needle-free ballistic injection has demonstrated a dose-sparing ability that is possibly based on a combination of targeting immune competent cells and inducing danger signals by inflicting dermal micro trauma, most microparticle formulations induced a predominantly Th2 based immune response [Weissmueller et al. (2013)]. Therefore, although potent, the quality of the immune response that is induced with IPI may be improved with the addition of an immune modulator such as antigen-coated nanoparticles.

Recently, the Prud'homme Lab at Princeton University has developed a nanoparticle self-assembly system for functionalised amphiphilic block-copolymer nanoparticles that uses antisolvent precipitation of impinging liquid jets to achieve highly reproducible, well size-controllable, and readily production-scalable nanoparticles (see methods section 2.3.1) [Johnson and Prud'homme (2003b); Chen et al. (2009)]. This platform has been shown to enhance the delivery of poorly soluble drugs [Ansell et al. (2008); Gindy et al. (2008)]. A collaboration between the Prud'homme Lab and the Oxford Vaccine Group was established to investigate the utility of this nanoparticle platform in vaccine delivery, with the aim to improve the immunogenicity of protein antigens that are delivered by needle-free powder injection.

This chapter presents the first results from this collaboration. First, the manufacture of monodisperse and surface-functionalised nanoparticles is described by design of experiments (DOE). The analysis focusses on the influence of various polymer concentrations on the eventual nanoparticle size. Second, the covalent conjugation of CRM_{197} to nanoparticles is illustrated by SDS-PAGE. Third, NP-CRM_{197}-containing dry-powder is manufactured by SFD and the impact of NP-addition on the physical characteristics of SFD dry-powder is discussed.

5.2 Results and Discussion

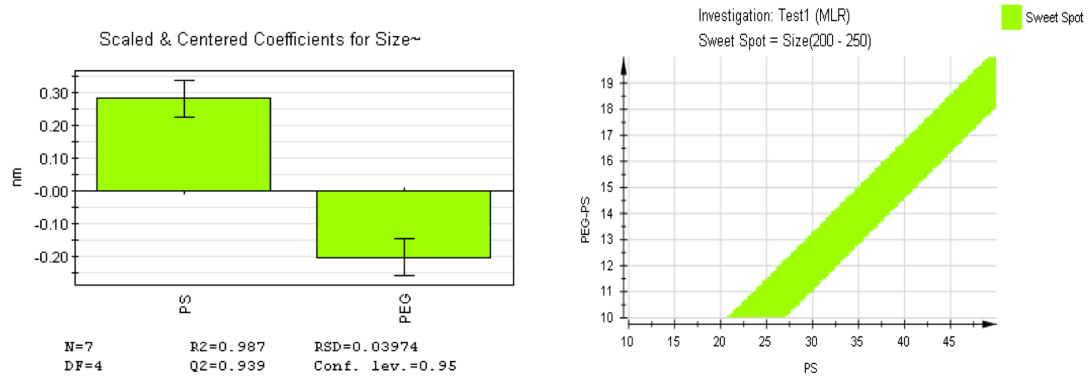
5.2.1 Investigation of Nanoparticle Size by Design of Experiments

It was investigated whether the size of NPs can be controlled by varying the concentration of PEG(5k)-b-PS(1.6k) between 10mg/mL to 20mg/mL, and PS(1.5k) between 10 mg/mL to 50mg/mL in THF. DOE was used to study the individual effects

of the hydrophobic PS, and the amphiphilic block co-polymer PEG(5k)-b-PS(1.6k) on the size of nanoparticles. DOE defines a design space and uses statistical methods to derive a minimum number of required experiments to obtain the desired information on the correlation between individual model factors. In this case, DOE required 7 nanoparticle batches that covered permutations in the low, middle, and high regions of polymer concentrations (Figure 5.2, a). Linear regression analysis, with NP size as outcome variable and polymer concentrations as predictor variables, showed that the polymer type has a significant impact on the final NP size (Figure 5.1, a). Particle size was log-normally distributed, and thus transformed before linear regression. Therefore, the final regression coefficients need to be scaled to reverse this transformation. For an increase of 1mg/mL of the amphiphilic block copolymer PEG(5k)-b-PS(1.6k) in the organic solution, the size of the resultant NPs was reduced by 1.58nm (=$10^{0.2}$nm). On the other hand, an increase by 1mg/mL of PS(1.5k) in the organic solution was associated with a 1.95nm (=$10^{0.29}$nm) increase of the final NP size (Figure 5.1, a).

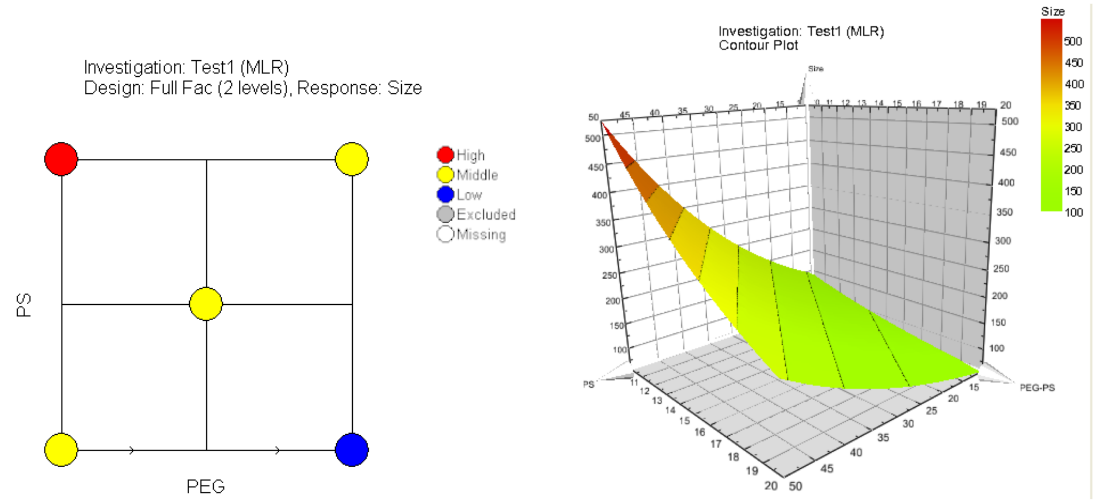
Figure 5.2 b) depicts, that towards high PS at low PEG-b-PS concentrations, the mean diameter of NPs increases almost exponentially. This can be explained on the basis of the NP's structural composition. Upon antisolvent mixing, the hydrophobic PS situates itself at the core of NPs, and the amphiphilic PEG-b-PS orients its hydrophobic chain towards the PS core and its hydrophilic chain towards the aqueous solution. When there are insufficient amounts of amphiphilic chains to encapsulate the PS core, PS aggregates and precipitates in non-spherical structures that rapidly increase in size. Conversely, an excess of PEG-b-PS leads to the formation of micelle populations which are on the order of 10nm, and can reduce the overall measured NP diameter drastically.

According to the DOE model, pathogen-sized NPs, with a range of 200nm to



(a) (b)

Figure 5.1: Nanoparticle Sizes as Function of PS and PEG by DOE: a) Linear regression coefficients of PS and PEG concentrations on $\log_{10}$-transformed NP size (R^2=0.987) were highly significant (p<0.001). The reproducibility of NP sizes was good with a mean of 185.1nm ±1.8nm (n=3). b) The sweet spot option of the MODDE 9.1 software depicts the parameter range of the model factors, here PEG and PS concentrations (green area), that will produce the desired size-outcome for nanoparticles (here 200nm–250nm).



(a) (b)

Figure 5.2: Nanoparticle Sizes as Function of PS and PEG by DOE: DOE investigated the effect of PS and PEG-PS concentration in THF on the eventual NP size. a) MODDE 9.1 software prescribed 5 combinations of PEG (10, 15, 30 mg/mL) and PS (10, 30, 50mg/mL) to create a design space based on 7 DLS measurements after FNP (middle point measured in triplicate). b) Shows the calculated design space estimated from DOE experimental values.

250nm, can be obtained with the polymer concentrations depicted in green on the sweet spot region (Figure 5.1, b). Validation for the DOE model used 12mg/mL PEG(5k)-b-PS(1.6k) and 30mg/mL PS(1.5k). FNP produced a monodisperse population of NPs with a mean diameter of 186.8nm±4.6nm and a PDI of 0.150. The error inherent to the DOE model in this case was thus 6.7%. Therefore, the model allows for the reasonably precise manufacture of monodisperse nanoparticles by self-assembly.

Table 5.1: Intensity-weighted DLS measurements of NP mean diameter throughout FNP manufacture and CRM_{197}-conjugation.

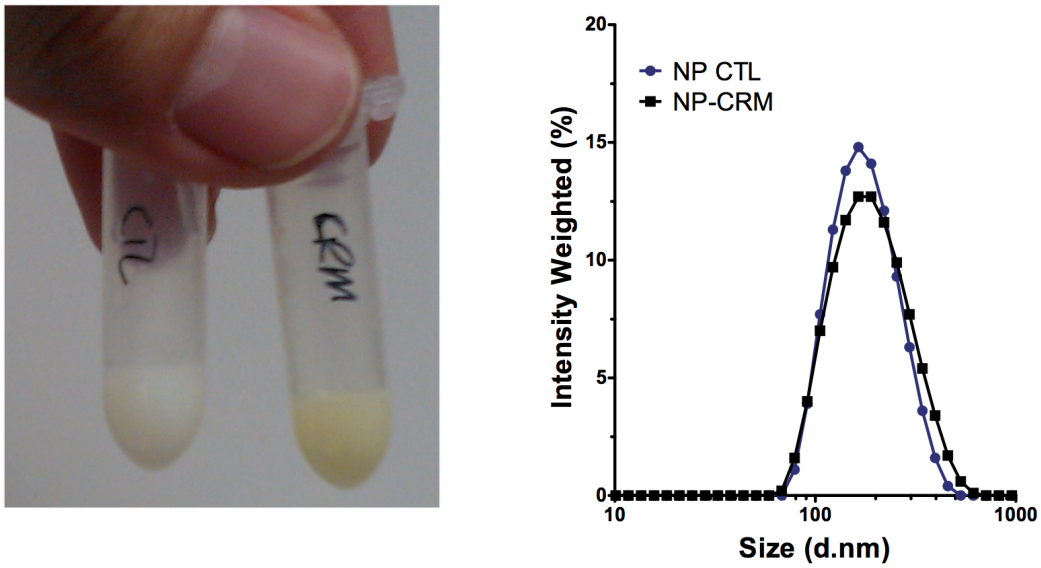
	CRM_{197} Stock	NPs in THF	NPs post THF removal	NP CTL post rxn	NP-CRM_{197} post rxn	NP-CTL washed	NP-CRM_{197} washed
Size (nm)	5.1±0.3	196.7±4.3	200.4±6.7	187.9±4.9	192.3±8.2	191.5±6.1	208.3±9.3
PDI	0.09±0.01	0.14±0.02	0.16±0.04	0.14±0.01	0.15±0.05	0.14±0.05	0.17±0.07

Throughout the manufacture process, NP sizes remained stable with excellent PDI (Table 5.1). THF removal after FNP caused a minor swelling of the polymer nanoparticles with an approximate 3.7nm increase in mean diameter. After agitation at elevated pH, there is a size decrease of NPs, which may be due to some NP degradation, or due to the change in the rheological properties of the buffer which may effect DLS measurements. The fact that the PDI remained low at around 0.15, suggests that NPs did not degrade or aggregate, which would result in the presence of smaller or larger particles, and would increase the PDI. Therefore, it is likely that most changes to salt concentrations and pH impact the mean diameterDLS size measurement. The reaction with CRM_{197} increased the mean particle diameter by approximately 5nm, relative to control which was suspended in the same buffer and pH but without CRM_{197}. The 5nm diameter increase corresponds to the approximate size of CRM_{197} monomer in buffer measured by DLS (Table 5.1). CRM_{197}-conjugated NPs showed a higher tendency to aggregate than unconjugated NP. These results suggest a successful NP-to-CRM_{197} conjugation with a fairly monodisperse final product with PDI=0.17±0.07 (Figure 5.3, b).

5.2.2 CRM_{197} Conjugation to NP

Approximately 6 to 9 capsular polysaccharide chains from *N. meningitides* serotype A, C, W, and Y may be conjugated to CRM_{197}'s 39 accessible lysine groups, which suggests that the amount of reactive primary amines that are available to link to the para-nitrophenol (pNP) group are few [Giannini et al. (1984); Berti et al. (2004)]. Given that NPs are much larger than the 4kDa–10kDa size of these capsular polysaccharides, it is questionable to what extent CRM_{197} can be successfully conjugated to NPs. One advantage of pNP chemistry is the yellow color of the pNP which allows for a visual monitoring of the reaction. Visual inspection suggests, that the yellow colour development of pNP is much stronger in the presence of CRM_{197} than in the same buffer conditions but without CRM_{197} (Figure 5.3, a). Therefore, even if there is partial hydrolysis of the pNP group from the PEG-b-PS polymer, it would have to be the same in the identical buffer, but the apparent difference in yellow color between the CRM_{197} condition and the control group suggests a higher concentration of free pNP in the CRM_{197} condition. This suggests that at least some CRM_{197} molecules are successfully conjugated to NPs.

The relative mass of NPs in solution was calculated and the amount of surface-bound CRM_{197} per mass of particle quantified using BCA. According to BCA analysis, the conjugation efficiency was 10.2%±3.1% by wt of CRM_{197}/NP. While this gives an estimate of how much CRM_{197} can be delivered per mass of NPs, it was further investigated whether CRM_{197} was chemically conjugated to NPs or whether the protein was merely adsorbed to the NP surface. Additionally, it was investigated whether CRM_{197} would react with multiple pNP groups on the NP surface and be multiply-bound to a NP. DLS measurements suggest an average mean diameter of CRM_{197} at 5nm, and around 180–200nm for the block-co-polymer NPs (Table 5.1). At 75% functionalisation, therefore, it is likely that multiple pNP-terminated poly-



(a) (b)

Figure 5.3: CRM_{197}-conjugation to NPs: Subfigure a) shows the buffer only control (CTL) and CRM_{197} reaction group of pNP-NPs. CRM_{197}-conjugation proceeds via the reaction of the PNP with a reactive primary amine on CRM_{197} and can be monitored by the yellow color that is characteristic of the PNP leaving group. b) The intensity weighted diameter size of NPs increases slightly upon CRM_{197}-conjugation to NPs but remains monodisperse.

mer chains are situated within the CRM_{197}-to-NP contact area and may interact. A multiple chemical linkage may provide stronger binding of CRM_{197} to NPs, but may also affect its tertiary structure.

The maximum surface loading capacity was determined for 75% functionalised PEG(5k)-b-PS(1.6k) NP at a 1-to-1 molar equivalent ratio of reactive primary amines on CRM_{197} to PNP functional groups on PEG(5k)-b-PS(1.6k) NP.The conjugation efficiency of CRM_{197} to PNP-terminated PEG(5k)-b-PS(1.6k) was assessed using modified SDS-PAGE and BCA.

The conventional coomassie blue SDS-PAGE protein stain, when combined with the yellow colour of the iodine PEG stain, first described and developed by Kurfürst (1992), produces a dark brown/purple colour where PEG and CRM_{197} are

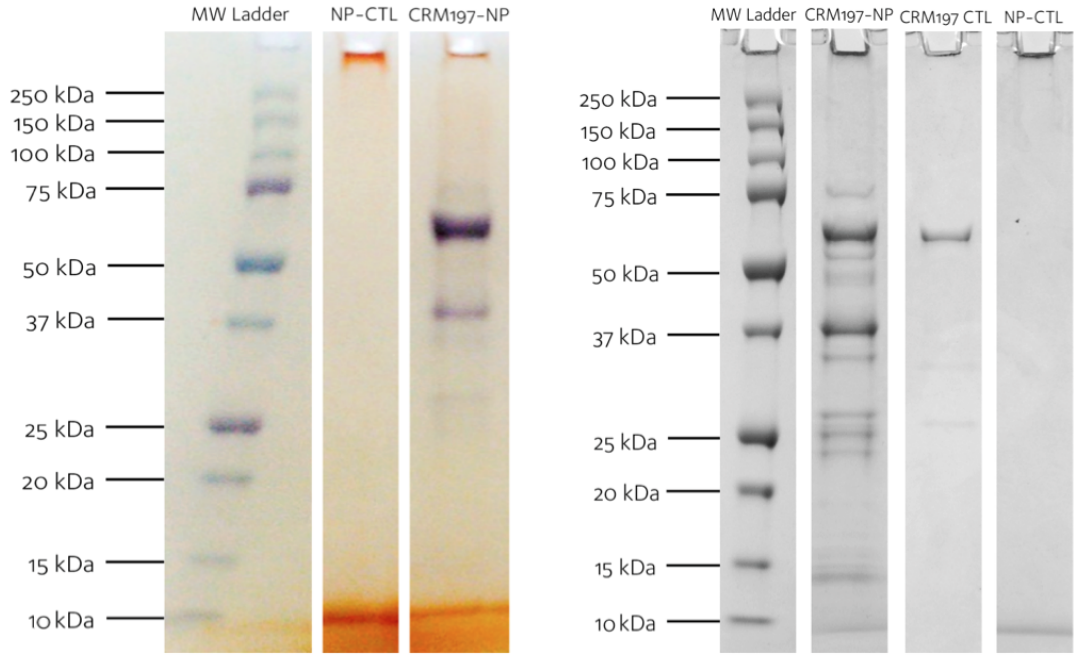


Figure 5.4: SDS-PAGE of CRM_{197}-conjugated NPs: a) The combination of the standard coomassie blue stain and an iodine PEG-stain provides a visual indicator of whether a band comprises of PEG (orange), CRM_{197} (blue), or PEG-CRM_{197} (brown/purple). b) Quantitative evaluation of NP-CRM_{197}-conjugation was performed on grey-scale images. A higher concentration of CRM_{197}-NP was used in subfigure b) than in a). CRM_{197} stock and pure NP samples were run as control (CTL) to CRM_{197}-conjugated NP on precast Tris-Glycine gels (4%-20%) and related to a BioRad Precision MW standard ladder (kDa sizes indicated). Bands were stained with coomassie and iodine.

Table 5.2: Molecular Weights by SDS-PAGE of NPs, CRM_{197}-conjugated NPs, and CRM_{197} Stock Solution.

Band	MW Standard (kDa)	CRM_{197}-NP (kDa)	CRM_{197} CTL (kDa)	NP CTL (kDa)
1	*outside of standard curve	NA	NA	NA
2	250.2±2.1	75.4±1.6	59.9±1.2	11.1±0.3
3	150.8±1.1	59.6±1.1	33.1±0.4	
4	98.9±0.9	54.3±1.5	25.6±0.2	
5	75.4±0.6	49.1±0.6		
6	50.3±0.9	38.2±0.6		
7	38.2±0.8	34.1±0.3		
8	23.7±0.6	26.4±0.2		
9	19.2±0.3	24.3±0.5		
10	14.3±0.3	22.5±0.2		
11	11.6±0.2	13.6±0.2		
12		9.1±0.2		

co-localised. As evidenced by Figure 5.4 a), there appears to be co-localisation of PEG and CRM_{197} at the top of the well and at 75kDa (Figure 5.4, b). The band at the top of the well that did not enter into the gel may comprise of aggregated CRM_{197} and NPs that were chemically conjugated to CRM_{197}. The band at 75kDa likely consist of CRM_{197}-PEG-b-PS conjugates. However, the chemical conjugation reaction, which is conducted at basic pH and under constant agitation at RT, seems to have partially hydrolysed CRM_{197}. Figure 5.4 b) used a higher CRM_{197}-NP concentration than Figure 5.4 a) and thus has a better contrast than the coloured image. The gel shows 12 distinct bands for the CRM_{197}-reacted NPs. The individual MW of these bands were determined by relation to the MW protein standards and are summarised in Table 5.2. The CRM_{197} control lane showed a monomer band at 59.9kDa in addition to a small amount of degraded protein at 33.1kDa and 25.6kDa (Table 5.2), which correspond to subunit B and the catalytic subunit A respectively. The dark band at the top of the well indicates higher order aggregates, which is in good agreement with the previously presented AF_4 data (chapter 3). CRM_{197} is a single continuous peptide, therefore the presence of two sub-units on a gel represent degradation of the protein and not cleavage of linking disulphides by dithiothreitol (DTT) in the sample buffer. The pure NP control shows a dark band at the top of the well indicating intact NPs. Although nanoparticles do not dissolve in SDS (data not shown), the presence of the electric field during SDS-PAGE pulled-apart some of the nanoparticles. Individual amphiphilic block copolymer chains have a theoretical size of 6.6kDa, but the band appears at 9.1kDa. This discrepancy can be reconciled by the fact that proteins and polymers do not necessarily move through the SDS-PAGE gel at the same rate, and the bands are related to the MW protein standards. The bands that are below 25kDa in the NP-CRM_{197}-lane and that are not explained by the controls, are likely hydrolysis products (Figure 5.5). The well-visible band that is present at about 75.4kDa can only correspond to the

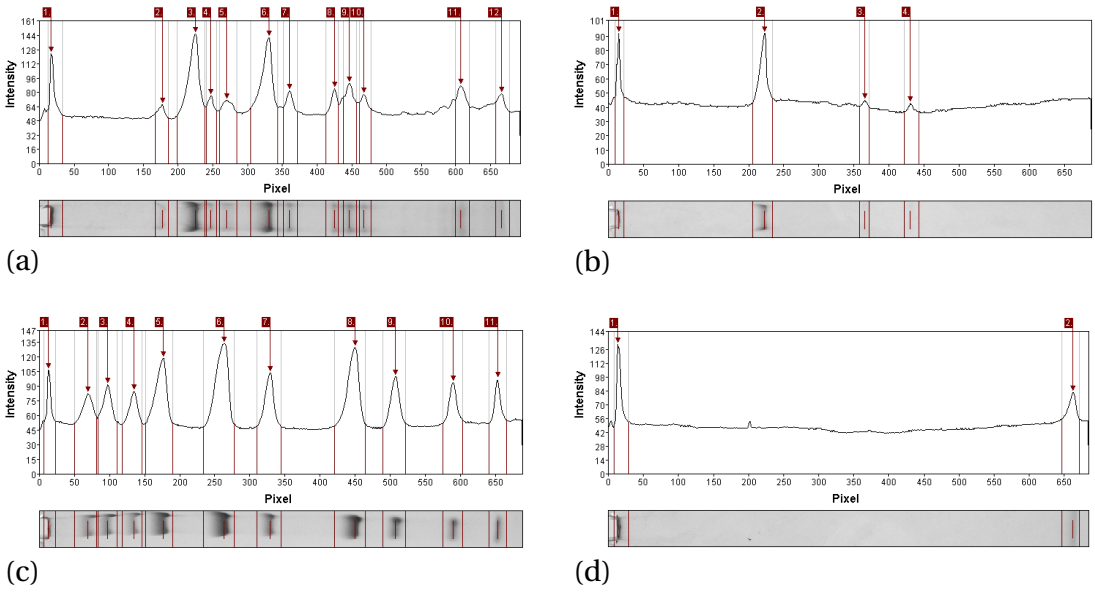


Figure 5.5: SDS-PAGE Quantitive Analysis of CRM_{197}-NP: MW band intensity analysis on SDS-PAGE lanes was conducted using GelAnalyzer2010a software. Data were baselined to the gel background, and band intensity peaks were integrated over the indicated band regions. Band regions are displayed for a) CRM_{197}-NP , b) CRM_{197} control, c) the MW standard ladder, and d) pure NPs control. Samples were run in triplicate.

PEG-CRM_{197} conjugate. As the polymer chain has a size of 9.1kDa on this gel, it appears likely that multiple chains may link to the monomer (75.4kDa), the B-subunit (49.1kDa), and the A-subunit (38.2kDa). The substitution therefore seems to range between 1 and 2 PEG-b-PS chains per subunit and intact CRM_{197} molecule.

To determine the relative concentrations of conjugated-to-free protein content in the NP-CRM_{197} well, and the amount of hydrolysis products, the relative intensities of the individual bands were compared (Figure 5.5). While the monomer accounted for 63.7% of the total intensity in the CRM_{197} control lane, an average of 5.1% and 6.7% were due to fragment B and fragment A respectively, and an average of 24.4% due to higher order molecular weight aggregates. For the NPs, 63.1% of the average total colour intensity was at the top of the well, while 36.9% was at 9.1kDa. This suggests that NPs are at least partially pulled apart during SDS-PAGE,

probably due to the presence of the electric field. Therefore, any CRM_{197} that is conjugated to NPs, would not enter into the gel but remain at the top of the well. Thus only CRM_{197} that was unconjugated or conjugated to the fraction of NPs that dissolved during SDS-PAGE is accounted for in the lower part of the lane. For the NP-CRM_{197} lane, 36.5% of the intensity was found at 59.6kDa, which suggests that a fraction the protein did not react, but was surface bound, or generally could not be removed from the product after the NP-CRM_{197} reaction. Only 3.4% of the intensity is accounted for by the 75.4kDa band, which suggests that only a small amount of intact CRM_{197} is chemically conjugated to PEG-b-PS chains. The second largest intensity in the lane with an average 32.4% relative intensity is at 38.2kDa. This indicates that at least one-third of CRM_{197} (that is not conjugated to intact NPs) hydrolysed during the reaction. Lower MW bands had intensities between 2%–5%, which suggests that the A and B subunits were further hydrolysed. To what extent some of these fractions were conjugated to PEG-b-PS, and whether chemical conjugation of CRM_{197} to PEG-b-PS may have increased the rate of hydrolysis could not be determined from the data.

5.2.3 NP in SFD Powder

Due to the comparatively low CRM_{197}-loading of NPs, the required antigen payload for immunisation had to be composed of NP-bound CRM_{197} and of free CRM_{197} suspended together in the same TMDD excipient matrix. Interestingly, the addition of the PEG(5k)-b-PS(1.6k)-shell and PS(1.5K)-core NPs reduced their porosity and thus improved both ρ_{tap} and ρ_{He} of the TMDD microparticles after SFD (Table 5.4) relative to TMDD formulations without NPs (Table 3.1). Due to similar mean particle D(v, 0.5) diameter and span, the impact parameter of NP-loaded TMDD microparticles was greater than those of pure TMDD microparticles (Table 3.1). The

addition of NPs did not markedly change the residual moisture content of the powder, but decreased T_g' of the freeze-concentrate and raised the T_g of the dry-powder formulation (Table 5.3). As previously discussed in Chapter 3, the morphologies of TMDD-NP microparticles show a wrinkled and spherical morphology, which is indicative of plastic flow compaction during primary drying. However, although there is little difference between the pure TMDD and NP-containing TMDD microparticles at low magnifications (100x), higher magnifications show a rough surface texture of the NP-containing TMDD (Figure 5.6). Upon closer inspection, individual small particles can be seen on the TMDD-NP surface. These small particles are likely individual PEG(5k)-b-PS(1.6k)-PS(1.5K) NPs.

Table 5.3: Physical Characteristics of TMDD-NP Powder Prepared by SFD.

Formulations	Solid content (% wt.)	CRM_{197} content	Size distribution D(v, 0.5) (μm), (Span)	He-Pycnometry (g/cm^3)	Tapped Density (g/cm^3)	Porosity (%)	Impact parameter ρvr (kg/ms)
TMDD-NP (3:3:3:1)	30% wt.	0.02g in 1g	46.54 (1.23)	1.545±1%	0.571±0.027	63.1	9.97
TMDD-NP-CRM	30% wt.	0.02g in 1g	50.5 (1.11)	1.642±1%	0.534±0.035	67.5	10.11

Table 5.4: Thermal Analysis of NP-Formulations: Glass transition, heat capacity change, and residual moisture.

Formulations	Solid content (% wt.)	CRM_{197} content	Residual Moisture (% w/w)	T_g' (°C)	ΔC_p' (J/g°C)	T_g (°C)	ΔC_p (J/g°C)
TMDD-NP (3:3:3:1)	30% wt.	0.02g in 1g	1.83±0.42	-31.12±0.18	0.747	48.20±0.31	0.821
TMDD-NP-CRM	30% wt.	0.02g in 1g	2.10±0.39	-30.51±0.15	0.815	41.19±0.27	0.846

5.2.4 Structural Analysis of CRM_{197} on NPs

According to Crane et al. (1997), CRM_{197} assumes an open conformation at neutral (and acidic) pH, while at basic pH it assumes a closed conformation. When Hib-PRP (polyribosylribitol phosphate) is attached to lysines on CRM_{197} (avg. 3-PRP per CRM_{197} molecule) a shift to longer wavelength for the tryptophan emissions occurs (from 333-334nm to 335-337nm at pH6.8) [Crane et al. (1997)]. Since PRP

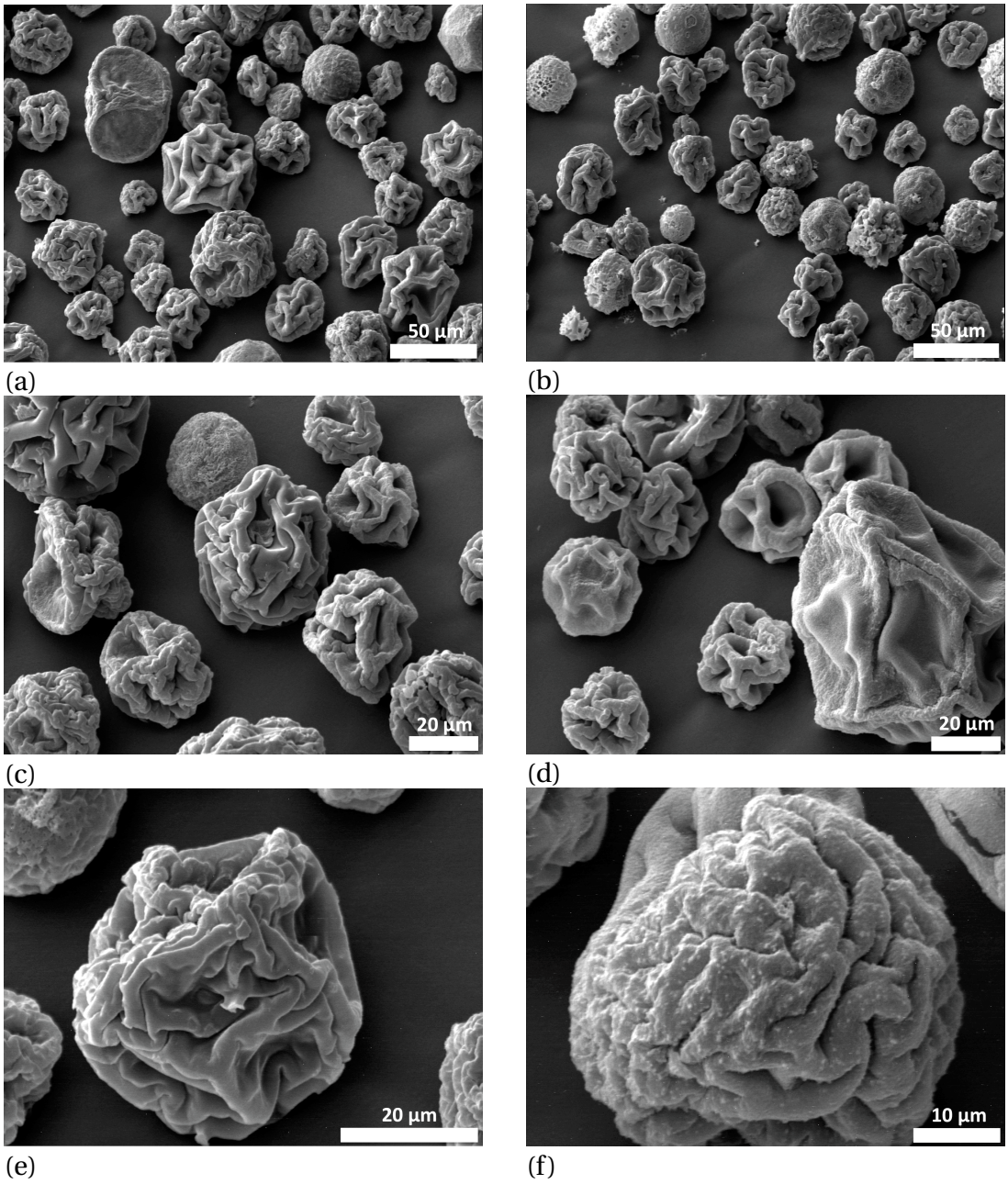


Figure 5.6: NP-loaded TMDD particles manufactured by SFD: SEM images of formulations with 30% wt TMDD or 30% wt TMDD-NP (1%wt NP) in 10mM K_2HPO_4 without CRM_{197}, sprayed into LN_2 using a 48kHz ultrasound nozzle at 3.6W followed by lyophilisation (1° drying at -10°C, and 2° drying at 20°C). a, c, e) TMDD particles at 500x, 1000x, and 3000x magnification. b, d, f) SEM of TMDD-NP at 500x, 1000x, and 4000x magnification.

is negatively charged, the observed shift may also be due to a pKa change of lysine groups after reductive amination. Due to the similar conjugation mechanism of PEG-b-PS to CRM_{197} the tertiary structure may be similarly affected. When conjugated to NPs, the TRP-emission maximum is red-shifted by 1nm (Table 5.5). The shift may be due to the difference in charge between PEG-b-PS (non-polar) and the anionic PRP, or possibly an effect of low concentration of PEG-b-PS-CRM_{197} to native state CRM_{197}. With similar considerations, FTIR spectra of the NP-bound CRM_{197} amide I band was deconvoluted using Lorenzian peak fitting according to the method described by Vonhoff et al. (2010). The results suggest an average 2% decrease in α-helix at only a minimal increase of 0.2% in intermolecular β-sheet content (Table 5.5). Intramolecular β-sheet increased by 6% on average. The observed changes in secondary structure could suggest that CRM_{197} adsorbs to the surface of NPs, perhaps in addition to chemical conjugation. This possibility may partially explain the presence of the strong monomer (59.6kDa±1.1kDa) band in SDS-PAGE gels even after thorough washing of the NP-CRM_{197} constructs. The measured difference between native and NP-bound CRM_{197} may be affected by relative concentrations of any remaining free CRM_{197} and surface-adsorbed CRM_{197} in the washed NP-CRM_{197} sample.

Table 5.5: Secondary and Tertiary Structure of CRM_{197} in the NP-conjugated State Assessed by FTIR, Deconvoluted and Peak-fitted.

	α-Helix (%)	Intra β-Sheet (%)	Turns (%)	Random Coil (%)	Inter β-Sheet (%)	TRP Emission$_{\alpha=295}$ (nm)
CRM_{197} on NPs	30.3±1.8	40.1±3.7	7.4±0.8	22.0±0.9	0.2±0.1	335 ± 0.5
CRM_{197} in PBS	32.3±0.5	34.2±1.2	8.2±0.7	25.3±1.8	0.0±0.0	334 ± 0.5
XRD[Bell and Eisenberg (1997)]	34	24	14	28	0	NA

5.3 CHAPTER SUMMARY

In chapter 5, a design space for functionalised PEG-b-PS nanoparticles was defined by DOE. The minimum diameter size that could be achieved was 55.4nm (10mg/mL

PS and 20mg/mL PEG), while the maximum size was 514.9nm (50mg/mL PS and 10mg/mL PEG). However, at the extreme values, the polydispersity of the respective nanoparticle batch was relatively high, suggesting the presence of micelles or aggregates for batches with small and large mean diameters respectively. Near monodispersity of nanoparticles (PDI $\approx$ 0.15) was achieved for particles between sizes of 100nm and 200nm. For a particle size of 185.1nm the model was 6.7% accurate with a reproducibility of $\pm$1.8nm. CRM_{197} conjugation to 75% functionalised PEG(5k) chains terminated with para-nitrophenol resulted in a 10.2%$\pm$3.1% by weight CRM_{197} loading on nanoparticles. Therefore, 10% of the total NP-CRM_{197} mass is CRM_{197}. However, the elevated pH that is used to increase the reaction speed of pNP-to-primary amine, resulted in increased chemical degradation of CRM_{197}. According to SDS-PAGE, of the CRM_{197}-conjugated NPs that dissolved during SDS-PAGE and did not get stuck at the top of the well, only 3.4% of intact CRM_{197} was covalently conjugated to PEG-b-PS. While the conjugation efficiency is low, different linking chemistry could be used in future experiments that would make the reaction more stoichiometric. A good alternative to pNP would be click-chemistry. About one third (32.4%) of CRM_{197} was present at 38.2kDa, a size that corresponds to the CRM_{197} subunit A with a double substitution of the PEG-b-PS chain. This may indicate that chemical conjugation of PEG-b-PS to CRM_{197} could increase its susceptibility to chemical degradation under these solution conditions.

The incorporation of NPs into 30% wt TMDD powders manufactured by SFD resulted in dry-powder with a similar diameter and span as 30% wt TMDD without NPs. However, the incorporation of NPs raised the dry-powder T_g by about 1°C, and decreased T_g' by about 1°C, at similar residual moisture contents relative to pure TMDD particles. The tapped density of TMDD-NP was higher compared to TMDD, and therefore the NP-loaded formulation had a reduced porosity and a

higher impact parameter. The structural retention of CRM_{197} on the surface of NPs, after removal of reaction byproducts, showed a 2% loss of α-helix, a 6% increase in intramolecular β-sheet, and only a minimal increase by 0.2% in intermolecular β-sheet on average. This suggests that CRM_{197} conjugation to PEG-b-PS chains on NPs induces some intramolecular deformations, but only little intermolecular association. Another argument in favour of only small structural changes is the red-shift of CRM_{197}'s tryptophan groups by merely 1nm. The magnitude and direction of this shift has also been observed after PRP polysaccharide conjugation [Crane et al. (1997)]. Given the structural integrity of CRM_{197} on the final NP-CRM_{197} construct, once reaction byproducts have been removed, and the well controllable NP manufacture process, the TMDD-NP formulation met the requirements for immunogenicity evaluation *in vivo* (Chapter 6).

CHAPTER 6

PARTICLE INJECTION AND IMMUNOGENICITY OF CRM_{197} FORMULATIONS

Chapter 6 analyses the penetration depth of particles when injected into murine skin and agar gels, and suggests a different approach to describe and predict particle location compared to previous models. Subsequently, the immunogenicity of dry-powder CRM_{197} formulations that were presented in the preceding chapters (3, 4, 5) is discussed based on the analysis of IgG and IgG subclass titres.

6.1 INTRODUCTION

Some of the key advantages of needle-free intradermal injection over conventional HNS rely on the precise targeting of the epidermal skin layer [Burkoth et al. (1999); Kendall et al. (2007); Dean et al. (2003)]. To date, only Kendall et al have proposed an analytical model that relates particle parameters and physical properties of the skin to particle penetration depth [Kendall et al. (2004a); Guha et al. (2010)]. Al-

beit greatly simplified, the Kendall model provides a good guideline for the physical properties of successful therapeutic IPI particles [Guha et al. (2010)]. However, the studies that showed agreement with the model used semi-empirical yield-stress values to fit the model and were substantially higher than the *sc* yield stresses determined by other groups [Mitchell et al. (2003); Kendall et al. (2004a); Wildnauer et al. (1971)]. Additionally, the large variation between the experimental data and the model raise the question of its predictive validity. A more accurate approach to ballistic injection modelling has recently been suggested by Guha et al. (2010), and uses a computational finite element model based on the Ogden strain energy function. This model's superior performance is attributed to the fact that it can better account for the complex structure of the skin, and the deformations of the particle during impact. However, computation times ranged from 5.5 to 56.5 hours, and like the Kendall model, the parameters were adjusted to fit published and observed penetration data [Guha et al. (2010)]. This raises the question whether there is a different way to look at particle injection modelling into the skin altogether that may be simple but also accurate. This chapter explores the possibility of a probabilistic description of particle penetration based on population distribution functions as supposed to a deterministic view that aims to predict the exact location in the skin.

Ultimately, the magnitude and quality of the elicited immune response *in vivo* determines the clinical value of a vaccine formulation and inoculation method. Although several studies on needle-free powder injection with protein-containing vaccines have been published, only nine different antigens were tested, with only three types of adjuvants (alum, CpG motifs, and enterotoxins), and all tested formulations were saccharide-based and therefore had a bolus-type dose delivery [Weissmueller et al. (2013)]. Except for CpG oilgodeoxynucleotides, adjuvantation further increased IPI's characteristic Th2 bias. However, some recent publications have

demonstrated the advantages of surface-bound antigen, which included a more balanced Th1/Th2 immune response [Moon et al. (2011, 2012)]. The aim of this dissertation was, in addition to formulating CRM_{197} as dry-powder for needle-free injection, to assess the impact on the nature and magnitude of the immune response when CRM_{197} was structurally immobilised on microparticles as well as on nanoparticles. While immunisation with CRM_{197} alone is not of direct clinical applicability, the use of the CRM_{197} protein in this body of work presents a good model to probe the capability of the various formulations. Among others, Hib, pneumococcal and meningococcal vaccines contain oligosaccharides that are covalently linked to CRM_{197} [Shinefield (2010)]. From a formulation standpoint, the structural preservation of CRM_{197} is the most challenging component of the vaccine during reformulation; as it is the protein that likely denatures [Peters et al. (1996)]. In the previous chapters, FT-IR or AF4 results suggested that the structure of CRM_{197} was sufficiently preserved to warrant *in vivo* testing.

6.2 Results and Discussion

6.2.1 Particle Penetration- Comparison of Three Particle Types in Agar and Murine Pinna

Although agar gels lack the complex composite structure of the dermis, they provide a highly reproducible model that can be tailored to have a similar mechanical bulk density as human skin by adjusting the agar concentration. Based on findings by Chen et al. (2004b) and Schiffter et al. (2010), 3% wt agar gels most closely model skin. However, agar gels are a relatively homogenous mass that comprises of 97% water, whereas the mechanical properties and structures of the dermal layers are

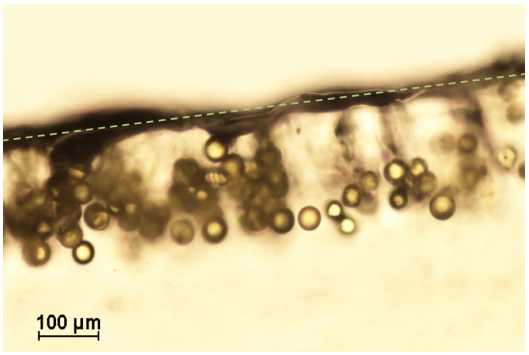
complex and highly variable. Therefore, the TMDD and kHA particles were tested in agar and in murine skin prior to *in vivo* studies and their relative penetration potential was juxtaposed. Injection depths of these particle types were compared to those of monodisperse polystyrene spheres to investigate the effect of particle heterogeneity. Pure TMDD particles, when injected into agar, dissolved completely which made accurate assessment of the penetration depth difficult. Therefore, carbon powder was loaded into TMDD particles, which left a black trace in the gel and a depot of carbon where the particles finally came to rest and dissolved.

Table 6.1: Particle Penetration Study in Agar and Murine Skin.

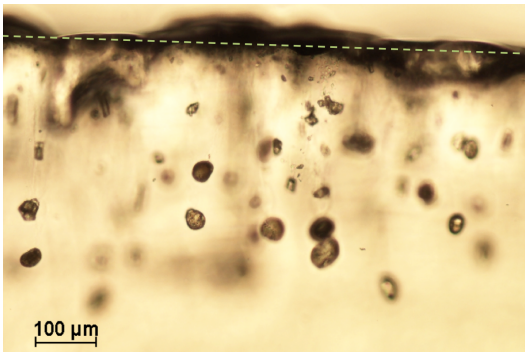
Particle Type	D(v,0.5) (μm), (Span)	He-Pycnometry (g/cm^3)	Tapped Density (g/cm^3)	Impact parameter ρvr (kg/ms)	Mean Penetration Depth Agar (μm) (StDev)	Mean Penetration Depth Skin (Pinna) (μm) (StDev)	Scaling Factor between Agar/Skin
Polystyrene	41.4, (0.26)	1.07±1%	0.94±0.13	13.6	173.7 (51.1)	42.1 (14.1)	4.1
kHA (1:6)	39.8, (1.32)	3.01±1%	2.81±0.15	39.1	205.5 (100.2)	41.7 (26.0)	4.9
TMDD-Carbon	51.16, (0.97)	1.49±1%	0.53±0.09	9.5	124.5 (43.5)	23.9 (8.2)	5.2

The mean particle diameters were similar but the span varied with polystyrene spheres being essentially most monodisperse, followed by TMDD-carbon, and then kHA particles being more polydisperse respectively (Table 6.1). The impact parameter suggests that kHA would penetrate deepest into agar and tissue, followed by polystyrene and then TMDD-carbon, which had a comparable density to NP-loaded TMDD microparticles. Injection depth measurements in agar confirmed this trend (Figure 6.1). However, there was not a clear correlation between particle size distribution and penetration depth variation. Polystyrene spheres, although very monodisperse, had a larger standard deviation in particle penetration than TMDD-carbon, both in agar and in skin. Possibly, mean penetration distance may affect the standard deviation.

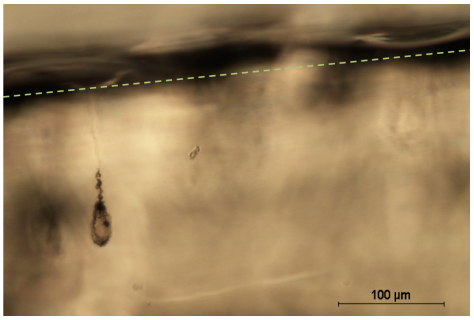
A comparison of mean penetration depths in agar suggests a ranking of kHA, PS, and TMDD from deepest to shallowest, while in skin the order was PS, kHA, TMDD.



(a)



(b)



(c)

Figure 6.1: Particle penetration into Agarose Gel: Agar 3% wt gels were injected with 0.25mg of particles at 60bar gas pressure. Gels were immediately sectioned and imaged. Particle penetration depth was measured in ImageJ as distance between the top of the agar and the location on a particle deepest in the gel. Measurements were related to a calibrated size scale. The dashed line (green) served as reference for penetration depth measurements and indicates the agar-to-air surface. Panels show penetration patterns into 3% agar for a) polystyrene spheres, b) kHA (1:6) bioceramic particles, and c) TMDD-Carbon particles manufactured by SFD, with the respective physical characteristics as described in Table 6.1.

Although PS particles penetrated deepest into skin on average, it was observed that some particles came to rest at the upper part of the gel or skin, which increased the standard deviation. Interestingly, while the mean penetration depths were different between all particles in agar ($p<0.001$), there was no difference between kHA and PS spheres in skin (Table 6.1). One possible explanation is that the dermal layer below the epidermis is more resistant to penetration and decelerates particles strongly once they reach a certain depth in the tissue. For the investigated particles, penetration depth in agar was approximately 4-to-5-fold higher than in skin. Since the bulk

density of agar and skin was approximately matched, the observed difference in particle penetration may be due to a different yield stress, and due to the highly complex composite structure of the skin and its other varying mechanical properties. However, histology analysis showed that all particle types successfully breeched the *sc* and targeted the epidermis and upper parts of the dermis.

6.2.2 Intradermal Particle Placement by Injection-site Location

A second dermal particle penetration study in a murine model was conducted to determine an injection location that achieved preferential targeting of the epidermis (Table 6.2). For this, histology samples were taken from the injection sites on the ear, abdomen, and base of tail (BOT) after needle-free injection to assess the thickness of the dermal layers, as well as the penetration depth of the kHA microparticles using microscopy (Figure 6.2). One-way ANOVA on histology measurements suggests that the thickness of the *ved* varied significantly ($p < 0.001$) between inoculation locations.

Table 6.2: Microscopy measurements on histology describing kHA powder placement in the skin and dermal dimensions.

Location	Viable Epidermal Thickness (μm), (Obs)	*Stratum Corneum* Thickness (μm), (Obs)	Particle Penetration Depth (μm), (Obs)
Pinna	36.3 ± 8.1, (135)	16.2 ± 5.9, (148)	53.7 ± 19.2, (69)
Abdomen	22.5 ± 5.2, (162)	6.6 ± 2.7, (161)	46.3 ± 19.2, (195)
Base of Tail	20.1 ± 9.8, (157)	9.9 ± 5.5, (187)	44.4 ± 19.0, (178)

The greatest *ved* mean thickness was observed for the pinna (36.3 μm), while mean *ved* thickness for abdomen and BOT ranged between 20.1 – 22.5 μm. The *sc* also had significantly different thicknesses ($p < 0.001$) at the various injection sites. The mean particle penetration depth (MPD) was significantly different ($p < 0.01$) between the three injection sites. The MPD was not different between abdomen

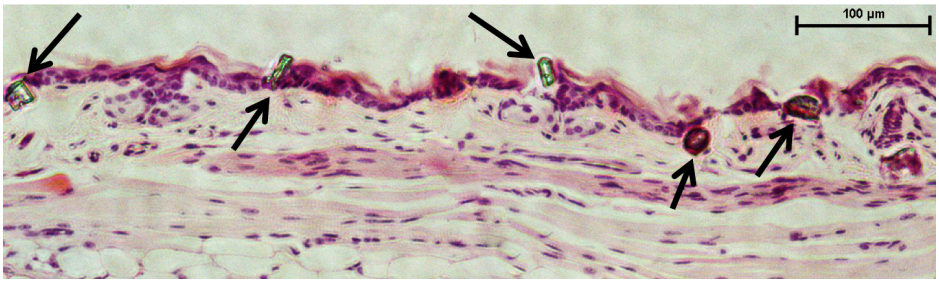


Figure 6.2: kHA Particle Injection into Murine Pinna: Microscopy slides of sectioned H&E histology were imaged with a Nikon Eclipse Ti microscope and analysed using ImageJ. Measurements of particle penetration depth were made according to Figure 2.7. kHA particles are indicated by arrows.

and BOT ($p > 0.05$). Co-localisation of particles with the epidermis is best when MPD approximates *sc* + *ved* (Figure 2.7). The best co-localisation of HA particles within the viable epidermis was observed for pinna injections with MPD = 53.7 μ ± 19.2 μ and *sc* + *ved* = 52.5 μ ± 14.0 μ (Table 6.2). MPD exceeded the *sc* + *ved* threshold at both other injection sites. Therefore, the dry-powder vaccine was injected needle-free into the pinna in the subsequent immunogenicity study.

Needle-free powder delivery to the optimal dermal layer reportedly presents a challenge in part due to highly variable skin characteristics [Kendall et al. (2004a,c)]. Previous ballistic delivery studies have emphasised the influence of *ved* and *sc* thickness on particle penetration depth, with an increase in layer thickness translating to reduced penetration into the skin [Kendall et al. (2007)]. In this study, we did not observe this effect on kHA penetration depth. A possible reason for this may be the varied kHA particle shape factor (spheroidal to prismatic) that could influence penetration properties. However, the thicker *sc* and *ved* layers in the pinna allowed for good co-localisation of kHA particles with the epidermis, whereas particles penetrated too deep at the other injection sites. Interestingly, while differences in *ved* and *sc* thickness are thought to also impact the particle distribution in the dermis, the obtained results show an almost identical variance about the mean despite sig-

nificantly different *ved* and *sc* dimensions (Table 6.2). This suggests that while *ved* and *sc* thickness can impact the eventual powder penetration depth, they may contribute less to the particle distribution in the skin than the underlying particle characteristics, the injection device, and the propulsion pressure.

6.2.3 Novel Approach to Injection Depth Modelling for Ballistic Particle Injection

The appeal of previous ballistic particle injection models, such as the Kendall or Ogden model for example, is the precise localisation of a particle in the skin based on various physical properties of the skin and the particle. However, this deterministic approach also invites large model variability. Given the inherently high variability of both particles and skin, the error between a model that is based on average values and actual experimental observation is substantial [Kendall et al. (2004c)]. A computational illustration of the Kendal model was based on their derived integrated equation:

$$D_{skin} = \frac{4\rho_p r_p}{3\rho_{sc}} \left\{ ln(\frac{1}{2}\rho_{sc} v_i^2 + 3\sigma_{sc}) - (3\sigma_t) \right\} \tag{6.1}$$

Model parameters were used as described by Kendall et al. (2004c). The penetration depths of particles as predicted by the Kendal model for different particle radii and densities is depicted in Figure 6.3 a) and b). Each point on the surface plot corresponds to one combination of particle radius and density for fixed skin parameters at a constant particle velocity of 650m/s.

Unlike TMDD and PS spheres, kHA did not dissolve during histology sample preparation and therefore the particle radius could be measured in histology sections and related to the penetration depth. Figure 6.3 overlays the Kendal model prediction of penetration depth with the observed penetration depths of kHA parti-

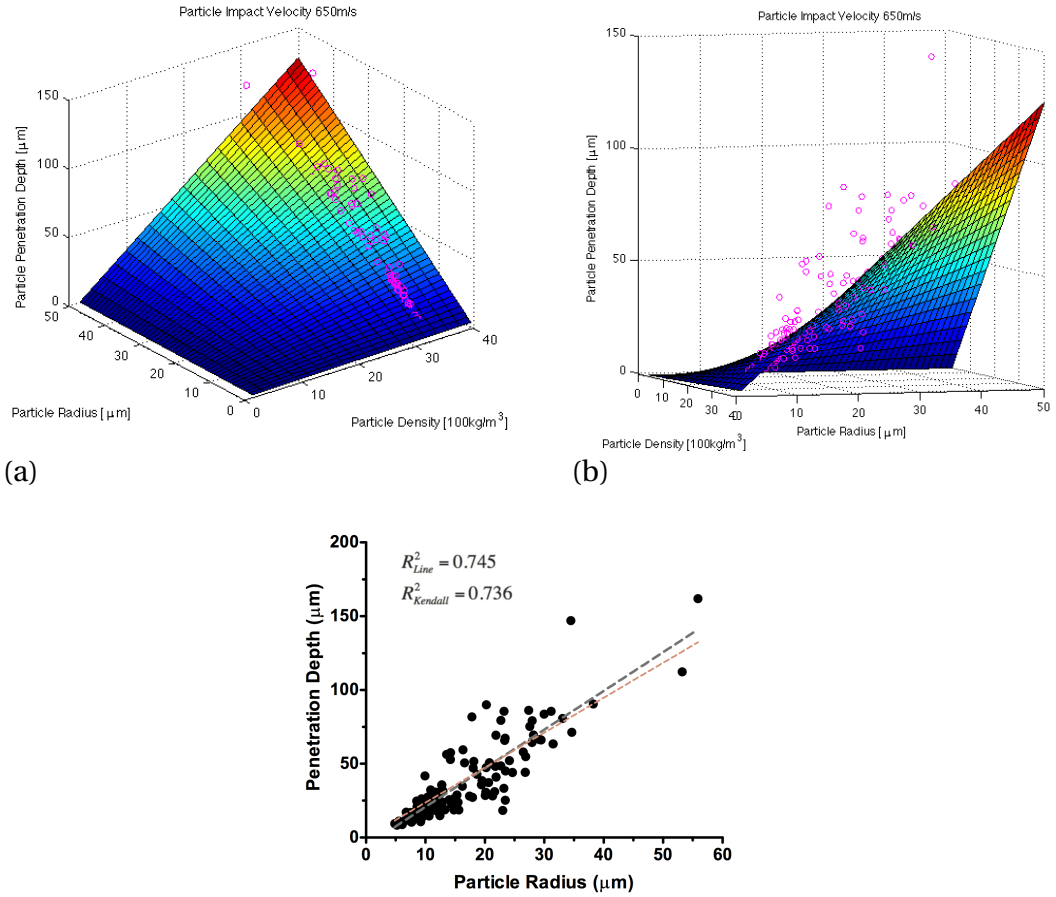
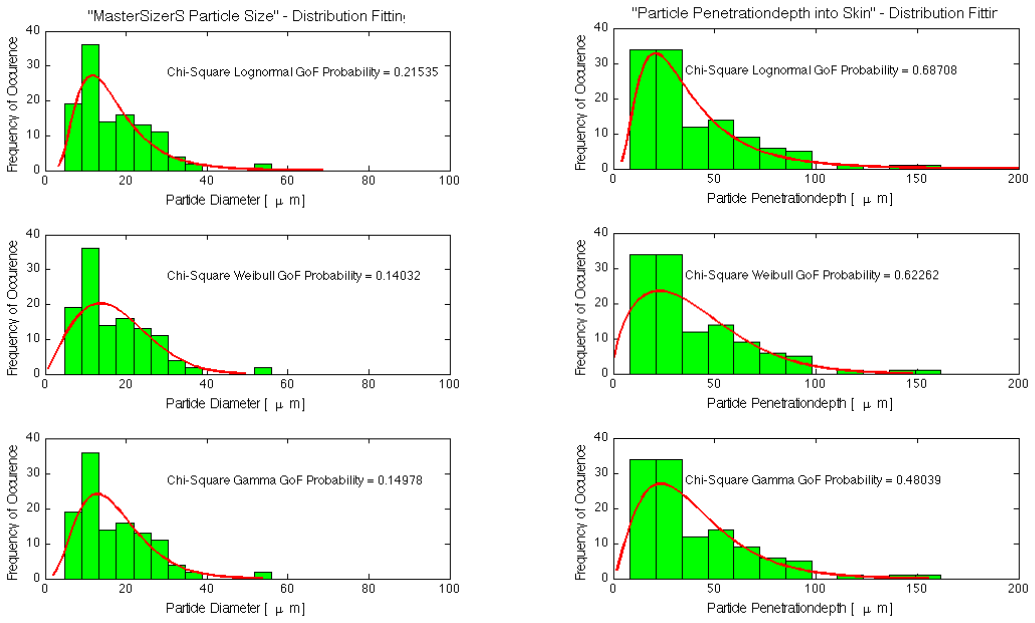


Figure 6.3: Kendall Model Fit to kHA Particles Injection Depth:
a, b) This MATLAB® model displays the predicted penetration depth space in skin as function of the particle radius and density based on the Kendall equation 6.1, and overlaid with experimental data using kHA particles (pink circles). Model values were: impact velocity of particle ($v_i = 650 m/s$), *sc* density ($\rho_{sc} = 1500 kg/m^3$), *sc* yield stress ($\sigma_{sc} = 40 GPa$), and are based on Kendall et al. (2004c). c) Shows the correlation between the Kendall model (orange line) and an unconstrained line equation (grey line) with experimental data of kHA particles injected into the murine pinna, assuming a constant particle density (3.2 g/cm^3).



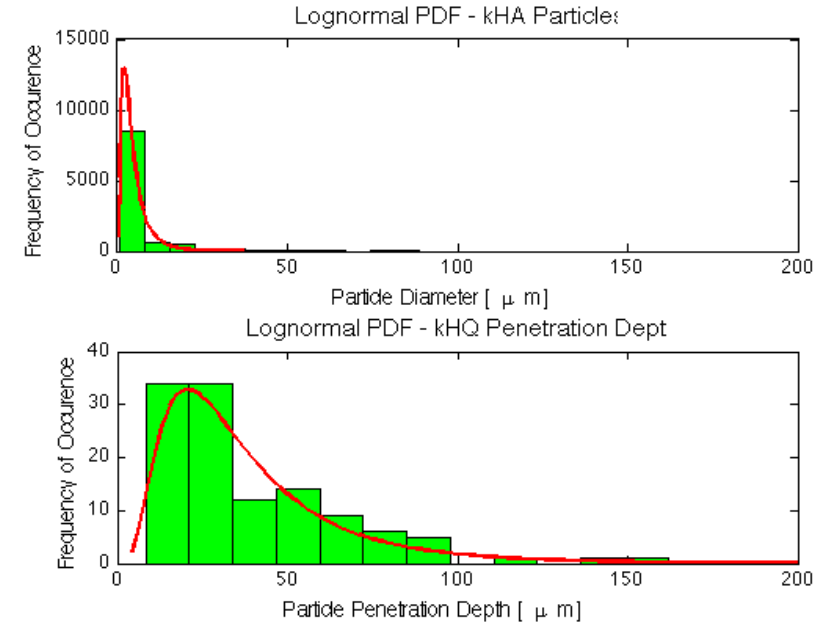
(a) (b)

Figure 6.4: Chi-square Goodness-of-fit Test on kHA Particle Size and Penetration Depth Data: Log-normal, Weibull, and Gamma distributions were fit to a) particle size, and b) particle penetration depth data using the MATLAB® functions 'lognfit(x)', 'wblfit(x)', and 'gamfit(x)'. Chi-square goodness-of-fit test in MATLAB® ('chi2gof(x)') was then applied to determine which distribution was a best fit.

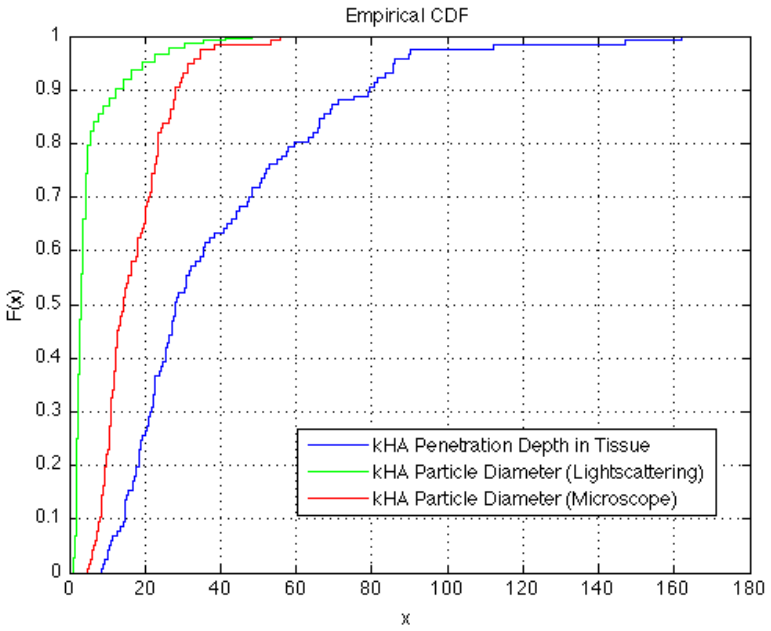
cles (empty pink circles) as function of their radius. It is apparent from visual inspection that the model only roughly describes kHA placement in the skin and that the model better approximates particle penetration depth for small particle radii than large. For a given particle density, velocity and physical properties of the skin, the Kendall model is directly proportional to the particle radius and can be described by a simple line equation: $f(x) = ax + b$. The correlation between the Kendall model and the actual kHA penetration depth values is poor with a correlation of R^2=0.745. In fact, when the individual parameters for skin properties identified by Kendall et al. (2004c) were used instead of a regression onto a simple line function, the correlation decreased to R^2=0.736 (Figure 6.3 c, orange line).

Instead of using a deterministic approach that describes each particle individually, perhaps it would be better to use a probabilistic approach that describes the particle and penetration depth population. By using probability density functions one may be able to account for part of the variability in the particle population and in the eventual penetration depth distribution. Although the 'resolution' of the result may be reduced to a percentage that describes the probability to observe a fraction of particles at a depth x in the skin, this information is sufficient to determine payload deposition. However, for this model to work, there needs to be a good correlation between the particle size distribution and the penetration depth distribution in the skin. The first step therefore is the determination of the probability density function that best approximates both particle size distribution and particle penetration depth distribution. According to a goodness of fit analysis conducted with MATLAB®, the distribution that best described both populations is the log-normal distribution (Figure 6.4), with 21.5% and 68.7% respectively. Unsurprisingly, this distribution describes many physical characteristics in biology and nature and most particle distributions [Limpert et al. (2001)]. Due to a low observation count, the absolute goodness-of-fit values are low, but since the observation count is the same across the different distributions, the assessment of the relative performance of the various distributions is valid.

It should be remarked that the abscissa of both subgraphs of Figure 6.5 a) are of the same property, namely length in μm, but describe different characteristics: mean kHA particle diameter in the upper section of subfigure a) and the penetration depth of kHA into murine skin in the lower section. It is apparent, that the conversion between these two log-normal probability density functions involves a shift in the distribution mean (μ) towards larger ordinate values, and an increase in standard deviation (σ). It should be noted here, that the shape of a log-normal



(a)



(b)

Figure 6.5: kHA Particle Distribution and Cumulative Density Function: a) Lognormal Density Functions were fitted to kHA particle size and penetration depth into tissue. b) These data and the mean diameter of kHA particles in the skin (measured by microscopy) were plotted as Cumulative Density Distributions using the MATLAB® function 'cdfplot(x)'.

distribution and its location on the ordinate axis are fully defined by the mean and standard deviation of the random variable (X) in question. The probability density function (PDF) for a log-normal distribution of a continuous random variable X is given by:

$$PDF = \begin{cases} f_{X(x;\mu\ \sigma)} = \frac{1}{x\sigma\sqrt{2\pi}} e^{\left(-\frac{(lnx-\mu)}{2\sigma}\right)^2} & \text{if } x > 0 \\ 0 & \text{if } x \leq 0 \end{cases}$$

The area under the PDF between two values (x_1 and x_2) corresponds to the faction of the log-normally distributed population that is flanked by these values. For example, the epidermis was determined to be at a depth between x_1=15μm, and x_2=50μm in the previous section. Integration of the particle penetration depth PDF between these limits corresponds to the percentage of particles that are likely deposited within this section. Therefore, the payload deposition of the vaccine dose within and outside of the epidermis can be determined. An easier way to view cumulative probability, is by integrating the lognormal PDF between 0 and ∞, to arrive at the cumulative distribution function (CDF).

$$CDF = \begin{cases} F_{X(x;\mu\ \sigma)} = \frac{1}{2}\left(1 - erf\left(\frac{\mu - lnx}{\sqrt{2}\sigma}\right)\right) & \text{if } x > 0 \\ 0 & \text{if } x \leq 0 \end{cases}$$

and

$$erf_{(z)} = \frac{2}{\sqrt{\pi}} \int_0^z e^{-t^2}\, dt \tag{6.2}$$

The error function ($erf_{(z)}$) is encountered upon PDF integration. Largely, this function does not have an analytical solution but can be approximated by serial expansion or computationally [Weisstein (2013)]. The CDF for particle diameter distributions prior to injection (green) and after injection (red), and penetration depth

distribution (blue) was computed in MATLAB® (Figure 6.5 b). Firstly, the shift between the green and red CDF at $F_{(x)}$=0, shows that only kHA particles with a size of approximately 6μm or larger penetrated into the skin. Based on the green CDF, only about 30% of all particles in the powder were larger than 6μm. Between the abscissa values corresponding to the previously measured thickness of the epidermis (x_1=15μm, and x_2=50μm), about 65% of the observed particle penetration depth falls within this region. Therefore, only 19.5% of the initial powder formulation was deposited in the epidermis, 1.5% of particles got stuck in the *sc*, and 9% penetrated deeper than the epidermis. Therefore, of the particles that did penetrate the *sc* the large majority targeted the epidermis. This result suggests that kHA particles diameters should range between 6μm and 15μm to reliably target the epidermis in the murine pinna.

Knowing how much of a vaccine dose was deposited at what location in the skin can be critically important, therefore a model that could predict the particle penetration depth (PPD) into the skin based merely on the particle size distribution (PSD) would be of considerable value. Although PPD and PSD both follow a lognormal distribution, a predictive model requires a clear correlation between the two. Theoretically, to transfer the CDF of PSD to the CDF of PPD one can superimpose an intermediate CDF such that:

$$\left(\frac{1}{2}-\frac{1}{\sqrt{\pi}}\int_0^{PSD} e^{-t^2}\,dt\right)+\left(C+A\int_0^{FIT} e^{-Bt^2}\,dt\right)=\left(\frac{1}{2}-\frac{1}{\sqrt{\pi}}\int_0^{PPD} e^{-t^2}\,dt\right) \qquad (6.3)$$

where A, B, C are constants and FIT are the parameters for the translational function. To test if in fact there was such a relationship between PPD (blue) and PSD (green), the horizontal distance (or Δx) between the respective CDFs for a given $F_{(x)}$ on Figure 6.5 b) was measured. The obtained ΔCDF values were then fitted with the function $f(x) = Ae^{-Bx^2} + C$. Figure 6.6 suggests that there is an excellent correlation (R^2=0.984). Therefore, it appears that the kHA particle size CDF and kHA

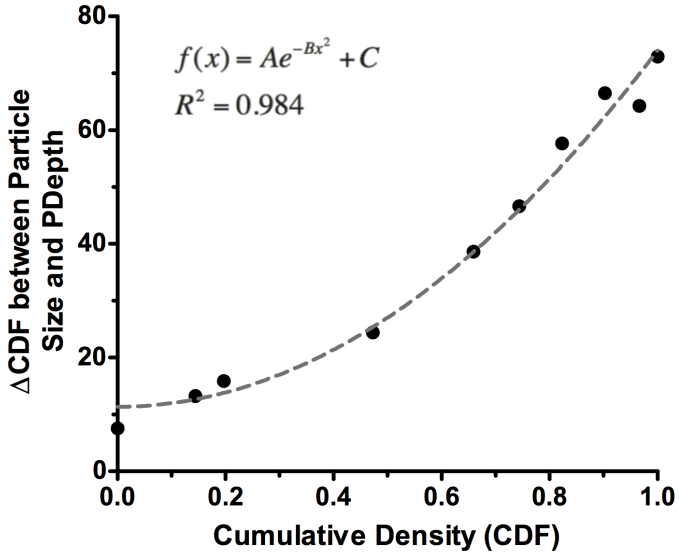


Figure 6.6: Correlation of Particle Size and Penetration Depth by Cumulative Density: The distance between the CDF of particle size distribution (light scattering, green) and the particle penetration depth (blue) (Figure 6.5) is plotted against the respective CDF (for probabilities from 0 to 1), and fitted to function $F(x) = Ae^{-Bx^2} + C$, by minimisation of least squares ($R^2 = 0.984$).

particle penetration depth CDF are strongly correlated, and therefore may be used to predict the particle distribution in the skin based on the particle size distribution.

Similarly to the Kendal model, this approach will likely be affected by the properties of the skin and particle characteristics. To derive value from this model, multiple experiments need to be conducted that correlate the particle size CDF to particle penetration depth CDF, and 'entrain' a correlation matrix of values that can map means and standard deviations between one log-normal to another. Subsequently, these distribution transformation factors maybe correlated by a function, and this function in turn may be used to estimate new transformation factors for particle size distributions that were not used to 'train' the model. However, the creation of such an extensive model did surpass the scope of this dissertation, but may provide inspiration for future work.

6.2.4 Needle-free vaccination: Immunogenicity of CRM_{197}-adsorbed Bioceramic Powders

Pathogen opsonisation, agglutination, and toxin neutralisation is facilitated by the presence of IgG in the serum. It was investigated whether kHA-CRM_{197}, with HA to flux ratio of 1:6, could induce similar IgG levels as the current clinical standard (e.g. alum-CRM_{197}). As depicted in Figure 6.7, anti CRM_{197} serum IgG titres were similar for alum-adsorbed CRM_{197} (Alum) and kHA-adsorbed CRM_{197} (kHA) groups 28 days after prime ($p > 0.05$). The mean titre for kHA needle-free (NF) was significantly higher ($p < 0.001$) than CRM_{197} alone (IM), but alum-adsorbed CRM_{197} was not despite its higher mean titre. This can be explained due to the lower standard deviation in the NF condition.

On day 48, 14 days after the booster dose with the same vaccine formulation and antigen amount respectively, alum-adsorbed CRM_{197} titres were 10-fold higher than in the kHA adsorbed CRM_{197} group, but the difference was not significant ($p > 0.05$). Both alum ($p < 0.05$) and kHA ($p < 0.01$) conditions showed significantly higher mean titres than CRM_{197} control in PBS. An approximate 15-fold increase in mean IgG levels was observed for kHA-CRM_{197}, and a 64-fold increase in the alum adjuvanted CRM_{197} condition between day 28 and 42. These results suggest a trend towards higher mean IgG titres with alum CRM_{197} (IM) compared to kHA-CRM_{197}(NF), but the difference was not statistically significant. Additionally, it was observed that individual kHA-CRM_{197}(NF) titres were grouped closely together around their mean, more so than the individual alum CRM_{197} (IM) group titres. This is also reflected in the smaller standard deviation error bar for kHA-CRM_{197} (NF).

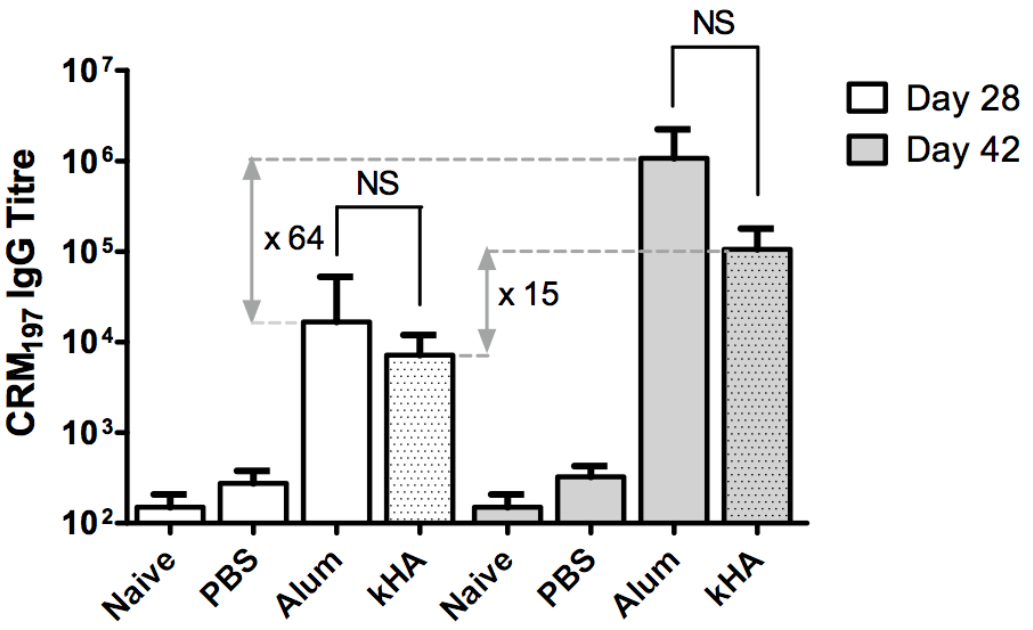


Figure 6.7: kHA-CRM_{197}-Study - IgG Titres: All treatment groups (n = 8) received 10μg CRM_{197} on days 0 (prime) and 28 (boost). Mice were bled on days 28 and 42. Naïve mice served as control group (n = 4). Pre-immunisation titres were less than 200. CRM_{197} adjuvanted with 85μg alum (Alum) and CRM_{197} alone in PBS were injected by IM with HNS (clear bars). kHA-CRM_{197} (kHA 1:6) powder was administered needle-free (dotted bars) into the pinna at 55 bar gas pressure. The mean titre and standard deviation are indicated for all groups. Comparisons of special interest are indicated by top brackets with significance-level as superscript. The mean titre ratio day42/day28 is presented for Alum and kHA groups. ANOVA was conducted at α = 0.05 significance level (* $p < 0.05$, ** $p < 0.01$, *** $p < 0.001$). P-values above that α-level were considered not significant (NS).

6.2.4.1 IgG Subclass Responses

We investigated whether the presentation of CRM_{197} in the kHA (1:6) surface-adsorbed state could influence the Th1/Th2 balance. The control group CRM_{197} in PBS by IM (PBS) showed a small (10-fold) IgG1/IgG2a bias on day 42. (Figure 6.8). The alum adjuvanted (Alum) and needle-free kHA (kHA) groups, on the other hand, showed a 1146-fold and 250-fold IgG1/IgG2a biased response respectively. This result suggests that alum and kHA potentiate a Th2-biased response. Two weeks after the booster dose (day 42), IgG1 and IgG2a mean titres for the alum and needle-

free kHA groups were similar ($p > 0.05$), despite a 10-fold higher IgG1 mean titre (Figure 6.8). As previously seen with IgG, individual kHA titres were more closely grouped around their mean than alum. However, both alum ($p < 0.05$) and kHA ($p < 0.01$) groups induced significantly higher mean titres than CRM_{197} alone. These results suggest that kHA-CRM_{197} induces a Th2 biased response.

The magnitude and quality of the induced immune response can provide insight into the effect of a novel antigen formulation [Plotkin (2010)]. In this study, needle-free immunisation with kHA-CRM_{197} induced significantly higher IgG antibodies 4 weeks after prime and 2 weeks after boost relative to CRM_{197} in PBS delivered by HNS. Furthermore, kHA-CRM_{197} elicited IgG, IgG1, and IgG2a responses that were similar to alum-adjuvanted CRM_{197} by IM. This is a noteworthy result because most needle-free immunisation studies with protein-containing vaccines reported in literature to date have not directly compared the needle-free formulation (e.g. kHA-CRM_{197}) to the clinical-standard adjuvanted protein antigen (e.g. alum CRM_{197}). The most common comparator in past studies has been the protein antigen alone with HNS by IM or SC [Weissmueller et al. (2013)]. Additionally, it has been demonstrated that a similar protein vaccine injected via IM gives a higher antibody response than when injected via SC [Chen et al. (2000)]. That we can match the antibody response achieved with the clinical-standard HNS strategy without the requirement for alum-adjuvantation and HNS with its associated disadvantages (see chapter 1.1), represents an important advance.

While immunisation with CRM_{197} alone is not of direct clinical applicability, the use of the CRM_{197} protein in this study presents a good model to probe the capability of the kHA formulation. Among others, Hib, pneumococcal, and meningococcal vaccines contain oligosaccharides that are covalently linked to CRM_{197} [Bröker et al. (2009)]. *In vivo* and FTIR results suggest that the structure of CRM_{197} was suf-

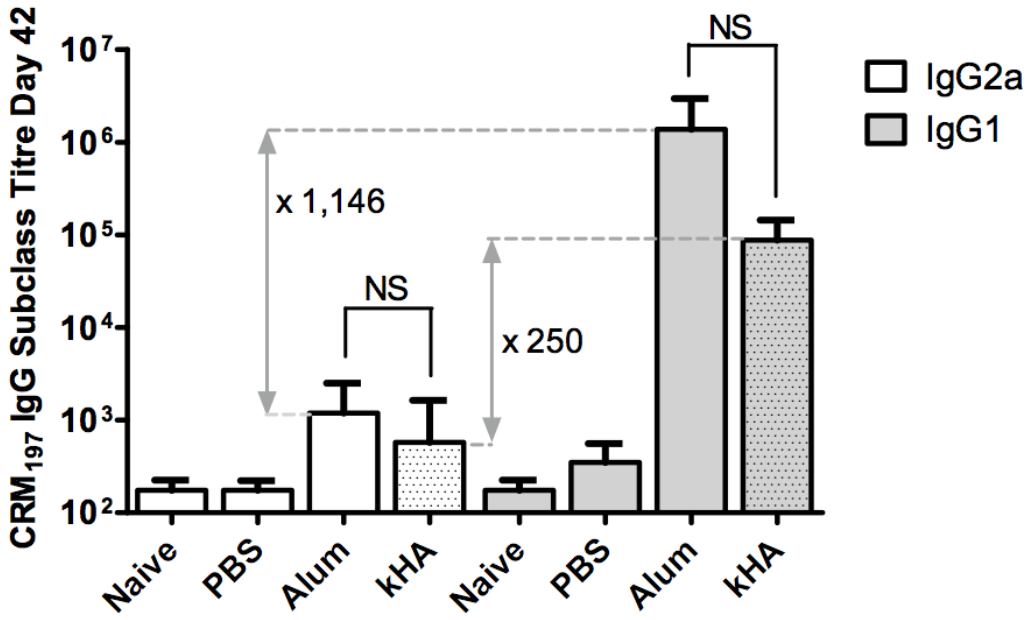


Figure 6.8: kHA-CRM_{197}-Study - IgG Subclass titres: IgG1 and IgG2a titres were determined on day 42 on the same sera as discussed in Figure 6.7. Mean titres are displayed for CRM_{197} in PBS (PBS) and for CRM_{197} adjuvanted with 85μg alum (Alum) injected by IM (clear bars), and for kHA-adsorbed CRM_{197} (kHA) injected needle-free (dotted bars). The mean titre ratio IgG1/IgG2a is indicated for Alum and kHA conditions. Comparisons of special interest are indicated by top brackets with significance-level as superscript. ANOVA was conducted at α = 0.05 significance level (* $p < 0.05$, ** $p < 0.01$, *** $p < 0.001$). P-values above that α-level were considered not significant (NS).

ficiently preserved. In chapter 4.2.4 it was shown that 3% of CRM_{197} is released from kHA *in vitro*, which raised the question of bioavailability for the remaining 97% of the payload. As kHA-CRM_{197} performed comparable to CRM_{197}-alum in a mouse model, it may be concluded that the bioavailability of CRM_{197} on kHA is similar to the bioavailability of CRM_{197}-alum. Since we demonstrated the immunogenicity of the protein carrier with this delivery method, it seems probable that the immunogenicity of complete glycoconjugates may behave similarly. This finding motivates the investigation of the kHA platform as a needle-free delivery vehicle for a variety of CRM_{197}based conjugate vaccines.

6.2.5 Needle-free vaccination: Immunogenicity of CRM_{197}-conjugated NPs loaded in TMDD Microparticles Manufactured by SFD

Polysaccharide conjugate vaccines frequently require multiple boosts to achieve sufficient immune activation to protect an individual. Additionally, children respond less well to immunisation than adults and titres wane quickly [Kelly et al. (2004)]. The main disease burden lies with infants and toddlers. Ideally, novel vaccines should elicit a strong first immune response with persistent titre levels. Needle-free vaccine delivery to the skin and nanoparticle adjuvants have individually reported improved vaccine immunogenicity. It was investigated whether the combination of needle-free intradermal delivery with nanoparticle antigen-carriers is more immunogenic than the current clinical standard.

In vivo, aqueous formulations of 5μg CRM_{197} were administered together with either a) PBS pH7.4, b) 85μg of alum pH7.4, c) 30% wt. trehalose/mannitol/dextran(10k)/dextran(150k) (3:3:3:1) pH7.2, or d) 2% wt. PEG-bPS-PS nanoparticles coated with CRM_{197} in 30% wt. trehalose/mannitol/dextran(10k)/dextran(150k) (3:3:3:1) pH7.2 (Table 2.1). These were administered IM with HNS. Needle-free formulations of TMDD-CRM_{197} and TMDD-CRM_{197}-NP manufactured by SFD and previously characterised in chapter 3 and chapter 5, were injected into the murine pinna.

On day 28 after prime with 5μg CRM_{197} in all conditions (Figure 6.9), CRM_{197} in PBS by HNS elicited mean titres that were significantly higher than naïve control ($p<0.05$). The comparatively low titres for this condition are characteristic of a soluble protein antigen injected without adjuvant. Surprisingly, the mean anti-CRM_{197} IgG antibody titre of CRM+NP by HNS was 11-fold higher than CRM+alum

($p<0.001$). The CRM+NP needle-free (NF) IgG antibody mean titre was 8-fold higher than the same dry-powder formulation but without NPs. These results suggest the exciting possibility that PEG-bPS-PS-CRM_{197} NPs potentiate the immune response and elicit higher titres than the clinical standard after one dose regardless of administration method. As expected, antibody titres for CRM+Alum, CRM+NPs by IM and CRM+NPs by NF were significantly higher than CRM alone (IM). Needle-free inoculation of CRM+NP induced similar titres to CRM+Alum (IM) but was less efficacious than CRM+NP by IM. CRM+NP (IM) elicits the highest antibody mean titre after one dose 28 days post injection. Pre-boost, only the NP-containing needle-free formulation was significantly more immunogenic than CRM_{197} in PBS. However, the unadjuvanted SFD formulation was not more immunogenic than unadjuvanted CRM_{197} which is surprising in light of past literature [Weissmueller et al. (2013)]. A possible reason may be that the SFD process reduced the immunogenicity potential of CRM_{197}, more than it reduced the potential of other antigens previously reported on in the literature.

Figure 6.10 summarises the mean CRM_{197} IgG titres on day 42 after prime and 14 days after the booster dose, with the same amount (5μg) and type of vaccine per group respectively. The small boost that is characteristic of unadjuvanted protein, induced a more significant difference of CRM_{197} in PBS relative to naïve control than on day 28 ($p<0.01$). More interesting is the finding that the mean anti-CRM_{197} IgG antibodies of CRM+NP by IM was 3.8-fold higher than CRM+alum (NS). Therefore, although not statistically significant, the trend suggests that CRM+NP by HNS may be a more immunogenic formulation than the clinical standard. Furthermore, the addition of CRM_{197}-conjugated NPs to the aqueous TMDD formulation, raised the mean titre by two orders of magnitude from 10^4 to 10^6. The potency of NPs as adjuvant is further exemplified by the 1.8-fold higher antibody titre of TMDD-NP

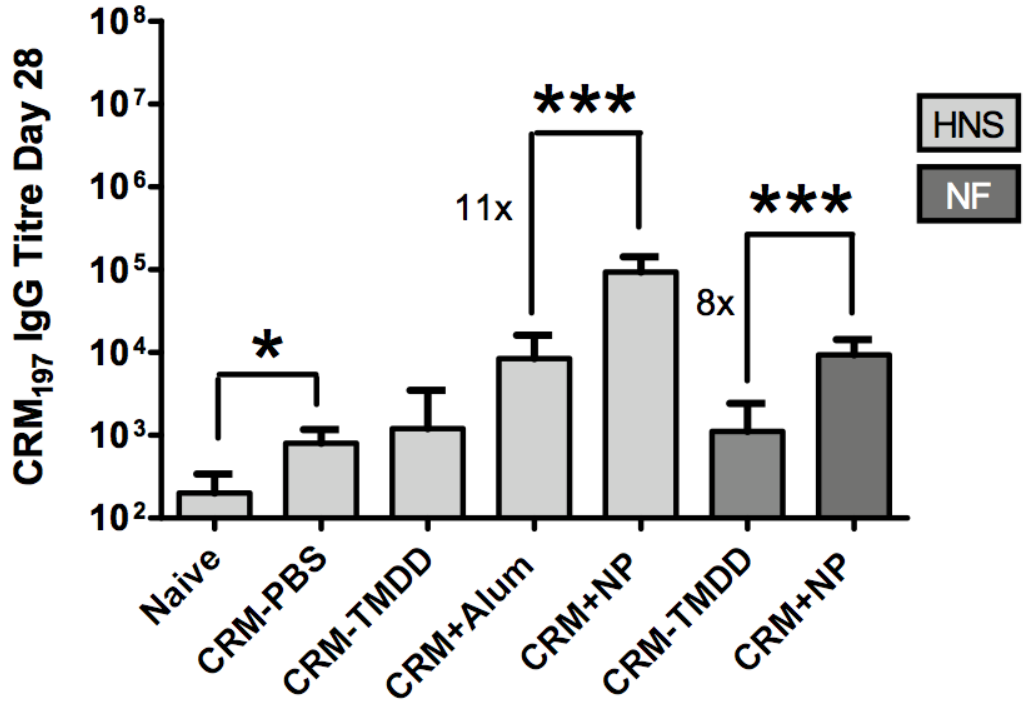


Figure 6.9: Day 28 - IgG titres of SFD With and Without NP: All treatment groups (n = 8) received 5μg CRM_{197} on days 0 (prime) and 28 (boost). Mice were bled on days 28 and 42. This figure depicts serum IgG titres on day 28. Naïve mice served as control group (n = 4). Pre-immunisation titres were less than 200. CRM_{197} adjuvanted with 85μg alum (Alum), CRM_{197} alone in PBS and CRM_{197} in 30% wt trehalose, mannitol, dextran (10k), dextran (150k) (3:3:3:1) were injected by IM with HNS (light bars). TMDD CRM_{197}-NP (CRM+NP), and TMDD-CRM_{197} (CRM+TMDD) powder was administered needle-free (dark bars) into the pinna at 55 bar gas pressure. The mean titre and standard deviation are indicated for all groups. Comparisons of special interest are indicated by top brackets with significance-level as superscript. ANOVA was conducted at $\alpha = 0.05$ significance level (* $p < 0.05$, ** $p < 0.01$, *** $p < 0.001$). P-values above that α-level were considered not significant (NS).

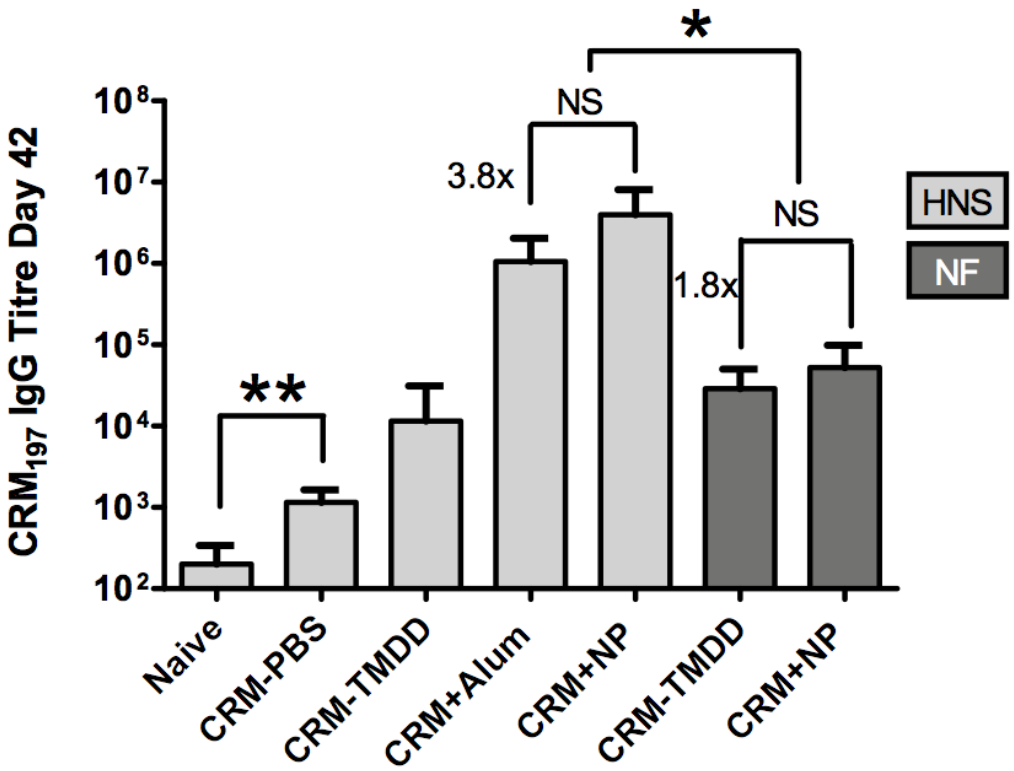


Figure 6.10: Day 42 - IgG titres of SFD With and Without NP: Immunisation schedule, vaccine formulations, and statistical analysis were previously described in Figure 6.9. This figure presents the IgG mean titres on day 42 (14 days after the booster dose). Treatment groups were compared to CRM_{197} in PBS by IM. Significant differences are indicated by asterisks. Comparisons of special interest are indicated by top brackets with significance-level as superscript. ANOVA was conducted at α = 0.05 significance level (* $p < 0.05$, ** $p < 0.01$, *** $p < 0.001$). P-values above that α-level were considered not significant (NS).

in the needle-free condition relative to needle-free TMDD. Most previous needle-free vaccine studies did not show the effect of the excipient matrix on the elicited titre response by including an IM control of the needle-free formulation. At both time points, however, aqueous TMDD-CRM_{197} showed the tendency to be more immunogenic than CRM_{197} in PBS. The observed adjuvanticity of TMDD may be due to the bacterial origin of dextran and trehalose, or possibly due to danger signals evoked in a local osmotic shock that is induced by the 30% wt saccharide formulation. Therefore, past studies that used TMDD formulations should be regarded as

being lightly adjuvanted. Needle-free conditions performed better than the unadjuvanted antigen by HNS ($p<0.01$), as was frequently reported in literature (see appendices). Unfortunately, needle-free CRM+NP and CRM-TMDD induced at least 20.1-fold lower titres than CRM+Alum or CRM+NP by HNS ($p<0.05$).

A direct comparison of titre levels on day 28 and day 42 show the largest boost response in the CRM_{197}-alum condition with a 124-fold increase in mean titre levels, while TMDD-CRM_{197}-NP by HNS only showed a 43-fold increase. This observation may be explained on the basis of alum's bioactivity: alum raises a local inflammatory response and thereby recruits APCs to its antigen depot [Morefield et al. (2005)]. This initial delay in antigen presentation may account for the difference in the initial antibody titre response seen between alum and NPs. Upon boost, a subsequent inflammation in the muscle is raised and may perhaps account for the higher boost response [Sokolovska et al. (2007)], particularly if PEG-b-PS NPs are less inflammatory than alum either based on their material properties, or based on their elimination from the tissue by drainage into the blood and lymphatics.

Subclass IgG titres allow for inference on the type of immune response. On day 42 past prime and 14 days past boost, IgG1 resembled IgG titres (Figure 6.11, 6.10). Adjuvanted CRM_{197} conditions by IM outperformed the needle-free formulations ($p<0.05$), and alum-CRM_{197} induced similar titres as NP-CRM_{197}. Based on their virus-like size, it was unexpected to see high IgG1 titres in the NP-CRM_{197} condition. IgG1 titres induced by CRM-TMDD (IM) were higher than titres induced by CRM-PBS (IM) ($p<0.05$). The CRM+NP needle-free IgG1 Ab mean titre was 8-fold higher than CRM-TMDD (HNS). Ab titres for CRM-TMDD, CRM+Alum, CRM+NPs by IM and CRM-TMDD, CRM+NPs by NF were significantly higher than CRM alone (IM). Again, needle-free CRM+NP induced 23.3-fold lower titres than CRM+Alum ($p<0.05$).

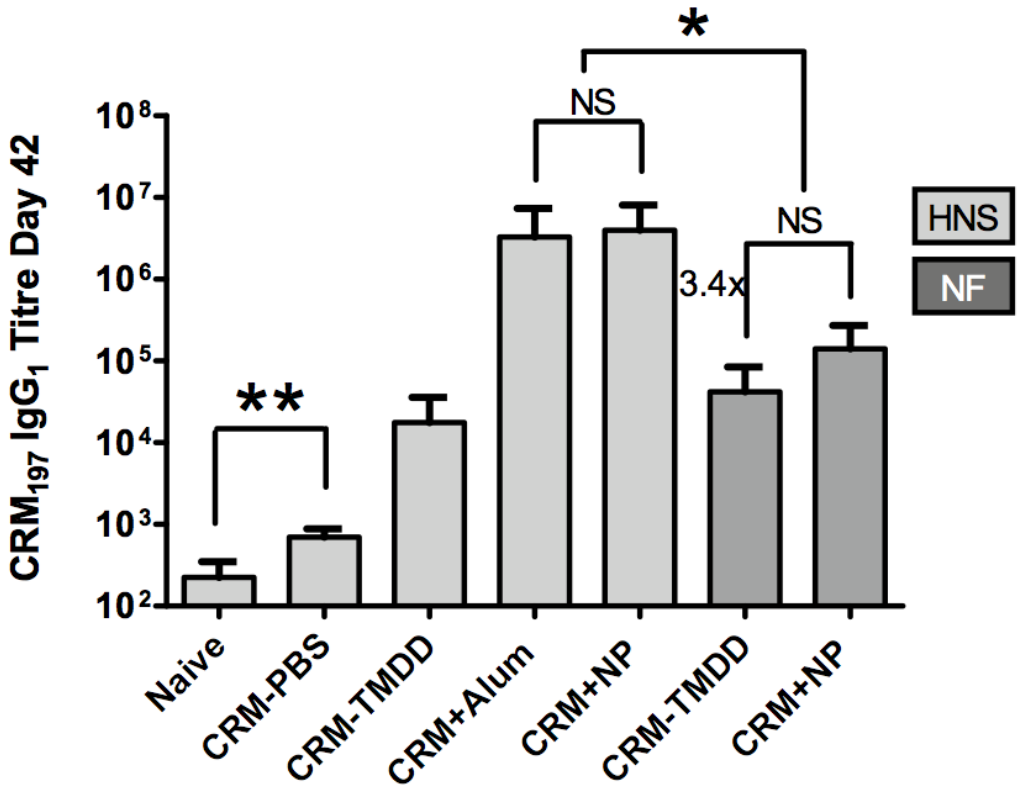


Figure 6.11: Day 42 - IgG1 Subclass titres of SFD With and Without NP: IgG1 titres were determined on day 42 on the same sera as discussed in Figure 6.10. Mean titres are indicated for all treatment conditions: CRM_{197} in PBS (PBS), CRM_{197} adjuvanted with 85μg alum (Alum), and CRM_{197} in 30% wt trehalose, mannitol, dextran (10k), dextran (150k) (3:3:3:1), all injected by IM (light bars). Needle-free conditions (NF) were TMDD-CRM_{197} and TMDD-CRM_{197}-NP (dark bars). Comparisons of special interest are indicated by top brackets with significance-level as superscript. ANOVA was conducted at α = 0.05 significance level (* $p < 0.05$, ** $p < 0.01$, *** $p < 0.001$). P-values above that α-level were considered not significant (NS).

6.2.5.1 IgG Subclass Responses

In Figure 6.12, subclass IgG2a ELISA showed a 36-fold higher mean anti-CRM antibody titre for CRM+NP by IM than for CRM+alum ($p<0.01$). This result underscores the potent Th1 activation potential of CRM_{197}-conjugated NPs. On the other hand, the IgG2a Ab titres induced by CRM+NP needle-free were not different from CRM-TMDD (NF) ($p>0.05$). This again may be due to the relative immobility of NPs in the skin. Ab titres for CRM+Alum, CRM+NPs by IM were significantly higher than

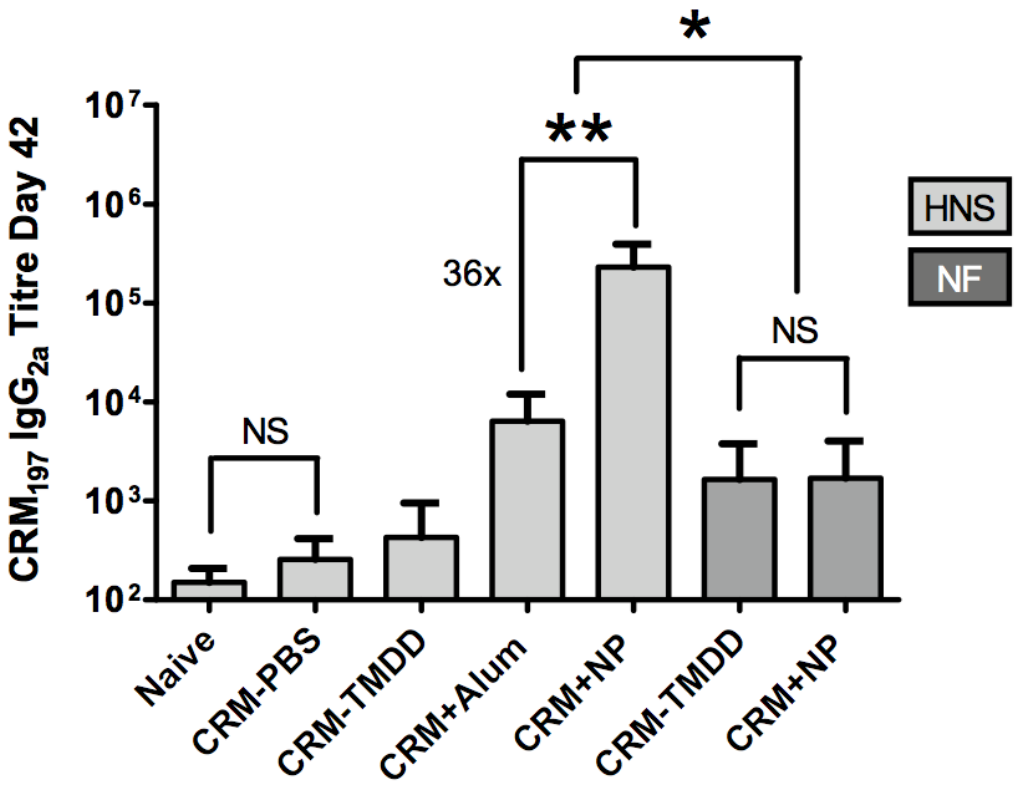


Figure 6.12: Day 42 - IgG2a Subclass titres of SFD With and Without NP: Immunisation schedule, vaccine formulations, and statistical analysis were previously described in Figure 6.9. This figure presents the IgG2a mean titres on day 42 (14 days after the booster dose). Comparisons of special interest are indicated by top brackets with significance-level as superscript. ANOVA was conducted at $\alpha = 0.05$ significance level (* $p < 0.05$, ** $p < 0.01$, *** $p < 0.001$). P-values above that α-level were considered not significant (NS).

CRM alone (IM). These results suggest that CRM+NP by IM elicits the highest Ab mean IgG2a titre after two doses and that the needle-free formulations were less immunogenic.

The underlying trends and observations of the *in vivo* comparison of needle-free and aqueous formulations with and without NPs are clear. Nanoparticles (CRM_{197}-conjugated PEG-b-PS shell, PS core) tend to increase anti-CRM_{197} IgG, IgG1, IgG2a mean titres. NP formulations have a less pronounced boost compared to alum (IM) or TMDD (NF). NPs are more immunogenic as adjuvant in aqueous formulations

than in dry-powders. Importantly, NPs induce a balanced Th1/Th2 antibody response and elicit superior IgG antibody titres after the first dose. Needle-free formulations, on the other hand, were less immunogenic than IM if they contained NPs, but more immunogenic than their IM controls in TMDD formulation and in PBS. It was furthermore observed that formulation excipients can impact IgG and IgG subclass mean Ab titres.

These findings raise the question, why did NPs in the SFD formulations not show similar IgG titre potentiation as the HNS condition? And why are aqueous NP formulations more immunogenic after the first dose than alum, but have a lower boostability? The answers to these questions drive at the mechanism by which NPs may impact the immune response. From logical deduction it follows that the main difference between the needle-free and HNS conditions is the injection site and injection modality, since both CRM_{197} and NP doses were the same. HNS and needle-free injection are differently traumatic to the surrounding tissue and past studies have suggested a slight immune response potentiation induced by dermal-micro trauma of BPI. Therefore, NF should be more immunogenic than HNS, but that is not the case. It is more likely, therefore, that the pivotal aspect here pertains to the difference in injection site or possibly particle injection depth. Muscle tissue is highly perfused while the upper dermal regions are almost blood-less. This suggests, that while skin-resident APCs can shuttle individual CRM_{197}-conjugated NPs to lymph nodes, injection into perfused tissue NPs may lead to circulating antigen in blood and lymphatics. This higher concentration of antigen-coated NPs in circulation could in turn increase the potential for antigen-specific T-helper cells to be activated.

While this is a plausible theory, its confirmation or rebuttal requires further investigation. Remarkable evidence in favour of the aforementioned theory was pre-

sented by Moon et al. (2012). In their study, surface presentation of the malaria antigen VMP001 on lipid nanoparticles showed the induction of high avidity antibodies agains VMP001 that lasted over a 1 year and required only a tenth of the dose compared to administration with conventional adjuvants. Upon further investigation, it was discerned that NPs promoted the formation of germinal centres, particularly in close proximity of the draining lymph nodes where NPs accumulated. Moon et al. (2012) concluded that NPs enhanced the expansion of antigen-specific follicular helper T cells more so than alum-bound or soluble VMP001, and suggest that “NP vaccines may be a promising strategy to enhance the durability, breadth, and potency of humoral immunity by enhancing key elements of the B-cell response". Durability, breadth and potency of the humoral immune response are arguably the key factors that could improve the current commercial glycoconjugate vaccines. The TMDD-CRM_{197}-NP formulation combines soluble antigen with surface bound antigen and may induce both, a broad and Th1/Th2 balanced response, as evidenced by the data, as well as high avidity and long-lasting antibodies via germinal centre formation. The latter aspect requires further investigation. However, the results presented in this chapter provide initial evidence that a NP-vaccine platform may improve the immune response elicited with glycoconjugates in a similar manner as they did with malaria antigen.

6.3 Chapter Summary

The different particle types (TMDD, PS, and kHA) yielded significantly different mean penetration depths at same acceleration pressures. The differences are consistent with their densities and also their impact parameter: kHA injected deepest, followed by PS, and SFD particles. For the investigated needle-free injection sites

on a mouse model (shaved abdomen and base of tail, or pinna), the mean particle penetration depth for kHA particles was largely contained within the thickness and location of the epidermis. For kHA particles, their size distribution and penetration depth was most closely described by a log-normal probability density distribution. A simple scaling factor was identified that related the cumulative density function of particle size with the CDF of particle penetration depth in the murine skin. Based on this factor, it was suggested that the particle size and the resultant penetration depth of kHA particles are significantly correlated (R^2=0.984). The Kendall model, on the other hand, showed a correlation of R^2=0.745 to the experimental data. On this basis, therefore, the presented approach may be expanded by further experiments into a model that predicts the penetration depth of a powder batch based on its size distribution, which is a property that is readily measured. While the ability to pin-pointing the exact location of individual particles based on their physical characteristics is lost, the probabilistic approach may improve the predictability of how much of the total vaccine dose is delivered to a certain location within the skin.

Needle-free inoculation with kHA-CRM_{197} induced significantly higher IgG antibodies 4 weeks after prime and 2 weeks after boost relative to CRM_{197} alone with HNS. Furthermore, kHA-CRM_{197} elicited IgG, IgG1, and IgG2a responses that were similar to alum-adjuvanted CRM_{197} by IM. This is a noteworthy result because most needle-free immunisation studies reported in literature to date do not compare the needle-free formulation to the adjuvanted protein antigen directly. The most common comparator in past studies has been the protein antigen alone with HNS by IM or SC [Weissmueller et al. (2013)].

Needle-free injection with SFD-powders were less immunogenic than the clinical standard (antigen a plus alum) by IM, but more immunogenic than pure antigen by IM. Interestingly, it was observed that the co-delivery of TMDD excipients in-

creased the immunogenicity of CRM_{197}, and should therefore be considered a light adjuvant. The addition of CRM_{197}-coated PEG-b-PS NPs into the TMDD matrix was significantly more immunogenic than the clinical control when administered by IM after the first dose. Unlike the alum-adjuvanted CRM_{197} IM injection, the liquid NP injection induced a balanced subclass IgG1/IgG2a response, which is indicative of a balanced immune activation. However, when NPs were incorporated into dry-powders and injected intradermally, they were not as immunogenic as the clinical control by IM. Possibly, the loss of potency may be linked to the aggregation of free CRM_{197} in the TMDD matrix during SFD, and a limited mobility of NPs in the dermis, compared to muscle. This finding suggests that in addition to their physical size also the mobility of nanoparticles in the tissue may substantially impact the immune response. In short, needle-free injection of kHA is potentially as good as alum-adjuvanted CRM_{197} (IM), but nanoparticles with CRM_{197} (IM) is the more promising antigen delivery platform.

CHAPTER 7

CONCLUSIONS AND FUTURE DIRECTIONS

Vaccines can prevent devastating disease but more therapeutic potential is yet to be realised. The previous chapters demonstrated the impact of novel delivery platforms and the utility and limitation of a thermodynamic approach to antigen stabilisation. The results suggest that the thermodynamic stability optimisation for CRM_{197} in solution does not ensure its structural stability during SFD formulation and that the type of antigen delivery platform profoundly impacts the magnitude and quality of the immune response. The presented data motivate further investigation into antigen presentation on vaccine delivery constructs, as well as an additional excipient screening approach to complement thermodynamic stability screens.

7.1 BACKGROUND AND AIMS

The use of hypodermic needle and syringe is associated with significant iatrogenicity and presents a substantial burden to global health. While a plethora of needle-free injection devices exist, vaccine reformulation is costly and presents a barrier to their widespread clinical application. Although dry-powder intradermal injection

may not be an economic alternative for all vaccine types, the cost and complexity of glycoconjugate vaccines make them a suitable candidate for reformulation. To provide a simple, needle-free, and broad-spectrum protein antigen delivery platform, three different approaches were investigated to address some of the current limitations needle-free intradermal particle injection:

- Firstly, the utility of Differential Scanning Fluorimetry, a novel high-throughput screening technology, was assessed in excipient screening with the aim to facilitate and hasten vaccine reformulation efforts.
- Secondly, a novel bioceramic material on hydroxyapatite basis was developed by molten salt synthesis, with the aim to obviate the costly lyophilisation step and to provide sustained antigen presentation and release *in situ*.
- Thirdly, CRM_{197} was surface-presented on a novel block copolymer nanoparticle construct and subsequently incorporated into conventional SFD powder with the aim to create a potent but benign adjuvant system that enhances the formulation immunogenicity and balances Th1 and Th2 responses.

7.2 Results in Context and Future Directions

7.2.1 Spray-lyophilisation of CRM_{197}

The dwindling R&D budget in the pharmaceutical industry incentivises a shift away from the "shots on target" approach. The formulation and reformulation of biotherapeutics has been largely empirical due to the complex and incompletely understood effects of additives on the structure and stability proteins. Instead of formulating, lyophilising, and analysing every possible formulation permutation, new

approaches such as design of experiments (DOE) are used and may reduce resource and time investments through computational experimental design. Additionally, new high throughput screening tools are of interest. Recently, differential scanning fluorimetry has emerged as new screening tool that can assess the thermal stability of proteins in solution. DSF has been extensively used to study ligand binding, but only recently has received application in formulation development. In this thesis, DSF was used to optimise the thermal stability of CRM_{197} in solution.

The findings presented in chapter 3 demonstrated that DSF is a powerful tool that readily identified co-solutes which improved the thermostability of CRM_{197} in solution. Additionally, the tertiary structure of CRM_{197} was significantly correlated with its thermal stability. For a redshift of tryptophan emissions by 1nm, which is indicative of protein unfolding, the thermal stability of CRM_{197} decreased by 1.4°C. However, despite the increased thermal stability of CRM_{197} in the presence of glycine (TGDD), its aggregation propensity was increased and resulted in a 44.4% loss of CRM_{197} monomer, which was 11.8% more than in the thermodynamically less stable TMDD formulation. Therefore, although DSF is well suited to identify co-solutes that thermodynamically stabilise proteins, it cannot provide inference on their kinetic stability. We recommend to augment the screening of excipients for thermodynamic stability of the antigen with an orthogonal technology that quantifies the compound's kinetic stability. While CRM_{197} aggregated substantially during SFD, BSA showed only a 1% monomer loss. Therefore, although SFD is a capable method to produce dry-powers with suitable mechanical characteristics for ballistic injection, the additional stresses of atomisation and shock-freezing are not well tolerated by all proteins.

Several interesting future directions can be pursued based on these findings. Unlike spray-freeze-drying, where solution shear and ultrasound cavitation are

dominant, the primary stresses exerted upon on a protein during conventional lyophilisation are predominantly of thermal and desiccatory nature. Therefore, the thermodynamic stability of a protein in a formulation, as identified by DSF, may be more predicative of structural retention during conventional lyophilisation. If this is the case, the use of DSF in pharmaceutical R&D could substantially reduce the time and costs of formulation development. Further high-throughput DSF experiments with CRM_{197} could investigate how solution additives impact its interdomain stabilisation. Perhaps, a better understanding of CRM_{197}'s subdomain interactions may facilitate future formulation efforts. CRM_{197} aggregation may be reduced by further optimisation of the solution conditions. However, it would be interesting to investigate how the formaldehyde cross-linking of CRM_{197} would impact its thermodynamic stability and structural preservation during SFD. Given that merely epitopes of the carrier protein are presented to T-cells, cross-linking may not reduce the apparent immunogenicity, but may decidedly increase the stability of the molecule during formulation and subsequent handling. In a next step, DSF screening could be applied to derive a thermostable formulation for a commercial glycoconjugate vaccine and to test the resuspended formulation for aggregate content after lyophilisation and SFD. The direct comparison of conventional lyophilisation with SFD may provide inference on whether DSF on liquid formulations is more closely correlated with the retention of the protein during lyophilisation than SFD.

7.2.2 Bioceramic Powder as Protein Delivery Vehicle

Lyophilisation can present a bottleneck to large-scale pharmaceutical manufacture. A reformulation and delivery modality that does not require lyophilisation would be a disruptive technology with substantial economic impact. The use of bioceramics has transformed medical treatment options in dentistry and bone repair. Addition-

ally, bioceramics have shown shown promise as drug delivery substrates. Particularly, hydroxyapatite has received much attention due to its biocompatibility and mechanical properties. However, its prismatic crystal structure is not ideal for ballistic delivery due to unfavourable aspect ratios. In this thesis, molten salt synthesis (MSS) was used to reshape hydroxyapatite into spheroidal single bioceramic particles, that are suitable for needle-free powder injection.

The results presented in chapter 4 demonstrated that the incorporation of potassium in HA occurs during molten salt synthesis and can increase or decrease the adsorption of BSA-TRITC. Material properties of potassium-doped apatitic were dependent on the salt-to-HA ratio during reaction and individual kHA particles could be manipulated to assume spheroidal morphology with increased density at a reasonably narrow size span of 1.2-2.1. To the best of our knowledge, this is the first report of potassium-doped HA single particles with a spheroidal morphology. Material characterisation showed that HA is the major phase of all K-doped particles with an increasing emergence of calcium phosphate minor phases at higher salt-to-HA ratios. These calcium phosphates are also present in dentine and human bone, which further underscores the biocompatibility of the kHA constructs. The surface chemistry of kHA corresponded closely to pure HA, as measured by FTIR, which is why biocompatibility of the material was assumed. The mechanical robustness of kHA particles was determined by single crystal nanoindentation, and the elastic modulus and hardness were determined to be comparable to human trabecular bone and dentine, which make them ideally suited for ballistic injection. Additionally, it was determined that CRM_{197} adsorption onto kHA was well described by the Langmuir isotherm, which is indicative of monolayer adsorption. CRM_{197} release *in vitro* showed an initial burst followed by sustained release for the remainder of the experiment. Even in the surface adsorbed state, the secondary structure of CRM_{197}

was well retained according to FTIR. However, the protein carrying capacity of kHA is limited.

The novel bioceramic particles can achieve surface adsorption and desiccation of CRM_{197} and BSA (and likely any negatively charged protein) within hours. Drying does not have to be conducted at reduced pressure under active cooling, but happens almost instantly by chemical dehydration in alcohol, and is followed by desiccation at room temperature. Future work could aim to further improve the surface sorption capacity of kHA via the incorporation of other ions during MSS. The loading capacity may further be improved by increasing the surface area of the particle, possibly by making the particles more porous. Additionally, it may be attempted to coat kHA particles with polymer. Depending on the polymer, an active pharmaceutical ingredient (API) may be incorporated into this coating, which may release the API in a time-controlled manner. A polymer coat may also be functionalised to surface present ligands such as pathogen associated molecular patterns (PAMPs) or other TLR activating moieties. These polymer-bioceramic particles may be used to deliver a prime and booster dose in the same injection, by delivering particles with substantially different release characteristics.

7.2.3 Functionalised Block Copolymer Nanoparticles As Novel Adjuvant

Nanoparticles have recently been identified as promising vaccine delivery platform. However, much conflicting data on the effect of antigen loading versus presentation and the effect of particle size on the immune response have been reported. In part, these conflicting results may be due to the large variability in sizes, antigens, and materials of the nanoparticles that were used. One of the exciting prospects

about nanoparticle vaccines is their ability to leverage innate immune mechanisms that enhance immune responses to a broad range of antigens. In part, this may be achieved through improved uptake and presentation by APCs and the induction of danger signals via PAMP receptors. In this thesis, in corporation with Prof. Prud'homme at Princeton University, the size and surface functionalisation of polymer nanoparticles were precisely controlled. Surface-conjugated CRM_{197} was analysed and subsequently incorporated into SFD powders for ballistic injection.

The results presented in chapter 5 showed that PEG-b-PS block co-polymer nanoparticles can be reliably size-engineered, and that the covalent surface conjugation of CRM_{197} can be achieved. However, the reaction conditions that were used to link NPs and CRM_{197} induced partial chemical degradation of the protein with a generally low yield of conjugation. While steric hindrance may play an important role in the yield of the reaction of NPs to CRM_{197}, the use of click-chemistry may make the reaction more stoichiometric and more rapid. However, the development of new chemistry for CRM_{197} conjugation may likely involve the functionalisation of CRM_{197}, which may require a new assessment of its toxicology *in vivo*. However, FTIR analysis on the purified NP-CRM_{197} constructs after the reaction suggested that the surface-conjugated CRM_{197} largely retained its secondary structure. Furthermore, fluorimetry determined that also the tertiary structure of NP-bound CRM_{197}, as assessed by tryptophan excitation/emission, was only slightly altered (red-shifted by 1nm), which indicates a good conformational retention.

Future work could investigate whether cross-linked CRM_{197} can be surface conjugated to NPs and whether the cross-linked molecule is more resistant to chemical degradation. The next logical step would be to move from the CRM_{197} carrier protein to a complete glycoconjugate vaccine. Potential complications may be that some of the reactive primary amine groups are already taken up by conjugated

polysaccharide chains. Additionally, glycoconjugates were reported to have an increased heterogeneity compared to the pure carrier protein, with a slightly unfolded tertiary structure that may be more prone to aggregation. Aside from these concerns, the NP platform may improve the immunogenicity of glycoconjugate vaccines. Furthermore, the presented NP platform may be used to specifically investigate the effect of particle size on the immune response, and can be used to study the effect of surface presented antigen versus soluble antigen (that is released from the NPs). More specifically, a NP-construct can be engineered that targets DCs (e.g. by DEC-205 targeting antibodies), attracts C3 complement (e.g. with accessible hydroxyl groups), and draws endogenous antibodies (e.g. by surface-presentation of pathogen epitopes). Thus, both B-cell and T-cell Ag-targeting and subsequent Ag presentation may be enhanced. Additionally, NPs may be used to study whether bacterial polysaccharides indeed need to be chemically linked to the carrier protein, or whether the carrier protein and the PS simply need to be co-delivered to APCs. An initial study could have the following treatment groups: 0) Naïve control, 1) MenY-CRM_{197} conjugate linked to NPs, 2) pure MenY PS linked to NPs , 2) pure CRM_{197} linked to NPs, and 4) pure MenY and CRM_{197} that are linked to the same NP but are not chemically conjugated. Additional groups may be: 5) CRM_{197} peptides from the chemically cleaved CRM_{197} protein and linked to NPs (without MenY), and 6) CRM_{197} peptides and MenY PSs that are linked to the same NP but are not chemically conjugated. Depending on the results of such an initial study, if a robust immune response merely requires a co-delivery of purified bacterial PS along with an immunogenic protein or peptides (but not their chemically conjugation), it would be easy to surface-present a large number of diverse PS on NPs along with proteins or peptides. Pneumococcal vaccines require many different subtype PSs and their manufacture is currently very inefficient and expensive due to difficulties of linking the plethora of different PSs to a single protein carrier. The NP platform

therefore may greatly facilitate the formulation of highly multivalent glycoconjugate vaccines. Immunological tests on nanoparticle-containing formulations should pay close attention to IgG persistence, Ab affinity, and titre levels in relation to NP characteristics. Memory B-cell counts and B-cell subtypes could be quantified and the long term immunity *in vivo* may be established using a challenge model. In addition to developing improved vaccines, fluorescently labelled NPs could be used to study basic immunology questions. For example, NPs could be used to target specific immune cells, and their movement in lymph nodes could subsequently be imaged. NPs could be used to investigate the effect of particle size on bioavailability, location, and circulation time *in situ*. NPs could be used to study the internalisation and surface-presentation of particulate antigen by APCs, and subsequent antigen presentation to other APCs via intravital fluorescence microscopy. These studies may provide valuable insights into the underlying immune mechanisms that impact adaptive immunity and may inform future vaccine development.

7.2.4 Particle Injection and Immunogenicity of CRM_{197} Formulations

The purchase price of hypodermic needle and syringe is low, but the costs to society can be high. The unsafe use of needles can lead to needle-stick injuries and thereby propagate bloodborne pathogens such as HIV and hepatitis B and C. The associated treatment costs can be exorbitant. In 2000, the use of a needle-free powder injector reported better treatment outcomes of needle-free injection compared to SC control. Multiple antigens have been injected needle-free, but device costs and limited success in clinical trials have hampered their widespread clinical use. If the thermostability of an expensive vaccine, such as bacterial glycoconjugates, can

be combined with improved immunogenicity, the savings in cold chain costs in addition to improved patient outcomes may make needle-free vaccination profitable and safe alternative. A competitive needle-free vaccine should be similarly or more immunogenic than the current clinical standard. Obstacles to successful intradermal powder injection include the payload targeting to the correct dermal layer, the empirical reformulation of protein antigens, and possibly, the bolus type injection that is achieved with saccharide excipient powders.

The final results chapter 6 introduced a probabilistic description of particle injection that may be more accurate in determining the fraction of antigen dose at a given depth in the skin compared to previous models. The chapter also evaluated the immunogenicity of the previously described CRM_{197} dry-power formulations. It was demonstrated that CRM_{197}-adsorbed kHA, and administered needle-free, elicited comparable titres to the current clinical standard of the alum-adjuvanted antigen by IM, but was not better. The presence of saccharides and polymers was shown to have an adjuvant-like effect on IgG titers. Nanoparticles that surface-presented CRM_{197} outperformed the clinical standard in magnitude and induced a well balanced Th1/Th2 response when administered IM, but not when administered as constituent of TMDD powder manufactured by SFD. In part, this may be due to the reduced CRM_{197} monomer content of SFD powders, and possibly in part due to the mobility of NPs in the respective target tissue.

These results suggest that antigen presentation in soluble, microparticle, or nanoparticle form has a profound impact on the immune response. Future studies should aim to confirm these results with a complete but monovalent glycoconjugate vaccine, such as MenY-CRM_{197}, for example, before expanding to multivalent glucoconjugates. An advanced understanding of the interactions between the immune system and nanoparticles may pave the way towards the design of vaccines that are

efficacious with a single dose. Currently, glycoconjugate vaccines require multiple injections to achieve lasting immunity. During the course of a vaccination program, the vaccine recipient is vulnerable and may contract debilitating or fatal disease. Repeated inoculations can triple healthcare costs in addition to inconveniencing vaccine recipients, especially in resource deprived nations where long journeys to health centres are required. Nano-carriers are promising vaccine delivery vehicles that can enhance the immune response to an antigen, and may thereby reduce the required vaccine dose and possibly obviate the need for repeated inoculations.

7.3 Societal Impact and Commercial Benefit

The availability of low-cost, easy to manufacture, and efficacious needle-free antigen delivery platforms may contribute to a reduction in needle-stick injuries, and may provide a renewed impetus to make life-saving polysaccharide conjugate vaccines available to resource-deprived countries.

High-throughput excipient screening with DSF may reduce the R&D time and resource investment required in vaccine formulation. DSF is well suited to identify thermally stabilising excipients for protein therapeutics. Therefore, this approach caters to the current key drivers within the pharmaceutical industry that aim to streamline the R&D work-flow.

The presented bioceramic vaccine delivery platform may be developed and marketed as a novel needle-free vaccine product that addresses the demand of a niche market. Furthermore, the kHA bioceramic may find application in dental and bone repair as part of medical devices such as prosthetics.

The highly immunogenic nanoparticle antigen platform may be developed into

a potent adjuvant system that may improve the immunogenicity of existing liquid and lyophilised formulations. As adjuvant, antigen- and PAMP-conjugated NPs could be optimised against and custom designed for a given vaccine type, such as bacterial glycoconjugates, and subsequently sold to vaccine manufacturers. Furthermore, targeted and fluorescently labeled NPs may be commercialised as versatile tool to study immunological mechanisms.

REFERENCES

ABBAS, A., LICHTMAN, A., AND POBER, J. *Cellular and molecular Immunology*. W.B. Saunders Company, Philadelphia, 4 edition, 2000.

AKERS, M., VASUDEVAN, V., AND STICKELMEYER, M. Formulation development of protein dosage forms. *Pharm Biotechnol*, 14:47–127, 2002.

ALCOCK, R., COTTINGHAM, M. G., ROLLIER, C. S., FURZE, J., DE COSTA, S. D., HANLON, M., SPENCER, A. J., HONEYCUTT, J. D., WYLLIE, D. H., GILBERT, S. C., BREGU, M., AND HILL, A. V. S. Long-term thermostabilization of live poxviral and adenoviral vaccine vectors at supraphysiological temperatures in carbohydrate glass. *Sci Transl Med*, 2(19):19ra12, Feb 2010.

ALMEIDA, N. L., OLIVEIRA, C. L. P., TORRIANI, I. L., AND LOH, W. Calorimetric and structural investigation of the interaction of lysozyme and bovine serum albumin with poly(ethylene oxide) and its copolymers. *Colloids Surf B Biointerfaces*, 38(1-2): 67–76, Oct 2004.

ANDERSON, P. W., PICHICHERO, M. E., STEIN, E. C., PORCELLI, S., BETTS, R. F., CONNUCK, D. M., KORONES, D., INSEL, R. A., ZAHRADNIK, J. M., AND EBY, R. Effect of oligosaccharide chain length, exposed terminal group, and hapten loading on the antibody response of human adults and infants to vaccines consisting of haemophilus influenzae type b capsular antigen unterminally coupled to the diphtheria protein crm197. *J Immunol*, 142(7): 2464–8, Apr 1989.

ANFINSEN, C. B. Principles that govern the folding of protein chains. *Science*, 181(4096):223–30, Jul 1973.

ANSELL, S. M., JOHNSTONE, S. A., TARDI, P. G., LO, L., XIE, S., SHU, Y., HARASYM, T. O., HARASYM, N. L., WILLIAMS, L., BERMUDES, D., LIBOIRON, B. D., SAAD, W., PRUD'HOMME, R. K., AND MAYER, L. D. Modulating the therapeutic activity of nanoparticle delivered paclitaxel by manipulating the hydrophobicity of prodrug conjugates. *J Med Chem*, 51:3288–3296, 2008.

ARAKAWA, T., EJIMA, D., KITA, Y., AND TSUMOTO, K. Small molecule pharmacological chaperones: From thermodynamic stabilization to pharmaceutical drugs. *Biochim Biophys Acta*, 1764(11):1677–87, Nov 2006.

AUGUSTINE, R., KALAPPURA, U. G., LAHEURTE, J.-M., AND MATHEW, K. T. Biocompatibility study of beta tricalcium phosphate bioceramics and chitosan biopolymer and their use as phantoms for medical imaging applications. *Microw Opt Techn Let*, 51:2923–2927, 2009.

AUTON, M. AND BOLEN, D. W. Predicting the energetics of osmolyte-induced protein folding/unfolding. *Proc Natl Acad Sci U S A*, 102(42):15065–8, Oct 2005.

AVCI, F. Y. AND KASPER, D. L. How bacterial carbohydrates influence the adaptive immune system. *Annu Rev Immunol*, 28:107–30, 2010.

AVCI, F. Y., LI, X., TSUJI, M., AND KASPER, D. L. A mechanism for glycoconjugate vaccine activation of the adaptive immune system and its implications for vaccine design. *Nat Med*, 17(12):1602–9, Dec 2011.

BAKER, D. AND AGARD, D. A. Kinetics versus thermodynamics in protein folding. *Biochemistry*, 33(24): 7505–9, Jun 1994.

BAL, S. M., DING, Z., VAN RIET, E., JISKOOT, W., AND BOUWSTRA, J. A. Advances in transcutaneous vaccine delivery: Do all ways lead to rome? *J Control Release*, 148(3):266–282, 2010.

BARBOUR, M. L., BOOY, R., CROOK, D. W., GRIFFITHS, H., CHAPEL, H. M., MOXON, E. R., AND MAYON-WHITE, D. Haemophilus influenzae type

b carriage and immunity four years after receiving the haemophilus influenzae oligosaccharide-crm197 (hboc) conjugate vaccine. *Pediatr Infect Dis J*, 12(6):478–84, Jun 1993.

BELL, C. E. AND EISENBERG, D. Crystal structure of nucleotide-free diphtheria toxin. *Biochemistry*, 36 (3):481–8, Jan 1997.

BELL, K. N., HOGUE, C. J., MANNING, C., AND KENDAL, A. P. Risk factors for improper vaccine storage and handling in private provider offices. *Pediatrics*, 107(6):E100, Jun 2001.

BELLAVIA, G., GIUFFRIDA, S., COTTONE, G., CUPANE, A., AND CORDONE, L. Protein thermal denaturation and matrix glass transition in different protein-trehalose-water systems. *J Phys Chem B*, 115(19): 6340–6, May 2011.

BENNETT, M. J., CHOE, S., AND EISENBERG, D. Domain swapping: entangling alliances between proteins. *Proc Natl Acad Sci U S A*, 91(8):3127–31, Apr 1994a.

BENNETT, M. J., CHOE, S., AND EISENBERG, D. Refined structure of dimeric diphtheria toxin at 2.0 a resolution. *Protein Sci*, 3(9):1444–63, Sep 1994b.

BENNETT, M. J. AND EISENBERG, D. Refined structure of monomeric diphtheria toxin at 2.3 a resolution. *Protein Sci*, 3(9):1464–75, Sep 1994.

BERTI, F., COSTANTINO, P., FRAGAI, M., AND LUCHINAT, C. Water accessibility, aggregation, and motional features of polysaccharide-protein conjugate vaccines. *Biophys J*, 86(1 Pt 1):3–9, Jan 2004.

BHAT, R. AND TIMASHEFF, S. N. Steric exclusion is the principal source of the preferential hydration of proteins in the presence of polyethylene glycols. *Protein Sci*, 1(9):1133–43, Sep 1992.

BLANCHARD-ROHNER, G. AND POLLARD, A. J. Long-term protection after immunization with protein-polysaccharide conjugate vaccines in infancy. *Expert Rev Vaccines*, 10(5):673–84, May 2011.

BLEWITT, M. G., CHAO, J. M., MCKEEVER, B., SARMA, R., AND LONDON, E. Fluorescence characterization of the low ph-induced change in diphtheria toxin conformation: effect of salt. *Biochem Biophys Res Commun*, 120(1):286–90, Apr 1984.

BONNET, F., EBERHART, L., WENNBERG, E., DODDS, S. J., VAN BELLINGHEN, L., ANNEMANS, L., KAVANAGH, S., AND CHOE, Y. Fentanyl hcl iontophoretic transdermal system versus morphine iv-pca for postoperative pain management: survey of healthcare provider opinion. *Curr Med Res Opin*, 25 (2):293–301, Feb 2009.

BOOY, R. Getting hib vaccine to those who need it. *Lancet*, 351(9114):1446–7, May 1998.

BOS, J. D. AND MEINARDI, M. M. The 500 dalton rule for the skin penetration of chemical compounds and drugs. *Exp Dermatol*, 9(3):165–9, Jun 2000.

BOSCH, B., HEIPERTZ, E. L., DRAKE, J. R., AND ROCHE, P. A. Major histocompatibility complex (mhc) class ii-peptide complexes arrive at the plasma membrane in cholesterol-rich microclusters. *J Biol Chem*, 288(19):13236–42, May 2013.

BOYD, J. H., DIVANGAHI, M., YAHIAOUI, L., GVOZDIC, D., QURESHI, S., AND PETROF, B. J. Toll-like receptors differentially regulate cc and cxc chemokines in skeletal muscle via nf-kappa b and calcineurin. *Infection and Immunity*, 74(12):6829–6838, 2006.

BREWER, J. M., POLLOCK, K. G. J., TETLEY, L., AND RUSSELL, D. G. Vesicle size influences the trafficking, processing, and presentation of antigens in lipid vesicles. *J Immunol*, 173(10):6143–50, Nov 2004.

BRÖKER, M., DULL, P. M., RAPPUOLI, R., AND COSTANTINO, P. Chemistry of a new investigational quadrivalent meningococcal conjugate vaccine that is immunogenic at all ages. *Vaccine*, 27 (41):5574–80, Sep 2009.

BURGER, M. S., ZULEGER, C. L., CHU, Q., GAO, X., PAYNE, L. G., AND CHEN, D. An antigen-independent but not antigen-specific t(h)1 response provides protection in the murine airway inflammation model. *J Allergy Clin Immunol*, 114 (6):1301–8, 2004.

BURKOTH, T. L., BELLHOUSE, B. J., HEWSON, G., LONGRIDGE, D. J., MUDDLE, A. G., AND SARPHIE, D. F. Transdermal and transmucosal powdered drug delivery. *Crit Rev Ther Drug Carrier Systems*, 16(4): 331–384, 1999.

CANEPA, P., CHIATTI, F., CORNO, M., SAKHNO, Y., MARTRA, G., AND UGLIENGO, P. Affinity of hydroxyapatite (001) and (010) surfaces to formic and alendronic acids: a quantum-mechanical and infrared study. *Phys Chem Chem Phys*, 13:1099–1111, 2011.

CANN, C., HARMER, M., HARVEY, K., AND ROSEN, M. Evaluation of a needle-free system for delivery of skin anaesthesia. *Anaesthesia*, 60(7):720, Jul 2005.

CANTER, J., MACKEY, K., GOOD, L. S., ROBERTO, R. R., CHIN, J., BOND, W. W., ALTER, M. J., AND HORAN, J. M. An outbreak of hepatitis b associated with jet injections in a weight reduction clinic. *Arch Intern Med*, 150(9):1923–7, Sep 1990.

CARDO, D. M., CULVER, D. H., CIESIELSKI, C. A., SRIVASTAVA, P. U., MARCUS, R., ABITEBOUL, D., HEPTONSTALL, J., IPPOLITO, G., LOT, F., MCKIBBEN, P. S., AND BELL, D. M. A case-control study of hiv seroconversion in health care workers after percutaneous exposure. centers for disease control and prevention needlestick surveillance group. *N Engl J Med*, 337(21):1485–90, Nov 1997.

CARPENTER, J. F., PIKAL, M. J., CHANG, B. S., AND RANDOLPH, T. W. Rational design of stable lyophilized protein formulations: Some practical advice. *Pharm Res*, 14(8):969–975, 1997.

CARPENTER, J. F., RANDOLPH, T. W., JISKOOT, W., CROMMELIN, D. J. A., MIDDAUGH, C. R., WINTER, G., FAN, Y.-X., KIRSHNER, S., VERTHELYI, D., KOZLOWSKI, S., CLOUSE, K. A., SWANN, P. G., ROSENBERG, A., AND CHERNEY, B. Overlooking subvisible particles in therapeutic protein products: gaps that may compromise product quality. *J Pharm Sci*, 98 (4):1201–5, Apr 2009.

CASADEVALL, N., NATAF, J., VIRON, B., KOLTA, A., KILADJIAN, J.-J., MARTIN-DUPONT, P., MICHAUD, P., PAPO, T., UGO, V., TEYSSANDIER, I., VARET, B., AND MAYEUX, P. Pure red-cell aplasia and antierythropoietin antibodies in patients treated with recombinant erythropoietin. *N Engl J Med*, 346(7):469–75, Feb 2002.

CAUX, C., VANBERVLIET, B., MASSACRIER, C., AZUMA, M., OKUMURA, K., LANIER, L. L., AND BANCHEREAU, J. B70/b7-2 is identical to cd86 and is the major functional ligand for cd28 expressed on human dendritic cells. *J Exp Med*, 180(5): 1841–7, Nov 1994.

CDC. Progress toward elimination of haemophilus influenzae type b disease among infants and children–united states, 1987-1993. *MMWR Morb Mortal Wkly Rep*, 43(8):144–8, Mar 1994.

CDC. Impact of vaccines universally recommended for children - united states, 1990-1998. *MMWR Morb Mortal Wkly Rep*, 48(12):243–248, 1999.

CHANG, J. Y., RAMSEIER, U., HAWTHORNE, T., O'REILLY, T., AND VAN OOSTRUM, J. Unique chemical reactivity of his-21 of crm-197, a mutated diphtheria toxin. *FEBS Lett*, 427(3):362–6, May 1998.

CHANG, L., SHEPHERD, D., SUN, J., OUELLETTE, D., GRANT, K. L., TANG, X., AND PIKAL, M. J. Mechanism of protein stabilization by sugars during freeze-drying and storage: Native structure preservation, specific interaction, and/or immobilization in a glassy matrix? *J Pharm Sci*, 94(7):1427–1444, 2005.

CHASE, M. W. Inhibition of experimental drug allergy by prior feeding of the sentisizing agent. *Proc Soc Exp Biol Med*, 61:257–259, 1946.

CHEN, D., BURGER, M., CHU, Q., ENDRES, R., ZULEGER, C., DEAN, H., AND PAYNE, L. G. Epidermal powder immunization: Cellular and molecular mechanisms for enhancing vaccine immunogenicity. *Virus Res*, 103(1-2):147–153, 2004a.

CHEN, D., ENDRES, R., MAA, Y. F., KENSIL, C. R., WHITAKER-DOWLING, P., TRICHEL, A., YOUNGNER, J. S., AND PAYNE, L. G. Epidermal powder immunization of mice and monkeys with an influenza vaccine. *Vaccine*, 21(21-22):2830–2836, 2003.

CHEN, D., ENDRES, R. L., ERICKSON, C. A., MAA, Y. F., AND PAYNE, L. G. Epidermal powder immunization using non-toxic bacterial enterotoxin adjuvants with influenza vaccine augments protective immunity. *Vaccine*, 20(21-22):2671–2679, 2002a.

CHEN, D., ENDRES, R. L., ERICKSON, C. A., WEIS, K. F., MCGREGOR, M. W., KAWAOKA, Y., AND PAYNE, L. G. Epidermal immunization by a needle-free powder delivery technology: immunogenicity of influenza vaccine and protection in mice. *Nat Med*, 6(10):1187–90, Oct 2000.

CHEN, D., ERICKSON, C. A., ENDRES, R. L., PERIWAL, S. B., CHU, Q., SHU, C., MAA, Y. F., AND PAYNE, L. G. Adjuvantation of epidermal powder immunization. *Vaccine*, 19(20-22):2908–2917, 2001a.

CHEN, D., PERIWAL, S. B., LARRIVEE, K., ZULEGER, C., ERICKSON, C. A., ENDRES, R. L., AND PAYNE, L. G. Serum and mucosal immune responses to an inactivated influenza virus vaccine induced by epidermal powder immunization. *J Virol*, 75(17):7956–7965, 2001b.

CHEN, D., ZULEGER, C., CHU, Q., MAA, Y. F., OSORIO, J., AND PAYNE, L. G. Epidermal powder immunization with a recombinant hiv gp120 targets langerhans cells and induces enhanced immune responses. *AIDS Res Hum Retrovir*, 18(10):715–722, 2002b.

CHEN, D. AND KRISTENSEN, D. Opportunities and challenges of developing thermostable vaccines. *Expert Rev Vaccines*, 8(5):547–57, May 2009.

CHEN, Q., SUKI, B., AND AN, K. Dynamic mechanical properties of agarose gels modeled by a fractional derivative model. *J Biomech Eng-T Asme*, 126:666–671, 2004b.

CHEN, T., D'ADDIO, S. M., KENNEDY, M. T., SWIETLOW, A., KEVREKIDIS, I. G., PANAGIOTOPOULOS, A. Z., AND PRUD'HOMME, R. K. Protected peptide nanoparticles: Experiments and brownian dynamics simulations of the energetics of assembly. *Nano Letters*, 9:2218–2222, 2009.

CHEN, X., FERNANDO, G. J. P., CRICHTON, M. L., FLAIM, C., YUKIKO, S. R., FAIRMAID, E. J., CORBETT, H. J., PRIMIERO, C. A., ANSALDO, A. B., FRAZER, I. H., BROWN, L. E., AND KENDALL, M. A. F. Improving the reach of vaccines to low-resource regions, with a needle-free vaccine delivery device and long-term thermostabilization. *J Control Release*, 152(3):349–55, Jun 2011.

CHI, E. Y., KRISHNAN, S., KENDRICK, B. S., CHANG, B. S., CARPENTER, J. F., AND RANDOLPH, T. W. Roles of conformational stability and colloidal stability in the aggregation of recombinant human granulocyte colony-stimulating factor. *Protein Sci*, 12(5):903–13, May 2003.

CHOE, S., BENNETT, M. J., FUJII, G., CURMI, P. M., KANTARDJIEFF, K. A., COLLIER, R. J., AND EISENBERG, D. The crystal structure of diphtheria toxin. *Nature*, 357(6375):216–22, May 1992.

COLLIER, R. J. Understanding the mode of action of diphtheria toxin: a perspective on progress during the 20th century. *Toxicon*, 39(11):1793–803, Nov 2001.

COSTANTINO, H. R., FIROUZABADIAN, L., HOGELAND, K., WU, C., BEGANSKI, C., CARRASQUILLO, K. G., CÂĹŽÂĽĚRDOVA, M., GRIEBENOW, K., ZALE, S. E., AND TRACY, M. A. Protein spray-freeze drying. effect of atomization conditions on particle size and stability. *Pharm Res*, 17(11):1374–1383, 2000.

COSTANTINO, H. R., FIROUZABADIAN, L., WU, C., CARRASQUILLO, K. G., GRIEBENOW, K., ZALE, S. E., AND TRACY, M. A. Protein spray freeze drying. 2. effect of formulation variables on particle size and stability. *J Pharm Sci*, 91(2):388–95, Feb 2002.

COSTANTINO, H. R. AND PIKAL, M. J. *Lyophilization of biopharmaceuticals*, volume v. 2 of *Biotechnology*. AAPS Press, Arlington, VA, 2004. ISBN 0971176760.

COSTIGAN, G., LIU, Y., BROWN, G. L., CARTER, F. V., AND BELLHOUSE, B. J. *Evolution of the design of Venturi devices for the delivery of dry particles to skin or mucosal tissue*. Springer Berlin Heidelberg, Beijing, China, July 2004.

CRANE, D. T., BOLGIANO, B., AND JONES, C. Comparison of the diphtheria mutant toxin, crm197, with a haemophilus influenzae type-b polysaccharide-crm197 conjugate by optical spectroscopy. *Eur J Biochem*, 246(2):320–7, Jun 1997.

CURTIS, R. A., ULRICH, J., MONTASER, A., PRAUSNITZ, J. M., AND BLANCH, H. W. Protein-protein interactions in concentrated electrolyte solutions. *Biotechnol Bioeng*, 79(4):367–80, Aug 2002.

DAMODARAN, S. AND SONG, K. B. Kinetics of adsorption of proteins at interfaces: role of protein conformation in diffusional adsorption. *Biochim Biophys Acta*, 954(3):253–64, Jun 1988.

DARLENSKI, R. AND FLUHR, J. W. Influence of skin type, race, sex, and anatomic location on epidermal barrier function. *Clin Dermatol*, 30(3):269–73, 2012.

DAS, P. Revolutionary vaccine technology breaks the cold chain. *Lancet Infect Dis*, 4(12):719, Dec 2004.

DEAN, H. J. AND CHEN, D. Epidermal powder immunization against influenza. *Vaccine*, 23(5):681–686, 2004.

DEAN, H. J., FULLER, D., AND OSORIO, J. E. Powder and particle-mediated approaches for delivery of dna and protein vaccines into the epidermis. *Comp Immunol Microbiol Infect Dis*, 26(5-6):373–388, 2003.

DEHN, J. A unified theory of penetration. *Int J Impact Eng*, 5(1-4):239–248, 1987.

DENET, A.-R., VANBEVER, R., AND PRÉAT, V. Skin electroporation for transdermal and topical delivery. *Adv Drug Deliv Rev*, 56(5):659–74, Mar 2004.

DHANKHAR, A., EVERS, M., AND MOLLER, M. Escaping the sword of damocles: Toward a new future for pharmaceutical research and development. *McKinsey Perspectives on Drug and Device Reseach and Development*, 2012.

DILL, K. A. AND CHAN, H. S. From levinthal to pathways to funnels. *Nat Struct Biol*, 4(1):10–9, Jan 1997.

DOBSON, C. M. Protein folding and misfolding. *Nature*, 426(6968):884–90, Dec 2003.

EDWARDS, M. S., NICHOLSON-WELLER, A., BAKER, C. J., AND KASPER, D. L. The role of specific antibody in alternative complement pathway-mediated opsonophagocytosis of type iii, group b streptococcus. *J Exp Med*, 151(5):1275–87, May 1980.

EISENTHAL, R., PETERSON, M. E., DANIEL, R. M., AND DANSON, M. J. The thermal behaviour of enzyme activity: implications for biotechnology. *Trends Biotechnol*, 24(7):289–92, Jul 2006.

EL KADY, A. A., MOHAMED, K. R., AND EL-BASSYOUNI, G. T. Fabrication, characterization and bioactivity evaluation of calcium pyrophosphate/polymeric biocomposites. *Ceram Int*, 35:2933–2942, 2009.

ELIEZER, D., YAO, J., DYSON, H. J., AND WRIGHT, P. E. Structural and dynamic characterization of partially folded states of apomyoglobin and implications for protein folding. *Nat Struct Biol*, 5(2): 148–55, Feb 1998.

FALNES, P. O., CHOE, S., MADSHUS, I. H., WILSON, B. A., AND OLSNES, S. Inhibition of membrane translocation of diphtheria toxin a-fragment by internal disulfide bridges. *J Biol Chem*, 269(11):8402–7, Mar 1994.

FANG, W.-J., QI, W., KINZELL, J., PRESTRELSKI, S., AND CARPENTER, J. F. Effects of excipients on the chemical and physical stability of glucagon during freeze-drying and storage in dried formulations. *Pharm Res*, 29:3278–3291, 2012.

FAWCETT, H. A. AND SMITH, N. P. Injection-site granuloma due to aluminum. *Arch Dermatol*, 120(10): 1318–22, Oct 1984.

FDA. Guidance for industry. immunogenicity assessment for therapeutic protein products. Technical report, Food and Drug Administration, February 2013.

FERNÁNDEZ-DE CASTRO, J., KUMATE-RODRÍGUEZ, J., SEPÚLVEDA, J., RAMÍREZ-ISUNZA, J. M., AND VALDESPINO-GÓMEZ, J. L. [measles vaccination by the aerosol method in mexico]. *Salud Publica Mex*, 39(1):53–60, 1997.

FINK, A. L. Protein aggregation: folding aggregates, inclusion bodies and amyloid. *Fold Des*, 3(1):R9–23, 1998.

FITZSIMONS, S. A., MULVIHILL, D. M., AND MORRIS, E. R. Denaturation and aggregation processes in thermal gelation of whey proteins resolved by differential scanning calorimetry. *Food Hydrocolloids*, 21:638–644, 2007.

FOIT, L., MORGAN, G. J., KERN, M. J., STEIMER, L. R., VON HACHT, A. A., TITCHMARSH, J., WARRINER, S. L., RADFORD, S. E., AND BARDWELL, J. C. A. Optimizing protein stability in vivo. *Mol Cell*, 36(5): 861–71, Dec 2009.

FUHLBRIGGE, R. C., DAVID KIEFFER, J., ARMERDING, D., AND KUPPER, T. S. Cutaneous lymphocyte antigen is a specialized form of psgl-1 expressed on skin-homing t cells. *Nature*, 389(6654):978–981, 1997.

GAMBLE, C. N. The role of soluble aggregates in the primary immune response of mice to human gamma globulin. *Int Arch Allergy Appl Immunol*, 30(5):446–55, 1966.

GAVI. Gavi alliance revised co-financing policy. Technical report, GAVI, 2010.

GAVI. Haemophilus influenzae type b vaccine support. Technical report, Global Allience for Vaccines and Immuniztions, August 2011.

GEIGER, T. AND CLARKE, S. Deamidation, isomerization, and racemization at asparaginyl and aspartyl residues in peptides. succinimide-linked reactions that contribute to protein degradation. *J Biol Chem*, 262(2):785–94, Jan 1987.

GIANNINI, G., RAPPUOLI, R., AND RATTI, G. The amino-acid sequence of two non-toxic mutants of diphtheria toxin: Crm45 and crm197. *Nucleic Acids Res*, 12(10):4063–9, May 1984.

GINDY, M. E., PANAGIOTOPOULOS, A. Z., AND PRUD'HOMME, R. K. Composite block copolymer stabilized nanoparticles: Simultaneous encapsulation of organic actives and inorganic nanostructures. *Langmuir*, 24:83–90, 2008.

GINDY, M. E. AND PRUD'HOMME, R. K. Multifunctional nanoparticles for imaging, delivery and targeting in cancer therapy. *Expert Opin Drug Del*, 6: 865–878, 2009.

GINEBRA, M. P., TRAYKOVA, T., AND PLANELL, J. A. Calcium phosphate cements as bone drug delivery systems: A review. *J Control Release*, 113(2):102–110, 2006.

GIRARDI, M. Cutaneous perspectives on adaptive immunity. *Clin Rev Allerg Immunol*, 33(1-2):4–14, 2007.

GIUDICE, E. L. AND CAMPBELL, J. D. Needle-free vaccine delivery. *Adv Drug Deliv Rev*, 58(1):68–89, Apr 2006.

GOEBELS, N., MICHAELIS, D., WEKERLE, H., AND HOHLFELD, R. Human myoblasts as antigen-presenting cells. *J Immunol*, 149(2):661–667, 1992.

GRUBER, J. V. *Principles of polymer science and technology in cosmetics and personal care.* Marcel Dekker, Inc, New York, 1999.

GUHA, R. A., SHEAR, N. H., AND PAPINI, M. Ballistic impact of single particles into gelatin: experiments and modeling with application to transdermal pharmaceutical delivery. *J Biomech Eng*, 132 (10), 2010.

GUPTA, P. N., MISHRA, V., SINGH, P., RAWAT, A., DUBEY, P., MAHOR, S., AND VYAS, S. P. Tetanus toxoid-loaded transfersomes for topical immunization. *J Pharm Pharmacol*, 57(3):295–301, Mar 2005.

GUPTA, R. Aluminum compounds as vaccine adjuvants. *Adv Drug Deliv Rev*, 32(3):155–172, 1998.

GUTIERRO, I., HERNÁNDEZ, R. M., IGARTUA, M., GASCÓN, A. R., AND PEDRAZ, J. L. Size dependent immune response after subcutaneous, oral and intranasal administration of bsa loaded nanospheres. *Vaccine*, 21(1-2):67–77, Nov 2002.

GUTTORMSEN, H. K., SHARPE, A. H., CHANDRAKER, A. K., BRIGTSEN, A. K., SAYEGH, M. H., AND KASPER, D. L. Cognate stimulatory b-cell-t-cell interactions are critical for t-cell help recruited by glycoconjugate vaccines. *Infect Immun*, 67(12):6375–84, Dec 1999.

HAENSLER, J., VERDELET, C., SANCHEZ, V., GIRERD-CHAMBAZ, Y., BONNIN, A., TRANNOY, E., KRISHNAN, S., AND MEULIEN, P. Intradermal dna immunization by using jet-injectors in mice and monkeys. *Vaccine*, 17(7-8):628–38, Feb 1999.

HAMILTON, J. G. Needle phobia: a neglected diagnosis. *J Fam Pract*, 41(2):169–75, Aug 1995.

HAN, J., ZHU, Z., QIAN, H., WOHL, A. R., BEAMAN, C. J., HOYE, T. R., AND MACOSKO, C. W. A simple confined impingement jets mixer for flash nanoprecipitation. *J Pharm Sci*, 101(10):4018–23, Oct 2012.

HANCOCK, B. AND ZOGRAF, G. Characteristics and significance of the amorphous state in pharmaceutical systems. *J Pharm Sci*, 86:1–12, 1997.

HARDING, I., RASHID, N., AND HING, K. Surface charge and the effect of excess calcium ions on the hydroxyapatite surface. *Biomaterials*, 26:6818–6826, 2005.

HENGSBERGER, S., KULIK, A., AND ZYSSET, P. A combined atomic force microscopy and nanoindentation technique to investigate the elastic properties of bone structural units. *Eur Cell Mater*, 1:12–7, Jan 2001.

HINGSON, R. A. AND FIGGE, F. H. J. A survey of the development of jet injection in parenteral therapy. *Curr Res Anesth Analg*, 31(6):361–6, 1952.

HOLBROOK, K. A. AND ODLAND, G. F. Regional differences in the thickness (cell layers) of the human stratum corneum: an ultrastructural analysis. *J Invest Dermatol*, 62(4):415–22, Apr 1974.

HOLMGREN, J. AND CZERKINSKY, C. Mucosal immunity and vaccines. *Nat Med*, 11(4 SUPPL.):S45–S53, 2005.

HUANG, P., DONG, A., AND CAUGHEY, W. S. Effects of dimethyl sulfoxide, glycerol, and ethylene glycol on secondary structures of cytochrome c and lysozyme as observed by infrared spectroscopy. *J Pharm Sci*, 84(4):387–92, Apr 1995.

IAFISCO, M., DI FOGGIA, M., BONORA, S., PRAT, M., AND ROVERI, N. Adsorption and spectroscopic characterization of lactoferrin on hydroxyapatite nanocrystals. *Dalton Trans*, 40(4):820–7, Jan 2011.

IMESON, D. A. AND LEDWARD, J. R. M. On the nature of the interaction between some anionic polysaccharides and proteins. *J Sci Food Agr*, 28(8):661–668, 1977.

JAENICKE, R. Stability and stabilization of globular proteins in solution. *J Biotechnol*, 79(3):193–203, May 2000.

JASWAL, S. S., SOHL, J. L., DAVIS, J. H., AND AGARD, D. A. Energetic landscape of alpha-lytic protease optimizes longevity through kinetic stability. *Nature*, 415(6869):343–6, Jan 2002.

JIANG, D., PREMACHANDRA, G. S., JOHNSTON, C., AND HEM, S. L. Structure and adsorption properties of commercial calcium phosphate adjuvant. *Vaccine*, 23(5):693–8, Dec 2004.

JOHNSON, B. AND PRUD'HOMME, R. Chemical processing and micromixing in confined impinging jets. *Aiche J*, 49:2264–2282, 2003a.

JOHNSON, B. AND PRUD'HOMME, R. Flash nanoprecipitation of organic actives and block copolymers using a confined impinging jets mixer. *Aust J Chem*, 56:1021–1024, 2003b.

JOHNSON, O. L., JAWOROWICZ, W., CLELAND, J. L., BAILEY, L., CHARNIS, M., DUENAS, E., WU, C., SHEPARD, D., MAGIL, S., LAST, T., JONES, A. J., AND PUTNEY, S. D. The stabilization and encapsulation of human growth hormone into biodegradable microspheres. *Pharm Res*, 14(6):730–5, Jun 1997.

JUMEL, K., HO, M. M., AND BOLGIANO, B. Evaluation of meningococcal c oligosaccharide conjugate vaccines by size-exclusion chromatography/multi-angle laser light scattering. *Biotechnol Appl Biochem*, 36(Pt 3):219–26, Dec 2002.

KAHLON, R., HU, Y., ORTEU, C. H., KIFAYET, A., TRUDEAU, J. D., TAN, R., AND DUTZ, J. P. Optimization of epicutaneous immunization for the induction of ctl. *Vaccine*, 21(21-22):2890–9, Jun 2003.

KALKA-MOLL, W. M., TZIANABOS, A. O., BRYANT, P. W., NIEMEYER, M., PLOEGH, H. L., AND KASPER, D. L. Zwitterionic polysaccharides stimulate t cells by mhc class ii-dependent interactions. *J Immunol*, 169(11):6149–53, Dec 2002.

KAMBOJ, K. K., KIRCHNER, H. L., KIMMEL, R., GREENSPAN, N. S., AND SCHREIBER, J. R. Significant variation in serotype-specific immunogenicity of the seven-valent streptococcus pneumoniae capsular polysaccharide-crm197 conjugate vaccine occurs despite vigorous t cell help induced by the carrier protein. *J Infect Dis*, 187(10):1629–38, May 2003.

KARANDE, P., JAIN, A., AND MITRAGOTRI, S. Discovery of transdermal penetration enhancers by high-throughput screening. *Nat Biotechnol*, 22(2):192–7, Feb 2004.

KAYED, R., HEAD, E., THOMPSON, J., MCINTIRE, T., MILTON, S., COTMAN, C., AND GLABE, C. Common structure of soluble amyloid oligomers implies common mechanism of pathogenesis. *Science*, 300:486–489, 2003.

KELLY, D. F., MOXON, E. R., AND POLLARD, A. J. Haemophilus influenzae type b conjugate vaccines. *Immunology*, 113(2):163–174, 2004.

KELLY, D. F., THORSON, S., MASKEY, M., MAHAT, S., SHRESTHA, U., HAMALUBA, M., WILLIAMS, E., DONGOL, S., WERNO, A. M., PORTESS, H., YADAV, B. K., ADHIKARI, N., GUIVER, M., THOMAS, K., MURDOCH, D. R., AND POLLARD, A. J. The burden of vaccine-preventable invasive bacterial infections and pneumonia in children admitted to hospital in urban nepal. *Int J Infect Dis*, 15(1):e17–23, Jan 2011.

KENDALL, M., MITCHELL, T., AND WRIGHTON-SMITH, P. Intradermal ballistic delivery of micro-particles into excised human skin for pharmaceutical applications. *J Biomech*, 37(11):1733–1741, 2004a.

KENDALL, M. A. F., QUINLAN, N., THORPE, S., AINSWORTH, R., AND BELLHOUSE, B. J. B. Measurements of the gas and particle flow within a converging-diverging nozzle for high-speed powdered vaccine and drug delivery. *Exp Fluids*, 37: 128–36, 2004b.

KENDALL, M. A. F., WRIGHTON SMITH, P. J., AND BELLHOUSE, B. J. Transdermal ballistic delivery of micro-particles investigation into skin penetration. In NA, editor, *Conference Proceedings*, Chicago IL, July 23-28 2000. EMBS, Annual International Conference.

KENDALL, M. The delivery of particulate vaccines and drugs to human skin with a practical, hand-held shock tube-based system. *Shock Waves*, 12:23–30, 2002.

KENDALL, M., MITCHELL, T. J., COSTIGAN, G., ARMITAGE, M., LENZO, J. C., THOMAS, J. A., VON GARNIER, C., ZOSKY, G. R., TURNER, D. J., STUMBLES, P. A., SLY, P. D., HOLT, P. G., AND THOMAS, W. R. Downregulation of ige antibody and allergic responses in the lung by epidermal biolistic microparticle delivery. *J Allergy Clin Immunol*, 117(2): 275–82, Feb 2006.

KENDALL, M., RISHWORTH, S., CARTER, F., AND MITCHELL, T. Effects of relative humidity and ambient temperature on the ballistic delivery of micro-particles to excised porcine skin. *J Invest Dermatol*, 122(3):739–46, Mar 2004c.

KENDALL, M. A. F., CHONG, Y.-F., AND COCK, A. The mechanical properties of the skin epidermis in relation to targeted gene and drug delivery. *Biomaterials*, 28(33):4968–77, Nov 2007.

KENT, M. S., YIM, H., MURTON, J. K., SATIJA, S., MAJEWSKI, J., AND KUZMENKO, I. Oligomerization of membrane-bound diphtheria toxin (crm197) facilitates a transition to the open form and deep insertion. *Biophys J*, 94(6):2115–27, Mar 2008.

KERMODE, M. Unsafe injections in low-income country health settings: Need for injection safety promotion to prevent the spread of blood-borne viruses. *Health Prom Int*, 19(1):95–103, 2004.

KERSTEN, G. AND HIRSCHBERG, H. Needle-free vaccine delivery. *Expert Opin Drug Deliv*, 4(5):459–74, Sep 2007.

KIMURA, T. *Molten Salt Synthesis of Ceramic Powders*, volume Advances in Ceramics - Synthesis and Characterization, Processing and Specific Applications. InTech, Singapore, 2011.

KINNEY, J., BALOOCH, M., MARSHALL, S., MARSHALL, G., AND WEIHS, T. Hardness and young's modulus of human peritubular and intertubular dentine. *Arch Oral Biol*, 41:9–13, 1996.

KLUNKER, S., TRAUTMANN, A., AKDIS, M., VERHAGEN, J., SCHMID-GRENDELMEIER, P., BLASER, K., AND AKDIS, C. A. A second step of chemotaxis after transendothelial migration: Keratinocytes undergoing apoptosis release ifn-γ-inducible protein 10, monokine induced by ifn-γ, and ifn-γ-inducible α-chemoattractant for t cell chemotaxis toward epidermis in atopic dermatitis. *J Immunol*, 171(2): 1078–1084, 2003.

KOCH, C., JENSEN, S., OSTER, A., AND HOUEN, G. A comparison of the immunogenicity of the native and denatured forms of a protein. *Apmis*, 104:115–125, 1996.

KOGAN, A. AND GARTI, N. Microemulsions as transdermal drug delivery vehicles. *Adv Colloid Interfac*, 123:369–385, 2006.

KON, E., MURAGLIA, A., CORSI, A., BIANCO, P., MARCACCI, M., MARTIN, I., BOYDE, A., RUSPANTINI, I., CHISTOLINI, P., ROCCA, M., GIARDINO, R., CANCEDDA, R., AND QUARTO, R. Autologous bone marrow stromal cells loaded onto porous hydroxyapatite ceramic accelerate bone repair in critical-size defects of sheep long bones. *J Biomed Mater Res*, 49:328–337, 2000.

KONDO, T., MCGREGOR, M., CHU, Q., CHEN, D., HORIMOTO, T., AND KAWAOKA, Y. A protective effect of epidermal powder immunization in a mouse model of equine herpesvirus-1 infection. *Virology*, 318(1):414–419, 2004.

KUMAR, S., MA, B., TSAI, C. J., SINHA, N., AND NUSSINOV, R. Folding and binding cascades: dynamic landscapes and population shifts. *Protein Sci*, 9(1): 10–9, Jan 2000.

KUPPER, T. S. AND FUHLBRIGGE, R. C. Immune surveillance in the skin: Mechanisms and clinical consequences. *Nat Rev Immunol*, 4(3):211–222, 2004.

KURFÜRST, M. M. Detection and molecular weight determination of polyethylene glycol-modified hirudin by staining after sodium dodecyl sulfate-polyacrylamide gel electrophoresis. *Anal Biochem*, 200(2):244–8, Feb 1992.

LAI, Z. AND SCHREIBER, J. R. Antigen processing of glycoconjugate vaccines; the polysaccharide portion of the pneumococcal crm(197) conjugate vaccine co-localizes with mhc ii on the antigen processing cell surface. *Vaccine*, 27(24):3137–44, May 2009.

LAILA-HUQ, N., CROSS, K. J., AND REYNOLDS, E. Molecular modelling of a multiphosphorylated sequence motif bound to hydroxyapatite surfaces. *J Molec Model*, 6(2):35–47, 2000.

LECHMANN, T. AND REINHART, W. H. The non-ionic surfactant poloxamer 188 (rheothrx) increases plasma and whole blood viscosity. *Clin Hemorheol Microcirc*, 18(1):31–6, Apr 1998.

LEE, E. H.-J., LEWIS, R. F., MAKUMBI, I., KEKITIINWA, A., EDIAMU, T. D., BAZIBU, M., BRAKA, F., FLANNERY, B., ZUBER, P. L., AND FEIKIN, D. R. Haemophilus influenzae type b conjugate vaccine is highly effective in the ugandan routine immunization program: a case-control study. *Trop Med Int Health*, 13(4):495–502, Apr 2008a.

LEE, J. C. AND TIMASHEFF, S. N. The calculation of partial specific volumes of proteins in guanidine hydrochloride. *Arch Biochem Biophys*, 165(1):268–73, Nov 1974.

LEE, J. W., PARK, J.-H., AND PRAUSNITZ, M. R. Dissolving microneedles for transdermal drug delivery. *Biomaterials*, 29(13):2113–24, May 2008b.

LEGEROS, R. Z., LIN, S., ROHANIZADEH, R., MIJARES, D., AND LEGEROS, J. P. Biphasic calcium phosphate bioceramics: Preparation, properties and applications. *J Mater Sci: Mater Med*, 14(3):201–209, 2003.

LELEUX, J. AND ROY, K. Micro and nanoparticle-based delivery systems for vaccine immunotherapy: an immunological and materials perspective. *Adv Healthc Mater*, 2(1):72–94, Jan 2013.

LESINSKI, G. B. AND WESTERINK, M. A. Vaccines against polysaccharide antigens. *Curr Drug Targets Infect Disord*, 1(3):325–34, Nov 2001.

LEV-RAM, M. Get your shots without any needles. *CNN Money*, November 2010.

LEVI, G. AND KAREL, M. Volumetric shrinkage (collapse) in freeze-dried carbohydrates above their glass-transition temperature. *Food Res Int*, 28:145–151, 1995.

LEVY, Y. AND ONUCHIC, J. N. Water and proteins: a love-hate relationship. *Proc Natl Acad Sci U S A*, 101 (10):3325–6, Mar 2004.

LI, S., SCHÖNEICH, C., AND BORCHARDT, R. T. Chemical instability of protein pharmaceuticals: Mechanisms of oxidation and strategies for stabilization. *Biotechnol Bioeng*, 48(5):490–500, Dec 1995.

LIMPERT, E., STAHEL, W., AND ABBT, M. Log-normal distributions across the sciences: Keys and clues. *Bioscience*, 51:341–352, 2001.

LIN, W.-H., GRIFFIN, D. E., ROTA, P. A., PAPANIA, M., CAPE, S. P., BENNETT, D., QUINN, B., SIEVERS, R. E., SHERMER, C., POWELL, K., ADAMS, R. J., GODIN, S., AND WINSTON, S. Successful respiratory immunization with dry powder live-attenuated measles virus vaccine in rhesus macaques. *Proc Natl Acad Sci U S A*, 108(7):2987–92, Feb 2011.

LIU, Y. Utilization of the venturi effect to introduce micro-particles for epidermal vaccination. *Med Eng Phys*, 29(3):390–397, 2007.

LIU, Y. AND KENDALL, M. A. F. Optimization of a jet-propelled particle injection system for the uniform transdermal delivery of drug/vaccine. *Biotechnol Bioeng*, 97:1300–1308, 2007.

LORY, S., CARROLL, S. F., BERNARD, P. D., AND COLLIER, R. J. Ligand interactions of diphtheria toxin. i. binding and hydrolysis of nad. *J Biol Chem*, 255 (24):12011–5, Dec 1980.

LOUIE, G. V., YANG, W., BOWMAN, M. E., AND CHOE, S. Crystal structure of the complex of diphtheria toxin with an extracellular fragment of its receptor. *Mol Cell*, 1(1):67–78, Dec 1997.

MAA, Y. F., NGUYEN, P. A., AND HSU, S. W. Spray-drying of air-liquid interface sensitive recombinant human growth hormone. *J Pharm Sci*, 87(2):152–9, Feb 1998.

MAA, Y. F. AND PRESTRELSKI, S. J. Biopharmaceutical powders: particle formation and formulation considerations. *Curr Pharm Biotechnol*, 1(3):283–302, Nov 2000.

MAA, Y. F., SHU, C., AMERI, M., ZULEGER, C., CHE, J., OSORIO, J. E., PAYNE, L. G., AND CHEN, D. Optimization of an alum-adsorbed vaccine powder formulation for epidermal powder immunization. *Pharm Res*, 20(7):969–977, 2003a.

MAA, Y. F., ZHAO, L., PAYNE, L. G., AND CHEN, D. Stabilization of alum-adjuvanted vaccine dry powder formulations: Mechanism and application. *J Pharm Sci*, 92(2):319–332, 2003b.

MAA, Y.-F., AMERI, M., RIGNEY, R., PAYNE, L. G., AND CHEN, D. Spray-coating for biopharmaceutical powder formulations: beyond the conventional scale and its application. *Pharm Res*, 21(3):515–23, Mar 2004a.

MAA, Y.-F., AMERI, M., SHU, C., PAYNE, L. G., AND CHEN, D. Influenza vaccine powder formulation development: spray-freeze-drying and stability evaluation. *J Pharm Sci*, 93(7):1912–23, Jul 2004b.

MAA, Y.-F., AMERI, M., SHU, C., ZULEGER, C. L., CHE, J., OSORIO, J. E., PAYNE, L. G., AND CHEN, D. Hepatitis-b surface antigen (hbsag) powder formulation: process and stability assessment. *Curr Drug Deliv*, 4(1):57–67, Jan 2007.

MADISON, K. C. Barrier function of the skin: "la raison d'être" of the epidermis. *J Invest Dermatol*, 121(2): 231–41, Aug 2003.

MALITO, E., BURSULAYA, B., CHEN, C., LO SURDO, P., PICCHIANTI, M., BALDUCCI, E., BIANCUCCI, M., BROCK, A., BERTI, F., BOTTOMLEY, M. J., NISSUM, M., COSTANTINO, P., RAPPUOLI, R., AND SPRAGGON, G. Structural basis for lack of toxicity of the diphtheria toxin mutant crm197. *Proc Natl Acad Sci U S A*, 109(14):5229–34, Apr 2012.

MALLAPRAGADA, S. K. AND NARASIMHAN, B. Immunomodulatory biomaterials. *Int J Pharm*, 364 (2):265–71, Dec 2008.

MANNING, M., PATEL, K., AND BORCHARDT, R. Stability of protein pharmaceuticals. *Pharm Res*, 6(11): 903–918, November 1989.

MANTEGAZZA, R., HUGHES, S. M., MITCHELL, D., TRAVIS, M., BLAU, H. M., AND STEINMAN, L. Modulation of mhc class ii antigen expression in human myoblasts after treatment with ifn-gamma. *Neurology*, 41(7):1128–1132, 1991.

MARINO, M., SCUDERI, F., PROVENZANO, C., AND BARTOCCIONI, E. Skeletal muscle cells: From local inflammatory response to active immunity. *Gene Ther*, 18(2):109–116, 2011.

MARSEE, D. K., WILLIAMS, J. M., AND VELAZQUEZ, E. F. Aluminum granuloma after administration of the quadrivalent human papillomavirus vaccine. report of a case. *Am J Dermatopathol*, 30(6):622–4, Dec 2008.

MARTINI, H., ENRIGHT, V., PERRO, M., WORKMAN, S., BIRMELIN, J., GIORDA, E., QUINTI, I., LOUGARIS, V., BARONIO, M., WARNATZ, K., AND GRIMBACHER, B. Importance of b cell co-stimulation in cd4(+) t cell differentiation: X-linked agammaglobulinaemia, a human model. *Clin Exp Immunol*, 164 (3):381–7, Jun 2011.

MAURY, M., MURPHY, K., KUMAR, S., SHI, L., AND LEE, G. Effects of process variables on the powder yield of spray-dried trehalose on a laboratory spray-dryer. *Euro. J. Pharm. Biopharm.*, 59:565–573, 2005.

MAVROPOULOS, E., COSTA, A. M., COSTA, L. T., ACHETE, C. A., MELLO, A., GRANJEIRO, J. M., AND ROSSI, A. M. Adsorption and bioactivity studies of albumin onto hydroxyapatite surface. *Colloids Surf B Biointerfaces*, 83(1):1–9, Mar 2011.

MAYES, S. AND FERRONE, M. Fentanyl hcl patient-controlled iontophoretic transdermal system for the management of acute postoperative pain. *Ann Pharmacother*, 40(12):2178–86, Dec 2006.

MAZMANIAN, S. K. AND KASPER, D. L. The love-hate relationship between bacterial polysaccharides and the host immune system. *Nat Rev Immunol*, 6(11):849–58, Nov 2006.

MICHAELIS, D., GOEBELS, N., AND HOHLFELD, R. Constitutive and cytokine-induced expression of human leukocyte antigens and cell adhesion molecules by human myotubes. *Am J Pathol*, 143 (4):1142–1149, 1993.

MILLER, D. P. AND LECHUGA-BALLESTEROS, D. Rapid assessment of the structural relaxation behavior of amorphous pharmaceutical solids: effect of residual water on molecular mobility. *Pharm Res*, 23(10): 2291–305, Oct 2006.

MILSTIEN, J., GALAZKA, A., AND KARTOGLU, U. Temperature sensitivity of vaccines. *WHO*, 2006.

MIRZAEI, H. AND REGNIER, F. Protein:protein aggregation induced by protein oxidation. *J Chromatogr B Analyt Technol Biomed Life Sci*, 873(1):8–14, Sep 2008.

MISRA, A., GANGA, S., AND UPADHYAY, P. Needle-free, non-adjuvanted skin immunization by electroporation-enhanced transdermal delivery of diphtheria toxoid and a candidate peptide vaccine against hepatitis b virus. *Vaccine*, 18(5-6):517–23, Oct 1999.

MITCHELL, T. *The ballistics of micro-particles into the mucosa and skin.* PhD thesis, Department of Engineering Science University of Oxford, Oxford, 2003.

MITCHELL, T., KENDALL, M., AND BELLHOUSE, B. A ballistic study of micro-particle penetration to the oral mucosa. *Int J Impact Eng*, 28:581–599, 2003.

MITRAGOTRI, S. Immunization without needles. *Nat Rev Immunol*, 5(12):905–916, 2005.

MIYANO, T., TOBINAGA, Y., KANNO, T., MATSUZAKI, Y., TAKEDA, H., WAKUI, M., AND HANADA, K. Sugar micro needles as transdermic drug delivery system. *Biomed Microdevices*, 7(3):185–8, Sep 2005.

MOON, J. J., SUH, H., BERSHTEYN, A., STEPHAN, M. T., LIU, H., HUANG, B., SOHAIL, M., LUO, S., UM, S. H., KHANT, H., GOODWIN, J. T., RAMOS, J., CHIU, W., AND IRVINE, D. J. Interbilayer-crosslinked multilamellar vesicles as synthetic vaccines for potent humoral and cellular immune responses. *Nat Mater*, 10(3):243–51, Mar 2011.

MOON, J. J., SUH, H., LI, A. V., OCKENHOUSE, C. F., YADAVA, A., AND IRVINE, D. J. Enhancing humoral responses to a malaria antigen with nanoparticle vaccines that expand tfh cells and promote germinal center induction. *Proc Natl Acad Sci U S A*, 109 (4):1080–5, Jan 2012.

MOREFIELD, G. L., SOKOLOVSKA, A., JIANG, D., HOGENESCH, H., ROBINSON, J. P., AND HEM, S. L. Role of aluminum-containing adjuvants in antigen internalization by dendritic cells in vitro. *Vaccine*, 23(13):1588–95, Feb 2005.

MOTTRAM, P. L., LEONG, D., CRIMEEN-IRWIN, B., GLOSTER, S., XIANG, S. D., MEANGER, J., GHILDYAL, R., VARDAXIS, N., AND PLEBANSKI, M. Type 1 and 2 immunity following vaccination is influenced by nanoparticle size: Formulation of a model vaccine for respiratory syncytial virus. *Mol Pharmaceut*, 4:73–84, 2007.

MURDAN, S., SOMAVARAPU, S., ROSS, A. C., ALPAR, H. O., AND PARKER, M. C. Immobilisation of vaccines onto micro-crystals for enhanced thermal stability. *Int J Pharm*, 296(1-2):117–121, 2005.

NAIL, S. L., JIANG, S., CHONGPRASERT, S., AND KNOPP, S. A. Fundamentals of freeze-drying. *Pharm Biotechnol*, 14:281–360, 2002.

NEUTRA, M. R. AND KOZLOWSKI, P. A. Mucosal vaccines: The promise and the challenge. *Nat Rev Immunol*, 6(2):148–158, 2006.

NIESEN, F. H., BERGLUND, H., AND VEDADI, M. The use of differential scanning fluorimetry to detect ligand interactions that promote protein stability. *Nat Protoc*, 2(9):2212–21, 2007.

NOVARTIS. 10 key facts at a glance – novartis influenza vaccines. Technical report, Novartis AG, 2012.

OGURA, M., PALIWAL, S., AND MITRAGOTRI, S. Low-frequency sonophoresis: current status and future prospects. *Adv Drug Deliv Rev*, 60(10):1218–23, Jun 2008.

O'HAGAN, D. T., OTT, G. S., DE GREGORIO, E., AND SEUBERT, A. The mechanism of action of mf59 - an innately attractive adjuvant formulation. *Vaccine*, 30(29):4341–8, Jun 2012.

O'HAGAN, D. T. AND VALIANTE, N. M. Recent advances in the discovery and delivery of vaccine adjuvants. *Nat Rev Drug Discov*, 2(9):727–35, Sep 2003.

OLIVER, W. AND PHARR, G. An improved technique for determining hardness and elastic-modulus using load and displacement sensing indentation experiments. *J Mater Res*, 7:1564–1583, 1992.

OOBATAKE, M., TAKAHASHI, S., AND OOI, T. Conformational stability of ribonuclease t1. ii. salt-induced renaturation. *J Biochem*, 86(1):65–70, Jul 1979.

OSORIO, J. E., ZULEGER, C. L., BURGER, M., CHU, Q., PAYNE, L. G., AND CHEN, D. Immune responses to hepatitis b surface antigen following epidermal powder immunization. *Immunol Cell Biol*, 81(1): 52–58, 2003.

OYEWUMI, M. O., KUMAR, A., AND CUI, Z. Nano-microparticles as immune adjuvants: correlating particle sizes and the resultant immune responses. *Expert Rev Vaccines*, 9(9):1095–107, Sep 2010.

PAGE, G., LEBECQUE, S., AND MIOSSEC, P. Anatomic localization of immature and mature dendritic cells in an ectopic lymphoid organ: Correlation with selective chemokine expression in rheumatoid synovium. *J Immunol*, 168(10):5333–5341, 2002.

PAN, H. AND DARVELL, B. W. Effect of carbonate on hydroxyapatite solubility. *Cryst Growth Des*, 10: 845–850, 2010.

PAPPENHEIMER, JR, A. M. AND GILL, D. M. Diphtheria. *Science*, 182(4110):353–8, Oct 1973.

PAPPENHEIMER, JR, A. M., UCHIDA, T., AND HARPER, A. A. An immunological study of the diphtheria toxin molecule. *Immunochemistry*, 9(9):891–906, Sep 1972.

PATEL, J., KOTHARI, R., TUNGA, R., RITTER, N., AND TUNGA, B. Stability considerations for biopharmaceuticals, part 1: Overview of protein and peptide degradation pathways. *Bio Process Int*, 9(1):20–31, 2011.

PATIL, R. T. AND SPEAKER, T. J. Carrageenan as an anionic polymer for aqueous microencapsulation. *Drug Deliv*, 5(3):179–82, 1998.

PELTOLA, H. Worldwide haemophilus influenzae type b disease at the beginning of the 21st century: global analysis of the disease burden 25 years after the use of the polysaccharide vaccine and a decade after the advent of conjugates. *Clin Microbiol Rev*, 13(2):302–17, Apr 2000.

PELTOLA, H., KÄYHTY, H., SIVONEN, A., AND MÄKELÄ, H. Haemophilus influenzae type b capsular polysaccharide vaccine in children: a double-blind field study of 100,000 vaccinees 3 months to 5 years of age in finland. *Pediatrics*, 60(5):730–7, Nov 1977.

PETER, C. G. Responses of children immunized with capsular polysaccharide of hemophilus influenzae type b. *Pediatrics*, 102(1 Pt 2):252–4, Jul 1998.

PETERS, G. H., VAN AALTEN, D. M., EDHOLM, O., TOXVAERD, S., AND BYWATER, R. Dynamics of proteins in different solvent systems: analysis of essential motion in lipases. *Biophys J*, 71(5):2245–55, Nov 1996.

PEY, A. L., RODRIGUEZ-LARREA, D., BOMKE, S., DAMMERS, S., GODOY-RUIZ, R., GARCIA-MIRA, M. M., AND SANCHEZ-RUIZ, J. M. Engineering proteins with tunable thermodynamic and kinetic stabilities. *Proteins*, 71(1):165–74, Apr 2008.

PHILO, J. AND ARAKAWA, T. Mechanisms of protein aggregation. *Curr Pharm Biotechnol*, 10(4):348–351, 2009.

PICKER, L. J., TREER, J. R., FERGUSON-DARNELL, B., COLLINS, P. A., BERGSTRESSER, P. R., AND TERSTAPPEN, L. W. Control of lymphocyte recirculation in man. ii. differential regulation of the cutaneous lymphocyte-associated antigen, a tissue-selective homing receptor for skin-homing t cells. *J Immunol*, 150(3):1122–36, Feb 1993.

PIKAL, M. J., DELLERMAN, K. M., ROY, M. L., AND RIGGIN, R. M. The effects of formulation variables on the stability of freeze-dried human growth hormone. *Pharm Res*, 8(4):427–36, Apr 1991.

PIKAL-CLELAND, K. A., CLELAND, J. L., ANCHORDOQUY, T. J., AND CARPENTER, J. F. Effect of glycine on ph changes and protein stability during freeze-thawing in phosphate buffer systems. *J Pharm Sci*, 91(9):1969–79, Sep 2002.

PIPKIN, P. A. AND MINOR, P. D. Studies on the loss of infectivity of live type 3 poliovaccine on storage. *Biologicals*, 26(1):17–23, Mar 1998.

PIZZA, M., GIULIANI, M. M., FONTANA, M. R., MONACI, E., DOUCE, G., DOUGAN, G., MILLS, K. H., RAPPUOLI, R., AND DEL GIUDICE, G. Mucosal vaccines: non toxic derivatives of lt and ct as mucosal adjuvants. *Vaccine*, 19(17-19):2534–41, Mar 2001.

PLOTKIN, S. A. Correlates of protection induced by vaccination. *Clin Vaccine Immunol*, 17(7):1055–65, Jul 2010.

POLLARD, A. J., PERRETT, K. P., AND BEVERLEY, P. C. Maintaining protection against invasive bacteria with protein- polysaccharide conjugate vaccines. *Nat Rev Immunol*, 9(3):213–220, 2009.

POLLARD, A. J. Childhood immunisation: what is the future? *Arch Dis Child*, 92(5):426–33, May 2007.

PONCE, R., ABAD, L., AMARAVADI, L., GELZLEICHTER, T., GORE, E., GREEN, J., GUPTA, S., HERZYK, D., HURST, C., IVENS, I. A., KAWABATA, T., MAIER, C., MOUNHO, B., RUP, B., SHANKAR, G., SMITH, H., THOMAS, P., AND WIERDA, D. Immunogenicity of biologically-derived therapeutics: assessment and interpretation of nonclinical safety studies. *Regul Toxicol Pharmacol*, 54(2):164–82, Jul 2009.

POON, S., BIRKETT, N. R., FOWLER, S. B., LUISI, B. F., DOBSON, C. M., AND ZURDO, J. Amyloidogenicity and aggregate cytotoxicity of human glucagon-like peptide-1 (hglp-1). *Protein Peptide Lett*, 16:1548–1556, 2009.

PRAUSNITZ, M. AND LANGER, R. Transdermal drug delivery. *Nat Biotechnol*, 26(11):1261–1268, 2008. cited By (since 1996) 123.

QUINLAN, N., KENDALL, M., BELLHOUSE, B., AND AINSWORTH, R. Investigations of gas and particle dynamics in first generation needle-free drug delivery devices. *Shock Waves*, 10:395–404, 2001.

QUINTANAR-GUERRERO, D., ALLEMANN, E., FESSI, H., AND DOELKER, E. Preparation techniques and mechanisms of formation of biodegradable nanoparticles from preformed polymers. *Drug Dev Ind Pharm*, 24:1113–1128, 1998.

RAMSAY, G. AND FREIRE, E. Linked thermal and solute perturbation analysis of cooperative domain interactions in proteins. structural stability of diphtheria toxin. *Biochemistry*, 29(37):8677–83, Sep 1990.

RAMSAY, G., MONTGOMERY, D., BERGER, D., AND FREIRE, E. Energetics of diphtheria toxin membrane insertion and translocation: calorimetric characterization of the acid ph induced transition. *Biochemistry*, 28(2):529–33, Jan 1989.

RATTS, R., ZENG, H., BERG, E. A., BLUE, C., MCCOMB, M. E., COSTELLO, C. E., VANDERSPEK, J. C., AND MURPHY, J. R. The cytosolic entry of diphtheria toxin catalytic domain requires a host cell cytosolic translocation factor complex. *J Cell Biol*, 160(7): 1139–50, Mar 2003.

REDDY, S. T., REHOR, A., SCHMOEKEL, H. G., HUBBELL, J. A., AND SWARTZ, M. A. In vivo targeting of dendritic cells in lymph nodes with poly(propylene sulfide) nanoparticles. *J Control Release*, 112(1):26–34, May 2006.

REES, D. C. AND ROBERTSON, A. D. Some thermodynamic implications for the thermostability of proteins. *Protein Sci*, 10(6):1187–94, Jun 2001.

REHMAN, I. AND BONFIELD, W. Characterization of hydroxyapatite and carbonated apatite by photo acoustic ftir spectroscopy. *J Mater Sci-Mater Med*, 8:1–4, 1997.

RICCHIUTO, P., BRUKHNO, A. V., AND AUER, S. Protein aggregation: kinetics versus thermodynamics. *J Phys Chem B*, 116(18):5384–90, May 2012.

RICE-FICHT, A. C., ARENAS-GAMBOA, A. M., KAHL-MCDONAGH, M. M., AND FICHT, T. A. Polymeric particles in vaccine delivery. *Curr Opin Microbiol*, 13(1):106–12, Feb 2010.

RING, J., STEPHAN, W., AND BRENDEL, W. Anaphylactoid reactions to infusions of plasma protein and human serum albumin. role of aggregated proteins and of stabilizers added during production. *Clin Allergy*, 9(1):89–97, Jan 1979.

ROBERT, C. AND KUPPER, T. S. Inflammatory skin diseases, t cells, and immune surveillance. *NEJM*, 341 (24):1817–1828, 1999.

ROCHELLE, C. AND LEE, G. Dextran or hydroxyethyl starch in spray-freeze-dried trehalose/mannitol microparticles intended as ballistic particulate carriers for proteins. *J Pharm Sci*, 96(9):2296–309, Sep 2007.

ROGERS, B., DENNISON, K., ADEPOJU, N., DOWD, S., AND UEDOI, K. Vaccine cold chain: part 1. proper handling and storage of vaccine. *AAOHN J*, 58(8): 337–4; quiz 345–6, Aug 2010.

ROSENBERG, A. S. Effects of protein aggregates: an immunologic perspective. *AAPS J*, 8(3):E501–7, 2006.

SALLUSTO, F., LENIG, D., FÖRSTER, R., LIPP, M., AND LANZAVECCHIA, A. Two subsets of memory t lymphocytes with distinct homing potentials and effector functions. *Nature*, 401(6754):708–712, 1999.

SAMUEL, D., KUMAR, T. K., GANESH, G., JAYARAMAN, G., YANG, P. W., CHANG, M. M., TRIVEDI, V. D., WANG, S. L., HWANG, K. C., CHANG, D. K., AND YU, C. Proline inhibits aggregation during protein refolding. *Protein Sci*, 9(2):344–52, Feb 2000.

SANDBY-MØLLER, J., POULSEN, T., AND WULF, H. C. Epidermal thickness at different body sites: relationship to age, gender, pigmentation, blood content, skin type and smoking habits. *Acta Derm Venereol*, 83(6):410–3, 2003.

SAUERBORN, M., BRINKS, V., JISKOOT, W., AND SCHELLEKENS, H. Immunological mechanism underlying the immune response to recombinant human protein therapeutics. *Trends Pharmacol Sci*, 31(2):53–9, Feb 2010.

SCHIFFTER, H. Spray-freeze-drying in the manufacture of pharmaceuticals. *Eur. Pharm. Rev.*, 12:67–71, 2007.

SCHIFFTER, H., CONDLIFFE, J., AND VONHOFF, S. Spray-freeze-drying of nanosuspensions: The manufacture of insulin particles for needle-free ballistic powder delivery. *J Royal Soc Interface*, 7 (SUPPL. 4):S483–S500, 2010.

SCHMITT, H. J., VON KRIES, R., HASSENPFLUG, B., HERMANN, M., SIEDLER, A., NIESSING, W., CLEMENS, R., AND WEIL, J. Haemophilus influenzae type b disease: impact and effectiveness of diphtheria-tetanus toxoids-acellular pertussis (-inactivated poliovirus)/h. influenzae type b combination vaccines. *Pediatr Infect Dis J*, 20(8):767–74, Aug 2001.

SCHNEERSON, R., BARRERA, O., SUTTON, A., AND ROBBINS, J. B. Preparation, characterization, and immunogenicity of haemophilus influenzae type b polysaccharide-protein conjugates. *J Exp Med*, 152 (2):361–76, Aug 1980.

SCOTT, J. A. G. The preventable burden of pneumococcal disease in the developing world. *Vaccine*, 25 (13):2398–405, Mar 2007.

SENIOR, K. New vaccination technologies that make needles redundant. *Lancet Infect Dis*, 11(1):16–7, Jan 2011.

SHEN, J.-W., WU, T., WANG, Q., AND PAN, H.-H. Molecular simulation of protein adsorption and desorption on hydroxyapatite surfaces. *Biomaterials*, 29:513–532, 2008.

SHINEFIELD, H. R. Overview of the development and current use of crm(197) conjugate vaccines for pediatric use. *Vaccine*, 28(27):4335–9, Jun 2010.

SIMPERLER, A., KORNHERR, A., CHOPRA, R., BONNET, P. A., JONES, W., MOTHERWELL, W. D. S., AND ZIFFERER, G. Glass transition temperature of glucose, sucrose, and trehalose: an experimental and in silico study. *J Phys Chem B*, 110(39):19678–84, Oct 2006.

SINGH, S. K., AFONINA, N., AWWAD, M., BECHTOLD-PETERS, K., BLUE, J. T., CHOU, D., CROMWELL,

M., KRAUSE, H.-J., MAHLER, H.-C., MEYER, B. K., NARHI, L., NESTA, D. P., AND SPITZNAGEL, T. An industry perspective on the monitoring of subvisible particles as a quality attribute for protein therapeutics. *J Pharm Sci*, 99(8):3302–21, Aug 2010.

SLUTTER, B., SOEMA, P. C., DING, Z., VERHEUL, R., HENNINK, W., AND JISKOOT, W. Conjugation of ovalbumin to trimethyl chitosan improves immunogenicity of the antigen. *J Control Release*, 143: 207–214, 2010.

SOKOLOVSKA, A., HEM, S. L., AND HOGENESCH, H. Activation of dendritic cells and induction of cd4(+) t cell differentiation by aluminum-containing adjuvants. *Vaccine*, 25(23):4575–85, Jun 2007.

SONNER, C., MAA, Y., AND LEE, G. Spray-freeze-drying for protein powder preparation: Particle characterization and a case study with trypsinogen stability. *J Pharm Sci*, 91:2122–2139, 2002.

STEFANI, M. AND DOBSON, C. M. Protein aggregation and aggregate toxicity: New insights into protein folding, misfolding diseases and biological evolution. *J Molec Med*, 81(11):678–699, 2003.

STEIN, J., CHENG, G., STOCKTON, B., FORS, B., BUTCHER, E., AND VON ANDRIAN, U. L-selectin-mediated leukocyte adhesion in vivo: Microvillous distribution determines tethering efficiency, but not rolling velocity. *J Exp Med*, 189:37–49, 1999.

STREET, T. O., BOLEN, D. W., AND ROSE, G. D. A molecular mechanism for osmolyte-induced protein stability. *Proc Natl Acad Sci U S A*, 103(38): 13997–4002, Sep 2006.

SUCHANEK, W. AND YOSHIMURA, M. Processing and properties of hydroxyapatite-based biomaterials for use as hard tissue replacement implants. *J Mater Res*, 13:94–117, 1998.

SULLIVAN, S. P., KOUTSONANOS, D. G., DEL PILAR MARTIN, M., LEE, J. W., ZARNITSYN, V., CHOI, S.-O., MURTHY, N., COMPANS, R. W., SKOUNTZOU, I., AND PRAUSNITZ, M. R. Dissolving polymer microneedle patches for influenza vaccination. *Nat Med*, 16(8):915–20, Aug 2010.

TANG, X. AND PIKAL, M. J. Design of freeze-drying processes for pharmaceuticals: practical advice. *Pharm Res*, 21(2):191–200, Feb 2004.

TAŞ, A. C. Molten salt synthesis of calcium hydroxyapatite whiskers. *J Am Ceram Soc*, 84(2):295–300, 2001.

TAS, A. X-ray diffraction data for flux-grown calcium hydroxyapatite whiskers. *Powder Diffr*, 16:102–106, 2001.

TAYLOR, L. S. AND ZOGRAFI, G. Sugar-polymer hydrogen bond interactions in lyophilized amorphous mixtures. *J Pharm Sci*, 87(12):1615–21, Dec 1998.

TEZEL, A., PALIWAL, S., SHEN, Z., AND MITRAGOTRI, S. Low-frequency ultrasound as a transcutaneous immunization adjuvant. *Vaccine*, 23(29):3800–7, May 2005.

THOMASIN, C., CORRADIN, G., MEN, Y., MERKLE, H., AND GANDER, B. Tetanus toxoid and synthetic malaria antigen containing poly(lactide)/poly(lactide-co-glycolide) microspheres: Importance of polymer degradation and antigen release for immune response. *J Control Release*, 41:131–145, 1996.

TIMASHEFF, S. N. Protein-solvent preferential interactions, protein hydration, and the modulation of biochemical reactions by solvent components. *Proc Natl Acad Sci U S A*, 99(15):9721–6, Jul 2002.

TORIN HUZIL, J., SIVALOGANATHAN, S., KOHANDEL, M., AND FOLDVARI, M. Drug delivery through the skin: molecular simulations of barrier lipids to design more effective noninvasive dermal and transdermal delivery systems for small molecules, biologics, and cosmetics. *Wiley Interdiscip Rev Nanomed Nanobiotechnol*, May 2011.

TOSINI, W., CIOTTI, C., GOYER, F., LOLOM, I., L'HÉRITEAU, F., ABITEBOUL, D., PELLISSIER, G., AND BOUVET, E. Needlestick injury rates according to different types of safety-engineered devices: results of a french multicenter study. *Infect Control Hosp Epidemiol*, 31(4):402–7, Apr 2010.

TROWSDALE, J. AND CAMPBELL, R. D. Complexity in the major histocompatibility complex. *Eur J Immunogenet*, 19(1-2):45–55, 1992.

TSUI, Y., DOYLE, C., AND CLYNE, T. Plasma sprayed hydroxyapatite coatings on titanium substrates part 1: Mechanical properties and residual stress levels. *Biomaterials*, 19:2015–2029, 1998.

UCHIDA, T., GILL, D. M., AND PAPPENHEIMER, JR, A. M. Mutation in the structural gene for diphtheria toxin carried by temperate phage. *Nat New Biol*, 233(35):8–11, Sep 1971.

VARMUS, H., KLAUSNER, R., ZERHOUNI, E., ACHARYA, T., DAAR, A., AND SINGER, P. Grand challenges in global health. *Science*, 302:398–399, 2003.

VEREZ-BENCOMO, V., FERNÁNDEZ-SANTANA, V., HARDY, E., TOLEDO, M. E., RODRÍGUEZ, M. C., HEYNNGNEZZ, L., RODRIGUEZ, A., BALY, A., HERRERA, L., IZQUIERDO, M., VILLAR, A., VALDÉS, Y., COSME, K., DELER, M. L., MONTANE, M., GARCIA, E., RAMOS, A., AGUILAR, A., MEDINA, E., TORAÑO, G., SOSA, I., HERNANDEZ, I., MARTÍNEZ, R., MUZACHIO, A., CARMENATES, A., COSTA, L., CARDOSO, F., CAMPA, C., DIAZ, M., AND ROY, R. A synthetic conjugate polysaccharide vaccine against haemophilus influenzae type b. *Science*, 305(5683):522–5, Jul 2004.

VISWANATH, B., RAGHAVAN, R., GURAO, N. P., RAMAMURTY, U., AND RAVISHANKAR, N. Mechanical properties of tricalcium phosphate single crystals grown by molten salt synthesis. *Acta Biomaterialia*, 4(5):1448–1454, 2008.

VOGELBRUCH, M., NUSS, B., KÖRNER, M., KAPP, A., KIEHL, P., AND BOHM, W. Aluminium-induced granulomas after inaccurate intradermal hyposensitization injections of aluminium-adsorbed depot preparations. *Allergy*, 55(9):883–7, Sep 2000.

VON ANDRIAN, U. H. AND MACKAY, C. R. T-cell function and migration: Two sides of the same coin. *NEJM*, 343(14):1020–1034, 2000.

VONHOFF, S., CONDLIFFE, J., AND SCHIFFTER, H. Implementation of an ftir calibration curve for fast and objective determination of changes in protein secondary structure during formulation development. *J Pharm Biomed Anal*, 51(1):39–45, Jan 2010.

WAKANKAR, A. A. AND BORCHARDT, R. T. Formulation considerations for proteins susceptible to asparagine deamidation and aspartate isomerization. *J Pharm Sci*, 95(11):2321–36, Nov 2006.

WANG, W. Lyophilization and development of solid protein pharmaceuticals. *Int J Pharm*, 203(1-2):1–60, Aug 2000.

WANG, W. Protein aggregation and its inhibition in biopharmaceutics. *Int J Pharm*, 289(1-2):1–30, 2005.

WANG, W. AND ROBERTS, C. J., editors. *Aggregation of Therapeutic Proteins*. John Wiley and Sons, Inc., Hoboken, New Jersey, 2010.

WANG, W., SINGH, S. K., LI, N., TOLER, M. R., KING, K. R., AND NEMA, S. Immunogenicity of protein aggregates–concerns and realities. *Int J Pharm*, 431 (1-2):1–11, Jul 2012.

WANG, X., LI, X., ITO, A., SOGO, Y., AND OHNO, T. Particle-size-dependent toxicity and immunogenic activity of mesoporous silica-based adjuvants for tumor immunotherapy. *Acta Biomater*, 9(7):7480–9, Jul 2013.

WEIR, E. AND HATCH, K. Preventing cold chain failure: vaccine storage and handling. *CMAJ*, 171(9):1050, Oct 2004.

WEISSMUELLER, N. T., SCHIFFTER, H. A., AND POLLARD, A. J. Intradermal powder immunization with protein-containing vaccines. *Expert Rev Vaccines*, 12(6):687–702, Jun 2013.

WEISSTEIN, E. W. "erf." from mathworld–a wolfram web resource. Technical report, Wolfram Web Resource, 2013.

WELDON, W. C., WANG, B.-Z., MARTIN, M. P., KOUTSONANOS, D. G., SKOUNTZOU, I., AND COMPANS, R. W. Enhanced immunogenicity of stabilized trimeric soluble influenza hemagglutinin. *Plos One*, 5:e12466, 2010.

WENIGER, B. Jet injection of vaccines: overview and challenges for mas vaccination with jet injections (jis). Technical report, United States Department of of Health and Human Services, 2003.

WHITE, P. J., ANASTASOPOULOS, F., CHURCH, J. E., KUO, C.-Y., BOYD, B. J., HICKEY, P. L. C., TU, L. S., BURNS, P., LEW, A. M., HEATH, W. R., DAVEY, G. M., AND POUTON, C. W. Generic construction of single component particles that elicit humoural and cellular immune responses without the need for adjuvants. *Vaccine*, 26(52):6824–31, Dec 2008.

WHO. Bulk density and tapped density of powders -document qas/11.450 final. Technical report, WHO, 2012.

WIENDL, H., HOHLFELD, R., AND KIESEIER, B. C. Immunobiology of muscle: Advances in understanding an immunological microenvironment. *Trends Immunol*, 26(7):373–380, 2005.

WILBURN, S. Q. AND EIJKEMANS, G. Preventing needlestick injuries among healthcare workers: a who-icn collaboration. *Int J Occup Environ Health*, 10(4):451–6, 2004.

WILDNAUER, R. H., BOTHWELL, J. W., AND DOUGLASS, A. B. Stratum corneum biomechanical properties. i. influence of relative humidity on normal and extracted human stratum corneum. *J Invest Dermatol*, 56(1):72–8, Jan 1971.

WOODROW, K. A., BENNETT, K. M., AND LO, D. D. Mucosal vaccine design and delivery. *Annu Rev Biomed Eng*, 14:17–46, 2012.

WORLD HEALTH ORGANIZATION. State of the world's vaccines and immunizations. *J Am Med Assoc*, 288 (20):2532, 2002.

WORLD HEALTH ORGANIZATION. Safety of injections. Technical report, World Health Organization, 2004.

WORLD HEALTH ORGANIZATION. Who position paper on haemophilus influenzae type b conjugate vaccines. (replaces who position paper on hib vaccines previously published in the weekly epidemiological record. *Wkly Epidemiol Rec*, 81(47):445–52, Nov 2006.

YANCEY, P. H., CLARK, M. E., HAND, S. C., BOWLUS, R. D., AND SOMERO, G. N. Living with water stress: evolution of osmolyte systems. *Science*, 217(4566): 1214–22, Sep 1982.

YIN, G., LIU, Z., ZHAN, J., DING, F., AND YUAN, N. Impacts of the surface charge property on protein adsorption on hydroxyapatite. *Chem Eng J*, 87:181–186, 2002.

YOHANNES, G., WIEDMER, S. K., ELOMAA, M., JUSSILA, M., ASEYEV, V., AND RIEKKOLA, M.-L. Thermal aggregation of bovine serum albumin studied by asymmetrical flow field-flow fractionation. *Anal Chim Acta*, 675(2):191–8, Aug 2010.

YOSHIOKA, S. AND ASO, Y. Correlations between molecular mobility and chemical stability during storage of amorphous pharmaceuticals. *J Pharm Sci*, 96:960–981, 2007.

YOSIPOVITCH, G., XIONG, G. L., HAUS, E., SACKETT-LUNDEEN, L., ASHKENAZI, I., AND MAIBACH, H. I. Time-dependent variations of the skin barrier function in humans: transepidermal water loss, stratum corneum hydration, skin surface ph, and skin temperature. *J Invest Dermatol*, 110(1):20–3, Jan 1998.

YU, Z., JOHNSTON, K. P., AND WILLIAMS, 3RD, R. O. Spray freezing into liquid versus spray-freeze drying: influence of atomization on protein aggregation and biological activity. *Eur J Pharm Sci*, 27(1): 9–18, Jan 2006.

ZEMPSKY, W. T., SULLIVAN, J., PAULSON, D. M., AND HOATH, S. B. Evaluation of a low-dose lidocaine iontophoresis system for topical anesthesia in adults and children: a randomized, controlled trial. *Clin Ther*, 26(7):1110–9, Jul 2004.

ZHANG, L., LU, D., AND LIU, Z. How native proteins aggregate in solution: a dynamic monte carlo simulation. *Biophys Chem*, 133(1-3):71–80, Mar 2008.

ZHANG, S., ADAMSON, D. H., PRUD'HOMME, R. K., AND LINK, A. J. Photocrosslinking the polystyrene core of block-copolymer nanoparticles. *Polym Chem*, 2:665–671, 2011.

ZHAORI, G., SUN, M., AND OGRA, P. L. Characteristics of the immune response to poliovirus virion polypeptides after immunization with live or inactivated polio vaccines. *J Infect Dis*, 158(1):160–5, Jul 1988.

ZHOU, D., GRANT, D. J. W., ZHANG, G. G. Z., LAW, D., AND SCHMITT, E. A. A calorimetric investigation of thermodynamic and molecular mobility contributions to the physical stability of two pharmaceutical glasses. *J Pharm Sci*, 96(1):71–83, Jan 2007.

ZIEGLER, A. S. Needle-free delivery of powdered protein vaccines: A new and rapidly developing technique. *J Pharm Innov*, 3(3):204–213, 2008.

APPENDIX A

APPENDIX - TABLES

The tables in the appendix present i) differential scanning fluorimetry and fluorimetry data, ii) lists of materials and consumables, iii) a summary of intradermal powder immunization studies with protein-containing vaccines, and iv) a summary of any challenge studies after IPI inoculation with protein-containing vaccines.

Table A.1: DSF - Salts and pH. Standard Deviation for T_m values range from ± 0.0°C to ± 0.5°C.

Type	Name	Concentration	T_m [°C]	pH, Buffer
Buffers	K_2HPO_4	10 mM	46.3	pH 7.2
	MES	10 mM	46.3	pH 7.2
	PBS	147.5 mM	44.9	pH 7.2
	Tris	10 mM	46.3	pH 7.2
pH	K_2HPO_4	10 mM	45.3	pH 5.5
	K_2HPO_4	10 mM	46.2	pH 6.0
	K_2HPO_4	10 mM	46.3	pH 6.5
	K_2HPO_4	10 mM	46.3	pH 7.0
	K_2HPO_4	10 mM	46.3	pH 7.5
	K_2HPO_4	10 mM	45.4	pH 8.0
	K_2HPO_4	10 mM	45.3	pH 8.5
Salts	KCl	1500 mM	40.5	pH 7.2, 10 mM K_2HPO_4
		750 mM	42.4	
		375 mM	44.4	
		188 mM	44.4	
	K_2SO_4	45 mM	45.3	pH 7.2, 10 mM K_2HPO_4
		22.5 mM	45.4	
		11.2 mM	46.3	
		5.6 mM	46.3	
	NaCl	1500 mM	38.5	pH 7.2, 10 mM K_2HPO_4
		750 mM	40.5	
		375 mM	41.5	
		188 mM	44.4	
	Na_2SO_4	225 mM	43.4	pH 7.2, 10 mM K_2HPO_4
		112.5 mM	43.3	
		56.3 mM	44.4	
		28.1 mM	46.3	

Table A.2: DSF - Saccharides. Standard Deviation for T_m values ranges from ± 0.0°C to ± 0.5°C.

Type	Name	Concentration	T_m [°C]	pH, Buffer
(Mono-) Saccharide	Glucose	1725 mM	47.3	pH 7.2, 10 mM K_2HPO_4
		862 mM	47.3	
		431 mM	46.3	
		215 mM	46.3	
	Mannitol	550 mM	47.2	pH 7.2, 10 mM K_2HPO_4
		275 mM	46.3	
(Di-) Saccharide	Lactose	420 mM	49.2	pH 7.2, 10 mM K_2HPO_4
		210 mM	48.3	
		105 mM	47.2	
		52 mM	46.3	
	Sucrose	435 mM	53.2	pH 7.2, 10 mM K_2HPO_4
		217 mM	52.2	
		108 mM	49.2	
		54 mM	46.3	
	Trehalose	1500 mM	51.2	pH 7.2, 10 mM K_2HPO_4
		750 mM	47.3	
		375 mM	47.3	
		187 mM	46.3	
(Tri-) Saccharide	Raffinose	2 mM	45.3	pH 7.2, 10 mM K_2HPO_4
		1 mM	45.3	

Table A.3: DSF - Polyols, polymers, polypeptitdes, and polysaccharides. Standard Deviation for T_m values range from ± 0.0°C to ± 0.5°C.

Type	Name	Concentration	T_m [°C]	pH, Buffer
Polyol	Ethyleneglycol	45% wt	36.6	pH 7.2, 10 mM K_2HPO_4
		22.5% wt	46.3	
		11.3% wt	47.2	
		5.6% wt	46.3	
	Glycerol	75% wt	48.3	pH 7.2, 10 mM K_2HPO_4
		37.5% wt	48.3	
		18.8% wt	48.3	
		9.4% wt	46.3	
Polymer	PEG (4k)	11.3% wt	46.3	pH 7.2, 10 mM K_2HPO_4
		5.2% wt	46.3	
		2.8% wt	46.3	
		1.4% wt	46.3	
	PVP-10	125 mM	44.3	pH 7.2, 10 mM K_2HPO_4
		62.5 mM	45.3	
Polypeptide	Gelatin	3.8% wt	47.3	pH 7.2, 10 mM K_2HPO_4
		1.9% wt	47.2	
		0.9% wt	47.2	
		0.5% wt	46.2	
Polysaccharide	Carrageenan	0.1% wt	39.3	pH 7.2, 10 mM K_2HPO_4
		0.05% wt	38.3	
	Dextran (10k)	15% wt	47.3	pH 7.2, 10 mM K_2HPO_4
		7.5% wt	47.3	
		3.8% wt	47.2	
		1.9% wt	46.3	
	Dextran (150k)	10% wt	45.3	pH 7.2, 10 mM K_2HPO_4
		5% wt	45.3	
	Pentastarch	18.8 mM	46.3	pH 7.2, 10 mM K_2HPO_4
		9.4 mM	46.3	
		4.7 mM	46.3	
		2.3 mM	46.3	
	Xanthan	0.1% wt	44.3	pH 7.2, 10 mM $K_2HPO_4$2
		0.05% wt	45.3	

Table A.4: DSF - Amino acids. Standard Deviation for T_m values range from ± 0.0°C to ± 0.5°C.

Type	Name	Concentration	T_m [°C]	pH, Buffer
Amino acid	Glutamic acid	37.5 mM	46.3	pH 7.2, 10 mM K_2HPO_4
		18.8 mM	46.3	
		9.4 mM	46.3	
		4.7 mM	46.3	
	Glycine	2250 mM	49.2	pH 7.2, 10 mM K_2HPO_4
		1125 mM	49.3	
		562.5 mM	48.3	
		281.3 mM	47.4	
	L-Histidine	187.5 mM	45.4	pH 7.2, 10 mM K_2HPO_4
		93.8 mM	45.4	
		46.9 mM	46.3	
		23.5 mM	46.3	
	Proline	3000 mM	47.3	pH 7.2, 10 mM K_2HPO_4
		1500 mM	47.3	
		750 mM	46.3	
		375 mM	46.3	

Table A.5: T_m and TRP Peak Emission. Standard deviations for T_m values ranged from ± 0.0°C to ± 0.5°C, and tryptophan excitation/emission peas from ± 0nm to ± 1nm.

Excipient	Peak Emission$_{\alpha=295}$ (nm)	T_m
Histidine	327.0	46.3
Glutamic Acid	325.3	46.3
Glycine	326.0	49.3
Proline	325.7	47.3
Guanidine HCl	349.7	
Suc+Treh	325.0	51.3
Suc+Treh+Gly	325.7	52.3
TMDD	326.0	49.3
Mannitol	326.0	47.2
Glucose	327.0	47.3
Lactose	325.3	46.3
Sucrose	325.3	52.2
Trehalose	327.3	49.2
Raffinose	327.3	45.3
K2HPO4 pH8.0	327.0	45.4
K2HPO4 pH7.2	326.3	46.3
K2HPO4 pH7.0	326.0	46.3
K2HPO4 pH6.0	327.0	46.2
Ethyl Glycol	327.3	36.6
Glycerol	325.7	48.3
Gelatine	325.3	47.2
PEG4k	327.0	46.3
PVP-10	327.7	44.3
Carrageenan	326.3	39.3
b-cyclodextrin	326.0	
Dextran 10k	327.0	47.3
Dextran 150k	328.0	45.3
Pentastarch	325.7	46.3
Xanthan	327.7	44.3

Table A.6: Catalogue Numbers for Chemicals and Reagents Used in the Experiments - Part I.

Type	Company	Catalogue Number
3,3',5,5'-Tetramethylbenzidine (TMB) Liquid Substrate System for ELISA	Sigma Aldrich, UK	T0440
Acetic acid	Fluka Analytical, UK	45741
Adju-Phos®	Brenntag Biosector, DEN	7784-30-7
Agar	Sigma Aldrich, UK	A5041
Al-Hydrogel®	Brenntag Biosector, DEN	21645-51-2
Albumin from bovine serum	Sigma Aldrich, UK	A2153
Albumin, Tetramethylrhodamine isothiocyanate bovine	Sigma Aldrich, UK	A2289
β-cyclodextrin hydrate	Acros Organics, UK	68168-23-0
Bovine serum albumin (BSA)	Sigma Aldrich, UK	A2153
Calcium Carbonate	Sigma Aldrich, UK	C6763
Calcium hydroxide	Sigma Aldrich, UK	31219
Calcium pyrophosphate	Sigma Aldrich, UK	401552
Carrageenan	Sigma Aldrich, UK	C1013
Coomassie R Brilliant Blue	Sigma Aldrich, UK	B7920
CRM_{197} (48mg/ml) in 10% sucrose 10mM K_2HPO_4 pH7.1	Novartis Vaccines and Diagnostics, IT	NA
D-(+) Trehalose dihydrate	Sigma Aldrich, UK	T9531
D-(+)-Glucose	Sigma Aldrich, UK	G7528
D-(+)-Raffinose pentahydrate	Sigma Aldrich, UK	R0514
Dextran (10kDa)	Sigma Aldrich, UK	D9260
Dextran (150kDa)	Sigma Aldrich, UK	D4876
Di(ethylene glycol) ethyl ether	Sigma Aldrich, UK	W509043
Dipotassium phosphate	Sigma Aldrich, UK	P3786
DL-Dithiothreitol (DTT)	Sigma Aldrich, UK	D0632
FlowLac® 100 (Lactose monohydrate)	Meggle Excipient & Technology, GER	A4921
Gelatine	Fisher Scientific, UK	900-70-8
Glutamic acid monosodium salt monohydrate	Sigma Aldrich, UK	49621
Glycerol	Acros Organics, BEL	15-89-20010
Glycine	Sigma Aldrich, UK	G8898
Goat Anti-Mouse IgG, Human ads-HRP	Southern Biotech, UK	1030-05
Goat Anti-Mouse IgG1, Human ads-HRP	Southern Biotech, UK	1070-05
Goat Anti-Mouse IgG12a, Human ads-HRP	Southern Biotech, UK	1080-05
Guanidinim hydrochloride	Acros Organics, BEL	50-01-1
Hydrochloric acid (1M) volumetric solution	Fisher Scientific, UK	J/4320/15
Hydranal® - Coulomat AG	Fluka Analytical, UK	34739
Hydroxyapatite	Sigma Aldrich, UK	13204
Kolliphor® HS15	BASF, GER	50259817
Kolliphor® K188	BASF, GER	50259527
Kolliphor® PS80	BASF, GER	50259531
L-Glutamine	Sigma Aldrich, UK	G8540
L-Histidine	Sigma Aldrich, UK	H8000

Table A.7: Catalogue Numbers for Chemicals and Reagents Used in the Experiments - Part II.

Type	Company	Catalogue Number
L-Proline	Sigma Aldrich, UK	P5607
Mannitol	Fisher Scientific, UK	M/2405/53
MES	Sigma Aldrich, UK	M3671
Methanol	Sigma Aldrich, UK	34860
NaOH (1M) Volumetric Solution	Fisher Scientific, UK	J/7620/15
Newborn calf serum	Sigma Aldrich, UK	N4637
$PEG_{(5k)}$-b-$PS_{(1.6k)}$	Prudhomme Lab, Princeton, USA	NA
Pentastarch	Fa. Frisenius Kabi, GER	2432
Perchloric acid 60%	Sigma Aldrich, UK	311413
Phosphate buffered saline (PBS) tablets	Sigma Aldrich, UK	P4417
Poly(ethylene glycol) 4000	Sigma Aldrich, UK	25322-68-3
$Polystyrene_{(1.5k)}$	Prudhomme Lab, Princeton, USA	NA
Polyvinylpyrrolidone	Sigma Aldrich, UK	PVP-10
Potassium bromide	Sigma Aldrich, UK	221864
Potassium Chloride	Sigma Aldrich, UK	P9333
Potassium Sulfate	Sigma Aldrich, UK	P0772
Printex® 95	Degussa AG, GER	4134121
Propan-2-ol 99.5+% (GLC) for HPLC CertiFied HPLC	Fisher Scientific	P/7507/17
Protein standard	Sigma Aldrich, UK	P0834
Sodium acetate	Sigma Aldrich, UK	S8625
Sodium bicarbonate	Sigma Aldrich, UK	S5761
Sodium Chloride	Sigma Aldrich, UK	S9625
Sodium citrate	Sigma Aldrich, UK	S1804
Sodium dodecyl sulfate	Fisher Scientific, UK	151-21-3
Sodium phosphate	Sigma Aldrich, UK	S8282
Sodium Sulphate	Sigma Aldrich, UK	239313
Sucrose	Fisher Scientific, UK	S/8600/60
Sulfuric acid	Sigma Aldrich, UK	320501
SYPRO® Orange Protein Gel Stain	Invitrogen, UK	S-6650
Tetrahydrofuran	Fisher Scientific, UK	T/0700/PR17
Trizma® base	Sigma Aldrich, UK	T6066
TWEEN® 20	Sigma Aldrich, UK	P1379
Xanthan gum from Xanthanomas Campestris	Sigma Aldrich, UK	G1253

Table A.8: Catalogue Numbers for Non-standard Consumables Used in the Experiments.

Type	Company	Catalogue Number
Amicon Ultra 15ml 100k MWCO	Millipore, NED	UFC910024
BD Micro-Fine™ 1ml U-100 Insulin (29G)	BD, UK	320411
Bicinchoninic Assay Kit - QuantiPro™ BCA Assay Kit	Sigma Aldrich, UK	QPBCA
Coors™ high-alumina crucible	Sigma Aldrich, UK	Z247642
Corning® 10k MWCO PES Spin-X UF Tubes 500μl	Sigma Aldrich, UK	431478
Corning® CellBIND® 96 Well Plates	Sigma Aldrich, UK	CLS 3340
Corning® Petri Dish	Sigma Aldrich, UK	430588
Cuvette disposable semi-micro 1.5mL	Fisher Scientific, UK	CXA-110-040H
Durapore 0.1μm VVPP filters	Millipore, NED	VVLP04700
EpoKwick Fast Cure Epoxy Kit	Buehler, GER	208128
Eppendorf Protein LoBind Tube 2.0ml	Eppendorf AG, GER	22431102
Lyophilisation Vials	Schott, GER	1123261
Medical grade helium cartridges	Particles Therapeutics Ltd, UK	NA
Optical PCR seals	Bio-Rad, UK	223-9444
Polystyrene divinylbenzene spheres	Duke Scientific Corp, USA	35-7B
Precise Tris- Glycine gel 4-20% , 15-Well	Thermo Scientific, UK	25274
PrecisionPlus Protein Dual-Color 500μl	BioRad, UK	161-0374
Protein Molecular Weight Kit	Sigma Aldrich, UK	MWGF1000
QuantiPro™ BCA Assay Kit	Sigma Aldrich, UK	QPBCA
Regenerated cellulose (RC) membrane 10k WMCO	Postnova, GER	Z-AF4-MEM-612
Slide-A-Lyzer MINI Dialysis Devices, 20K MWCO	ThermoScientific, UK	69590
Thermocouples	Omega Engineering Ltd, UK	5SRTC-TT-T1-36-1M
Tzero Aluminum Hermatic Lid	TA Instruments, UK	T111208
Tzero Alumium Hermetic Pan	TA Instruments, UK	T111019
White quantitative PCR low-proÞle plates	Thermo Scientific, UK	AB-0700/w

Table A.9: Part 1 of 5 – Findings of past IPI *in vivo* studies by vaccine type, study plan, antigen formulation and adjuvantation.

Vaccine	Adjuvant	Vaccine Load per Injection	Excipients	Formation	Species	Prime - Boost	Titer Response GMT	Reference
	[Device, (bar)]	[Route]	[Ratio]	[Particle diameter (μm)]	[n per condition]	[Bleed]		Year
Virus								
Formalin-inactivated Aichi/68 influenza virus	none	25μg, 5μg, 1μg	100mg/ml trehalose in dH2O	N2 desiccate, grind, sieve	BALB/c (female) (6wks)	day 0	IgG 25μg: IPI > SC (P<0.001) IgG 5μg: IPI > SC (P<0.001) IgG 1μg: IPI > SC (P<0.001)	Chen et al. (2000)
	[PowderJect ND, 50]	[IPI (abd); ctrl: SC]	[pure]	[20-53]	[n=8]	[day 28]		
	none	5μg	100mg/ml trehalose in dH2O	N2 desiccate, grind, sieve	BALB/c (female) (6wks)	day 0, 28	IgG^p: IPI > IM (P<0.05) IgG^p: IPI > SC (P<0.01) IgG^b: IPI > IM (P<0.01) IgG^b: IPI > SC (P<0.01)	Chen et al. (2000)
	[PowderJect ND, 50]	[IPI (abd); ctrl: IM, SC]	[pure]	[20-53]	[n=8]	[day 28, 42]		
1998-1999 season human influenza (A/Beijing 262/95-like, A/Sydney 5/97-like, B/Harbin 7/94-like strains)	none	1.5μg HA per strain, 4.5μg total	100mg/ml trehalose in dH_2O	N2 desiccate, grind, sieve	BALB/c (female) (6wks)	day 0, 28	IgG^b B/Beijing: IPI > SC (P<0.01) IgG^b A/Beijing: IPI > SC (P<0.01) IgG^b A/Sydney: IPI > SC (P<0.01) HIb: IPI (each strain) > SC - 2-4 fold	Chen et al. (2000)
	[PowderJect ND, 50]	[IPI (abd); ctrl: SC]	[pure]	[20-53]	[n=8]	[day 28, 42]		
Formalin-inactivated A/PR/8/34 (H1N1) influenza virus	5μg CT, 10μg CpG	5μg	100mg/ml trehalose in dH2O	N2 desiccate, grind, sieve	BALB/c (female) (6wks)	day 0, 28	IgG^b: IPI+CpG > IPI No Adj (P<0.01) - 5 fold IgG^b: IPI+CT > IPI No Adj (P<0.01) - 30 fold IgG^b: IPI+CpG+CT > No Adj (P<0.01) - 50 fold IgG^b: IPI+CT > IPI+CpG (P<0.01) and IPI+Adj > SC (P<0.01) IgA (intestine, saliva, vaginal, nasal) detected, CT+CpG condition had highest IgA GMC	Chen et al. (2001b)
	[PowderJect ND, 50]	[IPI (abd); ctrl: SC]	[pure]	[20-53]	[n=NA]	[day 0, 28,42]		
1998-1999 season human influenza (A/Beijing 262/95-like (H1N1)*, A/Sydney 5/97-like (H3N2)*, B/Yamanashi strain)	1, 5, or 10μg CTB; 0.1, 1, 10, 25μg LTR72; 1, 10, 25μg LTK63	1.5μg HA per strain, 4.5μg total or 3μg* total	100mg/ml trehalose in dH2O	N2 desiccate, grind, sieve	BALB/c (female) (6wks)	day 0, 28	HIb w/ CTB 5, 10μg: IPI+Adj > IPI No Adj (P<0.05) HIb w/ CTB 1, 5, 10μg: IPI+Adj > IM No Adj (P<0.01) HIb* w/ IPI and LTR72: 1μg Adj ≈ 10μg Adj ≈ 25μg Adj HIp,b* w/ LTR72 1, 10, 25μg: IPI+Adj > IPI+(No or 0.1μg) Adj (P<0.05) HIp,b* w/ LTK63 1, 10, 25μg: IPI+Adj > IPI (P<0.01) HIp,b* w/ IPI and LTK63: 1μg Adj ≈ 10μg Adj ≈ 25μg Adj	Chen et al. (2002a)
	[PowderJect ND, 50]	[IPI (abd); ctrl: IM(deltoid), IN]	[pure]	[20-53]	[n=8]	[day 0, 28,42]		

Table A.10: Part 2 of 5 – Findings of past IPI *in vivo* studies by vaccine type, study plan, antigen formulation and adjuvantation.

Vaccine	Adjuvant	Vaccine Load per Injection	Excipients	Formation	Species	Prime - Boost	Titer Response GMT	Reference
	[Device, (bar)]	[Route]	[Ratio]	[Particle diameter (μm)]	[n per condition]	[Bleed]		Year
Virus								
2000 to 2001 season trivalent influenza vaccine (A/New Caledonia/20/99 IVR-166 (H1N1), A/Panama/2007/99 RESVIR-17 (H3N2), and B/Yamanashi/166/98)	none, 5μg QS-21, 2.5μg LTR72, 2.5μg CT	1.5μg of HA per strain	trehalose:mannitol: dextran	SFD	BALB/c (female) (6wks)	day 0, 28	HIb A/Panama, B/Yamanashi: IPI No Adj > IM No Adj (P<0.05) 3-fold HIb A/New Caledonia: IPI No Adj ≈ IM No Adj HIb (any strain): IPI+ Adj (any) > Ctrl (IPI or IM) No Adj (P<0.05) There was no difference between the adjuvanted conditions. IgG^b and IgAb: IPI+Adj > Ctrl (IPI or IM) No Adj.	Chen et al. (2003)
	[PowderJect ND1, 40]	[IPI (abd); ctrl: IM]	[3:3:4]	[31-63]	[n=8]	[day 42]		
	none, 50μg QS-21	15μg of HA per strain	trehalose:mannitol: dextran	SFD	Rhesus macaques	day 0, 30	HIp: IPI+Adj ≈> IM No Adj (P>0.05) - 2 fold trend HIp: IPI+Adj > IPI No Adj (P<0.05) HIb: IPI+Adj > IPI No Adj or IM No Adj (P<0.05) HIb: IPI No Adj ≈ IM No Adj (P>0.05) HI day 60 ≈< HI day 44.	Chen et al. (2003)
	[PowderJect ND1, 45]	[IPI (arm); ctrl: IM]	[3:3:4]	[31-63]	[n=6]	[day 0, 14, 30, 44, 60, 74, 88]		
	none, 10μg LTR72	0.15, 0.3, 0.6 or 1.5μg of HA per strain	100mg/ml trehalose in dH2O	N2 desiccate, grind, sieve	BALB/c (female) (5-7wks);	day 0, 28	HIp,b: IPI 0.15, 0.3, 0.6 or 1.5μg HA + No Adj > IM equivalent dose HIp,b: IPI + No adj dose independent, IM + No adj positively correlated with dose HIp,b*A/Sydney, A/Beijing (0.15μg HA each): IPI+Adj > IPI No Adj	Chen et al. (2004a)
	[PowderJect ND, 40]	[IPI (abd); ctrl: IM]	[pure]	[20-53]	[n=8]	[day 0, 28,42]		
1999-2000 season human influenza (A/Beijing 262/95, A/Sydney 5/97-like, B/Yamanashi-like strains)	none	0.4 μg HA per strain, 1.2μg total	trahalose:mannitol: dextran 1) A: 9.45mg HA/mL 2) B: 14.99mg HA/mL 3) C: 5.62 mg HA/mL	SFD	BALB/c (female) (6wks)	day 0, 28	IgG^b:ReCon SFD (IM) ≈ Ctrl. IgG^b: ReCon SFD formulation A ≈ B ≈ C.	Maa et al. (2004b)
	[Hypodermic Needle]	[ReCon IPI (IM); ctrl: IM]	[4:4:2]	[19-105]	[n=8]	[day 42]		
Fluvirinf influenza vaccine 2001-2002 (Evans Vaccines, Ltd.) (A/New Caledonia/20/99(H1N1)-like, A/Moscow/10/99 (H3N2)-like, B/Sichuan/379/99-like strain)	none	15, 30μg HA per strain	mannitol:trehalose: dextran (10kD)	SFD	Human (20-50yrs; mean age 31; 22male, 14 female)	day 0	HI: group 1 (IM vaccine) ≈ group 2 (15μg IPI dose) (P>0.05) and HI: group 3 (30μg IPI) > group 1 and group 2, for days 14, 21, and 28.	Dean and Chen (2004)
	[PowderJect ND5.2, 45]	[IPI (arm); ctrl: IM(deltoid)]	[not reported]	[not reported]	[n=12; 3 groups]	[day 0, 14, 21, 28]		

Table A.11: Part 3 of 5 – Findings of past IPI *in vivo* studies by vaccine type, study plan, antigen formulation and adjuvantation.

Vaccine	Adjuvant	Vaccine Load per Injection	Excipients	Formation	Species	Prime - Boost	Titer Response GMT	Reference
	[Device, (bar)]	[Route]	[Ratio]	[Particle diameter (μm)]	[n per condition]	[Bleed]		Year
Virus								
Hepatitis-B surface antigen (HBsAg)	1) 30μg Al(OH)3 2) 6μg Al(OH)3	2μg	1) 3.0% (w/v) Alum, 1.9% (w/v) mannitol , 0.5% (w/v) glycine, 0.61% (w/v) dextran; 2) 0.6% (w/v) alum, 2.8% (w/v) mannitol, 1.2% (w/v) glycine, 0.58% (w/v) dextran	1) SFD, FD 2) SFD	BALB/c (female) (5-7wks);	day 0, 28	IgG^b: SFD formulation (F1, F2) > FD formulation (F1). IgG^b for formulation F1: IM > SFD > FD.	Maa et al. (2003b)
	[Hypodermic Needle]	[ReCon IPI (IP); ctrl: IP]		[38-53]	[n=8]	[day 0, 28,42]		
	IPI: 0.1, 1, 5, 10, 20μg CpG Ctrl: 2.5, 10, 25, 50μg Al(OH)3;	IPI/Ctrl: 0.1, 0.4, 1, 2μg;	trehalose	N2 desiccate, grind, sieve	BALB/c (female) (6-8wks);	day 0, 28	IgG^b: IPI(AVD) No Adj > IM(AVD)+alum (P<0.05); IM required 20-fold dose to achieve similar titers.	Osorio et al. (2003)
	[PowderJect ND1, 50]	[IPI (abd); ctrl: IM]	[pure]	[38-53]	[n=8]	[day 0, 28,42]		
	25μg Al(OH)3, 25μg AlPO4	1μg	40% (w/w) trehalose:mannitol: dextran in dH2O	SFD	Hairles Guinea Pigs (8-10wks) male/female	day 0, 28,49	IgG^b: ReCon IPI ≈ IM Ctrl (P>0.05) IgG^b: IPI ≈ IM Ctrl (P>0.05)	Maa et al. (2003a)
	[PowderJect ND, 40]	[IPI (left inguinal skin); ctrl: IM]	[3:3:4]	[20-70, mean 40]	[n=6]	[day 0, 28,49,63]		
	3.75μg Al(OH)3, 1.1μg Aluminium	0.05μg	10.3% (w/v) solid content: trehalose (3%), mannitol (3%), dextran (4%), Tween80 (0.02%)	Fluid-bed spray-coated lactose	BALB/c (female) (5-7wks);	day 0, 28	IgG^b: IPI Spray-Coated ≈ SC Ctrl (P>0.05)	Maa et al. (2004a)
		[IPI (NA); ctrl: SC]		[80-100, mean 76]	[n=8]	[day 42]		
	none	0.1μg	1) 35%(w/v), trehalose, mannitol, dextran (1kDa) in dH2O 2) 35%(w/v), trehalose, mannitol, dextran (10kDa) in dH2O 3) 35%(w/v), trehalose, mannitol, dextran (37kDa) in dH2O	1) SFD 2) SFD 3) SFD	BALB/c (female) (6-8wks);	day 0, 28	IgG^b: ReCon after 16 days storage: formulation F1 ≈ F2 ≈ F3 ≈ IM ctrl (no Adj.) > naïve.	Maa et al. (2007)
	[Hypodermic Needle]	[ReCon IPI (IM); ctrl: IM]			[n=4]	[day 0, 28, 56]		
	none 100μg Al(OH)3	5μg	35%(w/v), trehalose, mannitol, dextran (1kDa) in dH2O	SFD	Hairless Guinea Pigs (NA wks)	day 0, 28	IgG^p: IPI ≈ Ctrl IM + Adj > Ctrl IM no Adj (P<0.05) IgG^b: IPI ≈ Ctrl IM no Adj ≈ Ctrl IM + Adj	Maa et al. (2007)
	[PowderJect ND, 40]	[IPI (Abd); ctrl: IM]			[n=5]	[day 0, 28,42]		
HIV rgp 120 envelope protein	none	0.2, 1, 5μg	100mg/ml trehalose in dH2O	N2 desiccate, grind, sieve	BALB/c (female) (6-7wks);	day 0, 28	IgG^b: 0.2, 1, 5μg rgp120 IPI did not differ from one another, but were 18-340 fold greater than 5μg rgp120 IM (P<0.01).	Chen et al. (2002b)
	[PowderJect ND, 50]	[IPI (abd); ctrl: IM]	[pure]	[20-53]	[n=8-16]	[day 0, 28,42]		

Table A.12: Part 4 of 5 – Findings of past IPI *in vivo* studies by vaccine type, study plan, antigen formulation and adjuvantation.

Vaccine	Adjuvant [Device, (bar)]	Vaccine Load per Injection [Route]	Excipients [Ratio]	Formation [Particle diameter (μm)]	Species [n per condition]	Prime - Boost [Bleed]	Titer Response GMT	Reference Year
Virus								
Formalin inactivated equine herpesvirus-1 (EHV-1, strain 89 c25)	none	0.5 or 5.0 μg of isolated whole EHV-1 virus	trehalose in dH2O	N2 desiccate, grind, sieve	BALB/cBYJ (female) (5wks);	day 0, 28	IgG^{p} 0.5, 5μg: IPI > IPI Ctrl (P<0.01), 0.5μg IPI ≈ 5μg IPI (P>0.05) IgG^{b} 0.5μg: IPI > IPI Ctrl (P<0.001), 5μg IPI > IPI Ctrl (P<0.01), 0.5μg IPI ≈ 5μg IPI (P>0.05) $IgG^{p,b}$ 0.5, 5μg: IPI > 1mg of pCEHV-1 gD plasmid gene gun. $IgG^{p,b}$ 5μg: IM > IPI (Pp<0.05,Pb<0.01) $IgG^{p,b}$ 5μg: IM > IN (P<0.01), and 0.5, 5μg IPI ≈ IN.	Kondo et al. (2004)
	[PowderJect ND, 50]	[IPI (abd); ctrl: IPI(sugar only)]	20% (w/v)	[35-38nm]	[n=12]	[day 0, 28,42]		
Bacteria								
Diphtheria Toxoid (DT)	100μg AlPO4, 10μg CpG, or both	1μg, 5μg	trehalose	N2 desiccate, grind, sieve	BALB/c (female) (6wks)	day 0, 28	IgG^{b} 1μg: IPI No Adj > SC No Adj (P<0.05) IgG^{b} 1μg: IPI+CpG > SC+CpG (P<0.01) IgG^{b} 1μg: IPI+CpG > IPI No Adj (P<0.01) - 250 fold IgG^{b} 1μg: IPI+Alum > IPI No Adj (P<0.01)- 25 fold IgG^{b}1μg: SC+Alum and SC+CpG > SC No Abj (P<0.01) IgG^{b} 1μg: IPI+ Alum ≈ SC+Alumn IgG^{b} 5μg: IPI+CpG > IPI No Adj (P<0.01)	Chen et al. (2001a)
	[PowderJect ND, NA]	[IPI (abd); ctrl: SC]		[38-53]	[n=8]	[day 0, 28,42]		
	1) 25μg AlPO4; 2) 10μg AlPO4	3.63μg	1) 5% (w/v) trehalose; 2) 1.5% (w/v) trehalose, 0.6% (w/v) dextran, 0.4% (w/v) glycine	1) SD; 2) SFD	Hairles Guinea Pigs (NA wks)	day 0, 28	IgG^{b}: IPI SD (1) formulation elicited no IgG response. IgG^{b}: IPI SFD (2) formulation slightly lower than IM, but SD « IPI and IM.	Maa et al. (2003a)
	[PowderJect ND, 40]	[IPI (left inguinal skin); ctrl: IM]		[38-53]	[n=8]	[day 0, 28,42]		
	none	1μg	10.3% (w/v) trehalose (3%), mannitol (3%), dextran (4%), Tween80 (0.02%)	Fluid-bed spray-coated lactose	BALB/c (female) (5-7wks)	day 0, 28	$IgG^{p,b}$: ReCon IPI(SC) ≈ Ctrl (SC)	Maa et al. (2004a)
	[PowderJect ND, NA]	[ReCon IPI (SC); ctrl: SC]		[40-60, mean 31]	[n=8]	[day 0, 28,42]		
	none	1μg	10.3% (w/v) trehalose (3%), mannitol (3%), dextran (4%), Tween80 (0.02%)	Fluid-bed spray-coated lactose; SD	Hairles Guinea Pigs (NA wks)	day 0, 28	IgG^{b}: IPI Spray-Coated ≈ IPI Spray-Dried; IPI to Control not presented.	Maa et al. (2004a)
	[PowderJect ND, 40]	[IPI (left inguinal skin); ctrl: IM]		[40-60, mean 31]	[n=5]	[day 0, 28,42]		
Tetanus Toxoid (TT)	1) 25μg AlPO4; 2) 10μg AlPO4	3.63μg	1) 5% (w/v) trehalose; 2) 1.5% (w/v) trehalose, 0.6% (w/v) dextran, 0.4% (w/v) glycine	1) SD; 2) SFD	Hairles Guinea Pigs (NA wks)	day 0, 28	IgG^{b}: IPI SD (1) formulation elicited GMT ≈ 1000 response. IgG^{b}: IPI SFD (2) formulation slightly lower than IM (≈$1x10^{7}$), but SD ($1x10^{3}$) « SFD (≈ $7x10^{6}$) and IM.	Maa et al. (2003b)
	[PowderJect ND, 40]	[IPI (left inguinal skin); ctrl: IM]		[38-53]	[n=8]	[day 0, 28,42]		

Table A.13: Part 5 of 5 – Findings of past IPI *in vivo* studies by vaccine type, study plan, antigen formulation and adjuvantation.

Vaccine	Adjuvant [Device, (bar)]	Vaccine Load per Injection [Route]	Excipients [Ratio]	Formation [Particle diameter (μm)]	Species [n per condition]	Prime - Boost [Bleed]	Titer Response GMC	Reference
Tolerance								
Ovalbumin (OVA)	none, 20μg CpG, 0.5mg alum (IP) [PowderJect ND, 35]	10μg OVA [IPI (abd); ctrl: SC]	trehalose [not reported]	N2 desiccate, grind, sieve [38-53]	BALB/c (female) (6-8wks); 	IP sensitize: day 0, 7 IPI or SC: 21, 28, 35, 42, 49, 63 [day 21, 28, 35, 42, 49, 56, 84]	Day 84 IgG2a: IPI OVA+CpG > IPI OVA No Adj - 100 fold increase IgG2a: IPI OVA+CpG > SC - 100 fold increase	Burger et al. (2004)
	none, alum 4mg [ParticlesTherapeutics Venturi (60 dermal) and Fanno Flow (40 mucosal)]	25μg desensitize (IPI), 1μg sensitize (IP) [IPI dorsal skin or buccal mucosa; ctrl: IPI blank, SC]	not reported [not reported]	SFD [mean 45]	BALB/c (female) (6-10wks); [n=10]	IP sensitize: day 0, 34 IPI desensitize: day 7, 9 14, 16, 21, 23, 28, 30 [day 34, 51, 65]	Pre day 34: IgE: desensitized ≈ control Day 51, 63 IgE: IPI OVA < IPI blank (P<0.001), SC < IPI blank and no treatment (P<0.01); IPI OVA ≈ SC, mucosal IPI ≈ dermal IPI Day 51: IgG1: IPI OVA < IPI blank (P<0.001) IgG2a: IPI OVA ≈ IPI blank Day 65: IgG1: IPI OVA < IPI blank (P<0.01) IgG2a:IPI OVA ≈ IPI blank	Kendall et al. (2006)

Table A.9 - A.13 legend: IM=intra muscular. SC=subcutaneous. IP=intra peritoneal. IN=intra nasal. Abd=abdomen. Ctrl=control. Adj=adjuvant. SFD=spary freeze dry. SD=spray dry. FD=freeze dry. GMT=geometric mean titre. HI=haemagglutination inhibition. HA=haemagglutinin. Ig=immunoglobulin. ReConVac=reconstituted vaccine. CT=cholera toxin. CTB=non-toxix cholera toxin B subunit. LTR72= E coli heat labile toxin mutant protein, reduced toxicity. NA=not available. LTK63=E coli heat labile toxin mutant protein, no toxicity. CpG=cytosine-phosphatee-guanine. p=post prime. b=post boost. *=bivalent vaccine (indicates strains used). AVD=any vaccine dose. dH2O=deionized water. IPI=IPIdermal powder immunization.

Table A.14: Summary of IPI challenge studies.

Reference	Species	Duration [days]	Day post Immune	Vaccine Type Species	Challenge Type	Vaccine Dose [μg]	Injection Method	Adjuvant Type	Adjuvant Dose [μg]	Challenge Dose [LD50]	IgG Titer	Percent Survival
Chen et al. (2000)	Balb/C	14	32	inactive Aichi68	MouseAichi	25	IPI	None	NA	10	16000	100
						5	IPI	None	NA	10	10000	100
						1	IPI	None	NA	10	6300	100
						25	SC	None	NA	10	2500	70
						5	SC	None	NA	10	2000	60
						1	SC	None	NA	10	630	0
				BALB/C		0	Naïve	None	NA	10		0
Chen et al. (2000)	Balb/C	14	48	1998-1999 season human influenza	MouseAichi	1.5	IPI	None	NA	10	400000	90
						1.5	SC	None	NA	10	160000	0
				BALB/C		1.5	Naïve	None	NA	10		0
Chen et al. (2001b)	Balb/C	20	32	A/Sydney	MouseAichi	5	IPI	None	NA	10	900	40
						5	IPI	CpG	10	10	950	60
						5	IPI	CT	5	10	1100	100
						5	IPI	CT and CpG	15	10	1200	100
				BALB/C		5	Naïve	None	NA	10	1100	100
			46	1998-1999 season human influenza	MouseAichi	5	IPI	None	NA	10	11000	100
				A/Sydney	MouseAichi	5	IPI	None	NA	10	10000	90
Chen et al. (2002a)	Balb/C	22	28	1998-1999 season human influenza	MouseAichi	1.5	IPI	None	NA	10000PFU	23	30
						1.5	IPI	CTB	1	10000PFU	26	60
						1.5	IPI	CTB	5	10000PFU	30	100
						1.5	IPI	CTB	10	10000PFU	40	100
						1.5	IM	None	10	10000PFU	8	0
				BALB/C		1.5	Naïve	None	NA	10000PFU		0
Chen et al. (2003)	Macaques	28	60	2000 to 2001 season trivalent influenza	A/Sydney/5/97	15	IPI	None	NA	100000 TCID50	50	100
						15	IPI	QS-21	50	100000 TCID50	100	100
				Macaques		15	IM	None	NA	100000 TCID50	55	100

Table A.14 legend: IM=intra muscular. SC=subcutaneous. IP=intra peritoneal. IPI=IPIdermal powder immunization. Ig=immunoglobulin. CT=cholera toxin. CTB=non-toxix cholera toxin B subunit. LTR72= E coli heat labile toxin mutant protein, reduced toxicity. NA=not available. LD50=median lethal dose. PFU=plaque-forming unit. TCID=tissue culture infective dose.